Exploring and Modeling High-excitation Emission in the Ejecta and the Wind of Eta Carinae

A DISSERTATION
SUBMITTED TO THE FACULTY OF THE GRADUATE SCHOOL
OF THE UNIVERSITY OF MINNESOTA
BY

Andrea Mehner

IN PARTIAL FULFILLMENT OF THE REQUIREMENTS
FOR THE DEGREE OF
DOCTOR OF PHILOSOPHY

June, 2011

Acknowledgements

I am greatly indebted to my advisor Kris Davidson and to Roberta Humphreys. It was a great pleasure working with you over the last years! Thank you very much for your guidance and for sharing your knowledge and experience with me. I would like to thank the entire University of Minnesota Astronomy Department for making it possible for me to obtain my degree there. A special thanks to Alex Heger and Bob Gehrz for being on my preliminary and final exam committees. I want to thank John Martin for sharing the pain of the Gemini data reduction and Gary Ferland for his advise on Cloudy. I am especially grateful to Kazunori Ishibashi for inviting me to Nagoya University, Japan, and spending an enormous amount of time to get the HST Treasury STIS pipeline running again and instructing me on how to use it. I also want to thank my Diplom thesis advisor Eike Guenther for taking the time to explain astrophysical topics to a newcomer in the field and for sending me to observing runs in Chile and Spain during my time at the Thüringer Landessternwarte Tautenburg, Germany.

I want to thank my parents for never telling me what I should do in life. At least I only have myself to blame! And my sister for always being there and for frustrating me with her absolute belief that whatever I want will just magically happen. I want to thank my best friend Danny Garcia who made sure over the last years, sometimes by force, that I never forgot to have fun in life.

I also want to thank Philipp Nielsen for making me laugh. Henry Seidel for the endless hours at our kitchen table in Jena. Christoph Knappe, Mathias Weiß, and Martin Voitsch for making studying physics and life in Jena so enjoyable. Yaiza García Sánchez, who is the loveliest person and the best cook! Thank you so much for the time we spent together in Spain, Germany, and during nice vacations around the world. Steve Schulze for always dropping everything else to listen to my worries and complaints, or to just have random nonsensical conversations. Your more than inappropriate jokes and stories always made my day! Chelsea Tiffany for taking the time to talk to me whenever I needed a break during the first three years of my time in Minnesota when we shared an office. I want to thank her and Jennifer Delgado for our Friday lunches and dinners and for successfully distracting me from my work with their endless suggestions of books and movies. A big thanks also to Ke-Jung Chen for lightening up my day with his cheerful nature and for being such a loyal coffee and bubble tea companion.

My research was partially supported by several grants from the Space Telescope Science Institute (STScI) and the Graduate School at the University of Minnesota that awarded me with the Doctoral Dissertation Fellowship during 2010–2011.

Dedication

To those who made it possible for me to see the world.

Exploring and Modeling High-excitation Emission in the Ejecta and the Wind of Eta Carinae

by Andrea Mehner
under the supervision of Kris Davidson

ABSTRACT

Eta Carinae (η Car) is the most massive, most luminous star in our region of the Galaxy. It is an evolved massive star system and therefore provides many clues to the fate of the most massive stars. In the 1840s its unstable nature culminated in the *Great Eruption* when it briefly became the second brightest star in the sky and ejected more than ten solar masses, which today enshroud the surviving star as a bipolar nebula. The "supernova impostor" phenomenon and its aftermath constitute a major gap in the theory of massive stars, and η Car is the only example that can be studied in detail. Its recovery has been unsteady with unexplained photometric and spectral changes in the 1890s and 1940s.

Combining data from *HST* STIS and *Gemini-S* GMOS between 1998 and 2010, I analyzed several spectroscopic cycles that occur every 5.54 years. In addition, I used some data from the *VLT* UVES, *Magellan II* MIKE, and *Irénée du Pont* B&C instruments. Observations with a variety of different slit position angles made it possible to map the emission across the nebula and the complex outer ejecta of η Car permit to observe the star at different stellar latitudes via reflected light.

In order to study the distribution of gas and ionizing radiation around η Car and their implications for its likely companion star, I examined several high-excitation emission lines. The principal results are: (1) The high-excitation fluxes varied systematically and non-trivially throughout η Car's 5.5-year spectroscopic cycle. (2) A brief, strong secondary maximum occurred just before the 2003.5 spectroscopic event. (3) These emission lines are strongly concentrated at the Weigelt knots several hundred AU northwest of the star. With less certainty, [Ne III] appears to be somewhat more concentrated than [Fe III]. (4) A faster, blueshifted component appears concentrated near the star and elongated perpendicular to the system's bipolar axis. (5) Using the photoionization program Cloudy, I estimated the range of parameters for the hot secondary star that would give satisfactory high-excitation line ratios in the close ejecta; $T_{\rm eff} \approx 40,000$ K, $L \sim 4 \times 10^5\ L_\odot$, and $M_{\rm init} \sim 40$–$50\ M_\odot$, for example, would be satisfactory. The allowed region in parameter space is wider and mostly less luminous than some previous authors suggested.

Spectra obtained with *Gemini* GMOS throughout 2007–2010 were used to observe the 2009 spectroscopic event from different stellar latitudes. The He II λ4687 emission, only observed during the "events," was analyzed in spectra in direct view and in reflected polar-on spectra at FOS4. The time-delay of He II at FOS4 is about 18 days and therefore consistent with the predicted additional time-travel time at FOS4. The equivalent width and radial velocity behavior of He II at FOS4 mirrors the behavior observed in direct view. These findings imply a symmetric geometry for the origin of the He II emission and are difficult to reconcile with some proposed He II emitting regions and some orbital models. H I, He I, and Fe II lines, observed at different latitudes, reveal details about the changing wind during the "event."

N II $\lambda\lambda$5668–5712 emission and absorption lines behave qualitatively like the He I lines. Spectral lines of η Car's stellar wind regions can be classified into four physically distinct categories: 1) low-excitation emission such as H I and Fe II, 2) higher excitation He I features, 3) N II lines, and 4) He II emission. These categories have different combinations of radial velocity behavior, excitation processes, and dependences on the secondary star. In this sense the N II features resemble the He I lines, but they represent zones of lower ionization. This combination of attributes appears to be unique in η Car's well-observed spectrum. N II probably excludes some proposed models, such as those where He I lines originate in the secondary star's wind or in an accretion disk.

Spectra in 2009 and 2010 showed that major stellar-wind emission features in the spectrum of η Car have recently decreased by factors of order 2 relative to the continuum. This is unprecedented in the modern observational record. The simplest explanation is a rapid decrease in the wind density.

Work presented in this thesis was published in Mehner et al. (2010a,b, 2011).

Contents

List of Tables

List of Figures

Chapter 1

Astrophysical Motivations

Massive stars are extremely rare but they play an important role in the galactic and cosmic evolution. They were the first stars to form in the early universe and their ionizing radiation field, strong stellar winds, and supernova (SN) explosions influence star formation and enrich the interstellar and intergalactic medium. They evolve through different stages during their lifetime and produce various types of SNe. The evolution of massive stars is difficult to model, primarily because of their extreme mass loss which has a profound effect on the evolution. They lose about half of their mass during core-H burning. Mass loss after the main sequence becomes even more complicated as the star can experience episodic pre-SN mass ejections during the Luminous Blue Variable (LBV) phase. Very rare classes of objects such as LBVs imply very short but perhaps critical stages in the evolution of massive stars. Their existence has not been determined theoretically. In addition, effects of mixing, convection, rotation, and binarity are uncertain. Therefore, observations play an important role in testing the models.

Eta Car is by far the most observable very massive star ($M > 100\ M_{\odot}$), the only "SN impostor" that can be observed in great detail, and it has other extraordinary attributes (see reviews by many authors in Humphreys & Stanek 2005).[1] Eta Car gives us valuable clues to the behavior of extremely massive stars. The episodic nature of mass loss near the top of the H-R diagram, physics of giant eruptions and subsequent recovery,

---

[1] Throughout this thesis, if I omit individual references for either a minor detail or a well-known generality about η Car, see Humphreys & Stanek (2005); Gull et al. (2001); Morse et al. (1999); Davidson & Humphreys (1997); and numerous refs. cited therein.

behavior of outflows above the Eddington limit, polar winds caused by rotation, and several exotic nebular processes can be studied. It is the only really observable example of structural recovery from a "SN impostor" event.

Early observations between 1600 and 1800 showed η Car oscillating between 2nd and 4th magnitude in possible LBV-style eruptions. During LBV eruptions the wind becomes denser and more opaque, causing the photosphere to move outward until its characteristic temperature falls below 9000 K. Eta Car begun to vary more rapidly after 1820. In the late 1830s it became suddenly one of the brightest stars in the sky. During this *Great Eruption* from 1837–1858 more than 10 $M_\odot$ were ejected, forming the Homunculus nebula. The L/M ratio was substantially above the classical Eddington limit for about 20 years. Eventually, η Car faded to 8th magnitude as the eruption ended and circumstellar dust formed. The total luminous output of the eruption rivaled that of a SN, but the star survived and we now see it surrounded by ejecta. A *Second Eruption* from 1888–1895 is best understood as similar to a classical LBV eruption. During the 20th century, η Car has begun to brighten again. Today, 150 years after the close of its *Great Eruption,* η Car has not yet returned to thermal and rotational equilibrium (Maeder et al. 2005; Davidson 2005). Its recovery has been erratic, with unexplained photometric and spectral changes in the 1890s and 1940s (Humphreys et al. 2008).

1.1 High-excitation Emission – Connections with the 5.54-year Cycle and the Secondary Star

Eta Car and its ejecta produce more than 2000 identified emission lines, mostly of complex singly ionized species such as Fe^+ and Ni^+ (Gaviola 1953; Aller & Dunham 1966; Thackeray 1967; Viotti et al. 1989; Hamann et al. 1994; Zethson 2001). Satisfactory analyses of these low-ionization features have not been feasible, because they depend on radiative excitation processes which are extremely intricate. A few higher-ionization spectral lines, however, offer valuable clues because they are less complicated: [Ne III], [Ar III], [Fe III], etc. They originate in slow-moving gas that was ejected from η Car

100 to 200 years ago. They help to constrain the nature of a hot companion star which is thought to exist, but which has not been observed directly, and also give clues to the nature and distribution of ejecta within 3000 AU of the central star.

Several distinct types of spectra occur within $1''$ of η Car. (1) The stellar wind produces broad emission and absorption lines, several hundred km s^{-1} wide. (2) Slow-moving ejecta at $r \gtrsim 0.15''$ (i.e., more than 300 AU from the star) emit features narrower than 50 km s^{-1}. (3) The same ejecta contain dust which reflects the stellar-wind spectrum. (4) Faster ejecta also show both intrinsic and reflected spectra, though these are relatively faint in the central region. The excitation mechanisms of the high-excitation features are quite different from the narrow low-ionization lines. The latter are strongly influenced by radiative processes such as resonance absorption of a UV photon leading to the emission of two or more lower-energy photons. The high-ionization lines, however, depend on the same processes that dominate in ordinary nebulae – especially photoionization by a hot star.

The high-ionization lines have not been spatially mapped prior. Most of them are narrow and thus do not represent the 300–1000 km s^{-1} stellar wind. The first *HST* spectra of η Car showed that *low-excitation* features such as the narrow [Fe II] lines originate in the vicinity of the Weigelt knots, a set of three condensations 0.1–$0.3''$ northwest of the star (Weigelt & Ebersberger 1986; Davidson et al. 1995, 1997). These knots move outward rather slowly ($v \sim -40$ km s^{-1}), probably near the equatorial plane of the system (Hofmann & Weigelt 1988; Weigelt et al. 1995; Davidson et al. 1997; Zethson et al. 1999; Dorland et al. 2004; Smith et al. 2004)). Later, *HST* STIS data confirmed that low-excitation lines collectively account for much of the integrated brightness in that region (e.g. Gull et al. 1999; Johansson et al. 2000; Zethson et al. 1999). STIS could not resolve an individual Weigelt knot, but in cases where its slit crossed one of them, the spatial distribution of [Fe II] brightness peaked at the knot's position. Meanwhile many *HST* images showed the individual knots at various wavelengths, albeit not well resolved. Combining all these facts, most authors agree that the narrow low-excitation emission lines are largely concentrated in the Weigelt knots. The high-ionization features, on the other hand, had little influence on the *HST* images and on Weigelt's original speckle interferometry. Given their very different ionization states and excitation mechanisms, it is not safe to assume that they coincide with the knots.

They might represent diffuse lower-density gas surrounding the knots. This uncertainty inspired the work reported in section 3.1.

Observers noticed long ago that the high-excitation lines occasionally weaken or even disappear and then gradually return to their normal strength after a few months (Gaviola 1953; Thackeray 1967; Whitelock et al. 1983; Zanella et al. 1984). Eventually enough "events" had been observed to show that they recur with a period of 5.54 years (Damineli 1996; Whitelock et al. 1994; Damineli et al. 2008b). Many authors have discussed these phenomena, generally concluding that (1) there is a companion star in a highly eccentric 5.54-year orbit and (2) a spectroscopic event occurs near periastron due to a mass ejection and/or a disturbance in the wind and/or some sort of eclipse by the primary wind. The projected separation between the stars is less than 30 AU $\sim$ 13 mas, unresolvable by *HST,* and the secondary star has not been directly detected.

The simplest theories do not predict much variation of the high-excitation lines between spectroscopic events. In those models the two stars are usually more than 10 AU apart and the densest regions of the primary wind are usually on the far side of the secondary, from our point of view. Therefore η Car's spectrum at average times has received comparatively little attention. In section 3.2, interesting behavior between the 1998.0 and 2003.5 "events" is described.

The usefulness of a hot companion for exciting η Car's high-ionization lines has been recognized for more than a decade (Davidson 1997, 1999). This is an appealing idea because we can deduce information about the secondary star from the high-excitation spectral features, via photoionization modeling. The secondary star's quantitative parameters remain open to question. The opaque wind of the primary star probably has a characteristic temperature below 20,000 K (Hillier et al. 2001), too cool to account for the high-ionization lines. Its hypothetical companion, on the other hand, presumably must be a massive star in order to cause an "event," but not as massive as the primary and therefore less evolved; so we expect it to be hot. The X-ray spectrum implies a 3000 km s^{-1} wind (Pittard & Corcoran 2002). Since that object has not been observed directly, the wind speed is almost our only other clue to its parameters. Such a fast wind almost always implies $T_{\rm eff} \gtrsim 37,000$ K. Verner et al. (2005) suggested spectral type and luminosity class O7.5 I, but it is not clear that such an object would fulfill the requirements. This question is explored in section 3.4.

1.2 Secular Changes in the Wind

Eta Car may have entered a phase of accelerated development 12–15 years ago. From 1953 to the mid-1990s, ground-based 'V' photometry of star plus ejecta brightened at a rate of 0.024 mag yr^{-1}, with brief deviations smaller than ±0.3 mag (Fig. 2 in Davidson et al. 1999a). In the past decade, however, it has risen 0.6 mag above that earlier trend line (Fig. 3 in Fernández-Lajús et al. 2009). The central star shows a more dramatic increase, a factor of more than 3 in UV-to-visual *HST* data since 1998 (Martin & Koppelman 2004; Martin et al. 2006b; Davidson et al. 2009). A decrease in the amount of circumstellar dust may be responsible, but that requires some change in the wind and/or radiation field. Meanwhile the periodic spectroscopic events of 1998.0, 2003.5, and 2009.0 differed in major respects (Davidson et al. 2005; Richardson et al. 2010; Corcoran 2010). Very likely the mass-loss rate has been decreasing at an inconstant pace, while rotational spin-up may play a role (Humphreys et al. 2008; Martin et al. 2006b; Davidson et al. 2005; Smith et al. 2003).

All those discussions, however, seemed to face an embarrassing observational contradiction. From the first *HST* spectroscopy in 1991 until STIS failed in 2004, *η Car's spectrum showed no major change* except during the temporary spectroscopic events. One might have expected some sort of spectral evolution to accompany the rapid brightening after 1998. However, observations in 2007–2010 with *Gemini* GMOS and *HST* STIS reveal major spectral changes, discussed in chapter 4. They are not subtle; evidently the wind has been altered, at least temporarily and perhaps for the indefinite future.

1.3 The 2009 Spectroscopic Event

Beginning in the mid-1940s η Car began to exhibit occasional spectroscopic changes, now recognized as a 5.54-year spectroscopic/photometric cycle. Occasionally its high-excitation He I, [Ne III], [Fe III] emission lines disappear for a few weeks or months (Gaviola 1953; Zanella et al. 1984) while other changes also occur, specifically in the X-ray (e.g., Corcoran et al. 1997; Ishibashi et al. 1999b,a) and infrared flux (e.g., Whitelock et al. 1994; Feast et al. 2001). These spectroscopic events recur with a period close to 2023 days (Damineli 1996; Whitelock et al. 1994; Damineli et al. 1999, 2000; Whitelock et al. 2004; Martin et al. 2006a; Damineli et al. 2008b; Fernández-Lajús et al. 2010). They have been attributed to (1) eclipses of a hot secondary star by the primary wind (Damineli et al. 1997; Davidson 1997; Ishibashi et al. 1999b; Stevens & Pittard 1999; Pittard & Corcoran 2002), or (2) disturbances in the primary wind triggered by a companion star near periastron (Davidson 1997, 1999; Smith et al. 2003; Martin et al. 2006a), or (3) a thermal/rotational recovery cycle (Zanella et al. 1984; Davidson et al. 2000; Smith et al. 2003; Davidson 2005). These ideas are not mutually exclusive, and either (2) or (3) may indicate an undiagnosed instability near the Eddington limit (Davidson 2005; Martin et al. 2006a).

Observations during the 2003.5 "event" supported the wind-disturbance/instability suggestion, although an eclipse probably does occur with lesser consequences. Photometric behavior, a late X-ray flare, and an unpredicted He II λ4687 outburst (Steiner & Damineli 2004; Martin et al. 2006a) were especially significant. Very likely an instability near the base of η Car's latitude-dependent wind was triggered by the secondary star near periastron, see section 9 in Martin et al. (2006a).

Meanwhile the longer-term behavior changed dramatically. The central star brightened rapidly after 1998 (Davidson et al. 1999a; Martin & Koppelman 2004; Martin et al. 2006b, 2010), and major spectral features differed between the 1998.0 and 2003.5 "events" (Davidson et al. 2005). Destruction and/or lessened formation of dust played a role, but the root cause must involve a secular change in the UV flux or the wind density or both (Davidson et al. 1999a; Martin et al. 2006b). Thus, from the viewpoint of 2007–2008, observations of the expected 2009.0 "event" would merit a high priority for comparisons with 2003.5 and 1998.0. Unfortunately the Space Telescope Imaging Spectrograph on the Hubble Space Telescope (*HST* STIS) had failed in 2004, and thus was not available to separate the star from ejecta. Later, after the "event," STIS became operational again and proved that emission lines from η Car's wind had greatly weakened since 2004; the mass loss rate had probably decreased by a factor of the order of 2 or 3 in a time span of several years (Mehner et al. 2010b; see also Kashi & Soker 2009a; Corcoran et al. 2010). *Therefore the 2009.0 spectroscopic event occurred in physical circumstances appreciably different from its predecessors.*

Ground-based spectra of η Car represent an unresolved mixture of the central star plus bright ejecta located at $r \sim 0.2''$ to $1''$, and the high spatial resolution of *HST* STIS was not available from mid-2004 to mid-2009. Fortunately, though, the central star has brightened more than the nearby ejecta in the past decade, so ground-based observations of it have become relatively less contaminated than at earlier times.[2] Thus, starting in 2007, the star and several offset positions in the Homunculus nebula were observed with GMOS on the *Gemini-South* telescope. Apart from the question of secular changes, the intent was to measure some aspects of the spectroscopic event better than had been done in 2003 and earlier. A primary goal was to monitor the behavior of the peculiar He II $\lambda4687$ line with more frequent observations during the 2009 "event." Also, the spectrum reflected by dust in the SE Homunculus lobe, a "polar" view of the star, was observed to monitor the "event" from a different viewing angle.

1.4 Classification of Spectral Lines in the Stellar Wind

In η Car's broad-line stellar wind spectrum, the high-excitation helium features have different profiles and fluctuate differently from the "normal" lines of H I, Fe II, etc. Most authors now assume that the He I emission depends on photoionization by a hot companion star, see section 6 of Humphreys et al. (2008) and references therein. Observed He II emission is most likely excited by soft X-rays from unstable shocks (Martin et al. 2006a, but cf. Steiner & Damineli 2004, Kashi & Soker 2007, and Soker & Behar 2006). Features of these types are important because they show direct influences by the secondary star and the wind-wind collision region. The only clear examples have been helium lines, whose source geometry is both complex and controversial. I found similar characteristics in a set of N II features, which sample lower-ionization gas than the helium lines.

Broad H I and Fe II emission lines represent η Car's stellar wind spectrum that would be present even if the companion star did not exist (Hillier et al. 2001). Their main components always remain close to system velocity (roughly -8 km s^{-1}, Davidson et al. 1997; Smith 2004).

The He I emission lines, by contrast, shift progressively blueward through most of the 5.54-year spectroscopic cycle. When a spectroscopic event occurs they show a more abrupt negative shift, followed by a rapid positive reversal to renew the cycle (see mid

---

[2] Here "central star" really means the opaque primary wind. The secondary star is also included, but its spectrum is too faint to be observable at accessible wavelengths.

panel of Figure 7.1, and Figs. in Nielsen et al. 2007). The overall range of variation is about 0 to -250 km s^{-1}. Evidently these changes represent flows of highly ionized material, modulated by the secondary star. As the secondary moves in its orbit, it progressively illuminates regions with differing velocity fields, and may perturb some of them. The details are model-dependent: compare, e.g., Nielsen et al. 2007; Damineli et al. 2008a; Humphreys et al. 2008; Kashi & Soker 2007, 2008; Martin et al. 2006a; Davidson et al. 2001a.

He I *absorption* shows a similar pattern with variations between -300 km s^{-1} and -550 km s^{-1}. This behavior is mirrored by the puzzling He II λ4687 emission, observed during spectroscopic events (Steiner & Damineli 2004; Martin et al. 2006a). Hydrogen and Fe II lines have components that behave qualitatively like He I, but cannot be measured separately because they overlap the steady "normal" H I emission profiles.[3]

Until now no other species were found in η Car with velocity variations like the helium lines, and without strong steady components. In chapter 7, I report that lines of the N II $\lambda\lambda$5668–5712 multiplet do match this prescription. They are always present but were not discussed previously because they are weak. They are noteworthy because they probably depend on a form of excitation by the hot secondary star, but in different regions than the He I lines. They seem reasonable in some models, but are difficult to explain in others. For example, models where the helium emission originates in a small region close to the secondary star have difficulties in this respect.

Historically, hot windy objects such as P Cygni show strong N II emission and absorption (e.g., Beals 1935; Struve 1935; Swings & Struve 1940). Since nitrogen is abundant in η Car's CNO-processed wind, Hillier et al. (2001) expressed surprise that N II is not more conspicuous there. Some of the features discussed were identified by Gaviola (1953), but were too weak to be noted by Thackeray (1953). More recently they have been detected by Damineli et al. (1998) and Nielsen et al. (2009) without discussion. The lines discussed here are physically different from [N II] λ5756 which has much lower energy levels.

---

[3] Velocities quoted are measurements of *Gemini* GMOS observations during the 2009 spectroscopic event, see also Nielsen et al. (2007) and Steiner & Damineli (2004) for similar values during the 2003.5 "event."

Chapter 2

Observations and Analysis

2.1 *HST* STIS Data 1998–2004 and 2009–2010

Eta Car was observed with the *Hubble Space Telescope* Space Telescope Imaging Spectrograph (*HST* STIS) starting shortly after the spectroscopic event in 1998. Spectra of η Car were obtained throughout the following years until a power supply in STIS failed in 2004 August, rendering it inoperable. However, the obtained data set covered an entire 5.54-year spectroscopic cycle. Most of the observations were concentrated around the "event" in mid-2003. STIS was successfully repaired during the *HST* Servicing Mission #4 (SM4) in 2009 May and subsequent data of η Car were obtained in 2009 and 2010.

HST STIS provides the highest spatial resolution ever attained in spectroscopy of η Car. The STIS/CCD is a 1024×1024 pixel detector with $0.05''$ square pixels, covering a nominal $52''\times52''$ square field of view and operating from below λ2000 Å to about λ10,000 Å. Spectra were obtained with the $52''\times0.1''$ slit in combination with the G230MB, G430M, and G750M gratings over the entire wavelength regions at resolutions $R \sim 5000$–10,000. The observations included a variety of slit positions and orientations, with a concentration at position angle $PA = 332^\circ$ where the star and Weigelt knots B and D fell within the slit.[4] Altogether, a map of the slit locations resembles a quasi-random ensemble of intersecting lines (see, e.g., Figure 3.1). 2009 June and December

---

[4] The star and the three main Weigelt knots are labeled A, B, C, and D, with relative positions described by Weigelt & Ebersberger (1986); Hofmann & Weigelt (1988); Smith et al. (2004). Their separations expand by about 1% per year.

data mapped a region up to 1″ from the central source with parallel slit position offsets of 0.1″.

2.1.1 Data Reduction with the HST Treasury Pipeline

The HST Treasury Project for Eta Carinae reduced the *HST* STIS/CCD data including several improvements over the normal STScI pipeline and standard CALSTIS reductions.[5] Modeling and interpolating the pixels in a special way improved the effective resolution along the cross-dispersion axis, compared to most other published STIS/CCD data (Davidson 2006). The "scalloping" which is obvious in narrow extractions from data reduced by former methods is mostly eliminated by this new method. The data were rebinned so that one pixel in the reduced data corresponds to 0.5 original CCD pixel, about 0.025035″. Initial bad/hot pixel removal, wavelength calibration, and flux calibration matched or exceeded the STScI pipeline and CALSTIS.

Spectroscopic sensitivities and detector temperature change with time due to contamination of the optics. The subdwarf AGK +81D266 has been monitored regularly since 1997 for all three CCD low-dispersion gratings, using the 52″x2″ slit. For data obtained after SM4, the HST Treasury pipeline was updated using the sensitivity correction values from Goudfrooij et al. (2009). The flux calibration of the updated pipeline was checked by comparing spectra of *HST's* primary standard stars (the white dwarfs G191B2B, GD 153, GD 71, HZ43), and it's sensitivity monitor (the subdwarf AGK +81 266) reduced both with the updated HST Treasury Project pipeline and the standard STScI pipeline.

The instrument is less reliable after SM4 (Figure 2.1); the accuracy of the flux calibration at wavelengths $\lambda2500$ and $\lambda3300$ Å is only about 5%. The wavelength regions around $\lambda\lambda2500,3300$ Å are of interest for synthetic photometry of STIS spectra (Martin & Koppelman 2004; Martin et al. 2006b, 2010), but the results are representative of the entire spectral range. (No obvious explanation for the spike between 2003 November and 2004 January was found.) No major discrepancies in the flux calibration between the two pipelines were found, also because the recent STScI pipeline incorporates the same corrections for the spectroscopic sensitivities and detector temperature. While an

---

[5] The data archive for the HST Treasury Program on Eta Carinae is available online at http://etacar.umn.edu/.

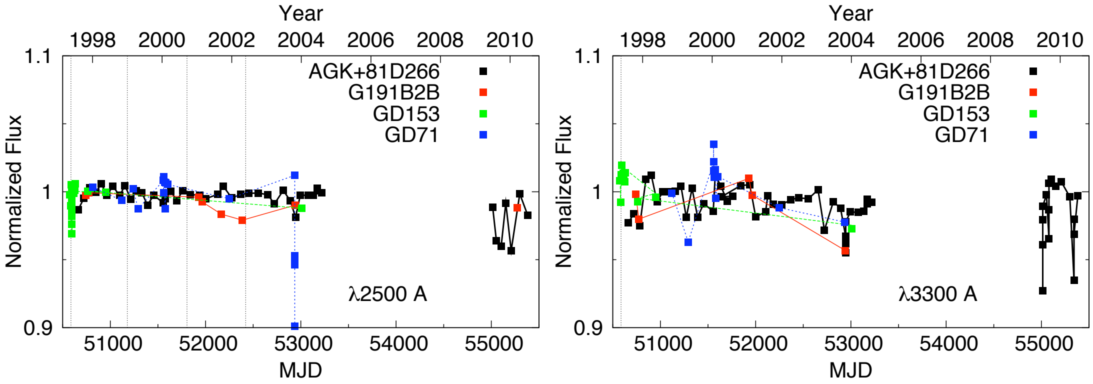

Figure 2.1: Normalized flux for *HST* standard stars at λλ2500,3300 Å (1997–2010). Epochs of linear fitting segments are indicated by vertical dotted lines, G230LB: 1997.38, 1999.00, 2000.71, 2002.40, 2011.00; G430L: 1997.38, 2011.00 (see Goudfrooij et al. 2009).

accuracy of 5% in the flux calibration seems large, the continuum flux differs of up to 10% in observations of η Car, even in consecutive exposures, caused by pointing errors in combination with the narrow $0.1''$ slit.

2.1.2 Spectral Analysis and Mapping Technique

For the analyses of the *HST* STIS data I used software tools that were developed by K. Davidson, M. Koppelman, M. Gray, and J. C. Martin.[6] Many local spectra centered at uniformly-spaced locations were extracted along the STIS slit; the interval between successive locations was $0.025''$ and each extraction was $0.1''$ wide. At η Car's distance, $D \approx 2300$ pc (Davidson & Humphreys 1997; Davidson et al. 2001b; Smith 2006), $0.1''$ corresponds to a projected size of about 230 AU.

For the spatial maps in chapter 3, data extending from November 1998, 11 months after the 1998.0 "event," to the beginning of June 2003, a few weeks before the 2003.5 "event" were used (Table 2.1). Fluxes were measured by integrating each line above the continuum, or in some cases above an underlying broad emission profile. Each measurement represented a spatial interval of about $0.1''$ along the slit, the extraction width mentioned above.

The assembly of a spatial map for each emission feature was a non-trivial exercise.

---

[6] The HST Treasury Project for Eta Carinae software is available online at http://etacar.umn.edu/

Table 2.1: Times of *HST* STIS observations used for spatial maps of high-excitation emission in section 3.1

Date (UT)	MJD	Slit PA[a] (°)	$N_{\rm slit}$
1998 Nov 25	51142	227	1
1999 Feb 22	51231	332	1
2000 Mar 21	51624	332	1
2001 Apr 18	52017	22	1
2001 Oct 01	52183	165	1
2002 Jan 20	52294	278	1
2002 Jul 05	52460	69	2
2003 Feb 13	52683	303	1
2003 Mar 29	52727	332	1
2003 May 05	52764	27	1
2003 May 17	52776	38	2
2003 Jun 02	52792	62	2

[a] PA ± 180° gives same spatial coverage.

Of course each STIS spectrogram sampled only the region covered by the slit, effectively a strip about $0.13''$ wide if one allows for *HST's* spatial resolution. On each observation date only one or two slit positions had been used; but these varied in orientation and some of them were offset from the star, so the whole ensemble sampled a useful fraction of the area within $0.5''$ of the star. Now consider any one of the measured emission lines. Subject to later verification, suppose that the feature's relative spatial distribution did not vary much – i.e., tentatively assume that maps at any two different times closely resemble each other except for a normalization factor. This statement does not apply to observations during an "event," which were not used. Since the line's brightness varied through the spectroscopic cycle, the values measured in each spectrogram were renormalized so that the feature in question always had an adjusted value of unity at the only place that was observed on every occasion: the central star. Fortunately some narrow-line gas exists along our line of sight to the star, producing [Ne III], [Fe III], and He I lines superimposed on its spectrum. These reference measurements were less precise than those elsewhere, because the superimposed narrow emission features were weak compared to the underlying stellar spectrum. For each offset slit position, the renormalization factor was adjusted to maximize the consistency at intersections with other slit positions.

The above procedure obviously depends on some insecure assumptions, but one can apply consistency tests. Some of the slit positions passing through the star were close together or were used on more than one occasion, and each offset slit position intersected several of the others (see Figures in section 3.1). Consequently a substantial number of points were independently re-observed at well-separated times. Note that each slit sample had only one adjustable parameter, its renormalization factor. Based on comparisons of the points re-observed in separate spectrograms, the overall self-consistency of each map turned out to be quite good, and no local inconsistency worse than the expected measurement errors were found. Therefore the assumptions were sufficiently valid. Incidentally, possible time-delay effects cannot strongly influence these maps, since the light-travel-time for $0.5''$ is only about a week at the distance of η Car, and the cooling time in a He^{+} region is less than a month for electron densities $n_{\mathrm{e}} > 10^{5}$ cm^{-3}.

2.2 *Gemini-S* GMOS Data 2007–2010

To cover the 2009.0 "event," long-slit spectroscopy was obtained at *Gemini-South* with the Gemini Multi-Object Spectrograph (GMOS) between 2007 and 2010. During the 2009 spectroscopic event observations were taken only a few days apart. A journal of all observations is given in Table A.1, including the slit position offsets relative to η Car at central wavelength, see issues below. In most cases, the B1200 line grating with a $0.5''$ slit was used at three tilt angles to cover the spectrum from $\lambda3700$ to $\lambda7500$ Å. The spectral resolving power is $R \sim 4400$. In a few cases slit widths of $0.25''$ and $0.7''$ were used, either to not overexpose the strong Hα line or to collect more of the refracted light (light from the star at certain wavelength might not even enter a narrow slit due to atmospheric differential refraction if a narrow slit is used). The slit, with a position angle of $PA = 160^{\circ}$, was placed at four different positions; on the star, at two offset positions $\pm0.75''$ to the star, and at a position known as "FOS4" in the SE lobe of the Homunculus ($-2''$ offset from the star).

Most observations were acquired with a blind offset from a reference star. In a blind offset a reference object is used for fine-tuning the slit centering. The accuracy of such offsets decreases with increasing distance to the reference star, here the accuracy was 0.1–$0.2''$. Unfortunately, in most observations the coordinates used for the reference star and η Car were from different coordinate systems, so that slit positions were about $0.4''$

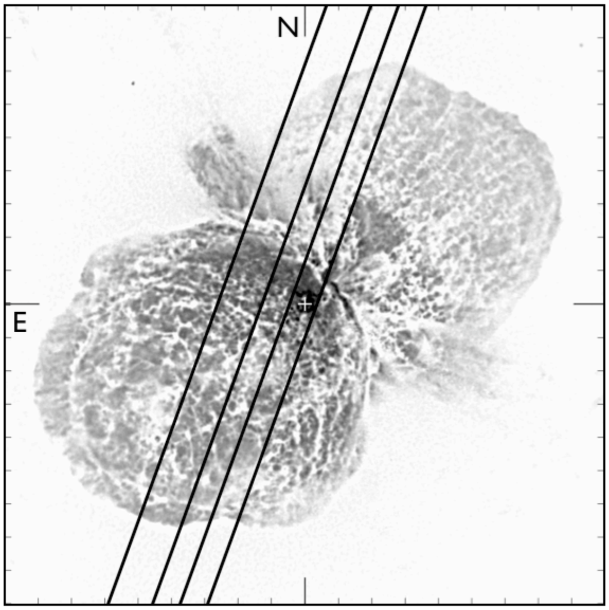

Figure 2.2: Schematic of slit positions of *Gemini* GMOS observations. Observations acquired with blind offset are at -2.42, -1.17, -0.42, and 0.33″ with respect to the central object.

offset from the intended ones (see Figure 2.2 for a schematic of the slit positions with respect to the central object). Additionally, GMOS is not equipped with an atmospheric dispersion corrector (ADC) and its absence has serious implications on the data as discussed below.

The *Gemini* GMOS data were reduced with the Gemini IRAF package, an external package layered upon IRAF. Standard stars are observed once during a semester for each configuration and may be used for approximate removal of telluric lines and for instrumental correction. However, the standard stars were not observed at parallactic angle and therefore light losses, especially in the blue, are large due to atmospheric differential refraction in combination with the narrow slit widths used. In theory one could try to correct for the atmospheric differential refraction but given the errors involved this would not improve the data.

The acquisition images could potentially be used for a relative flux calibration. Photometry of the stars observed on the acquisition images can be used to derive a correction factor from one epoch to another. Since most epochs were observed under photometric conditions, one could even use the published magnitudes of those stars for an absolute flux calibration. The IRAF daophot package was used to do photometry on 4 stars (CPD-59 2624, CL* Trumpler 16 MJ 513, CPD-59 2622, Cl* Trumpler 16 MJ 454) observed on all acquisition images. Same aperture size and sky annulus were chosen. From their individual flux counts a correction factor R for each epoch was derived; the relative flux levels are accurate to about 10% and better. Given the large uncertainties involved in the observations of η Car, the data were not corrected for this factor.

The wavelength calibration of the standard *Gemini* pipeline is about 40 km s^{-1}. To improve the wavelength calibration, interstellar absorption features in the spectrum of η Car were used. Diffuse interstellar absorption bands are weak, relatively broad, absorption features in the spectra that have their origin in the interstellar medium. The bands are most likely caused by large molecules, but their identity remains elusive. A survey of diffuse interstellar bands is presented by Jenniskens & Desert (1994). Strong diffuse interstellar bands are seen at $\lambda\lambda$4432,5782,5799,6205,6271,6286,6615 Å. The velocities of interstellar features are unvarying and therefore an error in the wavelength calibration will manifest itself as a shift in the interstellar absorption profiles. In the case of η Car there is a significant amount of circumstellar absorption which interferes with the interstellar absorption lines. For example, in GMOS spectra with central wavelength λ4300 Å the only measurable interstellar absorption line is the Ca II K line at λ3934.78 Å.[7] For observations with central wavelength λ5200 Å the interstellar absorption line at λ5782 Å was used. The absolute wavelength calibration scale was obtained with *HST* STIS spectra that have better wavelength calibrations.

2.2.1 Atmospheric Differential Refraction

Ground-based observations are subject to atmospheric effects including scattering, absorption, refraction, and atmospheric turbulence. In this section the effects of atmospheric differential refraction in the *Gemini* GMOS data are described. Atmospheric differential refraction has consequences in two major ways; 1.) The direction in which a telescope must be pointed changes with the amount being dependent upon zenith angle. 2.) A star viewed at large zenith angle may appear elongated by this effect.

---

[7] The Ca II H line at λ3969.59 Å blends with the Hϵ absorption. The Ca II K line in spectra of η Car has two components; 1) interstellar at -21 km s^{-1} and 2) circumstellar at -437 km s^{-1}.

This can be problematic for spectroscopy where some wavelengths of interest may not even pass through the slit of the spectrograph. Light may be lost from either end of the spectrum but observations blueward of λ4500 Å are affected the most. This effect is more pronounced under good seeing conditions, at higher airmass, and narrow slit widths. Relative line and continuum intensities may be erroneous if atmospheric differential refraction is neglected.

Because of the expectation that GMOS would be used mostly in the red, it is not equipped with an ADC. The differential refraction is rather large in the observations of η Car since they were mostly obtained far from the parallactic angle and a narrow slit width was used. No light would have escaped the slit if the slit position angles used were equal to the parallactic angle η,

$$sin(\eta) = \frac{sin(h)cos(\phi)}{[1 - (sin(\phi)sin(\delta) + cos(\phi)cos(\delta)cos(h))^2]^{1/2}} \ , \tag{2.1}$$

where h is the hour angle, ϕ the latitude, and δ the declination. This equation has to be used carefully since it depends on the hemisphere and the range of defined values for the parallactic angle. The more the slit position is rotated against the parallactic angle, the more light is lost in the blue and red. The elevation e,

$$sin(e) = sin(\delta)sin(\phi) + cos(\delta)cos(h)cos(\phi) \ , \tag{2.2}$$

is equal to 90° - zenith distance and the airmass is

$$airmass = 1/cos(90^\circ - e) \ . \tag{2.3}$$

Table 2.2 lists parallactic angle, elevation, and airmass of η Car at *Gemini-S* for different hour angles.

Filippenko (1982) calculated the effects of atmospheric differential refraction. At sea level ($P = 760$ mm Hg, $T = 15$°C) the refractive index of dry air is given by

$$(n(\lambda)_{15,760} - 1)10^6 = 64.328 + \frac{29498.1}{146 - (1/\lambda)^2} + \frac{255.4}{41 - (1/\lambda)^2} \ , \tag{2.4}$$

where λ in [μm] is the wavelength of light in vacuum. The index of refraction must be

Table 2.2: Parallactic angle, elevation, and airmass for observations of η Car with GMOS

Hour angle[a] (deg)	Parallactic angle[b] (deg)	Elevation (deg)	Airmass
-80.00	-81.66	30.70	1.96
-70.00	-89.94	35.73	1.71
-60.00	-80.99	40.75	1.53
-50.00	-71.21	45.64	1.40
-40.00	-60.27	50.24	1.30
-30.00	-47.80	54.32	1.23
-20.00	-33.49	57.61	1.18
-10.00	-17.35	59.78	1.16
0.00	0.00	60.54	1.15
10.00	17.35	59.78	1.16
20.00	33.49	57.61	1.18
30.00	47.80	54.32	1.23
40.00	60.27	50.24	1.30
50.00	71.21	45.64	1.40
60.00	80.99	40.75	1.53
70.00	89.94	35.73	1.71
80.00	81.66	30.70	1.96

[a] GMOS observations include hour angles between $-65°$ and $77°$.

[b] At latitude $\phi = -30.24°$ and declination $\delta = -59.70°$.

corrected for the lower ambient temperature and pressure at high altitudes,

$$(n(\lambda)_{\mathrm{T,P}} - 1) = (n(\lambda)_{15,760} - 1)\ \frac{P[1 + (1.049 - 0.0157\ T)10^{-6}P]}{720.883(1 + 0.003661\ T)}\ , \tag{2.5}$$

where P is pressure in [mm Hg] and T is the air temperature in [°C]. In addition, the presence of water vapor in the atmosphere reduces $(n-1)10^6$ by

$$\frac{0.0624 - 0.000680/\lambda^2}{1 + 0.003661\ T}\ f\ , \tag{2.6}$$

where f is the water vapor pressure in [mm Hg]. The water vapor is calculated using

$$f = \frac{H}{100}\ \frac{1}{133.322\ T^{8.2}}\ e^{(\mathrm{77.3450+0057t-7235/t})}\ , \tag{2.7}$$

where $t = T + 273.15$ and H the relative humidity. These equations are used to obtain the index of refraction $n(\lambda)$.

The atmospheric differential refraction in [″] relative to λ_{ref} in [Å] for an object at zenith angle z is

$$\Delta R(\lambda) = R(\lambda) - R(\lambda_{\mathrm{ref}}) \approx 206265[n(\lambda) - n(\lambda_{\mathrm{ref}})]tan(z)\ . \tag{2.8}$$

Table 2.3: Differential atmospheric refraction in [″] as a function of wavelength and airmass for different effective wavelengths in *Gemini* GMOS observations[a]

$\lambda_{\rm ref}$	Airmass[b]	3600	4000	4400	4800	5200	5600	6000	6400	6800	7200
3500	1.00	-0.000	-0.000	-0.000	-0.000	-0.000	-0.000	-0.000	-0.000	-0.000	-0.000
	1.10	-0.056	-0.237	-0.361	-0.462	-0.530	-0.586	-0.642	-0.676	-0.710	-0.732
	1.20	-0.082	-0.343	-0.522	-0.669	-0.767	-0.848	-0.930	-0.979	-1.028	-1.060
	1.30	-0.102	-0.429	-0.654	-0.837	-0.960	-1.062	-1.164	-1.225	-1.287	-1.328
	1.40	-0.120	-0.506	-0.771	-0.988	-1.132	-1.253	-1.373	-1.446	-1.518	-1.566
	1.50	-0.137	-0.577	-0.880	-1.127	-1.292	-1.430	-1.567	-1.649	-1.732	-1.787
	1.60	-0.154	-0.645	-0.983	-1.259	-1.443	-1.597	-1.751	-1.843	-1.935	-1.996
	1.80	-0.184	-0.773	-1.178	-1.509	-1.730	-1.914	-2.098	-2.208	-2.318	-2.392
	2.00	-0.213	-0.894	-1.363	-1.746	-2.002	-2.215	-2.428	-2.555	-2.683	-2.768
4750	1.00	0.000	0.000	0.000	-0.000	-0.000	-0.000	-0.000	-0.000	-0.000	-0.000
	1.10	0.394	0.214	0.090	-0.011	-0.079	-0.135	-0.192	-0.225	-0.259	-0.282
	1.20	0.571	0.310	0.130	-0.016	-0.114	-0.196	-0.277	-0.326	-0.375	-0.408
	1.30	0.715	0.388	0.163	-0.020	-0.143	-0.245	-0.347	-0.408	-0.470	-0.511
	1.40	0.843	0.458	0.193	-0.024	-0.169	-0.289	-0.410	-0.482	-0.554	-0.602
	1.50	0.962	0.522	0.220	-0.027	-0.192	-0.330	-0.467	-0.550	-0.632	-0.687
	1.60	1.075	0.584	0.246	-0.031	-0.215	-0.369	-0.522	-0.614	-0.706	-0.768
	1.80	1.288	0.699	0.294	-0.037	-0.258	-0.442	-0.626	-0.736	-0.846	-0.920
	2.00	1.491	0.809	0.341	-0.043	-0.298	-0.511	-0.724	-0.852	-0.980	-1.065
6300	1.00	0.000	0.000	0.000	0.000	0.000	0.000	0.000	-0.000	-0.000	-0.000
	1.10	0.608	0.428	0.304	0.203	0.135	0.079	0.023	-0.011	-0.045	-0.068
	1.20	0.881	0.620	0.440	0.294	0.196	0.114	0.033	-0.016	-0.065	-0.098
	1.30	1.103	0.776	0.551	0.368	0.245	0.143	0.041	-0.020	-0.082	-0.123
	1.40	1.301	0.915	0.650	0.434	0.289	0.169	0.048	-0.024	-0.096	-0.145
	1.50	1.485	1.045	0.742	0.495	0.330	0.192	0.055	-0.027	-0.110	-0.165
	1.60	1.658	1.167	0.829	0.553	0.369	0.215	0.061	-0.031	-0.123	-0.184
	1.80	1.987	1.398	0.994	0.662	0.442	0.258	0.074	-0.037	-0.147	-0.221
	2.00	2.300	1.618	1.150	0.767	0.511	0.298	0.085	-0.043	-0.170	-0.256
6500	1.00	0.000	0.000	0.000	0.000	0.000	0.000	0.000	0.000	0.000	0.000
	1.10	0.620	0.451	0.316	0.225	0.147	0.090	0.045	0.011	-0.023	-0.045
	1.20	0.897	0.652	0.457	0.326	0.212	0.131	0.065	0.016	-0.033	-0.065
	1.30	1.123	0.817	0.572	0.409	0.266	0.163	0.082	0.020	-0.041	-0.082
	1.40	1.325	0.964	0.675	0.482	0.313	0.193	0.096	0.024	-0.048	-0.096
	1.50	1.512	1.100	0.770	0.550	0.357	0.220	0.110	0.028	-0.055	-0.110
	1.60	1.689	1.229	0.860	0.614	0.399	0.246	0.123	0.031	-0.061	-0.123
	1.80	2.024	1.472	1.030	0.736	0.478	0.294	0.147	0.037	-0.074	-0.147
	2.00	2.342	1.704	1.193	0.852	0.554	0.341	0.170	0.043	-0.085	-0.170
6720	1.00	0.000	0.000	0.000	0.000	0.000	0.000	0.000	0.000	-0.000	-0.000
	1.10	0.642	0.462	0.338	0.237	0.169	0.113	0.056	0.023	-0.011	-0.034
	1.20	0.930	0.669	0.489	0.343	0.245	0.163	0.082	0.033	-0.016	-0.049
	1.30	1.164	0.837	0.613	0.429	0.306	0.204	0.102	0.041	-0.020	-0.061
	1.40	1.373	0.988	0.723	0.506	0.361	0.241	0.120	0.048	-0.024	-0.072
	1.50	1.567	1.127	0.825	0.577	0.412	0.275	0.137	0.055	-0.027	-0.082
	1.60	1.751	1.259	0.921	0.645	0.461	0.307	0.154	0.061	-0.031	-0.092
	1.80	2.098	1.509	1.104	0.773	0.552	0.368	0.184	0.074	-0.037	-0.110
	2.00	2.428	1.746	1.278	0.894	0.639	0.426	0.213	0.085	-0.043	-0.128

[a] Calculated with $P = 550$ mm Hg, $T = 10°$C, and water vapor $f = 3$ mm Hg.

[b] The average airmass in the *Gemini* GMOS observations is about 1.3.

Table 2.4: Filters used in target acquisition of *Gemini* GMOS observations

Filter	Effective wavelength (Å)	Epoch (file name)
u_G0332	3500	gI11_0010 – gI11_0070
g_G0325	4750	gH45*, gI54*
SII_G0335	6720	gH49*, gH52*, gI41*, gI42*, gI50* , gK02*
r_G0326	6300	Other

Table 2.3 lists the magnitude of atmospheric differential refraction as a function of wavelength and airmass for different reference wavelengths and average observing conditions; pressure $P = 550$ mm Hg, ambient temperature $T = 10°\mathrm{C}$, and water vapor $f = 3$ mm Hg. Most observations were obtained at an airmass of 1.3, and extreme red and blue wavelengths are displaced with respect to one another by over $1''$. This leads to considerable light loss if the aperture is not aligned along the direction of atmospheric refraction.

In order to determine the displacement of observations at wavelengths of interest from the intended position several considerations had to be taken into account.[8] After target acquisition (with effective wavelengths listed in Table 2.4) the telescope is tracked at a rate corrected for differential refraction at the effective wavelength of the guide star, $\lambda6500$ Å. The differential refraction at $\lambda6500$ Å from the effective wavelength of the acquisition gives the location of the star at $\lambda6500$ Å at time of acquisition. This location will not change until the next acquisition and serves as reference point. However, the central wavelength of each observation (if not $\lambda6500$ Å) will be offset from this reference point and will also change with time as the parallactic angle changes. In addition, the incorrect acquisition coordinates have to be taken into account. Table A.1 lists the offset between the slit position and the star at the central wavelength for all GMOS observations. This serves as a quick means to assess how much each observation is affected by differential refraction. However, the effect changes as one moves along the dispersion axis to other wavelengths. Particularly in the blue spectra, the effective position of the star can change by more than the width of the slit.

In the case of a point source one could in principle correct for the effect of atmospheric differential refraction (Filippenko 1982). For a star centered at λ_{ref} in a rectangular

---

[8] See also Technical memo number 14 on the HST Treasury Program website http://etacar.umn.edu/.

aperture of width $2a$ and length $2b$, the amount of light at λ entering the aperture is

$$I(\lambda) = (\frac{1}{\sqrt{2\pi}\sigma} \int_{-a}^{a} e^{-x^2/2\sigma^2} dx) \times (\frac{1}{\sqrt{2\pi}\sigma} \int_{-b}^{b} e^{-y^2/2\sigma^2} dy) \ , \tag{2.9}$$

with x being the axis vertical to the slit and y the axis along the slit. If the star is displaced from the aperture center by x_0 along the x-axis, then

$$\begin{aligned} I(\lambda) \quad &= \quad \frac{1}{2}(\frac{1}{\sqrt{2\pi}\sigma} \int_{-(a-x_0)}^{(a-x_0)} e^{-x^2/2\sigma^2} dx + \frac{1}{\sqrt{2\pi}\sigma} \int_{-(a+x_0)}^{(a+x_0)} e^{-x^2/2\sigma^2} dx) \\ &\quad \times (\frac{1}{\sqrt{2\pi}\sigma} \int_{-b}^{b} e^{-y^2/2\sigma^2} dy) \ . \end{aligned} \tag{2.10}$$

Figure 2.3 shows the percentage of light entering the aperture for different angles between slit position angle and parallactic angle and average observing conditions. The farther the slit is oriented from the parallactic angle, the worse is the loss of light, culminating when the slit is perpendicular to the parallactic angle. The calculation of the actual light loss is complicated by the fact that σ in equation 2.10 is mostly unknown and can only be estimated.

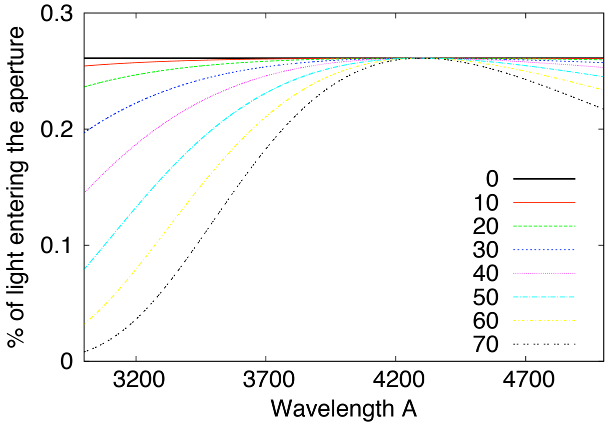

Figure 2.3: Percentage of light entering the aperture in *Gemini* GMOS observations depends on the angle between position angle and parallactic angle (key). Values used in the calculation are; $\phi = -30.24°$, $\delta = -59.70°$, slit position angle $PA = 160°$, $P = 550$ mm Hg, $T = 10°$C, $f = 3$ mm Hg, $\lambda_{\rm ref} = 4300$ Å, slit width $x = 0.5''$, slit length $y = 330''$, and $\sigma = 0.75''$.

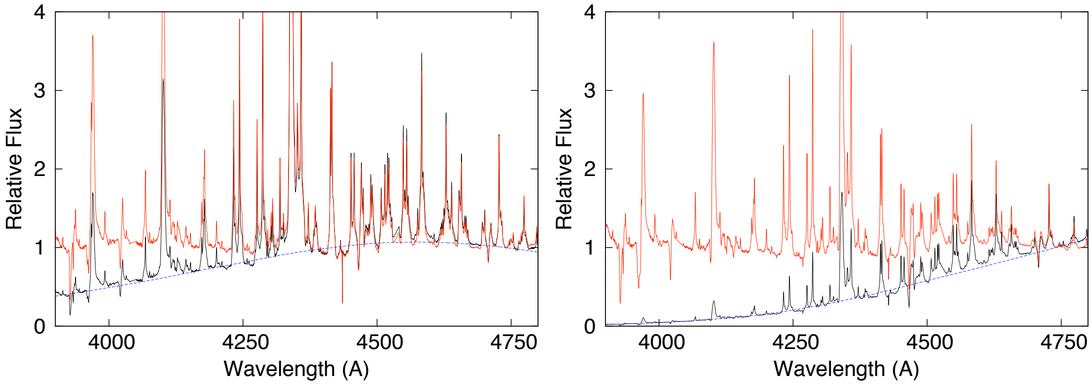

Figure 2.4: Examples of loess fits to *Gemini* GMOS spectra. Each panel shows a spectrum of the star (black solid curve), fitted loess curve (blue dashed curve), and the "flattened" spectrum (red solid curve).

2.2.2 Spectral Analysis

2-D spectrograms were prepared with the standard GMOS data reduction pipeline in the Gemini IRAF package and 1-D spectra were extracted via a routine developed by M. Gray and J. Martin (Martin et al. 2006a). At each wavelength the software integrates the counts along a line perpendicular to the dispersion, weighted by a mesa-shaped function centered on the local spectral trace. The mesa function used had a base-width = 11 pixels and a top-width = 7 pixels, about $0.8''$ and $0.5''$, respectively. The seeing was roughly 0.5–$1.5''$, so each GMOS spectrum discussed represents a region typically $\sim 1''$ across. The pipeline wavelength calibration was improved using the interstellar Ca II K absorption line at $\lambda 3935$ Å and the interstellar absorption line at $\lambda 5782$ Å.

Since η Car is an extended source one cannot correct for the light loss caused by the differential atmospheric refraction, discussed in the previous section. Each spectrum contains a range of spatial positions along the dispersion axis and therefore the spectrum comes in all shapes. For each spectral feature discussed in this thesis only observations were used that lie within $\pm 0.375''$ from the star or -1 to $-3''$ from the star in case of FOS4. In order to compare spectral features in data observed at different parallactic angles, it is necessary to "flatten" the tracings. The spectral shape varies considerately between observations and η Car's emission line spectrum makes it difficult to fit a continuum. However, a quadratic loess (locally weighted scatterplot smoothing) curve fit provides a reasonably good estimate of the spectral shape (Figure 2.4).

2.3 *VLT* UVES, *Magellan II* MIKE, and *Irénée du Pont* B&C Data

Eta Car was not observed with *Gemini* GMOS before 2007. In need of uniform data obtained with the same instrument settings I also analyzed *VLT* UVES data from 2002–2009.[9] The UVES observations are especially valuable since no other instrument covered the location at FOS4 consistently over such a long time interval. I reduced the spectra with the standard UVES pipeline available from ESO. The spectra were extracted using a mesa function 3 by 2 pixels wide, about $0.75''$ by $0.5''$. The seeing was 0.8 to $0.9''$ so this extraction corresponds to about $1''$ on the sky.

In addition I analyzed spectra obtained with *Magellan II* MIKE on 2010 June and *Irénée du Pont* B&C on 2011 February at Las Campanas Observatory.[10] Observations with the *Irénée du Pont* telescope included both the star and FOS4. The spectra were reduced using standard IRAF tasks.

---

[9] The UVES observations were obtained at ESO's Paranal Observatory and are available at http://etacar.umn.edu/.

[10] Information on both telescopes can be found at http://www.lco.cl/.

Chapter 3

High-excitation Emission Lines Near Eta Carinae and their Implications for the Secondary Star

In order to study the nature of the presumed secondary star, I analyzed a few well-understood emission lines that require ionizing photons with $h\nu > 16$ eV. The opaque wind of η Car has a temperature below $20,000$ K (Hillier et al. 2001) and can therefore not account for the high-excitation emission. X-ray spectra indicate a wind speed of the secondary star of about 3000 km s^{-1}, which implies a temperature $T_{\rm eff} > 37,000$ K. Therefore, the high-excitation emission lines discussed here probably indicate photoionization by a hot companion star. The photoionization code Cloudy was used to calculate models that match the relative intensities of [Ne III], [Ar III], He I, and other lines that require helium-ionizing photons ($h\nu > 25$ eV). Since the glare of the primary star makes the secondary star impossible to study directly, practically the only other quantitative information comes from the X-ray spectrum and from evolutionary constraints.

Using spectra obtained with the *HST* STIS, I examined the spatial distribution and the temporal behavior of [Ne III] λ3870, [Fe III] $\lambda\lambda$4659,4703, and the narrow component of He I λ6680 throughout an entire 5.54-year cycle. The different photon energies required for [Ne III], [Fe III], and He I emission allow to probe a range of physical parameters. He I λ6680 is a recombination line formed in a He^+ region, while [Ne III] and [Fe III] arise in Ne^{++} and Fe^{++} zones. Ionization potentials of H^0, Fe^+, He^0, Ar^+, and Ne^+ are 13.6, 16.2, 24.6, 27.6, and 41.0 eV, respectively. Thus, for reasons explained by Osterbrock & Ferland (2006), Fe^{++} occurs mainly in regions of H^+ and He^0 while Ne^{++} and Ar^{++} usually coexist with He^+.

3.1 Spatial Distribution

[Ne III] λ3870 Figure 3.1 shows a spatial map of the narrow [Ne III] λ3870 feature in slit positions observed with STIS. In order to compensate for time variations, I renormalized the measurements so that the value is always unity at the position of the star. Most of the flux originates in the region of the Weigelt knots, at distances 0.1–0.3″ from the star. The positions of the rather amorphous knots BCD are marked in the Figure. STIS could only marginally resolve them individually, but the peak corresponds to Weigelt knot C at r ≈ 0.21″ and position angle *PA* ≈ 300°. This corresponds well with measurements of knot C in *HST* images which gave r ≈ 0.22″ in 1999–2003 (e.g. Smith et al. 2004). Higher flux in [Ne III] λ3870 was also observed at the locations of Weigelt knots B and D at position angle *PA* ∼ 335°. Their peak intensities are roughly half that of knot C. However, it is not possible to distinguish between knots B and D based only on Figure 3.1.

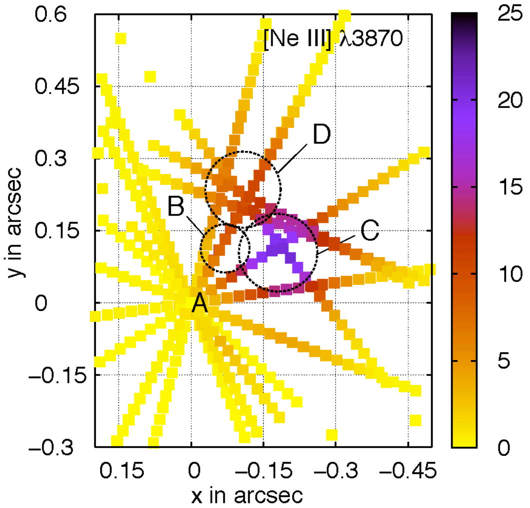

Figure 3.1: Spatial map of the narrow [Ne III] λ3870 line. Position A marks the central star while B, C, and D are the Weigelt knots. Flux values are normalized so that this emission line's net flux is unity at the star's position.

Given the spatial-resolution limits of all *HST* data, the identification of [Ne III] with the Weigelt knots in Figure 3.1 is practically as good as the evidence for their association with [Fe II]. Evidently the narrow-line [Ne III] emission does not chiefly represent a diffuse halo enveloping all the Weigelt knots, as seemed possible before.

[Fe III] $\lambda\lambda$4659,4703 I examined both [Fe III] λ4659 and λ4703 in order to compare them for mutual consistency. Their theoretical intensity ratio is 1.85 (Nahar & Pradhan 1996; Quinet 1996). Figure 3.2 shows maps of the narrow [Fe III] λ4659 and λ4703 fluxes, respectively. In the same manner as for [Ne III], I rescaled the measured [Fe III] fluxes so the net value at the location of the star was always unity. Before rescaling, the measured flux of [Fe III] λ4659 at that position was about 1.9 times as high as for [Fe III] λ4703 in each observation, close to the theoretical value. The two [Fe III] maps are in excellent agreement with each other. [Fe III] emission originates in a slightly larger region than [Ne III]. This is not very surprising, given the difference in ionization potentials; [Ne III] occurs where helium is singly ionized but [Fe III] originates in zones where hydrogen is ionized but helium is not.

Incidentally, a fainter additional [Fe III] condensation about 0.48″ NNE of the star was noticed, in data obtained in 2009 June. This knot is of interest because it has a *positive* Doppler velocity, about +27 km s^{-1} rather than the values around −40 km s^{-1}

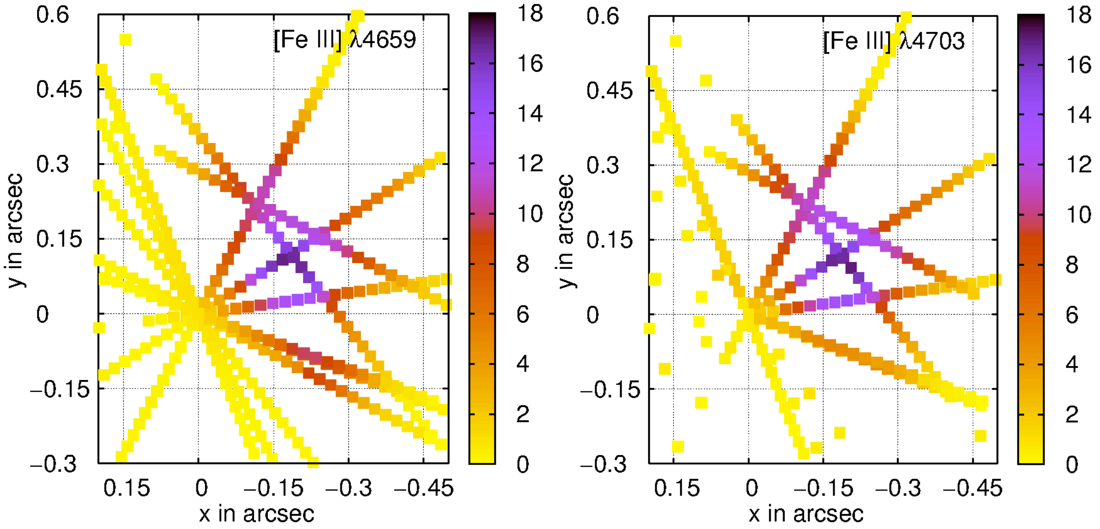

Figure 3.2: Spatial maps of the narrow [Fe III] λ4659 and λ4703 lines, with the same format as Figure 3.1. Both maps are based on the same spectrograms but measurements were independent.

seen in BCD. Its location was not sampled by the slit positions used in 1998–2004.

He I λ6680 He I λ6680 is a recombination line formed in He^+ (Osterbrock & Ferland 2006). In a spectrum of η Car, this feature usually consists of a broad component formed in the stellar wind, plus the narrow component from slow-moving ejecta. With the spectral resolution of STIS ($\sim$ 40 km s^{-1}), the underlying broad emission makes the narrow He I line far more difficult to measure than [Ne III] and [Fe III]. Consequently the He I λ6680 map (Figure 3.3) is of lower quality than the others and He I is not a clear enough indicator of the time dependence to include in Figure 3.5. There is no evident disagreement compared to [Ne III].

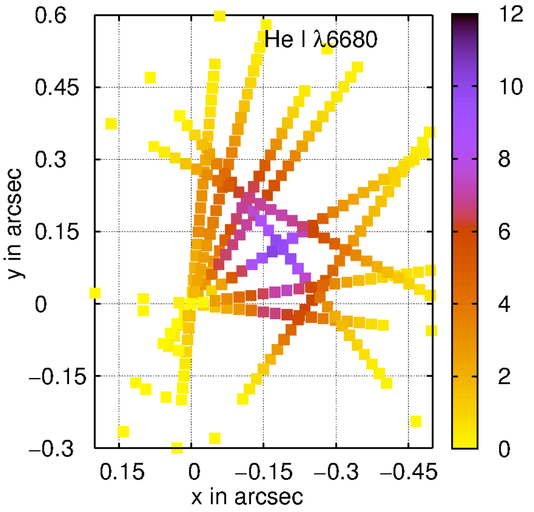

Figure 3.3: Map of the narrow He I λ6680 emission line, shown in the same way as Figures 3.1–3.2.

3.2 Temporal Behavior

The high-excitation emission lines are the classic indicators of η Car's spectroscopic events; every 5.54 years they abruptly disappear for a few weeks to months. Figure 3.4 shows the disappearance of the [Ne III] line λ3870 during the 2003.5 "event" on Weigelt knot D. The line strength began to weaken less than 100 days before the "event" and had still not recovered more than 200 days after the "event." The top panel of Figure 3.5 shows the time-dependent flux of the narrow [Ne III] λ3870 emission line that was seen superimposed on STIS spectra of the star (at resolution $\sim 0.1''$) through the spectroscopic cycle 1998–2004. [Ne III] evolved through four distinct stages (Figure 3.5):

1. The weak or near-zero state persisted for several months. This was long enough for a companion star to sweep through more than 180° of longitude around periastron,

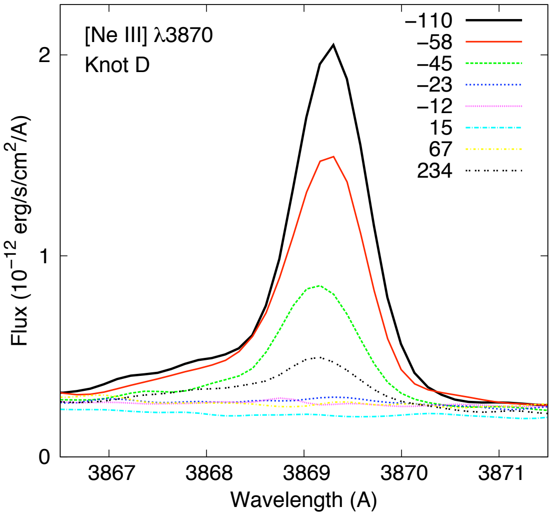

Figure 3.4: [Ne III] λ3870 during the 2003.5 "event" in Weigelt knot D. Days before (−) and after (+) the "event" are indicated in the plot. The line strength began to weaken less than 100 days before the "event" and had still not recovered more than 200 days after the "event."

if its orbit eccentricity is at least 0.8 as seems likely.

2. Subsequent growth to near-maximum intensity was interestingly slow, delaying the maximum until more than two years after the "event" – unlike what a simple model would predict.

3. Then, instead of leveling off, the intensity soon began to decline, following a sort of parabolic trajectory in time.

4. A few months before the 2003.5 "event," however, it briskly rose to a second maximum just before declining again to near-zero. This late-cycle rise resembled the behavior of the He II emission and the observed X-ray light curve (Ishibashi et al. 1999b; Martin et al. 2006a); perhaps the high-excitation emission at that time was somehow related to the X-rays or to the colliding-wind shocked zones. The softest X-rays may play a role then (Martin et al. 2006a).

This "double-peaked" cycle was measured in gas along the line of sight to the star, but at least stages 1–3 seem broadly valid on the Weigelt knots BCD as well. Some, but not all, of this behavior pattern was noted by Damineli et al. (2008a) for [Ar III]

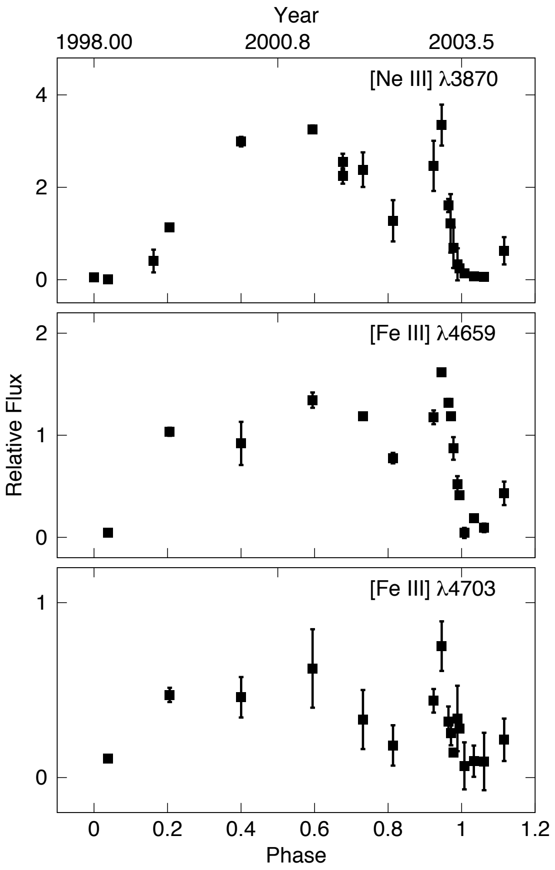

Figure 3.5: Strengths of the narrow [Ne III] $\lambda3870$ and [Fe III] $\lambda\lambda4659{,}4703$ emission lines measured in *HST* STIS spectra of η Car through its spectroscopic cycle. These represent gas along the line of sight to the star, seen with $0.1''$ spatial resolution and not including the Weigelt knots. Features in the knots vary in a similar way.

$\lambda7138$ at much lower spatial resolution. They measured equivalent widths (not fluxes) in ground-based spectra including the star plus ejecta out to r $\sim 1''$. Their Fig. 1 differs in two interesting respects: (1) The declines after mid-cycle do not match. At phase 0.8, for instance, the high-excitation lines had already fallen by 50% in the STIS results but less than 20% in the ground-based data. (2) Damineli et al. did not observe a brief, dramatic flux increase around phase 0.9. Most likely these discrepancies resulted from the very different spatial resolutions. The ground-based spectra include an amorphous unresolved mixture of emission regions, whereas Figure 3.5 refers to a well-defined $0.1''$ locale.

A simple model would have predicted an extended plateau in Figure 3.5. The [Ne III] flux shown there is superimposed on the star and has a negative Doppler velocity of about -40 km s^{-1}; so it must represent slow-moving gas located approximately between us and the star. If it was ejected 60–200 years ago, this gas has now moved several hundred AU from the star. If the orbit orientation is within the range favored by most authors (e.g., Ishibashi 2001; Okazaki et al. 2008), then during most of the 5.54-year cycle the initial part of a path from the hot secondary star to the Ne^{++} in question (i.e., toward us) should pass through the low-density secondary wind facing away from the primary star; see Fig. 2 in Pittard & Corcoran (2002). Previous data would have allowed a scenario in which the ionizing photons are not seriously depleted along such a path until they reach the observed Ne^{++} region. In that case the [Ne III] brightness superimposed on the star would change little during most of the cycle. Figure 3.5 contradicts this simple model.

If this time-pattern was caused by some complex variation of the circumstellar extinction, then in order to include BCD it must extend out to $r \gtrsim 800$ AU, which seems unlikely in terms of grain physics. Apparently, then, during most of the 1998–2003 cycle the amounts of Ne^{+2}, Fe^{+2}, etc. in BCD were significantly less than their maxima.

One can easily imagine qualitative explanations for the observed behavior after seeing it, but choosing the right one is harder. Most likely the ionizing photon path mentioned above *does* intersect a substantial and varying part of the dense primary wind. Gull et al. (2009) and Parkin et al. (2009), for instance, have discussed possible "conventional" models for the flow of dense gas outward from the binary system, allowing a substantial column density in the relevant sense. Soker (priv. comm.), on the other hand, remarks that Figure 3.5 is qualitatively consistent with a very different picture, in which the secondary star is usually on the far rather than the near side of the primary (Kashi & Soker 2008, 2009c,d). Note two points: (1) Every proposed model depends on a number of assumptions which are not easy to verify, and (2) the information in Figure 3.5 is essential for any realistic view of the problem. Instead of an ill-defined average of ejecta around the star, this Figure represents emission between us and the star at high spatial resolution.

In addition to [Ne III], Figure 3.5 shows the temporal variation of [Fe III] $\lambda\lambda$4659,4703 on the position of the star. They display the same qualitative behavior as [Ne III] λ3870.

Some of the narrow [Fe II] lines also showed temporary minima at phases around 0.8, qualitatively like [Ne III] and [Fe III], see Figure 8.1. They also showed a peak at phase 0.9 and a brief minimum during the 2003 "event." The [Fe II] lines varied differently from each other, but none of them showed a strong growth around phase 0.3 as [Ne III] did.

3.3 Blueshifted Components

In addition to the narrow lines discussed above, [Fe III] and [Ne III] also show separate, broader components extending between Doppler velocities -250 km s^{-1} and -400 km s^{-1}, see Figure 3.6. These also exist for other high-excitation lines such as [Ar III], [S III], [Si III], etc. In each case the blueshifted component is much wider than the narrow lines but much narrower than the normal stellar wind emission features (η Car's brightest Balmer lines usually have FWHM $\approx$ 400 to 500 km s^{-1}; see, e.g., Davidson et al. 2005).

Thackeray (1953, 1967) recognized emission components of [Fe III] and [S II] that were blueshifted by about -300 km s^{-1}. Aller & Dunham (1966) listed these and similar blueshifted Fe II and [Fe II] lines. Zanella et al. (1984) noted that some of them disappeared along with the ordinary narrow high-excitation lines during an "event," particularly including [Ne III]. They concluded that the blueshifted emission arose at larger distances from the star; but the Weigelt knots and polar/equatorial morphology were not known at that time. Comparing the 1992 spectroscopic event to the 1995 mid-cycle state, Damineli et al. (1998) confirmed the Zanella et al. statements about variability. Gull et al. (2009) recently showed STIS spectrograms (not tracings) of some of these features, but did not produce spatial maps like those presented below.

Quantitative measurement of the blueshifted [Ne III] λ3870 is difficult due to nearby Si II λ3864 and Cr II λ3867. I therefore concentrated on the blueshifted component of [Fe III] λ4659, centered at about λ4653 Å. To verify that it is [Fe III] emission, I compared the profiles of [Fe III] λ4659 and λ4703. Figure 3.6 shows that the blueshifted feature is undoubtedly a component of each [Fe III] line. This Figure also illustrates the complexity of the line profiles, tracing various ejection features. There is probably some material with intermediate Doppler shifts.

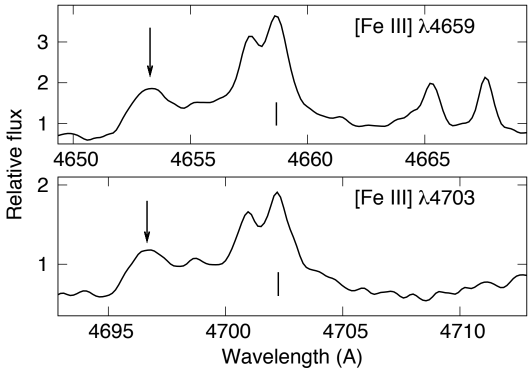

Figure 3.6: [Fe III] $\lambda\lambda$4659,4703 emission line profiles 0.25″ NE of the star. The arrows mark the broad negative-velocity emission and the vertical ticks the two narrow emission from two knots. The blueshifted feature is undoubtedly a component of [Fe III].

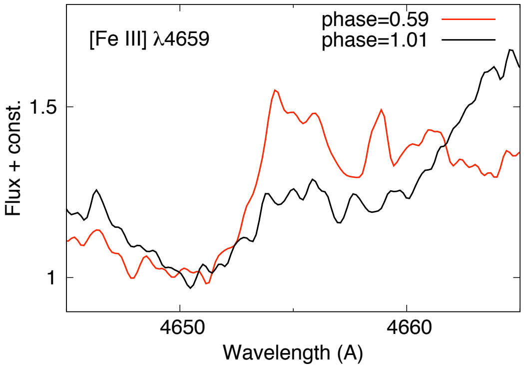

Figure 3.7: Comparison of [Fe III] λ4659 emission components on the star at two different phases in the 5.54-year cycle. The red solid line represents a phase of 0.59 near high-excitation maximum, while the black solid line shows phase 1.00 during the 2003.5 "event."

The temporal evolution of the blueshifted component follows the spectroscopic cycle in roughly the same way as the narrow lines. The normal and the shifted components appear and disappear together. Figure 3.7 compares the [Fe III] λ4659 emission line profile in spectra of the star at different phases in the cycle. The red curve refers to a phase of 0.59, close to the time when the narrow high-excitation emission was strongest. The black curve is the profile shortly after the 2003.5 "event," at phase $\approx$ 1.0. The narrow component at λ4659 Å disappeared completely, and the broad blue component was diminished.

Figures 3.8 and 3.9 map the flux of the blueshifted component of [Fe III] λ4659. Most of it originates in the inner 0.1″ region, less than 250 AU from the star. The distribution is not as sharp as a stellar point-source would be. *The emission region is detectably elongated to the northeast and southwest,* perpendicular to the axis of the bipolar Homunculus ejecta-nebula. Gull et al. (2009) mentioned "diffuse arcs" WSW and ENE of the star, but they meant velocity versus position correlations in spectrograms, not spatial arcs. "WSW" and "ENE" referred to the position angle of the STIS slit when those observations were made. Although they used direction names such as NE and ENE, those authors did not describe the quantitative elongation shown in Figure 3.9. Their discussion focussed instead on velocity-position-time effects that

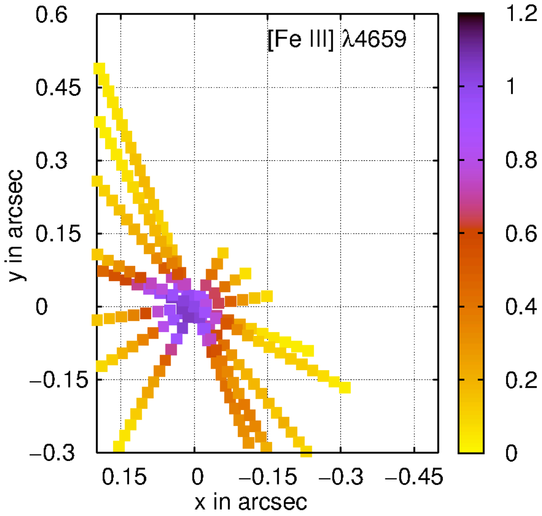

Figure 3.8: Spatial map of the relative flux in the blueshifted component of [Fe III] $\lambda4659$. The flux is normalized to unity at the position of the star.

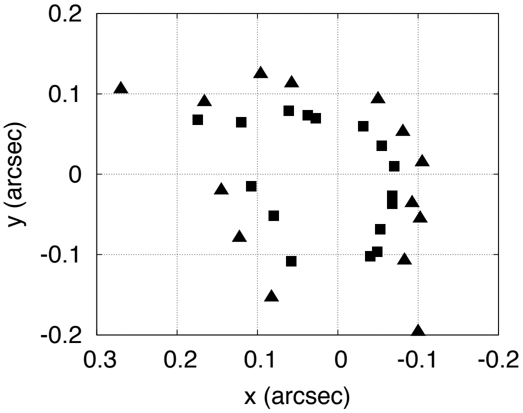

Figure 3.9: Expanded view of intensity contours of the blueshifted [Fe III] $\lambda4659$. Squares (■) and triangles (▲) indicate values of 0.5 and 0.25 respectively, relative to the value at the star's location. The contours are significantly elongated NE–SW, i.e., toward the upper left and lower right.

one can see directly in the spectrograms.

Considering the proximity of the blue component to the position of the star, its size, shape, and orientation, Figure 3.9 might trace the near side of a latitude-dependent structure in the outer stellar wind. Its observed blueshift of about -300 km s^{-1} is smaller than the wind speed seen at the bottoms of the P Cyg absorption features (e.g. Smith et al. 2003; Davidson et al. 2005), but these two quantities sample the gas in very different ways. Electron densities cannot greatly exceed 10^7 cm^{-3} in the relevant gas, because higher values would collisionally de-excite [Fe III], [Ne III], and [Ar III] too strongly. Assuming that η Car's mass-loss rate has the conventional value of $\sim 10^{-3}\ M_\odot$ yr^{-1} and that its equatorial wind is less dense than its polar wind by a factor of order 3 (Smith et al. 2003), n_e may fall below 10^7 cm^{-3} at *equatorial* radii $r \gtrsim 100$ AU $\sim 0.05''$. At higher latitudes the corresponding radius would be larger. Since these size scales are much larger than the 5.54-year orbit, very likely the dense, biconical inner polar wind ($r < 100$ AU) shields the outer, lower-density *high-latitude* zones from the secondary star's ionizing radiation. In other words, at high latitudes the ionizing radiation is probably absorbed by gas that is too dense to produce strong forbidden lines. Thus one expects the high-excitation forbidden lines to be concentrated toward latitudes less than

$\sim 50^\circ$ or so – resulting in an oblate emission region. If this picture is valid, evidently red-shifted emission from the far side cannot penetrate through the configuration. Local inhomogeneities or "clumping" do not alter the basic reasoning. Gull et al. (2009) have discussed relevant time-dependent structures at smaller size scales. Their models depend on a number of assumptions and do not make use of a polar wind; but in general they have little effect on the comments above. Arguably the most significant well-defined observational clue is the elongation shown in Figure 3.9 – a new result.

On the other hand, two other locations for emission farther from the star can be imagined. First, the -300 km s^{-1} Doppler shift is well-matched to the region where the line of sight to the star intersects the inner parts of the bipolar Homunculus ejecta-nebula and/or the "Little Homunculus" (Ishibashi et al. 2003). The main objection is that one might then expect the emission zone to have a projected size of $0.5''$ or larger. The other possibility involves a remarkable observed fact: the line of sight to the star has about two magnitudes more extinction than the view of the Weigelt knots (Davidson et al. 1995; Hamann et al. 1999; Hillier et al. 2001). Dust grains cannot exist much closer to η Car than $r \sim 150$ AU (Davidson & Humphreys 1997), but apparently some very localized dusty material lies between us and the star. Can its far side or inner side be the region where the blueshifted emission lines originate? Both the size scale in Figure 3.9 and the Doppler velocity seem reasonable. If this is the explanation, then the blueshifted line components must be *intrinsically* much brighter than the observable narrow lines but are obscured by the dust. The same statement also applies to emission in the outer wind. This model and the outer-wind idea mentioned earlier are not necessarily distinct from each other.

3.4 Photoionization Modeling and the Nature of the Secondary Star

The high-excitation emission lines at the Weigelt knots probably indicate photoionization by a hot star. Consider, for instance, [Ne III] λ3870. This is a familiar feature in moderately high-excitation photoionized nebulae, where Ne^{++} typically exists in a He^{+} zone maintained by ionizing photons with 25 eV $< h\nu <$ 54 eV (Osterbrock & Ferland 2006). Within that zone, [Ne III] emission is collisionally excited by thermal electrons.

In a non-photoionized model for the ejecta of η Car the creation of sufficient Ne^{++} by thermal *collisional* ionization would require some mechanism – e.g., low-speed shock waves – that can heat a substantial amount of material to $T \sim$ 20,000–30,000 K since Ne^{+} has an ionization potential of 41 eV. This is difficult to achieve because a single low-speed shock carries insufficient energy; and no such mechanism has been suggested by other data. Moreover, as Zanella et al. (1984) emphasized, [Ne III] behaves very differently from the low-excitation lines during each spectroscopic event. Thus, as a very probable working hypothesis, *I assume that [Ne III] λ3870 signals ordinary, relatively straightforward quasi-nebular photoionization.* So far, no author has argued against this assumption in the case of η Car. If correct then it is most likely true for [Ar III] and [Fe III] as well. The low-excitation features, by contrast, are strongly influenced by local absorption in various UV permitted lines – "radiative pumping" – which depends critically (and differently for each transition) on local velocity dispersions and density gradients. In other words the high-excitation lines are theoretically more tractable than Fe II, [Fe II], and other low-excitation features.

But where do the Ne^{+}-ionizing photons above 41 eV come from? Conventional models for the primary stellar wind are too cool (Hillier et al. 2001). The secondary star, however, is expected to have a high effective temperature. Its likely ability to create He^{+} and Ne^{++} in the ejecta was recognized as soon as its existence became probable (Davidson 1997, 1999). Since Fe^{++}, He^{+}, Ar^{++}, and Ne^{++} depend on stellar photon fluxes just above 16, 25, 27, and 41 eV, the relative strengths of high-excitation lines may indicate the energy distribution of the star's ionizing UV photons, and thereby its temperature. Therefore, I employ quasi-nebular photoionization calculations to model the relative high-excitation line strengths. Differences from earlier calculations described by Verner et al. (2005) will be noted in Section 3.4.4.

3.4.1 Procedure and Assumptions

Version 08.00 of the photoionization program Cloudy (Ferland et al. 1998) was used to simulate conditions observed at Weigelt knot C. Since the primary star can safely be neglected in the high-ionization zones, I assumed a simple configuration with one stellar source and a uniform-density cloud at distance $r \approx 10^{16}$ cm ≈ 700 AU which is reasonable for Weigelt knot C. A covering factor of 0.05 and a filling factor of unity for the gas were chosen. Possible UV extinction by dust within the He^+ region was neglected for three reasons: (1) local reddening of the [Fe II] emission is known to be small in the Weigelt knots (Hamann et al. 1999; Davidson et al. 1995) while the high-ionization zones should have smaller column densities; (2) dust grains associated with η Car tend to be abnormally large (Davidson & Humphreys 1997) and therefore relatively ineffective at $h\nu > 20$ eV; and (3) not enough information is available to realistically include the effects of local dust on the ionizing radiation. Altogether these assumptions represent an idealized view, but fortunately the line ratios used here depend only weakly on density and on geometrical details unless n_e exceeds 10^7 cm^{-3}. A higher-density regime appears unlikely because collisional de-excitation would then suppress the forbidden lines too much. If $n_\mathrm{e} \lesssim 10^7$ cm^{-3}, the results depend mainly on the star's effective temperature T_eff and the ionization parameter U_H, see section 3.4.3.

I assumed that the He^+ zone is ionization-limited, i.e., that it absorbs nearly all incident photons above 25 eV. This assumption is based on three observed clues: (1) lower-ionization regions clearly exist in and around the Weigelt knots, (2) almost no He I, [Ne III], and [Fe III] emission is seen at radii outside the locations of the knots, and (3) ratios of the He I, [Ne III], and [Fe III] lines do not vary much.

Studies of η Car's outer ejecta show a peculiar chemical composition due to the CNO cycle. The gas is helium- and nitrogen-rich while carbon and oxygen are scarce (Davidson et al. 1986; Dufour et al. 1999).[11] I considered two sets of abundances, "compositions A and B" which differ by a factor of two for elements heavier than helium (Table 3.1). The mass fraction of C+N+O (mostly N) is about 0.63% in composition A and 1.3% in B. The former value resembles some crude observational estimates for η Car (Davidson et al. 1986), while the latter is somewhat larger than Solar or Galactic material. The distinction between A and B turns out to affect the results only weakly, as explained in section 3.4.3. Note that carbon and oxygen are too scarce to play an appreciable role.

Weigelt knot C was chosen for this analysis because the high-excitation emission is strongest and best-defined there, see Figure 3.1. Knot C was observed well with *HST* STIS on 2003 February 13 (phase = 0.92) and 2003 May 17 (phase = 0.97). I used data

---

[11] The stellar wind spectrum appears consistent with the outer ejecta but does not indicate abundances as well (Hillier et al. 2001).

Table 3.1: Chemical compositions used in Cloudy simulations

$\log_{10}$ N(element)/N(H)	Comp. A[a]	Comp. B[b]
He	−0.70	−0.70
C	−5.00	−4.70
N	−3.10	−2.80
O	−5.00	−4.70
Ne	−4.00	−3.70
Si	−4.46	−4.16
S	−4.74	−4.44
Ar	−5.60	−5.30
Fe	−4.55	−4.25

[a] Default solar composition, except He, C, N, O.
[b] CNO fraction somewhat larger than solar.

Table 3.2: Selected high-excitation emission lines in Weigelt knot C

Spectrum	λ_{vac} (Å)	I.P.'s[a] (eV)	EW (Å)	$\mathrm{I}^b_{\mathrm{obs}}$	$\mathrm{I}^c_{\mathrm{corr}}$
[Ne III]	3869.85	40.96–63.45	10.24	3.63	1.00
Si III]	1892.03	16.34–33.49	3.84	2.78	2.10
[Ar III]	3110.08	27.63–40.74	0.42	0.17	0.06
[Ar III]	5193.26	27.63–40.74	0.39	0.11	0.024
[Ar III]	7137.76	27.63–40.74	6.36	2.24	0.40
[Ar III]	7753.24	27.63–40.74	1.93	0.59	0.10
He I	4027.33	24.59–54.42[d]	2.42	0.69	0.18
He I	6680.00	24.59–54.42[d]	5.44	2.54	0.47
He I	7067.20	24.59–54.42[d]	16.19	10.1	1.80
[S III]	6313.81	23.33–34.83	7.72	2.39	0.45
[S III]	9071.11	23.33–34.83	4.06	1.46	0.23
[S III]	9533.23	23.33–34.83	5.49	2.49	0.39
[Fe III]	4659.35	16.18–30.65	4.27	1.97	0.46
[Fe III]	4702.85	16.18–30.65	3.21	0.88	0.21

Ref: Atomic data from http://physics.nist.gov/ PhysRefData/ASD/.
[a] Relevant ionization potentials. For instance, Ne^+ and Ne^{++} have ionization potentials 40.96 and 63.45 eV.
[b] In units of 10^{-12} erg cm^{-2} s^{-1} within the 0.1″ sampled area.
[c] De-reddened intrinsic strength relative to [Ne III] λ3870.
[d] Recombination spectrum created in He^+ zone.

from 2003 February 13 with the slit passing through the star and knot C along position angle $PA = 303°$. On that date the high-excitation lines were still strong, whereas by May 17 they had declined seriously as the 2003.5 "event" approached. I measured well-isolated narrow high-excitation lines as target values for the photoionization models. The resulting equivalent widths and apparent intensities are listed in columns 4 and 5 of Table 3.2. An error of ±30% in an individual line strength, or perhaps even worse, would have little effect on the conclusions – partly because the photoionization models are very sensitive to the star's $T_{\rm eff}$, and partly because the He/Ne/Si/Ar abundance ratios are more uncertain than the observed line ratios.

The reddening was estimated from the [Ar III] $\lambda3110/\lambda5193$ and [Ar III] $\lambda7138/\lambda7753$ flux ratios. The intrinsic value of the former ratio, for instance, is reliably known because the $\lambda3110$ and $\lambda5193$ lines share the same upper level; and the case of $\lambda7138/\lambda7753$ is similar. Other reddening indicators are less trustworthy because they use more than one ion species or differing upper levels or other model-dependent factors. Since no physical model is available for η Car's anomalously large grains or for instrumental effects, a standard approximation for wavelength-dependent extinction was adopted: $A_\lambda \approx a + b/\lambda$. For small amounts of reddening this choice of mathematical form is not critical, provided that coefficient b is adjusted to give the right average slope from violet to red wavelengths. Fitting it to the [Ar III] measurements, surprisingly little reddening was found, $E_{\rm B-V} = A_{\rm B} - A_{\rm V} \approx 0.2$ magnitude.

This is only half the amount that the [Fe II] lines seem to indicate (Davidson et al. 1995; Hamann et al. 1999), but instrumental effects related to high spatial resolution probably account for most of the discrepancy. The normal wavelength dependence of *HST's* spatial resolution caused the slit throughput to decrease toward longer wavelengths for a localized source, and other effects also occurred in STIS data (Davidson 2006). Since these complications had smooth wavelength dependences, they are implicitly included in the *effective* or *apparent* reddening deduced from the [Ar III] line ratios. In other words, the $E_{\rm B-V}$ value mentioned above was really the true interstellar and circumstellar value minus a correction for instrumental effects. Meanwhile it is also possible that the [Fe II] method gives an overestimate of $E_{\rm B-V}$. No matter which effect dominates, the corrected relative line strengths are automatically valid to sufficient accuracy because the [Ar III] comparison method is based on known intrinsic ratios. As mentioned earlier, "sufficient accuracy" in this context would be ±30% or allowably even worse. Most of the values in Table 3.2 are expected to be better than this.

Thus, based on the [Ar III] lines, the following correction for net reddening was adopted:

$$I_{\rm corr} \;=\; 0.105 \exp\,(3740\,\text{Å}/\lambda)\, I_{\rm obs}\ . \tag{3.1}$$

Here the constant factor, which has no effect on the line ratios used in this photoionization analysis, is adjusted to give [Ne III] $\lambda3870$ a corrected value of 1.00. As a result

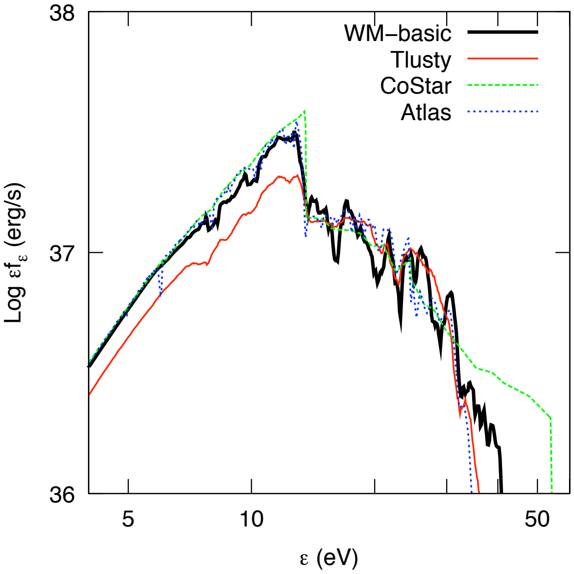

Figure 3.10: Stellar continua of Atlas, CoStar, Tlusty, and WM-basic atmosphere models with $T_{\rm eff} = 40,000$ K. Tlusty and WM-basic models were smoothed.

the corrected line strengths $I_{\rm corr}$ are intrinsic values relative to this line. They are listed in the last column of Table 3.2.

3.4.2 Stellar Model Atmospheres

I explored a multidimensional grid of photoionization models, varying the effective stellar temperature, ionization parameter, and gas density. The goal was to constrain these properties by comparing the calculated intensity ratios of high-excitation emission lines to the observed ones. Four theoretical stellar atmosphere grids available in Cloudy were considered. The Atlas models are LTE, plane-parallel, hydrostatic atmospheres with turbulent velocity distribution 2 km s^{-1} (Castelli & Kurucz 2004). The CoStar O-type models are non-LTE, line-blanketed model atmospheres, including stellar winds (Schaerer & de Koter 1997). The Tlusty models are non-LTE, line-blanketed, plane-parallel, hydrostatic O-star SEDs (Lanz & Hubeny 2003). The WM-basic O-star grids represent non-LTE, line-blanketed, wind-blanketed hot stars (Pauldrach et al. 2001).

Unfortunately these four types of theoretical models disagree with each other in their UV spectral energy distributions. Figure 3.10 shows the continuum of an O-type

Table 3.3: Comparison between different stellar atmosphere models[a]

Model	L (erg/s^{-1})	*log* $L/L_\odot$	*log* Q_H (photons s^{-1})	*log* Q_He (photons s^{-1})	*log* Q_NeIII (photons s^{-1})
Atlas	3.67e+38	4.98	48.72	48.27	46.09
CoStar	4.25e+38	5.04	48.90	48.70	48.32
Tlusty	3.27e+38	4.93	48.76	48.40	46.33
WM-basic	3.99e+38	5.02	48.82	48.51	47.04

[a] $T_\mathrm{eff} = 40,000$ K, $n_\mathrm{H}= 10^6$ cm^{-3} and log $U_\mathrm{H} = -1$

main sequence star with $T_\mathrm{eff} = 40,000$ K and $L = 10^5\,L_\odot$ according to each model. Their differences are worst at high photon energies, particularly above 40 eV. Table 3.3 lists the total luminosities and photon rates that can ionize H^0, He^0, and Ne^+ in a comparable set of the four model types. The CoStar models do not include line opacity and therefore overestimate the far-UV flux because photon line-absorption and subsequent re-emission at longer wavelengths is not taken into account. The lower flux in the He^0 continuum ($h\nu > 25$ eV) of the WM-basic model compared to the Atlas models is probably due to non-LTE effects producing deeper line cores in the blocking lines. The WM-basic code uses a consistent treatment of line blocking and blanketing (Smith et al. 2002) and was adopted here.

3.4.3 Resulting Constraints on the Secondary Star

The Weigelt knots encompass a wide range of densities (Hamann et al. 1999). I therefore varied the hydrogen density from 10^5 to 10^7 cm^{-3}, and for each density I varied the ionization parameter U_H between 10^{-2} and 10^2. The ionization parameter determines the sharpness of each ionization front, the coexistence of differing ionization stages, the ionized column density, and other physical attributes, as explained by Davidson & Netzer (1979). In Cloudy, U_H is defined as the dimensionless quantity $Q_\mathrm{H}/4\pi r_0^2 n_\mathrm{H} c$, where Q_H is the rate of hydrogen-ionizing photons ($h\nu > 13.6$ eV) emitted by the source star, r_0 is the distance from that source to the illuminated face of the cloud, n_H is the hydrogen density, and c is the speed of light. Here, of course, the photon supply above 25 eV rather than 13.6 eV is of interest. Cloudy produces ionization-limited plane-parallel models, obviously a crude approximation to the true geometry. Figure 3.11 shows the

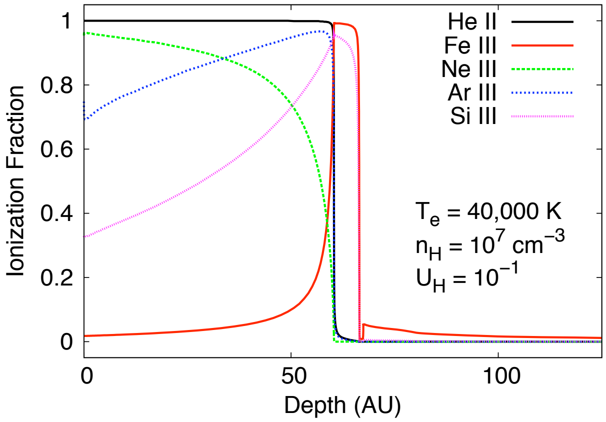

Figure 3.11: Ionization fractions of He II, Fe III, Ne III, Ar III, and Si III in Weigelt knot C. Simulated with WM-basic atmosphere model and $T_{\rm eff} = 40,000$ K, $n_{\rm H} = 10^7$ cm^{-3}, and $U_{\rm H} = 10^{-1}$.

ionization fractions of several species in Weigelt knot C in photoionization modeling of a possible scenario.

Table 3.4 and Figure 3.12 show the effective temperatures of WM-basic stellar atmospheres that give the observed strengths of Si III] λ1892, [Ar III] λ7138, and He I λ6680 relative to [Ne III] λ3870. ([Fe III] and [S III] are satisfactory in the models favored below.) For ionization parameters *log* $U_{\rm H} \gtrsim +1$ the required stellar temperature is roughly constant, while smaller values of *log* $U_{\rm H}$ require progressively higher $T_{\rm eff}$. Since these results involve a subtle blend of uncertainties, the shaded regions in Figure 3.12 represent factor-of-4 ranges for each line ratio. The best match to the observed data set occurs with *log* $U_{\rm H} < -1$ and $T_{\rm eff} \sim 40,000$ K. Here are some relevant considerations:

1. It is not surprising that chemical compositions A and B give similar results. Roughly speaking, the hydrogen and helium recombination lines indicate numbers of ionizing photons that have been absorbed, while the heavier-element emission lines account for much of the cooling and thus represent the total energy in the absorbed photons (Davidson & Netzer 1979; Osterbrock & Ferland 2006). If the overall abundance of heavy elements relative to H+He is altered, the equilibrium gas temperature automatically adjusts so that the ratio of heavy-element emission lines to hydrogen and helium lines does not change much. This ratio depends chiefly on the slope of the ionizing source's spectral energy distribution.

Table 3.4: WM-basic model predictions of $T_{\rm eff}$ for secondary star and composition A.

Density (cm^{-3})	*log* $U_{\rm H}$	*log* $Q_{\rm H}$ (photons s^{-1})	$T_{\rm eff}$(Ar 7138)^a (K)	$T_{\rm eff}$(He 6680)^a (K)	$T_{\rm eff}$(Si 1892)^a (K)	$T_{\rm avg}$ (K)	$\Delta T_{\rm avg}$ (K)	*log* $L/L_\odot$
10^5	-2.14	46.44	48700	40300	37600	42200^c	5800	2.84
10^5	-2	46.58	48700	38900	37200	$41600^{b,c}$	6200	2.99
10^5	-1	47.58	42300	35900	35100	$37800^{b,c}$	3900	4.08
10^5	0	48.58	39100	34200	33900	35700^b	2900	5.16
10^5	1	49.58	37700	33300	33500	34800^b	2500	6.22
10^5	2	50.58	36800	33000	33100	$34300^{b,c}$	2200	7.31
10^6	-2	47.58	43400	37600	41100	40700^c	2900	4.00
10^6	-1	48.58	38100	33900	36700	36500	2300	5.13
10^6	-0.67	48.91	37200	33600	37200	36000	2100	5.48
10^6	0	49.58	36600	32800	36600	35300^b	2200	6.18
10^6	1	50.58	36200	32600	36300	$35000^{b,c}$	2100	7.19
10^6	2	51.58	36600	32800	35900	$35100^{b,c}$	2000	8.19
10^7	-2	48.58	39400	38000	51900	43100	7700	4.97
10^7	-1	49.58	36100	34900	43700	38200	4800	6.06
10^7	0	50.58	36000	34500	38700	36400^c	2100	7.13
10^7	0.24	50.82	35700	34500	38400	36200^c	2000	7.38
10^7	1	51.58	35500	34900	38100	$36200^{b,c}$	1700	8.14
10^7	2	52.58	35600	34900	37800	$36100^{b,c}$	1500	9.14

[a] Relative to [Ne III] λ3870 Å.

[b] Models with He II region larger than 4×10^{15} cm.

[c] Models with log $L/L_\odot$ smaller then 5 or larger than 6.

2. For *log* $U_{\rm H} > -1$, He I λ6680 indicates generally lower values of $T_{\rm eff}$ than the other lines do. Very likely this clue is evidence for *log* $U_{\rm H} < -1$; but note that models which are density-limited, or limited by internal dust, or convex, can produce stronger helium lines relative to [Ne III].

3. Since relative abundances of individual heavy elements are quite uncertain in η Car, and the reddening correction is uncertain for the UV Si III] line, the systematic difference between [Ar III] and Si III] in Figure 3.12 is not very alarming.

4. Although the high-ionization emission lines are easier to model than low-ionization features, some special processes may occur. For example Si III] λ1892 may be enhanced by resonance-favored two-photon ionization of Si^+ (Johansson et al. 2006). Such effects are unusual, however, and unlikely to alter the basic conclusions. (If the Si III] effect is strong, it produces a discrepancy between He I and Si III] in photoionization models.)

5. Models with $n_{\rm e} \gtrsim 2 \times 10^7$ cm^{-3} produce insufficient [Ne III] and [Ar III] emission compared to He I and Si III], regardless of the stellar temperature. This is because the characteristic electron densities for collisional de-excitation of [Ne III] and

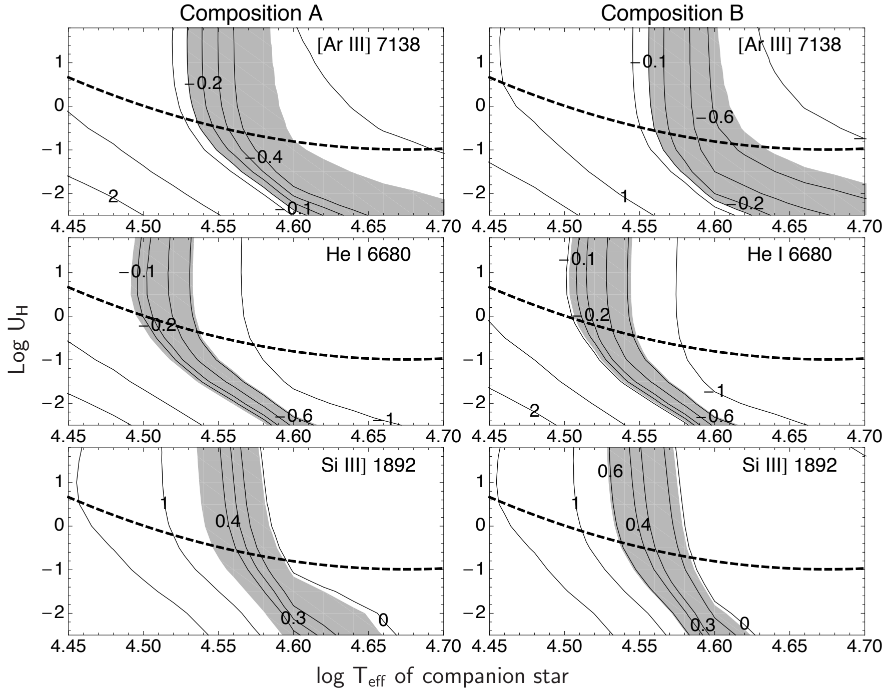

Figure 3.12: Contour plots of line intensity ratios [Ar III] λ7138/[Ne III] λ3870, He I λ6680/[Ne III] λ3870, and Si III] λ1892/[Ne III] λ3870 in photoionization models with $n_{\rm H}$= 10^6 cm^{-3}. Shaded areas correspond to the range of line intensity ratio between 0.5 and 2 times the observed value. Left and right columns refer to chemical compositions A and B, respectively. Models above the dashed curve are spatially too extended, violating criterion 6 in the text.

[Ar III] are roughly 10^7 and 5×10^6 cm^{-3} respectively.

6. Models with $n_{\rm e} << 10^6$ cm^{-3} are ruled out by geometrical considerations. For reasons mentioned in Section 3.4.1, the He$^+$ region cannot be much smaller than the ionization-limited thickness. This characteristic linear size x is proportional to $U_{\rm H}/n_{\rm e}$. In Table 3.4 and Figure 3.12 models are indicated that are unsuitable because $x > 250$ AU, i.e. an ionization-limited He$^+$ zone would be larger than the region of the Weigelt knots. This criterion excludes all models with $n_{\rm e} = 10^5$ cm^{-3}, and those which have $n_{\rm e} = 10^6$ cm^{-3} and *log* $U_{\rm H} > -0.65$.

7. A truly realistic model would include a range or distribution of gas densities, but there are not enough observables to do this. At present it can only be said that the "representative density" in a simplified model is very likely about half the

maximum density which exists in the real, non-uniform He^+ gas, in an order-of-magnitude sense. (This statement can be wrong if the configuration is unexpectedly complex.)

8. For a given gas density n_e and stellar temperature T_eff, one can estimate the luminosity L that would produce the assumed value of U_H in Weigelt knot C. As shown in the last column of Table 3.4, some choices of (n_e, U_H) lead to absurdly small or large values of L. Most important, the secondary star cannot exceed about $10^6\,L_\odot$ since its presence is not evident in the UV spectra obtained with *HST* STIS. (The primary star has $L \approx 5 \times 10^6\,L_\odot$.)

The H-R diagram in Figure 3.13 summarizes the conclusions about the secondary star, assisted by a few more clues. Here two broad curves mark the results of photoionization calculations with $n_\mathrm{e} = 10^7$ cm^{-3} and 10^6 cm^{-3}; the upper end of the latter curve is limited by criterion 6 above. If the assumption is correct that the two stars have the same age, evolutionary circumstances further constrain the parameters. The minimum age for the primary star to have become helium-rich is 0.5 Myr (Iben 1999), but it is most likely 2–3 Myr old based on its instabilities and probable association with the cluster Trumpler 16 (Walborn 1995). The lifetime of any star above $\sim\ 60\,M_\odot$ is roughly 3 Myr. Therefore, in Figure 3.13 isochrones for 0.5, 2, and 3 Myr as well as some evolutionary tracks are shown, all adapted from Martins et al. (2005). Another constraint can be based on the observed X-ray spectrum, which indicates a secondary wind speed close to 3000 km s^{-1} (Pittard & Corcoran 2002). Practically all stars with winds that fast have $T_\mathrm{eff} > 37,000$ K, marked by a vertical dotted line in Figure 3.13 (Kudritzki & Puls 2000; and references cited therein).

Altogether, the secondary star is expected to lie somewhere within the shaded polygon in Figure 3.13, with the following limits: (1) The right-hand boundary is the X-ray-implied minimum temperature. Even without this argument a similar limit would be deduced from criterion 6 listed above. (2) The upper limit is $L \approx 10^6\,L_\odot$, criterion 8. (3) The upper-left boundary is based on the photoionization criterion 5, $n_\mathrm{e} \lesssim 2 \times 10^7$ cm^{-3}. (4) The lower-left boundary is the 0.5 Myr isochrone, and perhaps this limit should be moved rightward in the diagram to some age greater than 1 Myr. A star with $M_\mathrm{ZAMS} \sim 40$ to 60 $M_\odot$ and $T_\mathrm{eff} \approx 40,000$ K, for example, would satisfy all these

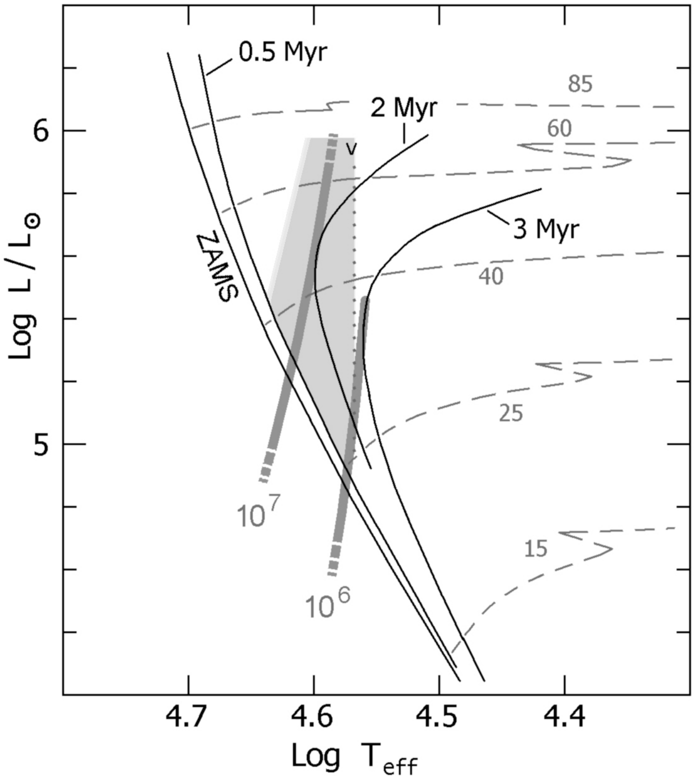

Figure 3.13: Likely positions for η Car's companion star in the H-R diagram. Solid curves show isochrones for 0.5, 2, and 3 Myr, while dashed curves show evolution tracks for initial masses 15 to 85 $M_\odot$, all adapted from Martins et al. (2005). The two broad lines show L vs. $T_{\rm eff}$ correlations in photoionization models with $n_{\rm H} = 10^7$ and 10^6 cm^{-3}. A small 'V' indicates a model suggested by Verner et al. (2005). The shaded polygon is the region allowed by various considerations (see text).

requirements. The corresponding spectral type would be O4 or O5 (Martins et al. 2005). If, however, the system is more than 2 Myr old, then the secondary's zero-age mass was probably less than 50 $M_\odot$. (All statements related to isochrones obviously depend on the evolution models, though.)

If the entire region around η Car were clearly visible, then the absolute brightnesses of the high-excitation emission lines would indirectly indicate the secondary star's luminosity. In fact the local extinction is far too patchy, but a crude estimate based on the observable [Ne III] brightness was attempted. In Cloudy calculations with reasonable input parameters, the ionizing star's luminosity was around 2300 times the luminosity of [Ne III] $\lambda 3870$. Measuring the total flux of this line in the Weigelt knots, and assuming reasonable factors for the extinction and the solid angle intercepted by the knots, I found $log\ L/L_{\odot} \sim 5.5$. This estimate is very rough, but it is consistent with Figure 3.13 and thereby suggests that the absolute fluxes are reasonable.

Pittard & Corcoran (2002) assumed that the secondary star has a mass-loss rate close to $10^{-5}\ M_{\odot}\ \mathrm{yr}^{-1}$, in order to obtain sufficient X-ray luminosity in their colliding-wind models. Such a high rate would be very unusual, and not entirely consistent with the discussion above. Possibly this is an argument in favor of a more luminous secondary star; but on the other hand the mass-loss estimate is not very robust. Only a small fraction of the wind's kinetic energy is converted to observable X-rays, via some complicated efficiency factors. The secondary wind speed however, almost directly determines the average temperature seen in the 2–10 keV X-ray spectrum. The 3000 km s^{-1} speed estimate is relatively more trustworthy than the mass-loss rate.

One can imagine models that are seriously affected by changes in the secondary star. For instance, conceivably it was originally more massive but has now become a Wolf-Rayet object. Soker (2007) has proposed another scenario, wherein the secondary star accreted a large amount of mass during the Great Eruption 160–170 years ago, and has not yet returned to its normal thermal equilibrium (see also Kashi & Soker 2009b). Apart from obvious complications and a lack of substantive evidence for them, models of these types are clearly not the *simplest* possibilities. They have multiple adjustable parameters. Note, incidentally, that these photoionization calculations do not favor an extremely hot star with $T_{\mathrm{eff}} > 45,000$ K.

3.4.4 Comparison with Previous Calculations

Verner et al. (2005) reported an earlier set of photoionization calculations very much like these, with the same goal; but they deduced appreciably different parameters for the secondary star. They also used Cloudy with WM-basic atmospheres, uniform density in the ionized material, etc. They used earlier STIS data, but the high-excitation line ratios were similar to the ones used here within the uncertainties. Verner et al. appear to have supposed that the high-ionization lines originate much closer to the star than the locations of the Weigelt knots, but this probably had little effect on their results. They described photoionization models with specific sets of parameters, but did not show systematic maps of parameter space as in Table 3.4 and Figures 3.12 and 3.13.

There are three notable differences between their results and the results presented here: The allowed region in Figure 3.13 is much larger than their discussion seems to imply, their suggested upper limit for $T_{\rm eff}$ is barely above the lower limit, and they assigned a maximal luminosity to the secondary star. Indeed Verner et al. proposed that it has $T_{\rm eff} \approx 37,200$ K and $log\ L/L_{\odot} \approx 5.97$, marked with a small "V" in Figure 3.13. (They classified it "O7.5 I", but according to Martins et al. (2005) an O5.5 supergiant would have that temperature.) Such an object is not excluded by the calculations, but it has three disadvantages: It has the minimum temperature required for a 3000 km s^{-1} wind, it requires the age of the system to be less than 2 Myr, and it has practically the largest allowable luminosity. However, there is no strong argument against lower luminosities. In summary, given the limited information currently available, the parameters suggested by Verner et al. are not the most suitable choices for assessing the nature of η Car's companion at this time.

Chapter 4

A Sea Change in Eta Carinae

Eta Car has a complex 5.54-year spectroscopic cycle, most likely regulated by a companion star in an eccentric orbit, as discussed by many authors in Humphreys & Stanek (2005). High-excitation emission lines temporarily vanish during periodic spectroscopic events, e.g., around 1998.0, 2003.5, and 2009.0, perhaps near periastron. The spectrum change described in this chapter is more conspicuous than any of those "events," and there is no strong reason to assume that it is related to the 5.54-year cycle. But such a linkage might exist, and in any case the cycle may influence any data comparison.

After a five-year hiatus, *HST* STIS obtained new spectra of η Car beginning in mid-2009. Observations in August 2009 and March 2010 occurred at phases 2.10 and 2.20, and fortunately some STIS data had been obtained approximately one and two cycles earlier, at phases 1.12 in 2004 and 0.21 in 1999. It is also prudent to examine data sets taken one cycle apart during 1998–2004. Therefore, spectra of the star are compared at phases 0.04 vs. 1.03, 1.12 vs. 2.10, and 0.21 vs. 2.20.[12] The 0.04/1.03 data were close to spectroscopic events but not within them; in most proposed orbit models they represent longitudes 100–140° past periastron, with star-star separations 2–5 times larger than at periastron. The 0.21/2.20 phases were well outside the "events" (Mehner et al. 2010a; Martin et al. 2010). The findings were verified and extended with *Gemini* GMOS observations in 2007–2010.

---

[12] Calendar dates 1998-03-19/2003-09-22, 2004-03-07/2009-08-19, and 1999-02-21/2010-03-03; MJD 50891/52904, 53071/55062, and 51230/55258.

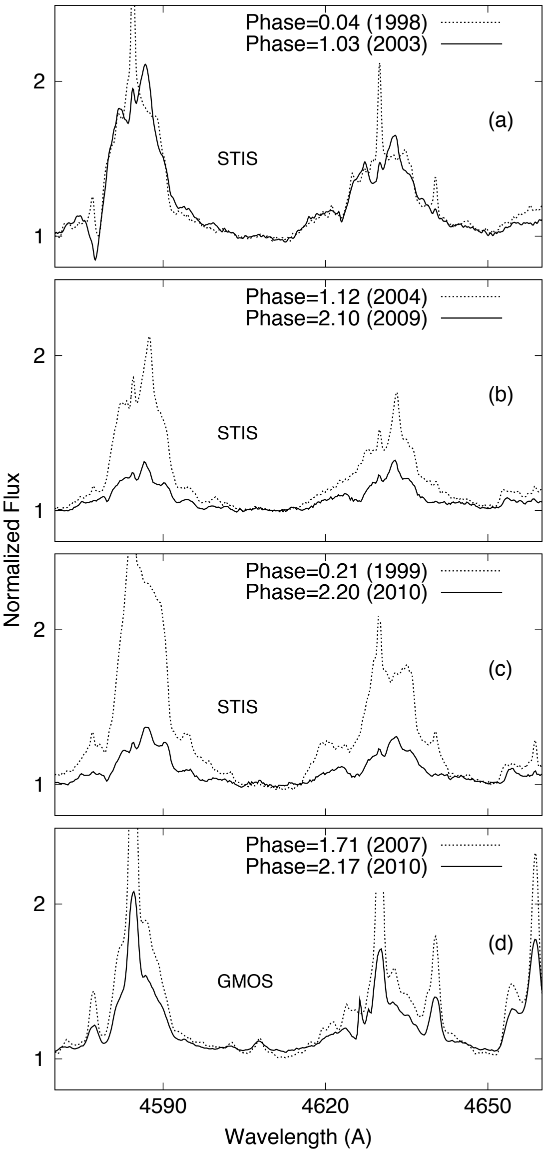

Figure 4.1: Blends of Fe II, [Fe II], Cr II, and [Cr II] near 4600 Å (1998–2010). Flux is normalized to unity at $\lambda4605$ Å. Panels (a,b,c) show *HST* STIS data in successive spectroscopic cycles, while (d) shows two *Gemini* GMOS spectra. Spatial resolution was about $0.1''$ for STIS and $1''$ for GMOS. The narrow features are not crucial here, since they originate far outside the stellar wind; their decrease relative to the star may be merely an indirect consequence of changes in circumstellar extinction. The blends shown here are dominated by Fe II $\lambda\lambda4584.1,4585.1,4630.6$, [Fe II] $\lambda4641.0$, and Cr II $\lambda4589.5$. A spectrum obtained at phase 2.28 shows no significant differences from the one at phase 2.20.

4.1 A Secular Change in Eta Carinae's Stellar Wind

During 1991–2004, *HST* FOS and STIS showed no definite secular change in η Car's stellar wind spectrum. The Hβ equivalent width, for instance, varied only ±10% (r.m.s.) outside spectroscopic events (Davidson et al. 2005). Figure 4.1a illustrates the similarity of broad wind features in two successive cycles before 2004. The qualitative ground-based record from 1900 to 1990 shows no discernible instance of a change like that reported below; see many refs. in Humphreys et al. (2008).

The 2009–2010 STIS data, however, reveal *the weakest broad-line spectrum ever seen in modern observations of this object,* relative to the underlying continuum. Low-excitation emission created in the stellar wind became far less prominent. For example, Figure 4.1 shows blends of Fe II, [Fe II], and Cr II near λ4600 Å. Phases 0.04 and 1.03 (1998 and 2003) were mutually consistent, but W_λ decreased by factors of 2–4 between phases 1.12 and 2.10 and likewise between 0.21 and 2.20. Most of the broad lines originate in the primary star's wind, see many papers and refs. in Humphreys & Stanek (2005). Fe II blends are common in the spectrum of η Car due to the richness of the Fe II ionic spectrum.

Gemini GMOS observations in 2007–2010 confirm the reality of these spectrum changes, Figure 4.1d. In 2010 the GMOS data show stronger emission lines than STIS does (Figures 4.1d vs. 4.1c), merely because the $1''$ ground-based spatial resolution allows significant contributions by ejecta far outside the stellar wind. Nevertheless, equivalent widths of low-excitation emission blends in the GMOS data decreased by factors of about 2 between June 2007 and March 2010. Most of the GMOS data at intermediate times were of lower quality, but they strongly suggest that the spectral change was progressive rather than abrupt (see Figure 4.2). Similar changes occurred throughout the violet-to-red wind spectrum. UV emission lines around λ2600 Å weakened relative to the continuum, while the overall brightness in that wavelength region increased by 20–30% between August 2009 and March 2010.

Table 4.1 and Figure 4.2 show the equivalent widths of some Fe II/Cr II blends close to λ4600 Å in *HST* STIS and *Gemini* GMOS data from 1998–2010. The lines did not weaken abruptly but rather gradually over the last 12 years. GMOS data fill in valuable data points during several years when STIS was unavailable, even though they sample a wider region around the star. The large difference in equivalent width at similar

Table 4.1: Equivalent widths of broad stellar wind features[a] in *HST* STIS and *Gemini* GMOS data (1998–2010)

	Name[b]	Date (UT)	MJD	Phase	EW$^{c}_{\lambda 4570-4600}$ (Å)	EW$^{c}_{\lambda 4614-4648}$ (Å)	EW$^{c}_{\lambda 4722-4740}$ (Å)
HST STIS	c821	1998 Mar 19	50891.4	0.038	11.02 ± 0.05	8.84 ± 0.01	1.85 ± 0.08
	c914	1999 Feb 21	51230.5	0.206	16.51 ±0.06	12.37 ± 0.10	1.78 ± 0.05
	cA22	2000 Mar 20	51623.8	0.400	15.99 ± 0.42	11.55 ± 0.21	1.69 ± 0.01
	cB29	2001 Apr 17	52016.8	0.595	11.81 ± 0.13	8.90 ± 0.21	1.38 ± 0.07
	cC05	2002 Jan 20	52294.0	0.732	14.40 ± 0.06	10.73 ± 0.04	1.75 ± 0.05
	cC51	2022 Jul 04	52459.5	0.813	13.72 ± 0.46	10.46 ± 0.28	1.73 ± 0.07
	cD12	2003 Feb 13	52683.1	0.924	9.39 ± 0.01	7.72 ± 0.10	1.54 ± 0.06
	cD24	2003 Mar 29	52727.3	0.946	9.31 ±0.03	7.49 ± 0.11	1.47 ± 0.03
	cD34	2003 May 05	52764.3	0.964	10.10 ± 0.07	7.98 ± 0.25	1.70 ± 0.07
	cD37	2003 May 19	52778.5	0.971	10.96 ± 0.06	8.58 ± 0.04	1.56 ± 0.02
	cD41	2003 Jun 01	52791.7	0.978	12.47 ± 0.29	9.69 ± 0.01	1.69 ± 0.01
	cD47	2003 Jun 23	52813.8	0.989	11.78 ± 0.11	10.38 ± 0.23	1.72 ± 0.11
	cD51	2003 Jul 05	52825.4	0.994	10.89 ± 0.81	8.87 ± 0.25	1.29 ± 0.08
	cD58	2003 Aug 01	52852.4	1.008	12.50 ± 0.44	9.90 ± 0.39	1.67 ± 0.10
	cD72	2003 Sep 22	52904.3	1.033	10.31 ± 0.10	8.36 ± 0.03	1.51 ± 0.06
	cD88	2003 Nov 17	52960.6	1.061	11.95 ± 0.14	9.25 ± 0.21	1.56 ± 0.02
	cE18	2004 Mar 07	53071.2	1.116	9.20 ± 0.27	7.69 ± 0.12	1.20 ± 0.04
	cJ49[d]	2009 Jun 30	55012.1	2.075	3.42 ± 0.27	3.39 ± 0.34	0.67 ± 0.07
	cJ63	2009 Aug 19	55062.0	2.100	2.58 ± 0.21	3.82 ± 0.03	0.63 ± 0.11
	cJ93	2009 Dec 06	55171.6	2.154	4.3 ± 0.15	3.78 ± 0.32	0.72 ± 0.13
	cK16	2010 Mar 03	55258.6	2.197	5.07 ± 0.10	4.19 ± 0.12	0.76 ± 0.08
	cK63	2010 Aug 20	55428.3	2.281	4.64 ± 0.18	4.18 ± 0.05	0.70 ± 0.15
Gemini GMOS	gH45	2007 Jun 16	54268.0	1.707	11.10 ± 0.20	10.23 ± 0.19	4.89 ± 0.08
	gH49	2007 Jun 30	54281.0	1.714	11.32 ± 1.07	9.70 ± 0.74	6.02 ± 0.16
	gI11	2008 Feb 11	54507.4	1.826	11.99 ± 0.76	11.44 ± 0.36	6.87 ± 0.21
	gI50	2008 Jul 05	54652.0	1.897	9.88 ± 0.10	8.58 ± 0.45	5.15 ± 0.12
	gI54	2008 Jul 17	54665.0	1.904	9.65 ± 0.04	8.78 ± 0.03	4.92 ± 0.12
	gI85	2008 Nov 08	54778.3	1.960	11.21 ± 0.00	11.81 ± 0.00	6.60 ± 0.00
	gI90	2008 Nov 27	54797.3	1.969	10.74 ± 0.96	10.47 ± 1.86	5.76 ± 0.43
	gI96	2008 Dec 18	54818.3	1.979	10.60 ± 1.03	10.85 ± 1.15	5.56 ± 0.30
	gI98	2008 Dec 25	54825.3	1.983	11.35 ± 0.57	11.63 ± 0.95	6.12 ± 0.06
	gI99	2008 Dec 31	54831.3	1.986	9.44 ± 0.38	10.26 ± 0.14	4.84 ± 0.53
	gJ01	2009 Jan 04	54835.3	1.988	10.03 ± 0.38	10.43 ± 0.86	5.19 ± 0.04
	gJ02	2009 Jan 09	54840.2	1.990	9.14 ± 0.54	10.08 ± 0.80	4.70 ± 0.18
	gJ03	2009 Jan 12	54843.3	1.992	8.33 ± 0.28	9.32 ± 0.08	4.23 ± 0.27
	gJ04	2009 Jan 15	54846.2	1.993	8.48 ± 1.42	8.72 ± 1.68	4.46 ± 1.10
	gJ05	2009 Jan 21	54852.3	1.996	7.51 ± 0.88	8.49 ± 0.69	4.44 ± 0.25
	gJ06	2009 Jan 24	54855.3	1.998	7.94 ± 0.52	8.27 ± 0.77	4.01 ± 0.28
	gJ07	2009 Jan 29	54860.4	2.000	9.04 ± 0.85	8.70 ± 1.15	4.69 ± 0.88
	gJ09	2009 Feb 05	54867.2	2.004	8.12 ± 0.33	8.49 ± 0.72	4.28 ± 0.03
	gJ13	2009 Feb 19	54881.2	2.011	6.86 ± 0.36	7.54 ± 0.68	4.04 ± 0.13
	gJ20	2009 Mar 17	54907.3	2.023	6.89 ± 0.58	6.94 ± 0.79	3.70 ± 0.34
	gJ32	2009 Apr 28	54949.1	2.044	7.84 ± 0.87	7.96 ± 1.39	5.13 ± 1.00
	gJ56	2009 Jul 23	55036.0	2.087	6.50 ± 0.31	6.18 ± 0.86	3.26 ± 0.61
	gK02	2010 Jan 08	55204.3	2.170	5.39 ± 0.39	5.09 ± 0.58	2.31 ± 0.18

[a] Mainly Fe II and Cr II blends.

[b] As listed on the Eta Carinae Treasury Project site at http://etacar.umn.edu/.

[c] Continuum was set at λ4605 and λ4740 Å.

[d] $\mathrm{EW}_{\lambda\lambda 4570-4600, 0.65''} = 6.23$, $\mathrm{EW}_{\lambda\lambda 4614-4648, 0.65''} = 5.27$, and $\mathrm{EW}_{\lambda\lambda 4722-4740, 0.65''} = 2.45$ Å, see text.

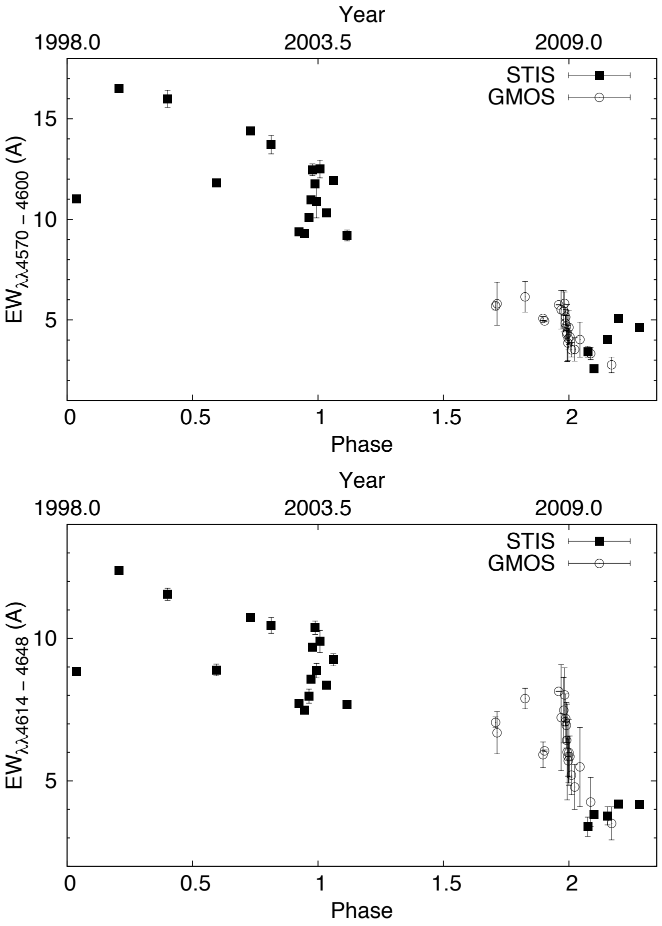

Figure 4.2: Equivalent widths of Fe II and Cr II blends at $\lambda\lambda$4570–4600 and $\lambda\lambda$4614–4648 Å in *HST* STIS (filled squares) and *Gemini* GMOS (open circles) spectra from 1998–2010. Equivalent widths of GMOS data were divided by 1.95 and 1.45, respectively, to account for the wider spatial sampling of this data set.

phases (see Table 4.1) is due to the fact that GMOS data include the broad extended emission of forbidden [Fe II] and [Fe III] lines discussed in section 8.1. The STIS 2009 June mapping data were used to simulate a ground-based spectrum with a spatial sampling of $0.65''$x$0.65''$. Equivalent widths from the simulated ground-based spectrum are; $\mathrm{EW}_{\lambda\lambda 4570-4600,0.65"} = 6.23$ Å, $\mathrm{EW}_{\lambda\lambda 4614-4648,0.65"} = 5.27$ Å, and $\mathrm{EW}_{\lambda\lambda 4722-4740,0.65"} = 2.45$ Å. Those values agree very well with the *Gemini* GMOS data obtained about one month after, see Table 4.1. A corresponding correction factor was applied to the GMOS measurements in Figure 4.2 to account for the wider spatial sampling.

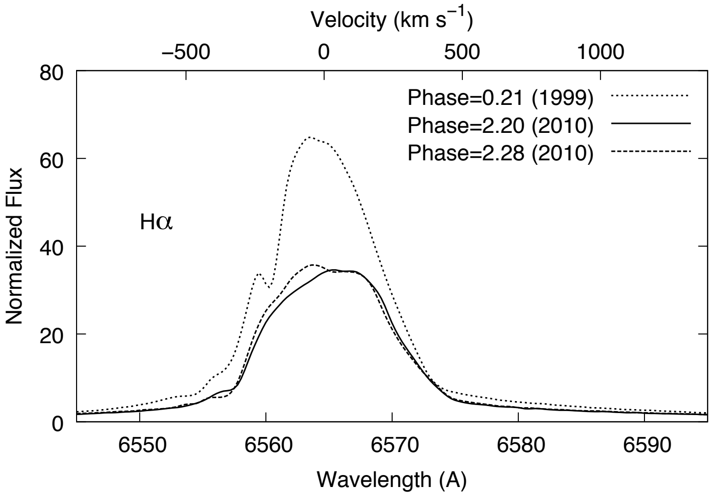

Figure 4.3: Hα about 400 days after the 1998 (phase=0.21) and 2009 (phase=2.20) "events." Flux is normalized to 1.0 at 6620 Å. The profile is altered and weakened. Note the disappearance of external narrow absorption near −145 km s^{-1}. A spectrum at phase 2.28 shows that 570 days after the 2009 "event" the line profile is still very similar to the profile at phase 2.20.

Additionally, the profile of Hα, the strongest emission line in the violet-to-red spectrum, is altered and weakened in the recent STIS data (Figures 4.3 and 4.4). Hα had a low flat-topped profile during the 2003.5 "event" and then partially recovered (Davidson et al. 2005); but now it is even weaker. The narrow Hα absorption near −145 km s^{-1} indicates unusual nebular physics far outside the wind (Johansson et al. 2005). Always present in 1998–2004, this feature had weakened by 2007 but reappeared during the 2009.0 "event" (Ruiz et al. 1984; Davidson et al. 1999b, 2005; Martin et al. 2010; Richardson et al. 2010). By March 2010 it had practically vanished. Measurements of Hα with different instruments since 1998 show a rapid decline in equivalent width during the 2003.5 and the 2009 "events." However, only after the 2009 "event" does the equivalent width not recover to former strength. Higher Balmer lines confirm this finding, see Figure 4.5 for tracings of observations in 1999 and 2010 of Hβ, Hϵ, Hζ, and Hη. (Hγ and Hδ were not observed with *HST* STIS after the 2009 "event.")

High-excitation He I emission did not weaken along with the features noted above, but the P Cygni absorption features of helium greatly strengthened after the 2009 "event" (Figure 4.6). The strengthened absorption feature is also seen in other He I

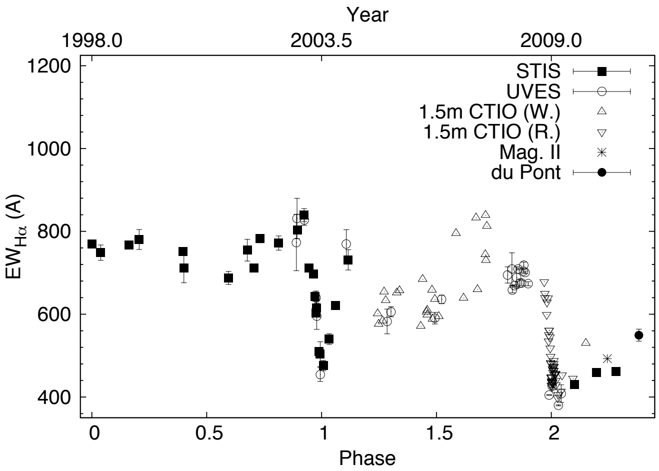

Figure 4.4: Equivalent width of Hα between 1998–2010 from STIS (filled squares), UVES (open circles), 1.5m CTIO (open triangles faced up, the open triangles faced down are from Richardson et al. 2010), Magellan II (star), and Irénée du Pont (filled circle).

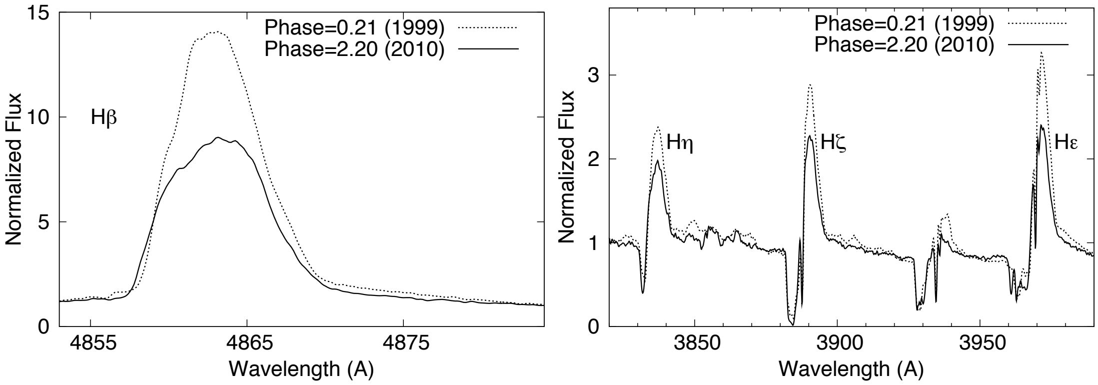

Figure 4.5: Higher Balmer emission line profiles show a similar weakening as Hα.

lines such as $\lambda\lambda$4027,4714. This requires caution because He I varies intricately during each cycle. Note, however, that only a few occasions in 1998–2004 showed absorption as deep as that seen at phase 2.20 in 2010 March; and phase 0.21 showed practically none.

It needs to be emphasized that the stellar wind emission lines have weakened relative to the continuum; outlying ejecta will require a separate investigation. The simplest explanation is a decrease in η Car's primary wind density, which seems natural for the long-term recovery as well as other recent data (Davidson et al. 2005; Martin et al.

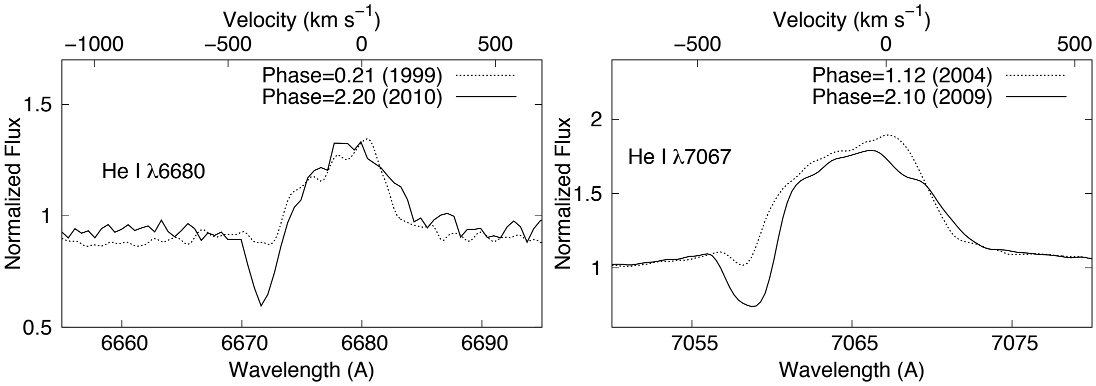

Figure 4.6: He I λ6680 in 1999 and 2010, and He I λ7067 in 2004 and 2010. P Cygni absorption features are greatly strengthened.

2006b; Humphreys et al. 2008; Kashi & Soker 2009a; Martin et al. 2010). The surprise is in the rapidity of this development. Long ago it was expected that after the year 2050 this object will appear much as it did to Halley and Lacaille three centuries ago, a hot fourth-magnitude star with a transparent rather than opaque wind (Davidson 1987). But now the schedule appears to be accelerated; if the recent trend continues, the star will approach that goal in only a decade. Even if the spectrum regresses to its earlier state, these developments are crucial because the observational record shows no precedent for them.

In a rough attempt to determine by how much the mass loss rate has decreased over the last 10 years, I adopted the method by Leitherer (1988) which uses Hα emission to determine the stellar mass loss rate. Hα luminosity is related to the stellar mass loss rate, stellar radius, velocity law, and effective temperature. Assuming only the mass loss rate is responsible for the observed spectral changes, I found that the mass loss rate declined by a factor of 2–3 between 1999 and 2010. This is in good agreement with estimates based on the X-ray light curve by Kashi & Soker (2009a) and Corcoran et al. (2010). However, more detailed analysis is necessary and especially the latitudinal dependence of the mass loss has to be investigated further, see also section 4.2.

Other alternatives to the decreasing-wind interpretation include, e.g., a change in the latitude-dependence of the wind (Smith et al. 2003), or the unusual models for η Car favored by Kashi & Soker (2007, 2009a,b). Many complications exist. For instance, a lessened wind density should cause the photosphere (located in the opaque wind) to shrink and become hotter, eventually leading to a *decrease* in visual-wavelength flux. Indeed this may have occurred in 2006 (Fernández-Lajús et al. 2009; Martin et al. 2010), but circumstellar dust and other factors probably dominate.

Numerous observables figure in the problem. For example, He I lines have behaved differently from the lower-excitation features. Helium emission and absorption processes in η Car's wind depend on the companion star and have other special characteristics, see section 6 of Humphreys et al. (2008). The constant He I emission components may be explained with the competing effect of changes in the He I ionization (Najarro et al. 1997). Also relevant are the 2–10 keV X-rays formed in the wind-wind collision zone. Kashi & Soker (2009a) have suggested that the earlier-than-expected recovery of X-rays after the 2009.0 spectroscopic event may signal a decrease in the wind density. Independent of that problem, in early 2010 the 2–10 keV flux has been about 20% below the level seen in two previous 5.54-year cycles (Corcoran 2010). This decrease is much less extreme than the spectroscopic changes described above; perhaps these effects depend on latitude differences between the direct view of the wind and conditions near the wind-wind shocks (Smith et al. 2003; Davidson 2005; Humphreys et al. 2008). Realistic wind models will need to be non-spherical and even non-axisymmetric. However, that the X-ray lightcurve is fainter after the 2009 "event" compared to previous cycles supports the theory of η Car's wind becoming weaker since $F_{\text{X-Ray}} \sim \dot{M}$. Corcoran et al. (2010) suggested that the cycle-to-cycle variations and the early recovery from the 2009 X-ray minimum might have been the result of a decline in η Car's wind momentum flux. They find that the mass loss rate might have decreased by a factor of 4 between 2000 and 2006.

4.2 Are Changes Observed at Higher Stellar Latitudes?

It is difficult to answer the question if the stellar wind emission lines are decreasing at higher latitudes as well. This is primarily due to the limited observational coverage of FOS4. FOS4 was observed with *Gemini* GMOS, during the 2009 "event," and with *VLT* UVES between 2002 and 2009. *HST* STIS covered FOS4 only on rare occasions.

Figure 4.7 shows the equivalent widths of the Fe II and Cr II blend at $\lambda\lambda$4570–4600 Å on the star and at FOS4 with GMOS and UVES during the last two cycles. The

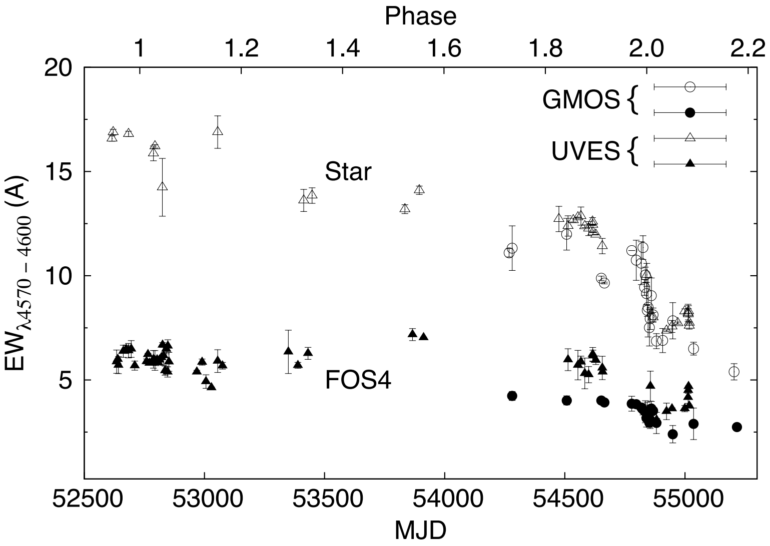

Figure 4.7: Equivalent width of the Fe II and Cr II blend at λλ4570–4600 Å on the star (empty symbols) and at FOS4 (filled symbols) with GMOS and UVES. The emission in direct view of the star declines by a factor of about 2–3 over the last 10 years, at FOS4 only by a factor of about 1.5–2.

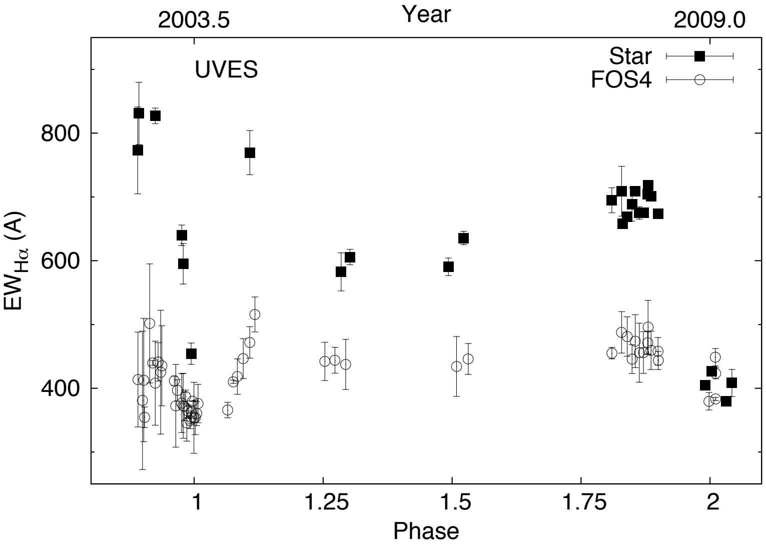

Figure 4.8: Hα in spectra on the star and at FOS4 in UVES spectra obtained between 2002 and 2009. While the emission decreases on the star in direct view, no change is observed at FOS4.

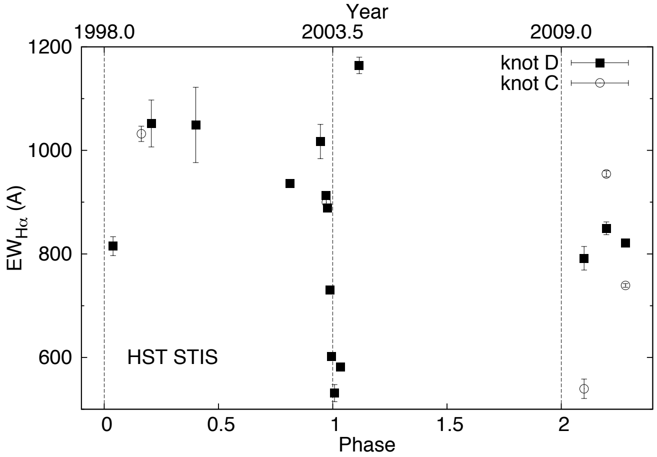

Figure 4.9: Equivalent width of Hα at Weigelt knots C (open circles) and D (filled squares) over the last 2 cycles showing a small decline of about 10–20%.

equivalent width in direct view of the star declined by a factor of about 2–3. At FOS4 the emission also declined, but only by a factor of 1.5–2.

Figure 4.8 compares Hα equivalent widths in spectra of the star in direct view and reflected at FOS4 obtained with UVES between 2002 and 2009. While the emission decreased by a factor of ~ 2 in spectra of the star in direct view, Hα emission at FOS4 remained constant.

If the observed changes in emission strength discussed in section 4.1 are caused by a decrease in mass loss rate, then the effect is latitude dependent with the mass loss rate at higher latitudes decreasing at a lesser rate.

4.3 Do Spectra of the Weigelt Knots Show Long-term Changes?

Spectra of the Weigelt knots show high-excitation emission, probably indicating photoionization by a hot companion star, and reflected light from η Car. Given the rapid change in the stellar wind spectrum, discussed in section 4.1, and the rapid brightening of the central star over the last 15 years (Martin & Koppelman 2004; Martin et al. 2006b; Davidson et al. 2009), spectral changes might also be expected in the nearby ejecta. For instance, an early recovery of the high-excitation emission lines after the 2009 "event"

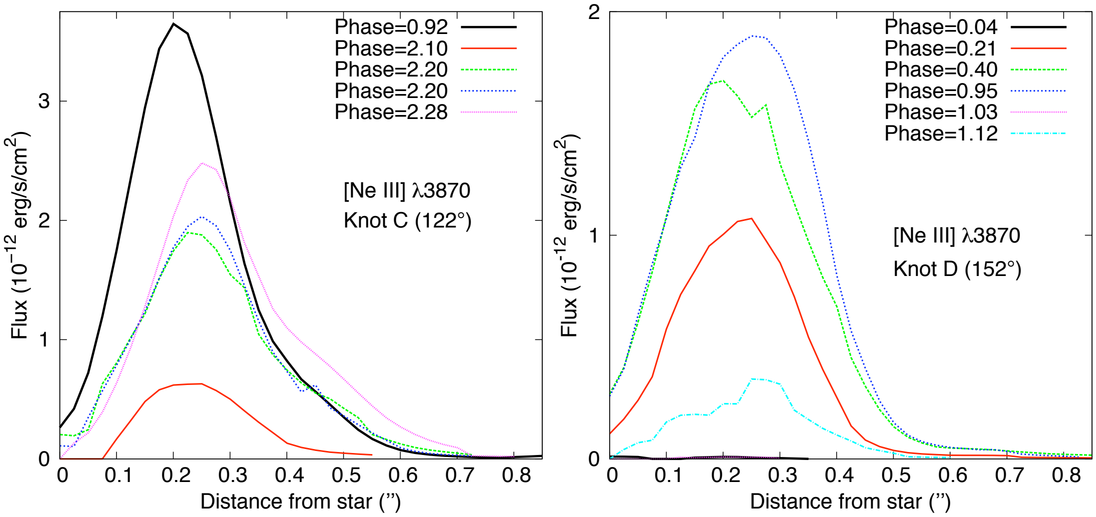

Figure 4.10: Flux of the narrow [Ne III] λ3870 emission line at different phases along slit positions $PA = 122°$ and $PA = 153°$ that include Weigelt knots BCD. The peak of the emission (and therefore the knot) appears to move slowly outwards from the central source over time.

and an increasing continuum brightness on the Weigelt knots seem reasonable.

HST STIS observations covered the Weigelt knots BCD several times over the last 10 years. Figure 4.9 shows measurements of the equivalent width of Hα on Weigelt knots C and D over the last two cycles. Further observations over the next years are required to confirm the apparent decrease of about 10–20% in equivalent width at the knots. Factors such as slightly varying slit position angles, pointing, and the outward moving knots might play a role which has to be quantified. In any way, the observed decline is smaller than observed directly on the star.

Figure 4.10 shows the flux of the narrow [Ne III] λ3870 emission along two slit positions for different phases. Observations with slit position angle $PA = 122°$ include Weigelt knot C and with slit position angle $PA = 152°$ include Weigelt knots BD. The knots have moved outward from the central source by about $0.05''$ between 2003 and 2010 but more detailed analysis is necessary. Smith et al. (2004) and Dorland et al. (2004) examined the kinematics of the Weigelt knots CD in *HST* images and spectra. Smith et al. (2004) derived an ejection date of 1908±12 yr (assuming linear motion) and suggested that because of radiative acceleration the knots may have been ejected during the 1890 outburst of η Car. Dorland et al. (2004) proposed that the ejection of Weigelt

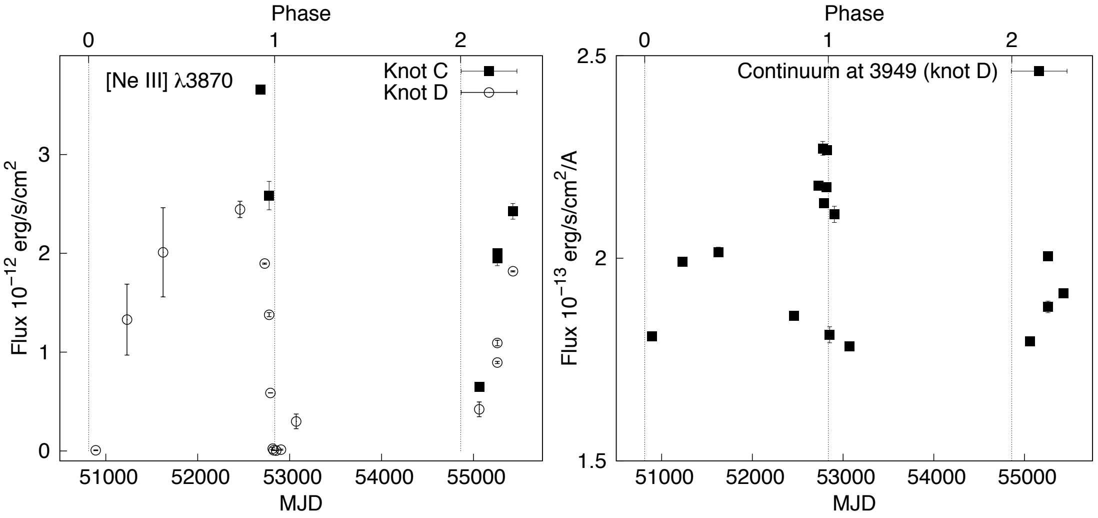

Figure 4.11: LEFT: [Ne III] λ3870 in Weigelt knots CD since 1998. It is possible that the lines recovered earlier after the 2009 "event." RIGHT: Continuum at λ3949 Å on knot D. The continuum is relatively constant on the Weigelt knots over the last two cycles (excluding the 2003.5 "event").

knots CD was related to the 1941 "event" when the star begun to brighten suddenly. If the knots were ejected during the *Second Eruption* in 1890 one needs to explain why the onset of the high-excitation emission took 50 years (until 1944, Humphreys et al. 2008). An ejection date in the early 1940s raises the question which mechanism could have ejected the knots then. However, since other high-excitation lines such as He I lines were also missing in η Car's spectrum before 1944 (Humphreys et al. 2008), the knots might very well have been present before. In this scenario something, e.g., an extremely strong wind or the "shut-down" of the secondary star's radiation due to accretion of material from the primary star, prevented high-energy photons to escape and reach the knots and the 1944 "event" might have been primarily a dramatic decrease in wind density.

Figure 4.11 shows the flux of the narrow [Ne III] λ3870 emission on Weigelt knots CD since 1998 to illustrate potential longterm changes in the high-excitation emission lines. The lines seem to have recovered faster to former maximum intensity after the 2009 "event" than after the 1998 "event." It is not clear yet what causes the drop in high-energy photons during the "events." If η Car's wind has been decreasing recently, an early reappearance of the high-energy emission might be expected since the secondary star would re-emerge earlier out of the dense primary wind which might prevent high-energy photons from reaching the knots. Because of the limited coverage one has to be cautious to draw any conclusions. Also, the reflected stellar continuum around $\lambda3950$ Å from the Weigelt knots seems to be very constant during the last 10 years (excluding the 2003.5 "event").[13] This is in contrast to what was expected given the increase in brightness of the central source. However, the brightening of the central star, which is probably mainly due to dust extinction in our line of sight, might not be equal in all directions.

---

[13] Artigau et al. (2011) found that the normalized IR flux at the knots is decreasing from 2002 to 2005, i.e. the knot-to-star brightness ratio is decreasing. With increasing brightness of the central star this finding might be consistent with a constant brightness of the knots in the IR.

Chapter 5

He II λ4687 Emission

5.1 The 2009 "Event"

He II λ4687 emission outbursts, briefly seen at two stages of the spectroscopic event, indicate floods of very soft X-rays at critical times. At its maximum the λ4687 emission – just one spectral line – is similar to the peak luminosity of observable 2–10 keV X-rays (though they do not occur at the same time). Martin et al. (2006a) explored the relevant physics, which can be summarized as follows:

- The observed He II λ4687 is almost certainly a $He^{++} \rightarrow He^{+}$ recombination line. Freshly shocked gas in the wind-wind collision zone does not produce enough λ4687 emission via normal cooling. Thus a non-routine source of He^{+}-ionizing photons ($h\nu > 54$ eV) is probably required.

- Nearly all authors agree that the two stars produce very little radiation above 54 eV. Therefore the relevant photons are most likely soft 54–500 eV X-rays produced in the wind-wind shock structure. Shocked gas of the primary wind, with pre-shock velocities below 600 km s^{-1}, is favorable for creating soft X-rays.

- The most suitable locale for λ4687 emission is either in the primary wind just before it encounters the colliding-wind shock structure, or in locally cooled condensations in the shocked region. These two choices occupy roughly the same large-scale spatial region, because radiative cooling destabilizes the primary-wind shock (Pittard & Corcoran 2002; Soker 2003). In either case λ4687 is excited by the soft X-rays mentioned above.

- The most plausible energy source is the primary wind. A first assessment predicts a soft X-ray shortage by a factor of 3–10, but several effects increase the efficiency. Instabilities in the shocked region tend to increase the number of very soft X-ray photons; Martin et al. described radiative-transfer effects that amplify λ4687; and a brief rise in the primary wind outflow (hinted by other observations) would also help. With reasonable parameters, these details can enhance the He II λ4687 flux by a factor of order 10.
- Models become quantitatively easier if the average photon energy falls well below 200 eV. This occurs if the faster secondary-wind shock becomes unstable, in which case the entire wind-wind interface "disintegrates" or "collapses." A chaotic ensemble of subshocks and oblique shocks would then occur for a few days. Such an "event" may explain the brevity of the λ4687 flash as well as the disappearance of 2–10 keV X-rays.

The above summary is not universally accepted. Steiner & Damineli (2004) proposed that He II emission occurs in the acceleration zone of the *secondary* wind, a much smaller region than the locations mentioned above. If one employs consistent physical parameters, their model predicts a λ4687 flux that is two or three orders of magnitude too weak (Martin et al. 2006a; Soker & Behar 2006). Soker & Behar (2006) also focused on the inner wind of the secondary star, but their model is very different, emphasizing a collapse of the wind structure followed by accretion onto the secondary. They gave qualitative arguments for larger-than-normal He II λ4687 emission, but did not quantify the excitation physics; they *postulated* that sufficient emission would occur in specified circumstances. Their model includes some very appealing components. Recently, Teodoro et al. (2011) explained the appearance of He II with a softening of the X-ray spectrum close to periastron passage. Due to radiative inhibition, caused by the strong radiation field of the primary star, the wind of the secondary has a slower velocity at the shock, therefore producing a much softer spectral energy distribution. The He II disappears when the shock front collapses onto the surface of the secondary star.

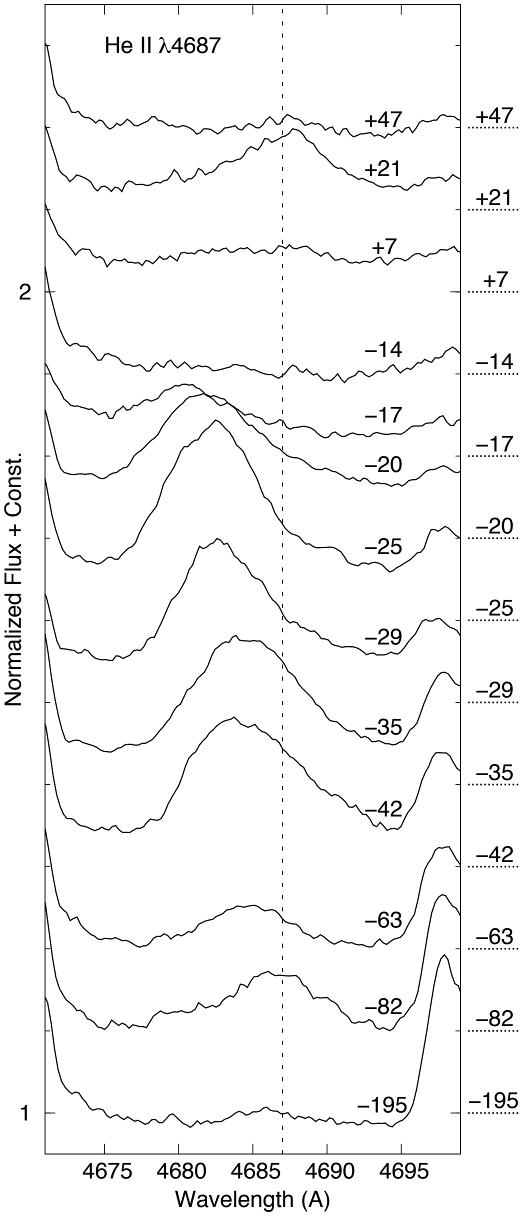

Figure 5.1: Time sequence of the He II λ4687 emission during the 2009 "event" in *Gemini* GMOS observations. Continuum was normalized to unity at λ4740 Å and is indicated with horizontal dotted lines for each tracing, offset between tracings is 0.1. Number of days before (−) and after (+) the 2009 "event" (MJD=54860, following the definition by the HST Treasury Program on Eta Carinae) are indicated next to each spectrum. The dotted vertical line indicates the position of He II λ4687 at zero radial velocity.

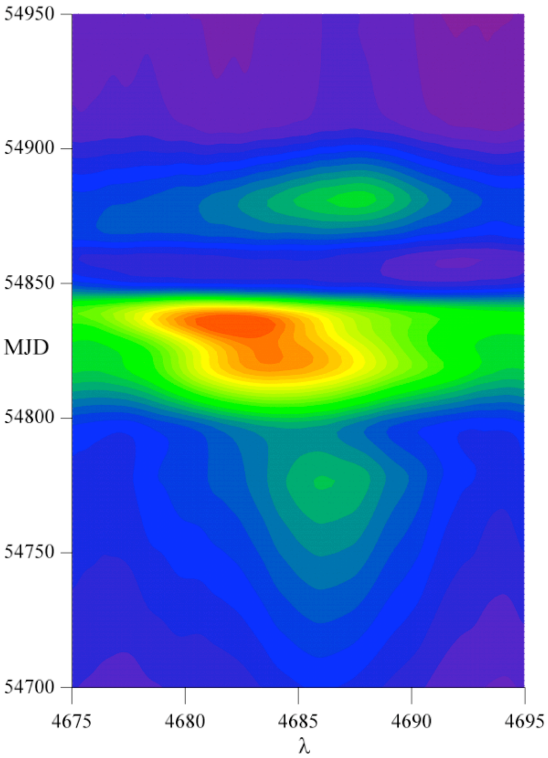

Figure 5.2: Contour plot of the He II λ4687 emission during the 2009 "event." The emission appears near zero radial velocity, moves towards the left, disappears, and then shortly reappears near zero radial velocity again. He II is present for only about 150 d. The line wings are very broad during maximum emission.

Figure 5.1 shows a time sequence of the He II λ4687 during the 2009.0 "event," based on *Gemini* GMOS data. In this Figure one sees a wave that first moves leftward, and then is reflected from a fictitious boundary at the left side. (Note the reversed asymmetry of the profile at $t = +21$ d vs. -20 d.) Teodoro et al. (2011) have described other observations that agree very well with these data. The underlying continuum level marked at the right side of Figure 5.1 is significantly lower than near the time of maximum He II brightness as assumed by Steiner & Damineli (2004) and Gull & Damineli (2010), see also Figure 5.2. This leads to a factor of 2–3 in both the maximum integrated λ4687 flux and its true width. Following Martin et al., I interpolated the underlying continuum between 4605 and 4744 Å. If this is wrong, then either the continuum has an extraordinary local maximum around 4685 Å or else the 4605 and

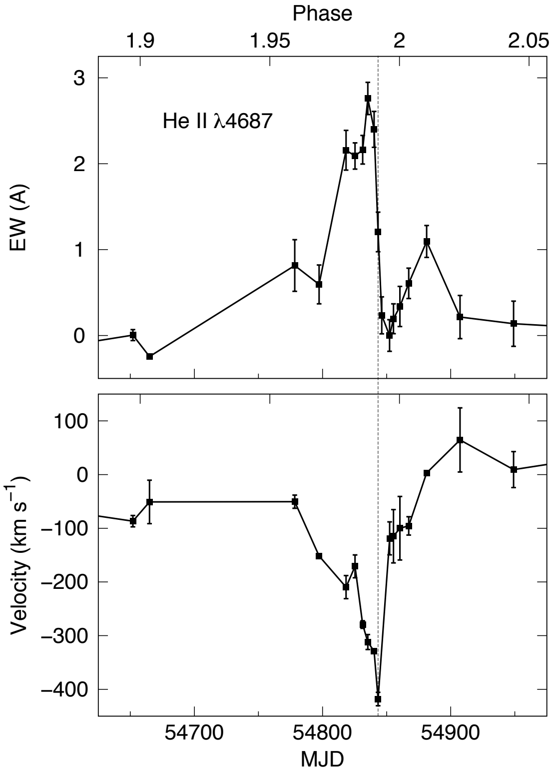

Figure 5.3: Equivalent width and radial velocity measurements of He II λ4687 emission on the star during the 2009 "event" in *Gemini* GMOS data. The dotted vertical line indicates the time of maximum negative radial velocity which occurs at the flux-decline-midpoint. This is also true for previous events (Steiner & Damineli 2004).

4744 Å regions both have unusual-looking absorption features – but *only during the "event"* in either case. These possibilities seem quite unlikely, but the lower continuum has surprising consequences. If it is correct, the He II feature extends across 20 Å or more ($\Delta v > 1200$ km s^{-1}) and has a much larger maximum flux than one would guess from the appearance of Figure 5.1 without other information. One cannot be sure that the true velocity dispersion is that large, since Thomson scattering with $\tau_{\mathrm{e}} > 1$ may conceivably broaden the feature. Figure 5.1 also shows smaller anomalies that are not discussed here – e.g., the profile seen at $t = -42$ d was blueshifted more than either of its neighbors at -63 and -35 d.

Figure 5.3 shows the time development of equivalent width and Doppler velocity for He II λ4687 in the *Gemini* GMOS data (values are listed in Table 5.1). Here "equivalent

Table 5.1: Equivalent width of He II λ4687 in *HST* STIS and *Gemini* GMOS data on the star (1998–2010)

	Name[a]	Date (UT)	MJD	Phase	EW (Å)	ΔEW (Å)	v_{rad}^{b} (km s^{-1})	Δv_{rad} (km s^{-1})
HST STIS	c821	1998 Mar 19	50891.4	0.038	0.16	0.05	-264.60	18.38
	c914	1999 Feb 21	51230.5	0.206	-0.08	0.06	–	–
	cA22	2000 Mar 20	51623.8	0.400	-0.12	0.07	-260.34	3.65
	cB29	2001 Apr 17	52016.8	0.595	-0.03	0.06	-48.32	142.51
	cC05	2002 Jan 20	52294.0	0.732	0.01	0.05	-138.77	2.75
	cC51	2022 Jul 04	52459.5	0.813	0.14	0.04	-34.63	73.14
	cD12	2003 Feb 13	52683.1	0.924	0.44	0.04	-238.91	65.56
	cD24	2003 Mar 29	52727.3	0.946	0.56	0.04	-249.13	40.26
	cD34	2003 May 05	52764.3	0.964	1.01	0.04	-230.93	15.33
	cD37	2003 May 19	52778.5	0.971	1.11	0.08	-188.77	1.69
	cD41	2003 Jun 01	52791.7	0.978	1.63	0.08	-188.32	10.33
	cD47	2003 Jun 23	52813.8	0.989	2.59	0.06	-389.85	24.87
	cD51	2003 Jul 05	52825.4	0.994	0.16	0.06	–	–
	cD58	2003 Aug 01	52852.4	1.008	0.18	0.08	–	–
	cD72	2003 Sep 22	52904.3	1.033	0.15	0.01	-122.00	177.96
	cD88	2003 Nov 17	52960.6	1.061	0.15	0.04	-72.61	157.86
	cE18	2004 Mar 07	53071.2	1.116	0.17	0.04	42.12	8.01
	cJ49	2009 Jun 30	55012.1	2.075	0.20	0.04	–	–
	cJ63	2009 Aug 19	55062.0	2.100	0.18	0.04	–	–
	cJ93	2009 Dec 06	55171.6	2.154	0.25	0.01	–	–
	cK16	2010 Mar 03	55258.6	2.197	0.25	0.08	–	–
	cK63	2010 Aug 20	55428.3	2.281	0.22	0.03	–	–
Gemini GMOS	gH45	2007 Jun 16	54268.0	1.707	-0.25	0.02	15.09	6.11
	gH49	2007 Jun 30	54281.0	1.714	-0.19	0.01	-39.60	46.88
	gI11	2008 Feb 11	54507.4	1.826	-0.34	0.03	-35.39	54.12
	gI50	2008 Jul 05	54652.0	1.897	0.01	0.06	-86.80	10.60
	gI54	2008 Jul 17	54665.0	1.904	-0.25	0.01	-50.83	40.44
	gI85	2008 Nov 08	54778.3	1.960	0.82	0.30	-50.46	12.29
	gI90	2008 Nov 27	54797.3	1.969	0.60	0.23	-151.68	2.73
	gI96	2008 Dec 18	54818.3	1.979	2.16	0.23	-209.59	21.47
	gI98	2008 Dec 25	54825.3	1.983	2.09	0.15	-170.93	21.29
	gI99	2008 Dec 31	54831.3	1.986	2.16	0.17	-279.30	7.06
	gJ01	2009 Jan 04	54835.3	1.988	2.76	0.19	-311.94	13.91
	gJ02	2009 Jan 09	54840.2	1.990	2.40	0.21	-328.94	4.58
	gJ03	2009 Jan 12	54843.3	1.992	1.21	0.23	-418.11	12.49
	gJ04	2009 Jan 15	54846.2	1.993	0.24	0.22	-118.72	30.72
	gJ05	2009 Jan 21	54852.3	1.996	0.00	0.18	-114.85	49.71
	gJ06	2009 Jan 24	54855.3	1.998	0.20	0.17	-99.95	59.14
	gJ07	2009 Jan 29	54860.4	2.000	0.34	0.23	-95.55	17.06
	gJ09	2009 Feb 05	54867.2	2.004	0.61	0.18	3.08	3.97
	gJ13	2009 Feb 19	54881.2	2.011	1.10	0.19	64.57	59.78
	gJ20	2009 Mar 17	54907.3	2.023	0.22	0.25	9.28	33.48
	gJ32	2009 Apr 28	54949.1	2.044	0.14	0.26	41.08	15.08
	gJ56	2009 Jul 23	55036.0	2.087	0.06	0.30	13.70	0.00
	gK02	2010 Jan 08	55204.3	2.170	0.08	0.19	-56.88	7.80

[a] As listed on the Eta Carinae Treasury Project site at http://etacar.umn.edu/.

[b] Due to low S/N in STIS data it is not possible to measure the radial velocity of the He II in all spectra.

width" refers to flux between 4675 and 4694 Å (-770 to $+450$ km s^{-1}), consistent with Martin et al. (2006a); other spectral features prevent measurement of the line wings. "Velocity" refers to the line's peak. *The first or major maximum practically matches the 2003.5 "event."* The flux grew concurrently with the decline of 2–10 keV X-rays (see section 5.1.2); the maximum equivalent width agrees with the 2003 value within measurement uncertainties; the maximum extended over about 4 weeks; and the decline occurred in a timescale of only six days. The main source of uncertainty involves the underlying continuum level, and flux variations near the peak in Figure 5.3 are not necessarily significant. However, the double peak might be related to the X-ray flaring (Teodoro et al. 2011). The most precise time marker for λ4687 is the midpoint of its decline, which occurred at MJD 54843 compared with MJD 52821 for the previous spectroscopic events according to Steiner & Damineli (2004) – a difference of 2022 ± 2 d which matches the consensus 2023-day spectroscopic period (MJD 54843 corresponds to phase 1.992). He II λ4687 emission appeared initially at about zero radial velocity, but shifted to blue wavelengths as it strengthened. Within measurement errors, the most negative Doppler velocity coincided with the decline-midpoint as was also the case during previous "events." At the flux maximum, MJD 54835, the line peak was at $v_{\rm rad} \approx -310$ km s^{-1}; but then it rapidly moved to -420 km s^{-1} in the next 8 days.

On the other hand, *the second, smaller He II maximum might have differed from its 2003.5 predecessor.* During the 1992.5, 1998, and 2003.5 "events" the second maximum occurred perhaps 70–90 days after the first (Steiner & Damineli 2004). The second maximum in 2009, however, occurred only 40–60 days after the first. (The large uncertainty in timing results from the reduced frequency of observations more than a month after the most rapid stage of the "event.") However, recently Teodoro et al. (2011) revised measurements of earlier "events" and included formerly unpublished data to find that the timing of the second maximum is consistent from cycle to cycle. However, *HST* STIS data cast doubt on their results, see section 5.1.2.

The strengths of the second maximum seems to be consistent with earlier "events." In Damineli and Steiner's Fig. 2, the second peak was almost 40% as bright as the first. This was also the case during the 2009 "event" (Gull & Damineli 2010; Teodoro et al. 2011) and in our measurements, see Figure 5.3. Two details in Figure 5.3 are especially noteworthy. First, the λ4687 emission did not suddenly reappear after an interval; instead it began to grow steadily within a few days of its disappearance, and continued to do so for at least a month in the middle of what we usually consider the "event." Evidently the emitting region was not entirely eclipsed by the primary wind. A second fact of interest is the rapid change in Doppler velocity. About four weeks after the emission around -420 km s^{-1} disappeared, it was replaced by a feature near zero velocity, and with a reversed asymmetry in its profile as mentioned earlier. The overall range of ~ 400 km s^{-1} considerably exceeds the maximum projected velocity variation in any proposed orbit model (generally < 200 km s^{-1} if $\Delta t < 100$ d).

5.1.1 Connection with He I

He I lines are very different from other high-excitation emission lines, which originate in the nearby Weigelt knots, e.g., helium lines increase shortly before the "event" when other high-excitation lines are already decreasing. They are also different from lower-excitation wind lines such as H I and Fe II which are centered near system velocity (-8 km s^{-1}, Davidson et al. 1997; Smith 2004). They have broad asymmetric P Cygni type profiles and are very complex. A large number of He I lines are in the spectral range of STIS and GMOS, but many are either blended or too faint for a reliable analysis; even in narrow extractions are the lines influenced by emission from surrounding ejecta. Both He I emission and absorption components vary in intensity and radial velocity throughout the cycle, see Figures 5.4 and 5.5 for time sequences of several He I lines obtained with STIS and GMOS.

Qualitatively, the behavior of He I $\lambda4714$ resembled that of the nearby He II $\lambda4687$ line (Figure 5.6, see also Table 5.2). Mostly constant during the cycle, the equivalent width of the He I emission increased before the 2009 "event" and then dropped rapidly into a minimum. The emission lines shifted monotonically blueward throughout the cycle, with an abrupt, large velocity shift of over 100 km s^{-1} to velocities of about -250 km s^{-1} near the "event," followed by a sharp rise to almost zero radial velocity.

The complexity of the He I emission makes measurements of the radial velocities difficult and inaccurate. The He I absorption lines, on the other hand, are easy to measure. The radial velocity of the absorption lines showed a similar radial velocity behavior as the He I and He II emission, with velocity shifts between -300 km s^{-1} and -600 km s^{-1}, see Figure 5.6. Nevertheless, the interpretation is not straightforward

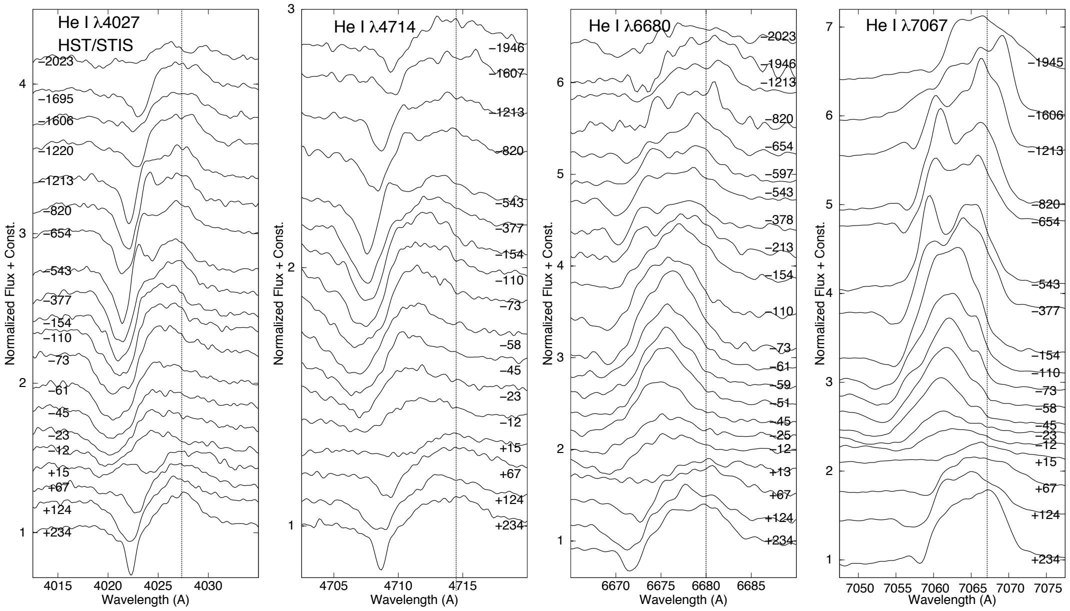

Figure 5.4: He I $\lambda\lambda$4027,4714,6680,7067 during the 2003.5 "event" with *HST* STIS. Numbers indicate days before (–) and after (+) the "event." Vertical lines indicate the zero radial velocity.

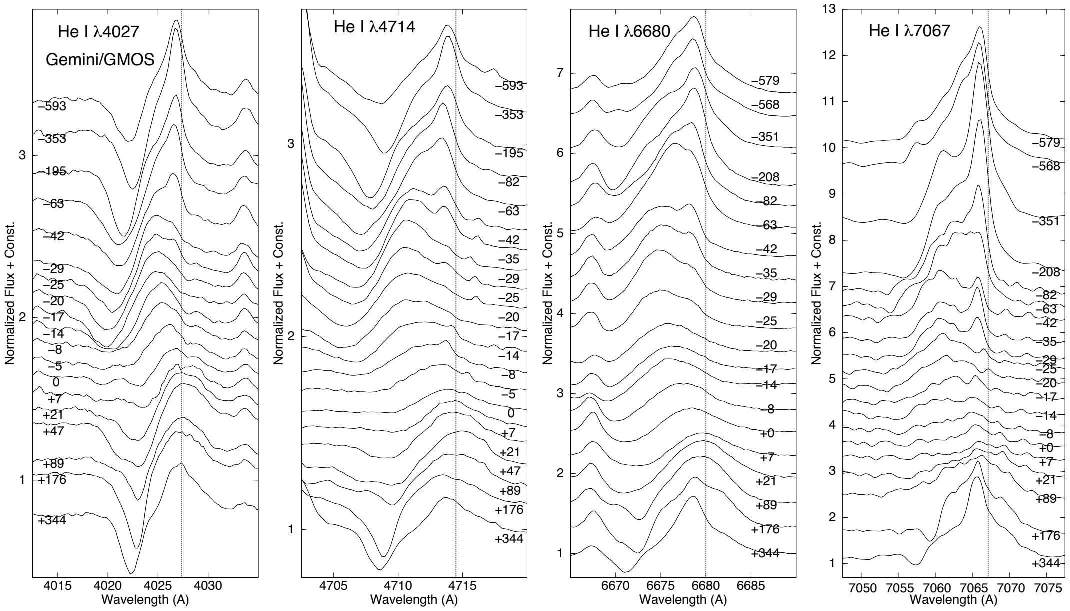

Figure 5.5: He I $\lambda\lambda$4027,4714,6680,7067 during the 2009 "event" with *Gemini* GMOS, see Figure 5.4.

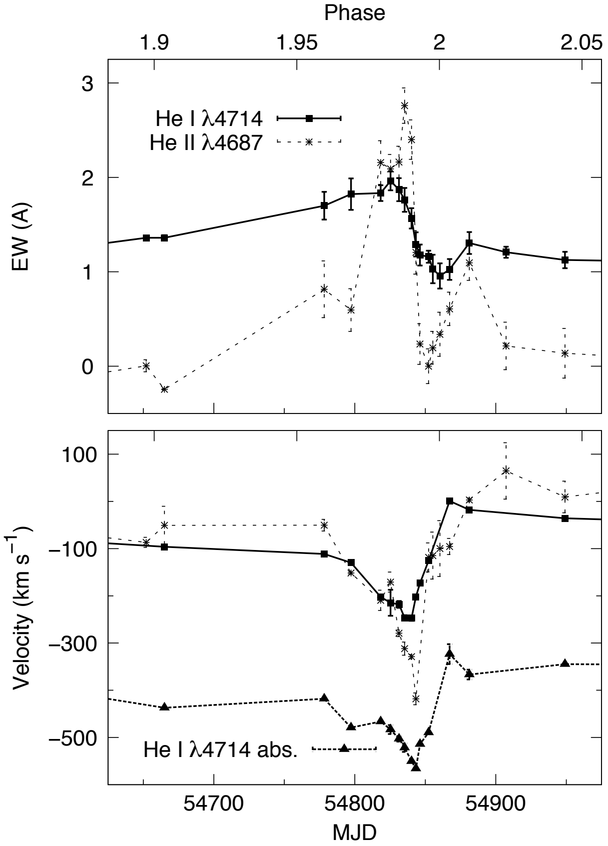

Figure 5.6: Equivalent width and radial velocity of He I λ4714 emission (filled squares) on the star during the 2009 "event" observed with *Gemini* GMOS. The radial velocity of the absorption line is also shown (filled triangles). The crosses show the values for He II λ4687 emission; the correlation is obvious.

since it is not well understood where the absorbing material is located; either the wind of η Car, the colliding wind interface, the wind of the secondary, or a combination (see, e.g., Humphreys et al. 2008; Nielsen et al. 2007; Kashi & Soker 2007). Also, the absorption strength of He I is steadily increasing over the last 10 years, which has to be given extra consideration.

The main differences of He I compared to He II were the slower decline of the He I emission, the He I P Cyg absorption, and, of course, the fact that He I did not eventually disappear after the "event." These remarks apply to other triplet He I lines as well. Apart from He I lines, only some N II lines showed similar radial velocity shifts, see chapter 7.

Table 5.2: Equivalent width and radial velocity of He I λ4714 emission and absorption in *Gemini* GMOS data (2007–2010)

Name	Date	MJD	Phase	$\mathrm{EW}^{\mathrm{em}}$ (Å)	$\Delta\mathrm{EW}^{\mathrm{em}}$ (Å)	$\mathrm{EW}^{\mathrm{abs}}$ (Å)	$\Delta\mathrm{EW}^{\mathrm{abs}}$ (Å)
gH45	2007 Jun 16	54268.02	1.707	1.16	0.04	-0.21	0.01
gH49	2007 Jun 30	54281.00	1.714	1.19	0.06	-0.16	0.02
gI11	2008 Feb 11	54507.39	1.826	1.31	0.04	-0.45	0.00
gI11	2008 Feb 13	54509.15	1.827	1.08	0.00	-0.41	0.00
gI50	2008 Jul 05	54652.01	1.897	1.36	0.00	-0.37	0.01
gI54	2008 Jul 17	54664.99	1.904	1.36	0.03	-0.57	0.01
gI85	2008 Nov 08	54778.32	1.960	1.70	0.15	-0.32	0.05
gI90	2008 Nov 27	54797.32	1.969	1.82	0.17	-0.27	0.05
gI96	2008 Dec 18	54818.33	1.979	1.83	0.08	-0.08	0.03
gI98	2008 Dec 25	54825.34	1.983	1.96	0.10	-0.07	0.02
gI99	2008 Dec 31	54831.34	1.986	1.87	0.12	-0.07	0.04
gJ01	2009 Jan 04	54835.31	1.988	1.76	0.13	-0.04	0.02
gJ02	2009 Jan 09	54840.22	1.990	1.57	0.11	-0.10	0.03
gJ03	2009 Jan 12	54843.31	1.992	1.29	0.13	-0.13	0.05
gJ04	2009 Jan 15	54846.23	1.993	1.18	0.11	-0.07	0.05
gJ05	2009 Jan 21	54852.32	1.996	1.16	0.06	0.03	0.10
gJ06	2009 Jan 24	54855.34	1.998	1.03	0.15	0.06	0.03
gJ07	2009 Jan 29	54860.36	2.000	0.96	0.13	0.10	0.06
gJ09	2009 Feb 05	54867.24	2.004	1.03	0.11	0.11	0.06
gJ13	2009 Feb 19	54881.23	2.011	1.31	0.12	-0.06	0.02
gJ20	2009 Mar 17	54907.28	2.023	1.21	0.06	-0.21	0.06
gJ32	2009 Apr 28	54949.07	2.044	1.13	0.09	-0.11	0.04
gJ56	2009 Jul 23	55036.01	2.087	1.11	0.05	-0.43	0.01
gK02	2010 Jan 08	55204.33	2.170	1.04	0.07	-0.31	0.02

Name	Date	MJD	Phase	$v_{\mathrm{rad}}^{\mathrm{em}}$ (km/s)	$\Delta v_{\mathrm{rad}}^{\mathrm{em}}$ (km/s)	$v_{\mathrm{rad}}^{\mathrm{abs}}$ (km/s)	$\Delta v_{\mathrm{rad}}^{\mathrm{abs}}$ (km/s)
gH45	2007 Jun 16	54268.02	1.707	-56.99	3.94	-376.14	6.24
gH49	2007 Jun 30	54281.00	1.714	–	–	–	–
gI11	2008 Feb 11	54507.39	1.826	-67.49	4.50	-362.94	4.95
gI11	2008 Feb 13	54509.15	1.827	–	–	–	–
gI50	2008 Jul 05	54652.01	1.897	–	–	–	–
gI54	2008 Jul 17	54664.99	1.904	-96.11	0.90	-437.05	1.80
gI85	2008 Nov 08	54778.32	1.960	-111.38	0.00	-417.96	0.00
gI90	2008 Nov 27	54797.32	1.969	-129.82	0.00	-479.03	0.00
gI96	2008 Dec 18	54818.33	1.979	-202.34	0.00	-466.31	0.00
gI98	2008 Dec 25	54825.34	1.983	-214.74	27.44	-483.16	9.45
gI99	2008 Dec 31	54831.34	1.986	-218.24	7.20	-502.88	5.85
gJ01	2009 Jan 04	54835.31	1.988	-246.44	5.51	-521.54	8.97
gJ02	2009 Jan 09	54840.22	1.990	-247.18	5.85	-550.27	0.90
gJ03	2009 Jan 12	54843.31	1.992	-202.02	0.45	-565.85	0.45
gJ04	2009 Jan 15	54846.23	1.993	-173.08	0.00	-514.01	0.00
gJ05	2009 Jan 21	54852.32	1.996	-125.37	0.00	-489.52	0.45
gJ06	2009 Jan 24	54855.34	1.998	–	–	–	–
gJ07	2009 Jan 29	54860.36	2.000	–	–	–	–
gJ09	2009 Feb 05	54867.24	2.004	0.89	0.45	-323.51	21.14
gJ13	2009 Feb 19	54881.23	2.011	-17.87	0.90	-366.76	10.34
gJ20	2009 Mar 17	54907.28	2.023	–	–	–	–
gJ32	2009 Apr 28	54949.07	2.044	-35.68	0.00	-344.82	0.00
gJ56	2009 Jul 23	55036.01	2.087	-43.53	5.41	-345.88	1.94
gK02	2010 Jan 08	55204.33	2.170	-37.59	11.69	-386.80	0.00

As is the case for the He II emission, the origin of the He I emission and absorption lines is still under debate because the velocity shifts throughout the cycle described above cannot easily be explained and reconciled with other observations such as, e.g., the X-ray light curve. Nielsen et al. (2007) proposed that the He I emission lines originate in the primary wind, where the helium is ionized or excited by the secondary star. Kashi & Soker (2007) assumed that the He I emission lines are formed in the acceleration zone of the less massive secondary star and that the velocity variations are caused by its orbital motion. However, if so, the secondary star would have tremendously bright He I emission lines for its luminosity. Both authors also mention that the lines might be associated with the wind shock.

Very likely the similar velocity changes of He I and He II imply that He II $\lambda4687$ originated in roughly (but not exactly) the same spatial locale as the He I emission. In one type of model helium emission represents gas located between the two stars, and mainly in the primary wind. In the early stages of an "event" the secondary star is more or less on our side of the primary, hence the negative Doppler velocities in that part of the primary wind. A few weeks later the secondary star has passed behind the primary to a location where the primary-wind velocity is zero or positive. With a different orbit orientation one can modify this story to fit the near side of the complex shock structure instead. The velocity behavior at FOS4 discussed in chapter 9 adds further details and complications. Latitude dependent changes in the He I line profiles during the 2009 "event" will be discussed in chapter 6.

5.1.2 Connection with the 2–10 keV X-ray Light Curve

Valuable clues can be found in the timing of the He II $\lambda4687$ intensity and the 2–10 keV X-ray light curve. Martin et al. (2006a) emphasized that during the 2003.5 "event" the growth of the He II $\lambda4687$ line coincided with the *decrease* of 2–10 keV X-rays as the spectroscopic event developed. Figure 5.7 shows this phenomenon and compares the He II equivalent width with the X-ray light curve during the last "events" (1998, 2003.5, and 2009).[14] At maximum He II emission the X-rays have already decreased

---

[14] The values from Steiner & Damineli (2004) were scaled by a factor of 3 to make comparison easier since these authors estimated the continuum at $\lambda4675$ and $\lambda4694$ which lead to a factor of 2–3 difference in the integrated flux when compared to measurements using the method employed by Martin et al. (2006a).

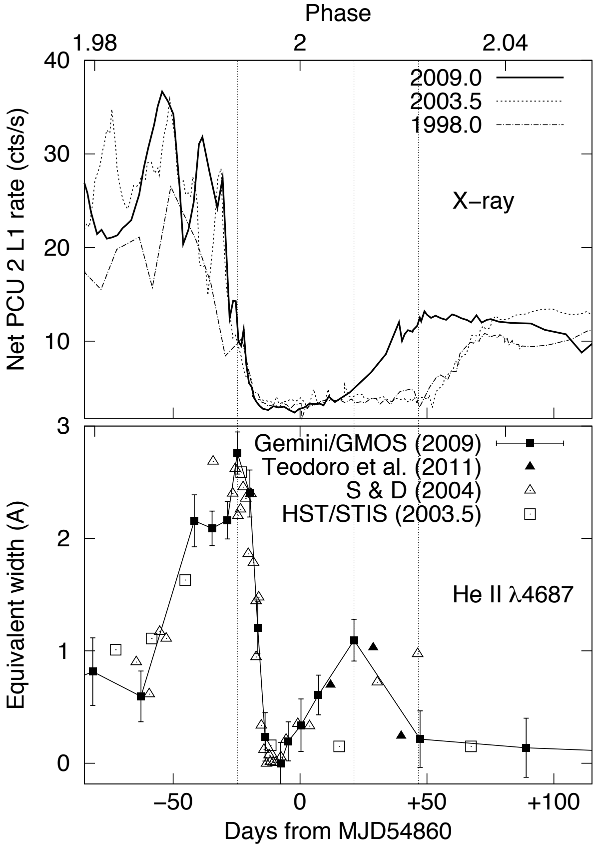

Figure 5.7: TOP: X-ray light curve during the 1998, 2003.5, and 2009 "events" (from http://asd.gsfc.nasa.gov/Michael.Corcoran/eta_car/etacar_rxte_lightcurve/index.html). BOTTOM: Equivalent width of the He II λ4687 emission during the 2009 "event" with *Gemini* GMOS (filled squares), and during the 1992.5, 1998, and 2003.5 "events" (open triangles, these are scaled values from Steiner & Damineli 2004). Filled triangles are selected data points from Teodoro et al. (2011) which constrain the timing of the second peak during the 2009 "event" further. *HST* STIS data from 2003 (open squares) cast doubt on their results for previous "events," see text. Values for older "events" are shifted by multiples of 2023 days.

substantially for all three "events." Equally important, an secondary He II maximum occurs shortly before the X-rays begin to recover at the end of each "event." This is especially obvious since the early X-ray reappearance after the 2009 "event" is accompanied by an early appearance of the second He II maximum. The described relative timing of He II and X-ray emission may indicate that the colliding-wind shock structure breaks up near periastron passage, as several authors have conjectured (Davidson 2002;

Soker 2003; Martin et al. 2006a; Damineli et al. 2008a; Parkin et al. 2009; Teodoro et al. 2011). In the shock-instability scenario one can interpret the second He II emission peak, with a pattern approximately reverse to that seen for the first peak, as corresponding to the formation of a large-scale shock structure when the relevant densities become sufficiently low for it to be quasi-stable. The overall time scale was similar to that seen in the earlier episode.

Davidson (2002) was the first author to remark that a set of known shock instabilities, rather than the eclipse scenario that was popular at that time, can best explain the rapid disappearance of η Car's 2–10 keV X-rays during a spectroscopic event. Soker (2003) described some quantitative details, and Martin et al. (2006a) emphasized the relevance of He II λ4687 to this concept. Various researchers later favored essentially the same idea (Damineli et al. 2008a; Parkin et al. 2009; Teodoro et al. 2011). Two specific variants, physically different but with similar consequences, occur as follows.

- A shock structure tends to be unstable if radiative cooling exceeds expansion cooling (Stevens et al. 1992). The slow primary-wind shock of η Car is very unstable in this regard, but the faster secondary-wind shock stabilizes the overall structure in most calculated models (Pittard & Corcoran 2002; Soker 2003). Martin et al. (2006a) argued semi-quantitatively that the secondary shock may become unstable *near periastron,* causing the entire shock structure to disintegrate within a few days.

- Soker & Behar (2006) drew attention to a different phenomenon that Stevens & Kallman (1990) had studied for X-ray binaries in general. Near periastron, soft X-rays from the shocked region may alter the ionization state of the secondary star's wind. A higher degree of ionization tends to weaken the line-driven acceleration, resulting in a slower wind speed. This in itself would reduce the 2–10 keV flux; but another consequence is that the balance of wind momenta is altered, pushing the shocks closer to the secondary star. In an extreme case the primary wind can entirely suppress the secondary wind.

Other instabilities certainly occur, such as Kelvin-Helmholtz which mixes gas from the two winds, and obvious thermal instability as shocked gas cools below 10^6 K. In some respects the second process listed above may be more suitable than the first, but

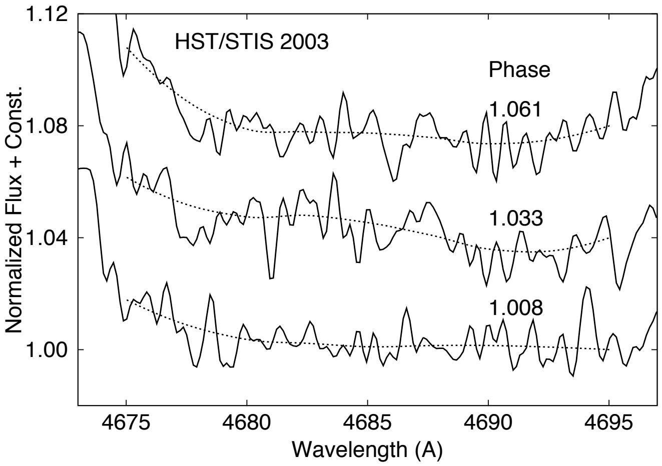

Figure 5.8: Tracings of the wavelength region at λ4687 Å in *HST* STIS data shortly after the 2003.5 minimum. Phase 1.008 is during the second maximum found by Teodoro et al. (2011). However, the STIS tracing shows no emission feature and also the equivalent width measured with the method proposed by Martin et al. (2006a) is small (see Figure 5.7).

both of them can have similar consequences. Observable 2–10 keV X-rays rapidly and tremulously disappear as the highest temperature decreases; a flood of soft X-rays is created by the chaotic ensemble of local shocks as the overall structure breaks up; and the secondary wind may temporarily cease to exist. (Alternatively, it might survive in a slower form).

However, recently Teodoro et al. (2011) have remeasured the OPD data used by Steiner & Damineli (2004) with the method employed by Martin et al. (2006a) in addition to formerly unpublished data from several other telescopes. They found that the behavior of the He II λ4687 emission is repeated from cycle to cycle, and that its second maximum is *not* correlated to the X-rays but that the second maximum during earlier "events" occurred at the same phase as during the 2009 "event." *HST* STIS data during the 2003.5 "event," shown in Figure 5.7, cast doubt on their new results. The STIS spectrum at MJD 54875 (corresponds to MJD 52852 = phase 1.008, because shifted by 2023 days) is basically "flat" at λ4687 Å, see Figure 5.8. This data point practically rules out an He II emission peak at that phase during the 2003.5 "event." However, it cannot be rules out that the second peak occurred at a later phase as found by Steiner & Damineli (2004).

5.2 He II λ4687 Emission Outside the "Events?"

In this section I address the controversy whether or not He II λ4687 emission is present outside the spectroscopic events. Steiner & Damineli (2004) observed an equivalent width of the He II emission of 0.05–0.15 Å during most of the cycle in data obtained at the 1.6 m telescope of the Pico dos Dias Observatory, but Martin et al. (2006a) found no emission outside the "events" in higher resolution space-based *HST* STIS spectra. The question if He II λ4687 is present outside the "events" is important because this line has a far higher excitation level ($\sim$ 54 eV) than any other UV to IR line seen in η Car. I used high-spatial resolution *HST* STIS data to investigate the possibility that He II λ4687 emission originates from an extended region around the star. Several data sets (the 1998–2004 data, mapping data in 2009, and long-exposure data in 2010) allow for three different approaches outlined below.

First, a few points regarding this "He II controversy:"

- Steiner & Damineli (2004), who detected the He II emission, only published smoothed tracings of spectra taken during the 2003.5 "event." It is therefore not known if an emission feature at λ4687 Å is present in their data outside the "events" or if the small equivalent width they measure throughout the cycle is due to their choice of the continuum level.

- Steiner & Damineli (2004) rectified the continuum with a third order polynomial. Unfortunately it is unclear where they set the continuum, but given their published equivalent widths, both the continuum and the integration range were likely at about λ4675 and λ4694 Å. In contrast, Martin et al. (2006a) chose a continuum at λ4605 and λ4744 Å and integrated over the wavelength range λ4675 to λ4794 Å. Different results are therefore not surprising.

- Martin et al. (2006a) investigated a possible emission feature by performing a conventional least-squares fit to $f(\lambda) = A + B\lambda + C\Phi(\lambda)$ over 57 pixels within λ4677 to λ4693 Å. They assumed an emission profile, $\Phi(\lambda)$, of FWHM $\approx$ 550 km s^{-1} and a central Doppler velocity of -250 to $+150$ km s^{-1} and found no emission in the *HST* STIS data.

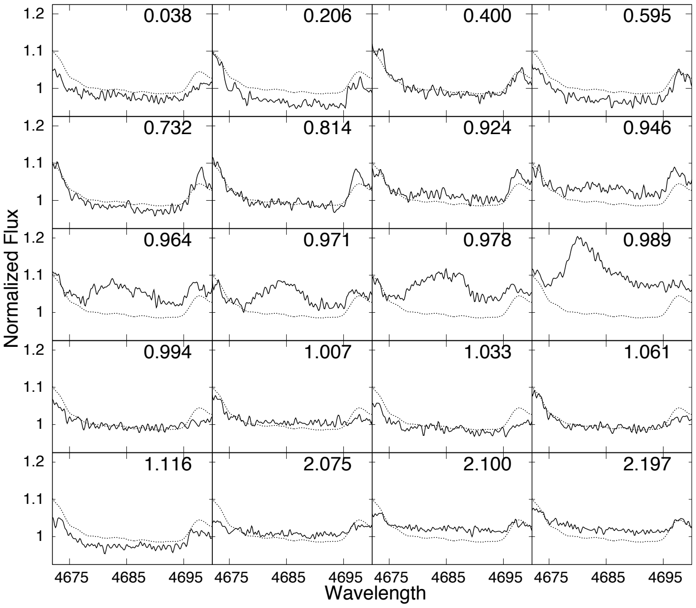

Figure 5.9: *HST* STIS spectra around $\lambda4687$ Å from 1998–2010. Corresponding phases are indicated in each panel. The dotted curve is an average spectrum outside the "events." The continuum was set to unity at $\lambda4744$ Å.

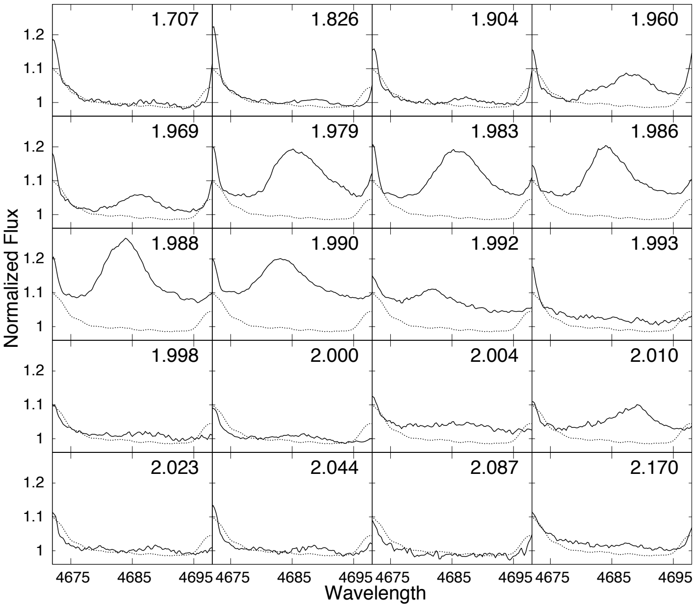

Figure 5.10: See Figure 5.9 but for *Gemini* GMOS data from 2007–2010.

- Damineli et al. (2008a) stated: “This line remains absent from the spectrum most of the cycle (Steiner and Damineli 2004; Martin et al. 2006);...”

- Recently, Teodoro et al. (2011) reemphasized that the He II feature is present at a low level throughout the entire cycle. Adopting the method used by Martin et al. (2006a) they found that He II was present 8 months before and was still present 17 months after the 2009 “event” (with EW $\sim$ 0.1 Å). Their Fig. 4 shows a little bump around λ4685 Å which rises about 1–2% above the flux level at λ4675 and λ4694 Å.

Figures 5.9 and 5.10 show tracings of *HST* STIS and *Gemini* GMOS data with extraction width of $0.1''$ and $0.75''$, respectively. For comparison, an average STIS spectrum outside the “events” is also shown. To investigate differences between ground-based and space-based observations the equivalent width of the λ4687 Å feature was measured in STIS and GMOS data with the method employed by Martin et al. (2006a), see Figure 5.11. The equivalent width outside “events” in ground-based data is certainly not “per se” significantly larger than in space-based data. To the contrary, the equivalent width in the GMOS data outside the 2009 “event” is smaller than in the STIS data. Main causes are the different spectral shapes due to instrumental effects and the different spatial sampling of these two data sets. (Also, only the GMOS spectra were rectified.) Figure 5.11 indicates that the He II emission was present between phases 0.8 and 1.2, i.e. ±400 days around the 1998.0 and 2003.5 “events,” or that at least the continuum at λ4687 Å was elevated for this extended time period. After the 2009 “event” the continuum at λ4687 is still elevated at phase 2.2 both in STIS and GMOS spectra (see also Figures 5.9 and 5.10).

The question remains if a small emission feature is present in ground-based spectra throughout the cycle but not in space-based data. If the case, it would either indicate that He II emission originates from an extended region around the star or that the feature is a blend of emission lines from nearby ejecta.

HST STIS data from 1998–2004 cover a large range of slit position angles and can therefore be used to investigate if He II λ4687 originates from extended regions around the star. The flux between λ4675 to λ4694 Å was measured in spectra extracted along the slits with extraction width of $0.1''$ and an interval between successive extractions of

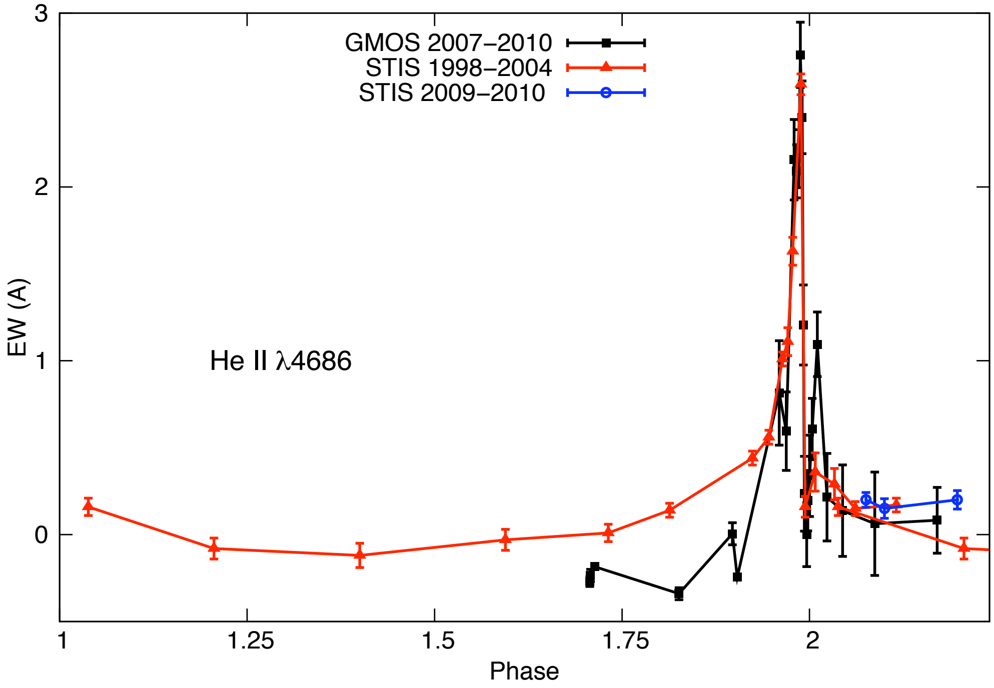

Figure 5.11: He II λ4687 equivalent width in *HST* STIS data from 1998–2010 and *Gemini* GMOS data from 2007–2010. STIS measurements from previous cycles are shifted by 2023 and 4046 days for comparison.

0.025″. The measured flux values along each slit were normalized such that the flux value at λ4740 Å had a value of unity on the star. This was necessary since the star brightened considerably between 1998 and 2004. In order to find possible emission features in the outer wind, "quarter-ring" spectra were constructed for all four quadrants; 0.1″ wide at distances 0.1, 0.2, 0.3, 0.4, and 0.5″ from the star. For example, the fluxes measured at a distance of 0.3″ from the star in slits with position angles between 270° and 360° were averaged. This "quarter-ring" spectrum was then compared to equally obtained spectra at distances of 0.1, 0.2, 0.4, and 0.5″ from the star. The same was done for the three other quadrants; 180–270°, 90–180°, and 0–90°. Concentric "ring" spectra were constructed in a similar way, i.e. spectra that represent emission originating from 0.1″ wide rings at different distances from the star.

Figure 5.12 compares a spectrum which represents the normalized average flux on the star with the spectrum of a concentric ring of 0.1″ width and a radius of 0.275″

from the star. Several weak emission lines are present between λ4675 and λ4695 Å in the "ring" spectrum, which samples the region of the Weigelt knots. N I λ4680 Å and [Fe II] λ4689 Å, with radial velocities of -39 km s^{-1} and originating from the Weigelt knots, can be identified (see also Zethson 2001). There is no evidence of broad He II emission but note the emission feature at λ4685 Å with unclear identification.

Do the small emission lines seen in Figure 5.12 contribute to the observed λ4687 Å emission feature? Panel (a) in Figure 5.13 shows the average flux at λ4685 Å versus distance from star for all four quadrants (normalized to unity at the position of the star). Note the higher flux 0.1–0.4″ NW from the star, the region of the Weigelt knots, and the lower flux NE from the star. These values were multiplied by $\frac{\pi}{2}r$ in order to find the flux contribution with distance for each quadrant, see panel (b). Of course most flux originates close to the star but there is a local maximum at 0.275″ NW from the star, the location of the Weigelt knots. Panels (c) and (d) show average spectra for each quadrant at distances 0.075 and 0.275″ from the star. These spectra are very *flat* and no obvious broad emission feature is observed. However, since observations were obtained throughout the cycle, this could also be caused by wavelength shifts of the potential λ4687 Å feature.

The 1998–2004 STIS data can be used to simulate ground-based spectra with different aperture sizes. The above mentioned concentric "ring" spectra, which represent the average flux in a ring at a certain radius from the star, were multiplied by $2\pi r$ and thus spectra of rings with radius r and width 0.1″ were obtained. The left panel of Figure 5.14 shows some examples of spectra at different distances r from the star. Ground-based spectra can be simulated by adding them up. The right panel shows two spectra, one with a simulated aperture size of 0.65″ and another with aperture size of 1.25″. The simulated spectra show a slight upwards slope towards the blue and several emission lines, but no broad He II λ4687 emission.

HST STIS data obtained in 2009 June and December mapped the inner region of η Car with slit position offsets of 0.1″ up to a distance of 1.0″ from the star. This good spatial coverage makes it possible to simulate ground-based data by adding up the flux from a region around the star (2.0″ for 2009 June and 1.5″ for 2009 December). The advantage compared with the above described analysis is that here the observations were obtained within several minutes and that the slits covered the entire inner region

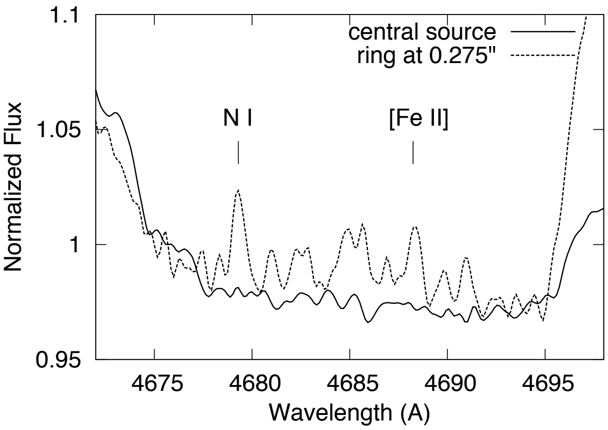

Figure 5.12: Stellar spectrum (solid curve) and spectrum from a concentric ring at 0.275″ from the star (dashed curve). Fluxes are renormalized so the continuum at λ4740 Å corresponds to unity. N I λ4680 Å and [Fe II] λ4689 Å originate from the Weigelt knots.

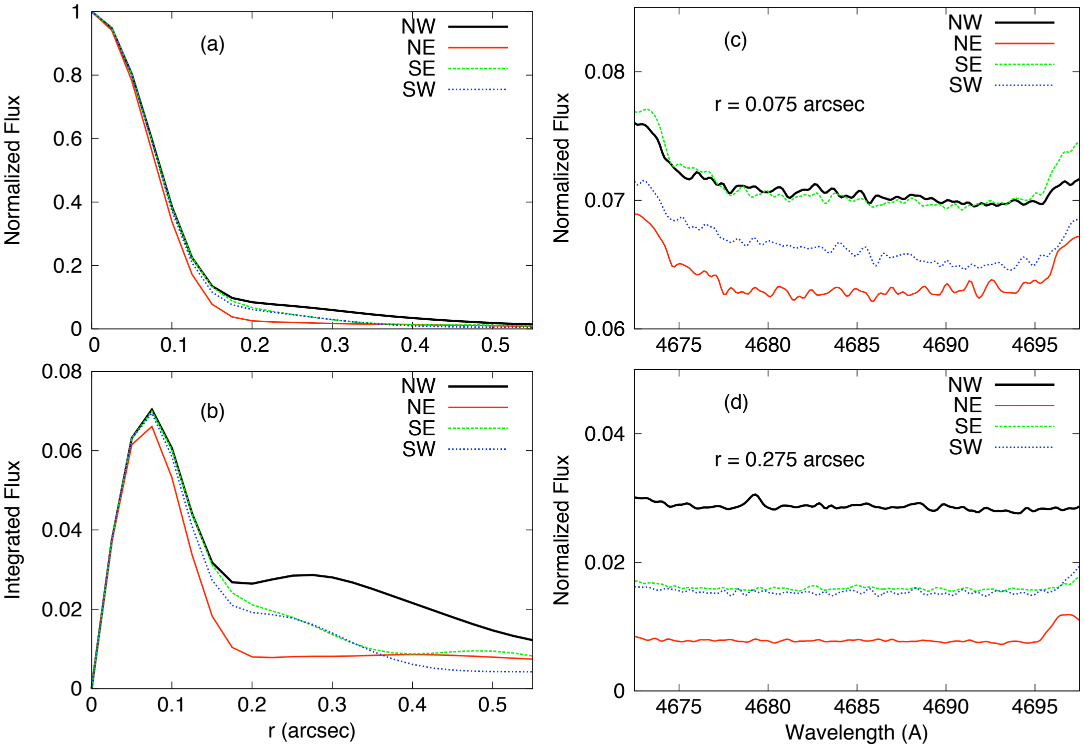

Figure 5.13: (a) Normalized flux at λ4685 Å with respect to distance from the star. (b) Same as above but values were multiplied by $\frac{\pi}{2}r$. (c) Integrated flux for each of the four quadrants at $r = 0.075''$, (d) Same as (c) but for $r = 0.275''$.

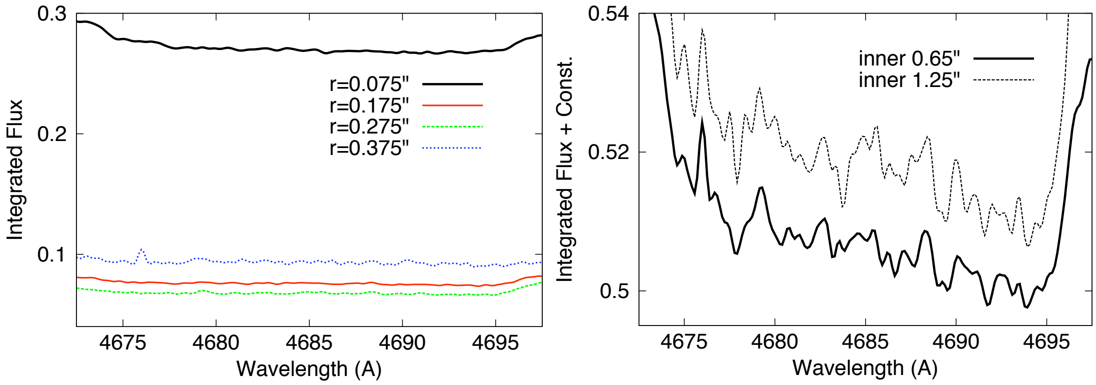

Figure 5.14: LEFT: Normalized flux at $\lambda 4685$ Å of concentric rings at different distances from the star. Each rings has a width of $0.1''$. RIGHT: Spectrum with an aperture size of $0.65''$ (solid curve, summation of ring spectra with $r = 0.075, 0.175, 0.275''$) and spectrum with an aperture size of $1.25''$ (dotted curve, summation of ring spectra with $r = 0.075, 0.175, 0.275, 0.375, 0.475, 0.575''$).

around η Car. The result is shown in Figure 5.15 (black curves). The Figure also shows narrow $0.1''$ extractions on the star (blue curves). The same emission lines can be identified in the narrow extractions of the star and the spectra of the combined flux from the entire region around the star. The resemblance between the spectra is also strong when comparing the spectra from June to the ones obtained in December.[15] To determine the "flatness" of the wavelength region shown, a loess curve was fitted to the spectra. In the smoothed curves, all spectra show a broad emission feature at $\lambda 4685$ Å. However, this feature rises less than 1% above the continuum next to it.

HST STIS observations with long exposure times of up to 60 s were obtained in 2010 March. Figure 5.16 compares one spectrum which was added from two 60 s exposures to improve the S/N ratio and one obtained with *Gemini* GMOS at about the same phase ($\approx$ 2.2), well after the 2009 "event." Several small emission lines are present in the concerned wavelength region that can easily be identified in both spectra, even though they where taken more than 50 days apart. The GMOS spectra show a small "bump" around $\lambda 4687$ rising about 1% above the nearby wavelength regions. This bump is almost comparable in size with the one found by Teodoro et al. (2011). However, it is questionable if this feature is He II or a blend of several narrow emission lines.

In 2011 February (at phase 2.38) observations were obtained with the 2.5 m *Irénée du*

---

[15] On a side note, more than half of the total flux originates in the inner $0.1''$.

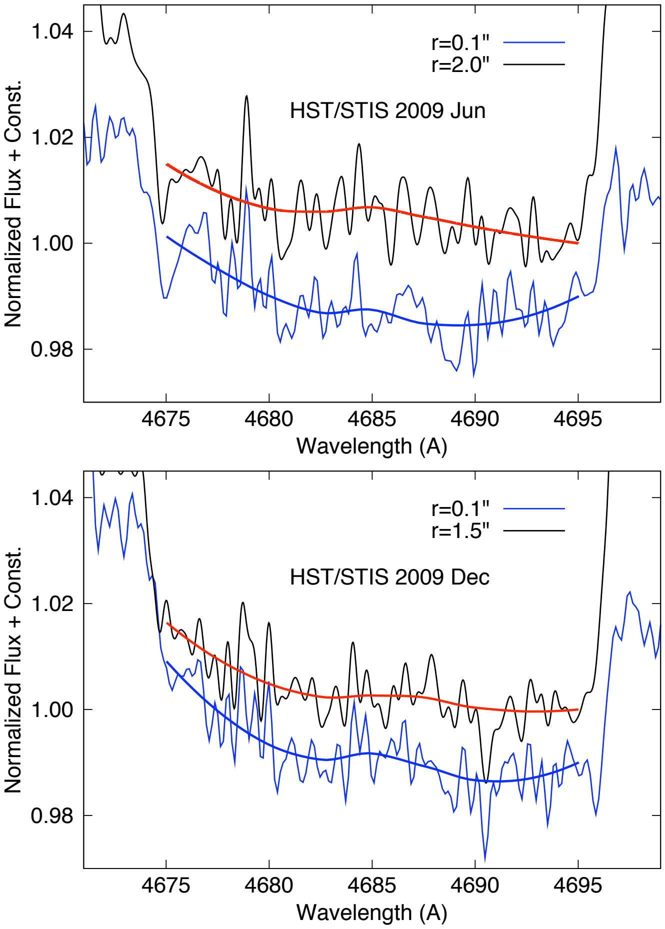

Figure 5.15: Simulated ground-based spectra around λ4687 Å using *HST* STIS 2009 June and December mapping data. For each epoch, a narrow 0.1″ extraction on the star (blue curves) and the combined flux of the inner 1.5″ or 2″ region (black solid curves) are shown. The fitted loess curves to each spectrum show a small bump at λ4685 Å in all cases. However, the feature rises less than 1% above the flux level at nearby wavelengths.

Pont telescope. Figure 5.17 shows a spectrum which was added from six 10 s exposures. An emission peak at λ4687 Å is obvious, but its peak rises less than 1% above the nearby continuum.

A small emission feature at λ4687 Å is present in high-resolution space-based data and also in ground-based data. However, comparison between these different data sets suggest that no broad He II emission is present. Instead, small emission (such as Fe I, Co I, N I, Ni I, Zr I, Ne I, or even narrow He II emission originating in the Weigelt

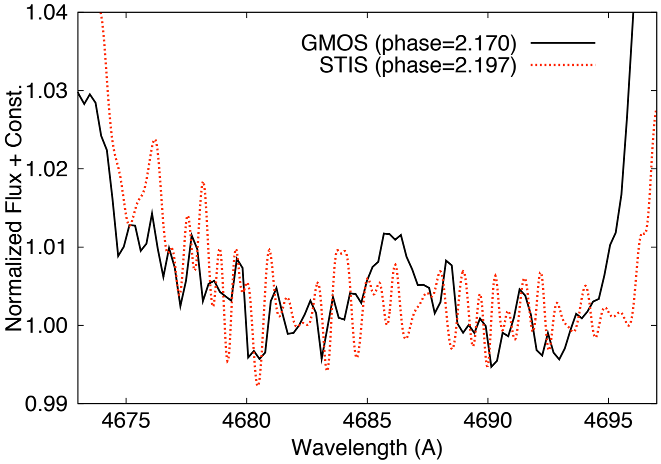

Figure 5.16: *HST* STIS spectrum (dotted red curve) and *Gemini* GMOS spectrum (solid black curve) at similar phases after the 2009 "event." Several lines and features can be identified in both spectra.

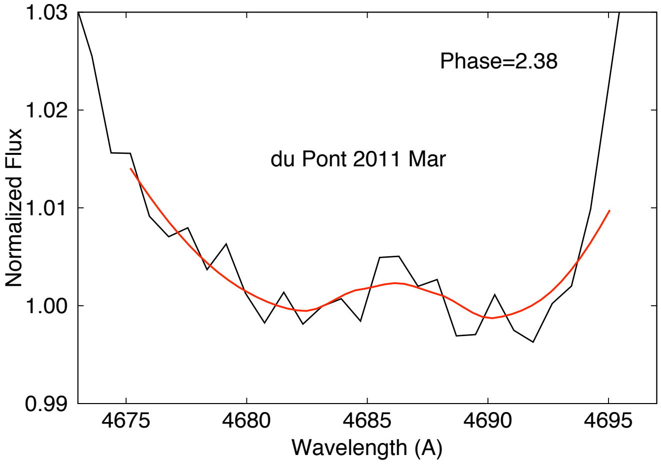

Figure 5.17: Spectrum around λ4687 Å at phase 2.38 obtained with the *Irénée du Pont* telescope (combination of six 10 s exposures). A small emission feature is observed at λ4687 Å. The red curve is a loess fit to the spectrum.

knots, in gas along our line of sight, or from the stellar wind) lines might contribute to the broad emission feature observed in ground-based data.

Chapter 6

FOS4 – The Reflected Spectrum from the Pole

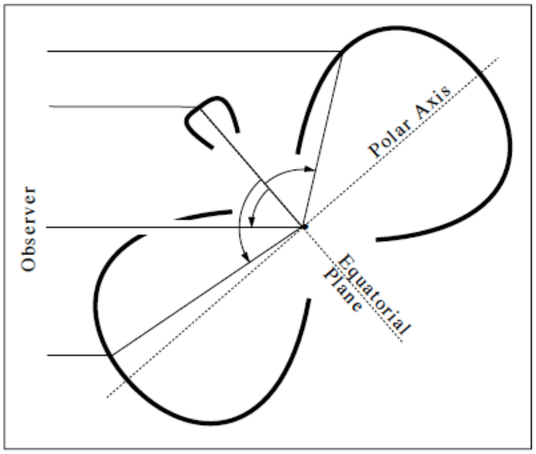

Figure 6.1: Schematic diagram of the Homunculus nebula (from Smith et al. 2003). Shown is the relationship between position along the slit (vertical axis) and stellar latitude for reflected light in the nebula.

The known geometry of the bright, hollow reflection nebula of η Car allows to correlate a position in the nebula with a stellar latitude, assuming that stellar polar axis and Homunculus axis are aligned. Figure 6.1 shows the relationship between position in the slit and stellar latitude. FOS4 is a bright location in the nebula at the center of the foreground SE lobe that gives a reflected more pole-on view (latitude ~75°, Smith et al. 2003) of the stellar wind, with a time-delay of about 20 days relative to the direct view, which is representative of the more equatorial (latitude ~45°, Davidson et al. 2001b) spectrum. The exact location of FOS4 is about $3.7''$ south and 2.5–$3.5''$ east of the central object. The spectral lines in the reflected spectra at FOS4 are red-shifted in wavelength by about 100 km s^{-1} due to the expansion of the Homunculus nebula (Stahl et al. 2005). The spectrum at FOS4 is also important for ground-based data since it is much less

Table 6.1: Expected time-delay at locations close to FOS4

Offset[a] ($''$)	Velocity (km s^{-1})	Time-delay (t$_{\rm Hom}$=150yr) (d)	Time-delay (t$_{\rm Hom}$=160yr) (d)
-0.15	93.2	17.0	18.2
0.00	99.6	18.2	19.4
0.15	105.3	19.2	20.5
1.50	172.5	31.5	33.6

[a] 0.00$''$ is FOS4, negative offset values are north, positive south of FOS4.

contaminated by nebular lines than the observations of the star directly.

6.1 Time-delay of He II λ4687 at FOS4

The expected time-delay of reflected spectra at FOS4 compared to spectra in direct view can be calculated using a simple model, with a constant expansion velocity of the Homunculus. The time-delay is linearly dependent on the velocity shift (Meaburn et al. 1987; Stahl et al. 2005):

$$t_{\rm delay} = \frac{v_{\rm shift}}{c} \times t_{\rm Hom} \ , \tag{6.1}$$

where $v_{\rm shift}$ is due to the redshift of spectra because of the expansion of the Homunculus and $t_{\rm Hom}$ is the age of the Homunculus. At FOS4 the redshift $v_{\rm shift}$ equals 100 km s^{-1}, for spectra north of FOS4 the redshift is smaller, and for spectra south of FOS4 larger. Since the Homunculus nebula was ejected during the *Great Eruption,* $t_{\rm Hom}$ = 150–160 yr and a time-delay of about 17–20 days is expected (see Table 6.1 for expected time-delays at locations close to FOS4).

However, Stahl et al. (2005) reported a time-delay of the appearance and disappearance of He II λ4687 emission in *VLT* UVES observations of FOS4 during the 2003.5 "event" of only 10 days compared to observations on the star by Steiner & Damineli (2004). If true, this would have considerable consequences on theoretical models. I therefore used the good time-coverage of *Gemini* GMOS observations during the 2009 "event" to re-investigate this result.

Figure 6.2 shows equivalent width measurements of the He II λ4687 emission in *Gemini* GMOS data in spectra extracted at positions listed in Table 6.1. Values are shifted according to their expected time-delay for $t_{\rm Hom}$ = 150 yr and $t_{\rm Hom}$ = 160 yr. A time-delay at FOS4 of about 18 days and $t_{\rm Hom}$ = 150 yr fits the data best. Figure 6.3

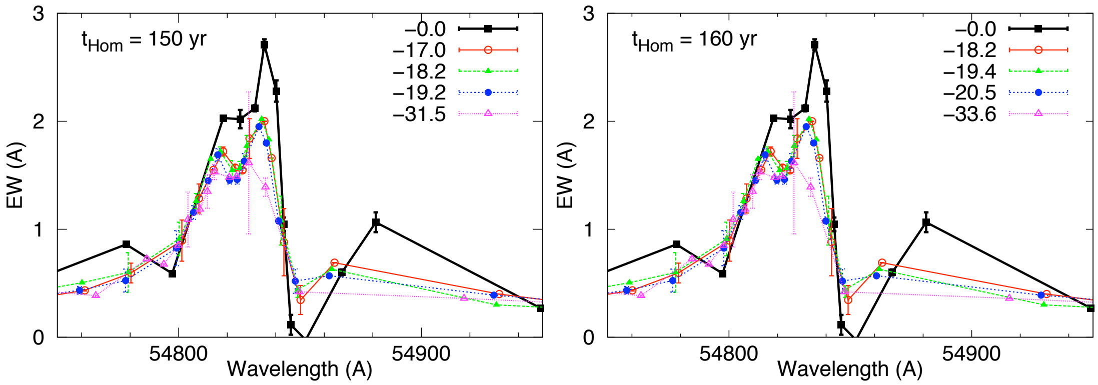

Figure 6.2: Equivalent widths of He II λ4687 on the star (solid black curve) and in the SE lobe of the Homunculus (colored curves). The green curve are measurements at FOS4. The key indicates the expected time-delay in days at each position (see Table 6.1 for details). The measurements obtained from the reflected spectra in the SE lobe were shifted according to their calculated time-delays. A time-delay at FOS4 of 18 days and $t_{\rm Hom} = 150$ yr fit the observations best.

Table 6.2: Equivalent width and radial velocity of He II λ4687 in *Gemini* GMOS data at FOS4 (2007–2010)

Name[a]	Date (UT)	MJD	Phase	EW (Å)	ΔEW (Å)	$v^b_{\rm rad}$ (km s^{-1})	$\Delta v_{\rm rad}$ (km s^{-1})
gH49	2007 Jun 30	54281.0	1.714	0.01	0.06	-65.35	36.95
gI11	2008 Feb 11	54507.4	1.826	0.09	0.02	-1.98	12.34
gI50	2008 Jul 05	54652.0	1.897	0.06	0.00	-103.55	73.12
gI54	2008 Jul 17	54665.0	1.904	-0.11	0.00	0.03	0.00
gI85	2008 Nov 08	54778.3	1.960	0.53	0.16	-74.09	22.96
gI90	2008 Nov 27	54797.3	1.969	0.76	0.23	-56.36	34.22
gI96	2008 Dec 18	54818.3	1.979	0.99	0.21	-102.72	8.30
gI98	2008 Dec 25	54825.3	1.983	1.32	0.19	-99.79	20.30
gI99	2008 Dec 31	54831.3	1.986	1.62	0.17	-105.04	19.77
gJ01	2009 Jan 04	54835.3	1.988	1.80	0.12	-113.81	14.67
gJ02	2009 Jan 09	54840.2	1.990	1.63	0.27	-118.80	11.54
gJ03	2009 Jan 12	54843.3	1.992	1.52	0.20	-139.17	19.14
gJ04	2009 Jan 15	54846.2	1.993	1.94	0.24	-178.40	28.82
gJ05	2009 Jan 21	54852.3	1.996	2.23	0.20	-283.84	40.12
gJ06	2009 Jan 24	54855.3	1.998	1.88	0.22	-264.67	17.40
gJ07	2009 Jan 29	54860.4	2.000	0.94	0.24	-252.99	54.45
gJ09	2009 Feb 05	54867.2	2.004	0.52	0.13	-137.90	65.81
gJ13	2009 Feb 19	54881.2	2.011	0.75	0.13	-60.42	33.02
gJ32	2009 Apr 28	54949.1	2.044	0.42	0.10	-35.23	43.64
gJ56	2009 Jul 23	55036.0	2.087	0.24	0.20	13.52	5.50

[a] As listed on the Eta Carinae Treasury Project site at http://etacar.umn.edu/.

[b] Note that the CCD rows were not corrected for their slightly different velocities due to the expansion of the Homunculus nebula. Measurements are therefore smeared by about 20 km s^{-1} or about 4 days. However, this does not influence the results.

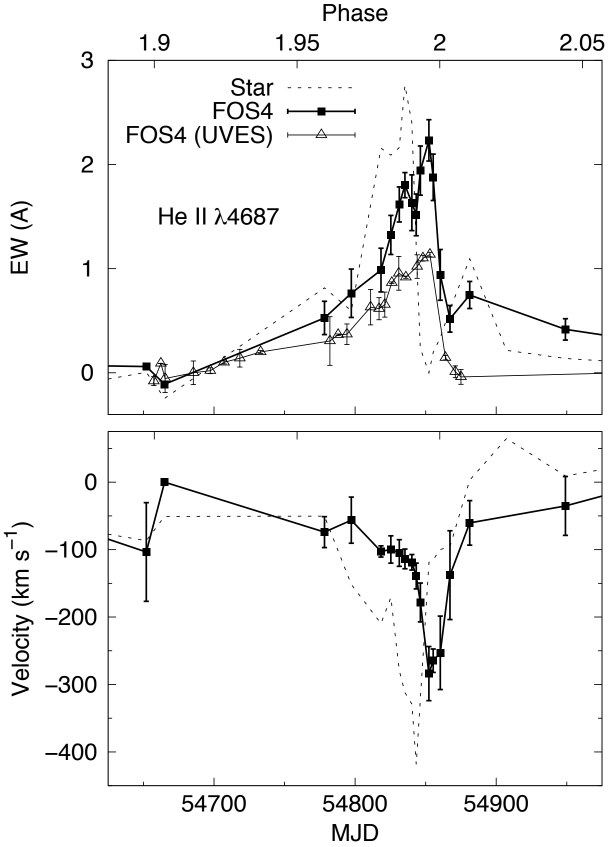

Figure 6.3: Equivalent widths and radial velocities of He II $\lambda 4687$ at FOS4 during the 2009 "event" observed with *Gemini* GMOS (filled squares). Equivalent widths from *VLT* UVES data during the 2003.5 "event," shifted by 2023 days are also shown (open triangles). The thin dashed curves are measurements at the location of the star. A time-delay of about 18 days is obvious.

compares the equivalent width and radial velocity of He II $\lambda 4687$ on the star and FOS4 (see also Table 6.2). Both, equivalent widths and radial velocities are consistent with a time-delay of 18 days, as are similar measurements of other spectral features, see for example equivalent widths of He I emission in Figure 9.4.

The GMOS data show clearly that the time-delay between the direct view on the star and the pole-on view at FOS4 is about 18 days. Therefore, I re-measured the *VLT* UVES data using the method employed by Martin et al. (2006a). UVES spectra with width of $1''$ were extracted at $2.99''$ east and $3.88''$ south of the central source. Figure 6.3 includes these measurements, shifted by one cycle, i.e. 2023 days. The measurements agree very well with the GMOS data of FOS4 in 2009. The shorter time-delay observed by Stahl et al. (2005) was likely caused by the low S/N of the UVES spectra, choice of continuum, time sampling, comparison between different data sets, and one outlier in their measurements.

The He II $\lambda 4687$ emission appears very similar when viewed from different directions, i.e. in direct view of the star and reflected at FOS4, when the time-delay is taken into account. Values for the equivalent widths and radial velocities are slightly smaller at FOS4 than in direct view. In this context it is interesting to note that, unless the orbit inclination is far from $i = 45°$, the He II emission can probably not be directly related to the orbital motion of the secondary star as proposed by Soker & Behar (2006). FOS4 views almost the plane of the orbit and therefore no large radial velocity variations should be observed in spectra at FOS4. Assuming we view the orbit with an inclination of 40–45°, the maximum radial velocity observed in direct view, ~ -400 km s^{-1}, implies velocities in the plane of the orbit of 550 km s^{-1}. The maximum observed radial velocity at FOS4 (70–75° inclination from the orbital plane), ~ -250 km s^{-1}, implies velocities in the plane of the orbit of 750–1000 km s^{-1}. If the He II emitting region were in the acceleration zone of the secondary star as proposed by Soker & Behar (2006), He II would be required to form at different distances from the star, closer in our direct line of sight and farther out at the polar view. In chapter 9, I assumed that the He II emission originates from the wind-wind cone and calculated the observable velocities in direct view and at FOS4.

6.2 The Changing Wind during the 2009 "Event"

HST STIS data revealed that some features depend on viewing direction and that the global stellar wind geometry changes during the cycle (Smith et al. 2003). However, the observed line profile variations could also be due to changes of ionization in the wind of η Car (Richardson et al. 2010). The most dramatic changes in the wind occur at low latitudes, while the dense polar wind remains relatively undisturbed during an "event." Departures from spherical symmetry are critical for theories of winds and instabilities in the most massive stars. Smith et al. (2003) analyzed only three epochs after the 1998 "event;" 1998 March (phase = 0.04), 1999 February (phase = 0.21), and 2000 March (phase = 0.40). The good time-sampling of the *Gemini* GMOS observations can be used to monitor changes before, during, and after the 2009 "event." I therefore analyzed the progression of several spectral features, such as Hδ, He I λ4714, and several Fe II and Cr II blends around λ4600 throughout the 2009 "event."

6.2.1 Hydrogen

Hα and Hβ emission lines are so bright in η Car that all Hα and many of the Hβ observations centered on the star were overexposed in *Gemini* GMOS observations.[16] Hγ is potentially contaminated by narrow emission lines and I therefore analyzed Hδ. Figure 6.4 shows sample tracings across the SE lobe at different times close to the 2009 "event," demonstrating the behavior of the Hδ P Cygni profile. GMOS observations before the "event," from 2007 June to the beginning of 2009 January, revealed no significant changes in the Hδ P Cygni profiles at all latitudes; no P Cygni absorption was observed at low latitudes but strong P Cygni absorption was observed at higher latitudes. This is considered evidence that the density and/or ionization structure of η Car's current stellar wind outside an "event" is nonspherical (Smith et al. 2003). For most of η Car's spectroscopic cycle wind densities are suspected to be higher near the poles, in accordance with theories of equatorial gravity darkening in massive rotating stars (Maeder & Meynet 2000; Maeder & Desjacques 2001; Owocki 2005). These theories also predict higher wind velocities at high latitudes. However, the tracings for $t = -353$ d and $t = -82$ d ($t = 0$ corresponds to MJD 54860 and phase 2.0) before the 2009 "event" in Figure 6.4 show that $v_\infty \approx 550$ km s^{-1} for the Hδ P Cygni absorption at all latitudes during η Car's normal state, and therefore I find no indication for higher wind velocities at high latitudes. This finding differs from Smith et al. (2003) who corrected for the redshift due to the expanding nebula by aligning the blue wing of Hα while I used several forbidden lines, known to originate from the Weigelt knots with constant velocities, to align the spectra. However, it needs to be further investigated if the different methods to align the spectra alone can account for the observed discrepancies in the v_∞ values or if the wind geometry changed over the last decade.

As already discussed in Smith et al. (2003) and Stahl et al. (2005), the strong latitude dependence of Balmer P Cygni profiles does not apply during the "events." In only a

---

[16] *Gemini* GMOS does not support exposure times below 1 s.

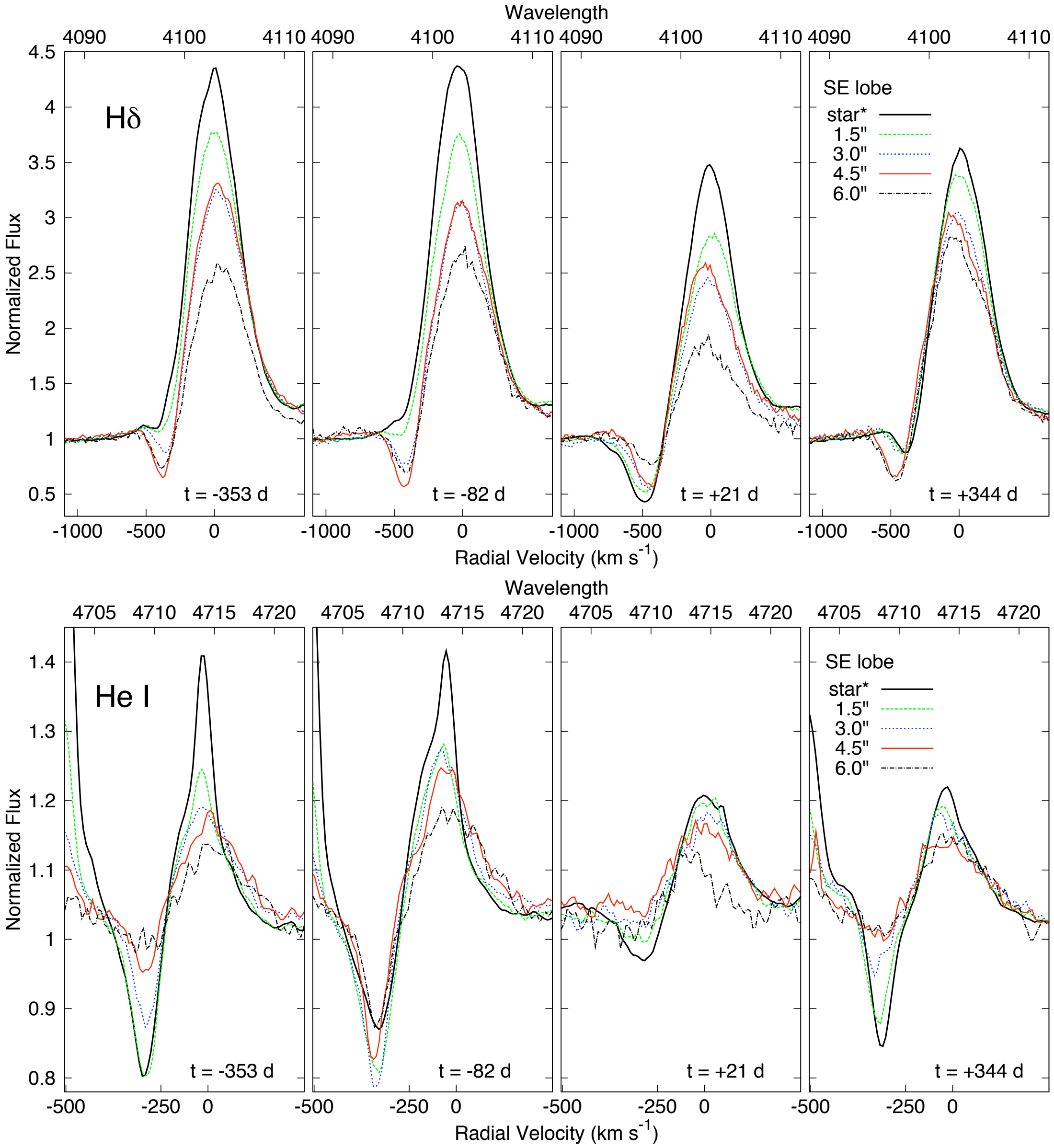

Figure 6.4: TOP: Hδ in tracings across the SE lobe in observations at different times indicated by t, with $t = 0$ at MJD 54860. The key indicates the offset along the slit from the central source. Spectra are shifted to account for their different redshifts. The black curve corresponds to a spectrum on the star and the red curve corresponds to a spectrum which is close to the position FOS4. Bottom: Tracings across the SE lobe showing He I λ4714 at different stellar latitudes.

few days, between 2009 January 4 (phase = 1.988) and January 9 (phase = 1.990), Hδ P Cygni absorption suddenly appeared at lower latitudes and strengthened to the same depth as at higher latitudes. Strong absorption at all latitudes was observed until 2009 March 17 (phase = 2.023), i.e. for at least 70 days during the "event." Observations from 2009 April 28 (phase = 2.044) to 2010 January 8 (phase = 2.170) show weak absorption at low latitudes while higher latitudes have strong P Cygni profiles, indicating the return to its pre-event state.

The strength of P Cygni absorption in Balmer lines depends on the population of the n=2 state. Because of high optical depth in Lyα in dense winds, the n=2 state acts as a metastable level and gives rise to strong Balmer absorption. Strong Balmer absorption requires sufficient density to cause H recombination in the outer wind. Thus, the increasing strength of Balmer absorption toward the pole can be explained if η Car's wind has higher densities towards the pole. Weak Balmer absorption at low latitudes could be due to higher ionization or lower density in that part of η Car's wind. P Cygni absorption is always present for higher Balmer lines at all latitudes which may indicate that they are formed closer to the star (Weis et al. 2005). Still, during the events, higher Balmer absorption lines deepen at lower latitudes while the absorption strength at higher latitudes remains nearly constant.

6.2.2 Helium

Figure 6.4 shows sample tracings of He I $\lambda 4714$ at different latitudes close to the 2009 "event." Outside the "event," in GMOS observations from 2007 June to 2008 July, He I lines had strong P Cygni absorption in spectra at low latitudes and only very weak P Cygni absorption in spectra at higher latitudes (see also Smith et al. 2003). Because of their limited time-sampling, Smith et al. (2003) were not able to observe changes in the He I P Cygni absorption. This lead them to conclude that for most of the cycle He I absorption is present on the star and not present at higher latitudes. Their Fig. 18 implies that the absorption at low latitudes disappears during the "event," though this fact is not explicitly stated in the paper. However, in GMOS data shortly before the 2009 "event," the He I absorption increased at higher latitudes. On 2008 November 8 ($t = -82$ d in Figure 6.4 corresponding to phase 1.960) the P Cygni absorption was strong at all latitudes. Over the next 2 months the absorption strength at all

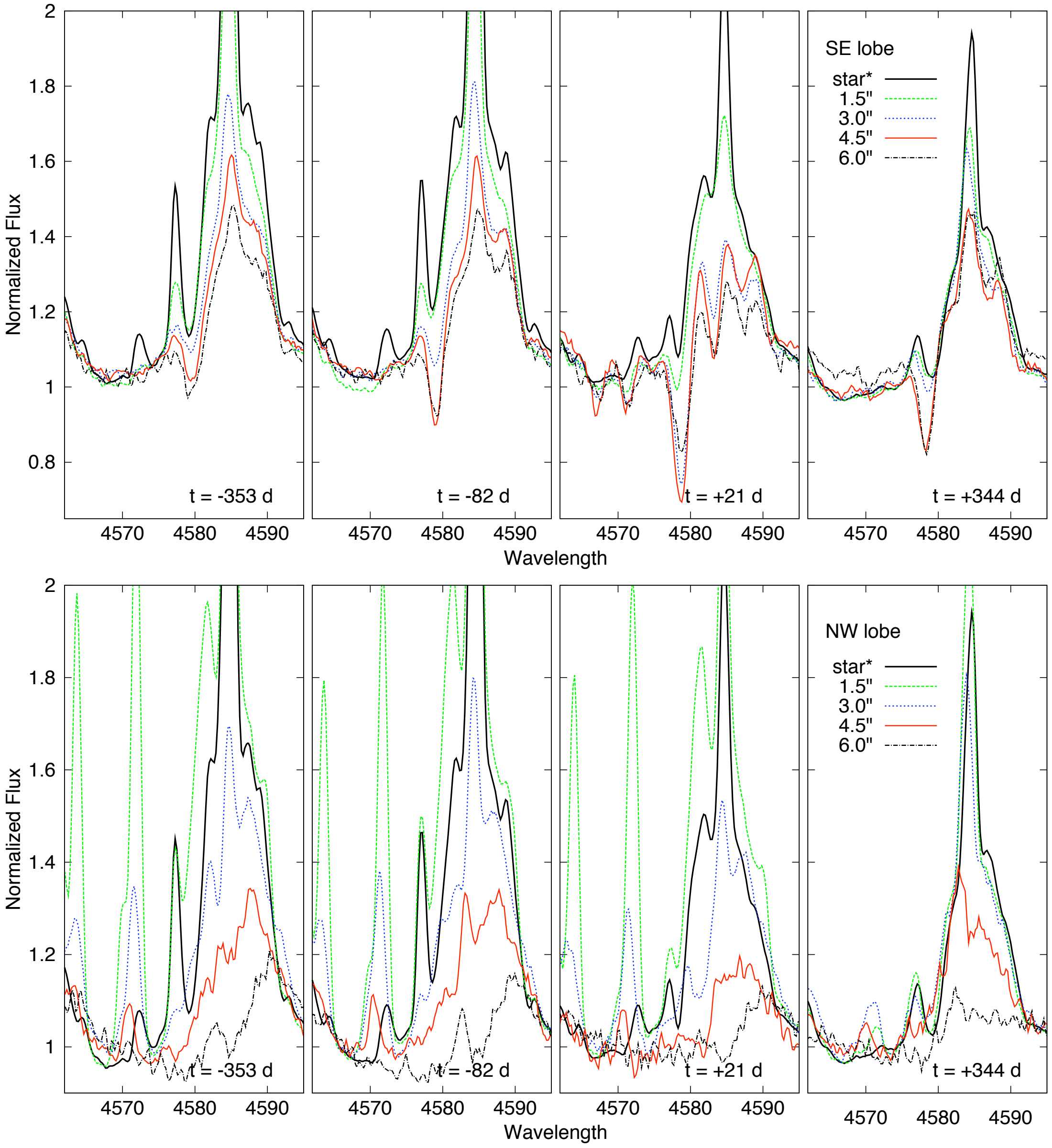

Figure 6.5: Tracings along the SE and NW lobes showing broad stellar wind emission around Fe II λ4585 close to the 2009 "event." The distance from the central star is indicated in the key, a distance of 4.5″ in the SE lobe is representative of a spectrum at FOS4. Spectra at higher latitudes are shifted to account for the expansion of the Homunculus. During the "event" the absorption lines strengthened at FOS4. No absorption is observed in direct view or across the NW lobe.

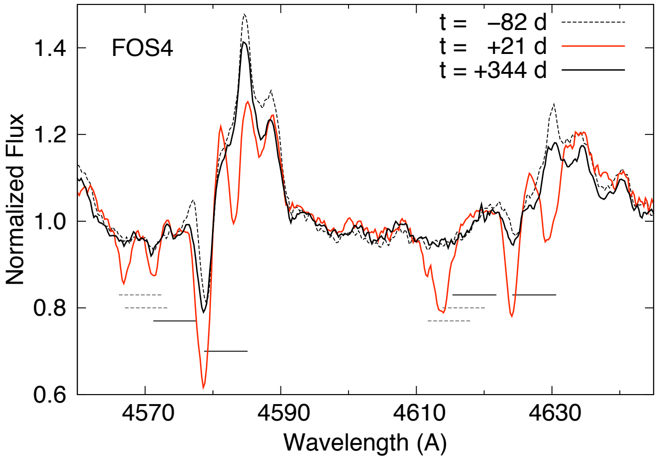

Figure 6.6: Absorption components at FOS4 deepened for a few months during the 2009 "event" (solid red curve). They can be identified with absorption components at −400–450 km s^{-1} of Fe II lines (solid black arrows) and Cr II, Mg I, and Ti II lines (dotted arrows).

latitudes slowly decreased. During this time-span the P Cygni absorption strength was very similar at all latitudes. Between the end of 2009 January (phase = 2.000) until 2009 April (phase = 2.044) almost no absorption was observed. The last two observations, obtained on 2009-07-24 and 2010-01-08, showed strong P Cygni absorption at low latitudes but only very weak absorption at higher latitudes. Note that changes in the He I P Cygni absorption occurred at least 2 months earlier than changes in the H I P Cygni absorption and that it recovered later than the H I P Cygni absorption (up to 3 months) to its pre-event state.

Smith et al. (2003) find that while the He I emission fades at low latitudes during the 1998 "event" the emission was relatively undisturbed at higher latitudes. However, the GMOS data show that the equivalent width of the He I emission during the 2009 "event" at FOS4 followed basically the same pattern as the emission directly on the star, see Figure 9.4.

6.2.3 Fe II and [Fe II] Emission and Absorption Lines

As already noted by Smith et al. (2003), the Fe II lines resemble the Balmer lines in that the Fe II P Cygni absorption increases with increasing latitude and that the emission is weaker at higher latitudes.

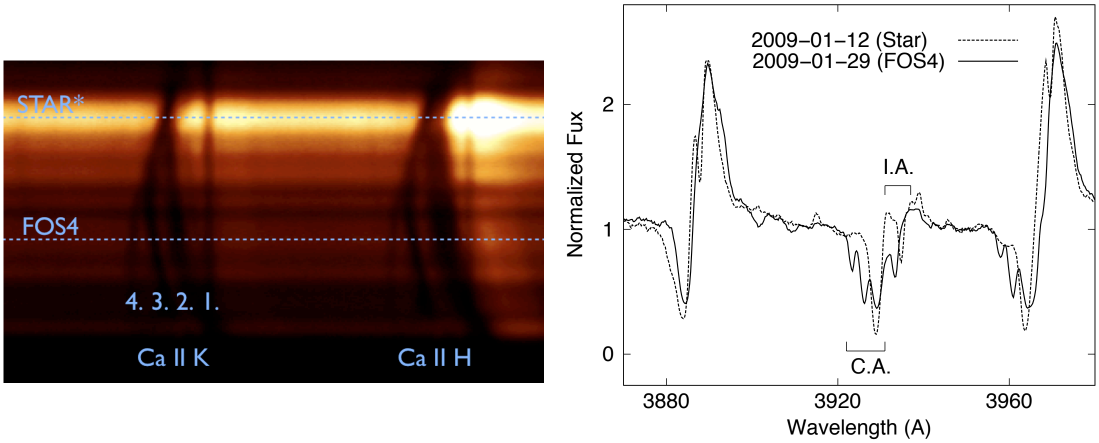

Figure 6.7: LEFT: 2-D spectrum showing the four components of the Ca II H and K lines. RIGHT: Spectra of He I $\lambda3890$, Ca II H and K, and Hϵ on star (dashed curve) and at FOS4 (solid curve). Spectra at FOS4 are shifted to account for the expansion of the Homunculus, therefore the interstellar absorption line does not coincide. Interstellar and circumstellar lines are indicated with "I.A." and "C.A.".

Figure 6.5 shows broad stellar wind emission features centered at Fe II $\lambda4585$ in tracings across the SE and NW lobes. Spectra before 2008-11-08 ($t = -82$ d corresponding to phase 1.960) showed only weak absorption at FOS4 with maximum strength at ~ -400–450 km s^{-1}, but the absorption feature then deepened and stayed strong until 2009-07-24 (phase = 2.087), i.e. for about 250 days. The absorption was strongest around 2009 February 19 ($t = +21$ d). The deepening of the Fe II absorption at FOS4 was also observed during the 2003.5 "event" (Stahl et al. 2005). Other species, such as Cr II, Mg I, and Ti II, also developed absorption lines. No absorption features were observed in spectra at lower latitudes or across the NW lobe but large differences are not expected there since the latitudes range only up the about 55°. The Figure 6.6 shows the appearance of several absorption lines at FOS4 at distinct times around the 2009 "event."

6.2.4 Ca II K Absorption

Several absorption components of Ca II are present in spectra of η Car; interstellar and circumstellar. The Ca II H line at $\lambda3970$ Å blends with the Hϵ absorption, so only the Ca II K line at $\lambda3933$ Å can be investigated (Figure 6.7). In spectra of the

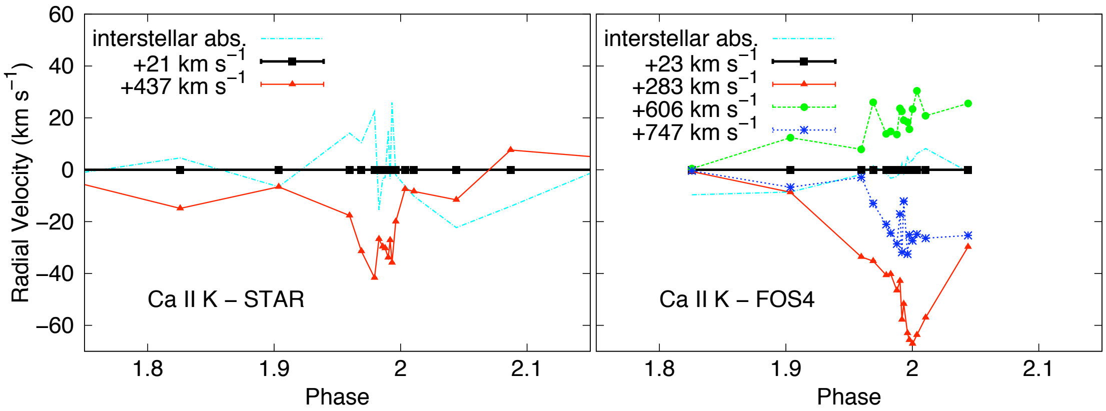

Figure 6.8: Radial velocity of Ca II K absorption lines. Light blue curve corresponds to the interstellar absorption line with a velocity of ~ -22 km s^{-1}. The velocity of this line should be constant (black curve), and is therefore used to calibrate the other velocity measurements. The red curve shows the circumstellar absorption line which can be traced along the entire Homunculus. Observations at locations in the Homunculus also show two additional faster absorption components (green and dark blue curves).

star in direct view two components are observed; 1) interstellar at -21 km s^{-1} and 2) circumstellar at -437 km s^{-1}. At FOS4 four different absorption components are observed; 1) interstellar at -23 km s^{-1}, 2) circumstellar at -283 km s^{-1}, 3) at -606, and 4) at -747 km s^{-1} (these velocities were not corrected for the expansion of the Homunculus). The circumstellar absorption line varies in radial velocity during the "event." It is not clear where the fast components 3) and 4) originate. However, both appear to trace the Homunculus nebula and converge with component 2) at the star (see left panel of Figure 6.7). The absorption might occur in outer faster ejecta with similar shape as the Homunculus (Davidson et al. 2001b; Smith 2008). During the "events," broad circumstellar Ca II absorption on the star became much deeper. At FOS4 the absorption strength of Ca II deepened somewhat during the "event."

Chapter 7

N II $\lambda\lambda$5668–5712

7.1 A New Class of Spectral Features

Broad emission and absorption lines of the N II $2s^2 2p3s\ ^3\mathrm{P^o}$ – $2s^2 2p3p\ ^3\mathrm{D}$ series at $\lambda\lambda$5668–5712 Å exhibit radial velocity variations during the 2009 spectroscopic event similar to the helium lines; see Figure 7.1 and Table 7.1. Figure 7.2 shows the energy levels involved. Note that the lower level, $2p3s\ ^3\mathrm{P^o}$, is more than 18 eV above the N II ground level but is connected to it by a permitted transition. Figure 7.1 compares spectra of η Car obtained from 2007 June to 2010 January showing N II λ5668, He I λ4714, and He II λ4687. Weak N II $\lambda\lambda$5668–5712 emission and absorption is always present in the spectrum of η Car. The maximum strength of the absorption component has a radial velocity of about -300 km s^{-1} with respect to the emission peak. During the 2009 spectroscopic event, emission and absorption features shifted about 250 km s^{-1} towards the blue, simultaneous with the He I emission and absorption lines and the He II λ4687 emission.

Table 7.1: Observed N II λ5668–5712 transitions[a]

Wavelength (Å)	Transition	$\mathrm{E_i}$ (cm^{-1})	$\mathrm{E_k}$ (cm^{-1})	$\mathrm{A_{ki}}$ (s^{-1})
N II 5 668.20	$2s^2\ 2p\ 3s\ ^3\mathrm{P}_1 - 2s^2\ 2p\ 3p\ ^3\mathrm{D}_2$	148940.17	166582.45	3.45e+07
N II 5 677.60	$2s^2\ 2p\ 3s\ ^3\mathrm{P}_0 - 2s^2\ 2p\ 3p\ ^3\mathrm{D}_1$	148908.59	166521.69	2.80e+07
N II 5 681.14	$2s^2\ 2p\ 3s\ ^3\mathrm{P}_2 - 2s^2\ 2p\ 3p\ ^3\mathrm{D}_3$	149076.52	166678.64	4.96e+07
N II 5 687.79	$2s^2\ 2p\ 3s\ ^3\mathrm{P}_1 - 2s^2\ 2p\ 3p\ ^3\mathrm{D}_1$	148940.17	166521.69	1.78e+07
N II 5 712.35	$2s^2\ 2p\ 3s\ ^3\mathrm{P}_2 - 2s^2\ 2p\ 3p\ ^3\mathrm{D}_2$	149076.52	166582.45	1.17e+07

[a] http://physics.nist.gov/PhysRefData/ASD

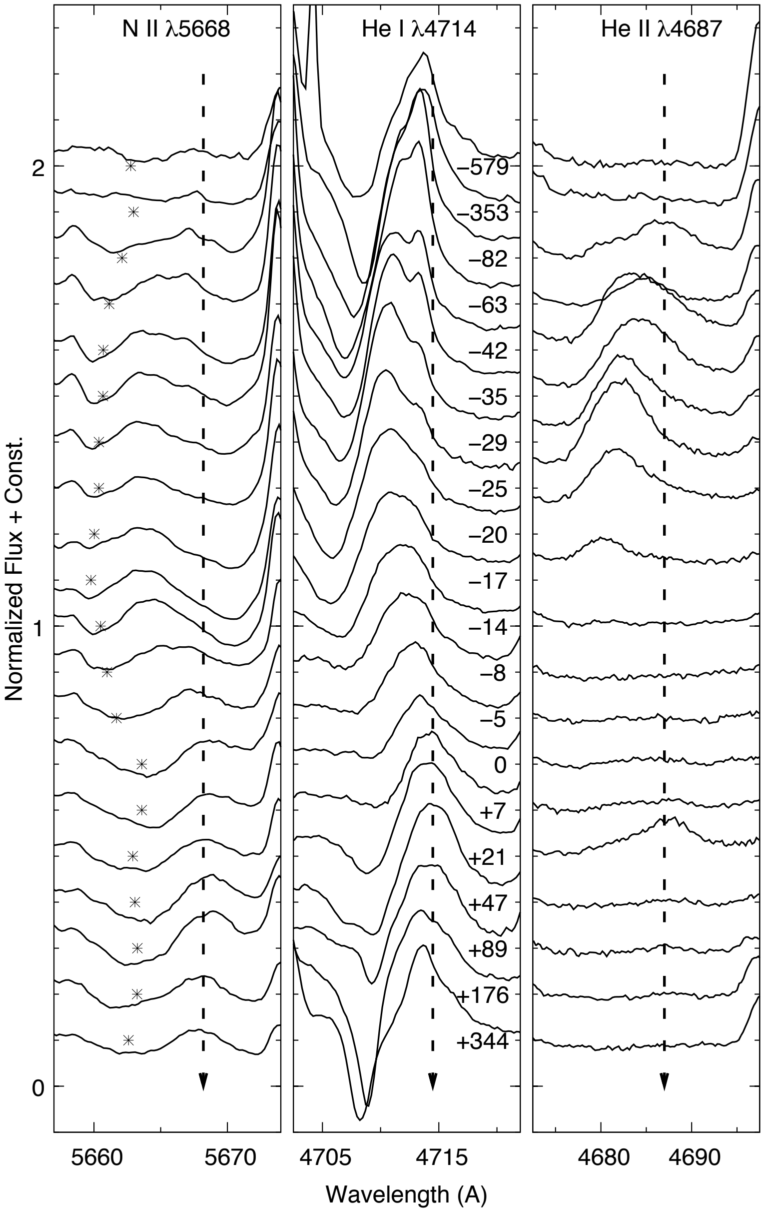

Figure 7.1: N II λ5668, He I λ4714, and He II λ4687 in spectra of η Car obtained with *Gemini* GMOS from 2007 June to 2010 January. Days before (-) and after (+) the 2009 spectroscopic event at MJD 54860 are displayed next to each tracing. Arrows indicate the zero velocities of the emission lines. *Note that most of the 5.5 year cycle is represented by the top two and bottom two samples and that [Fe II] λ5675 blends with the N II $\lambda\lambda$5678,5681 absorption.*

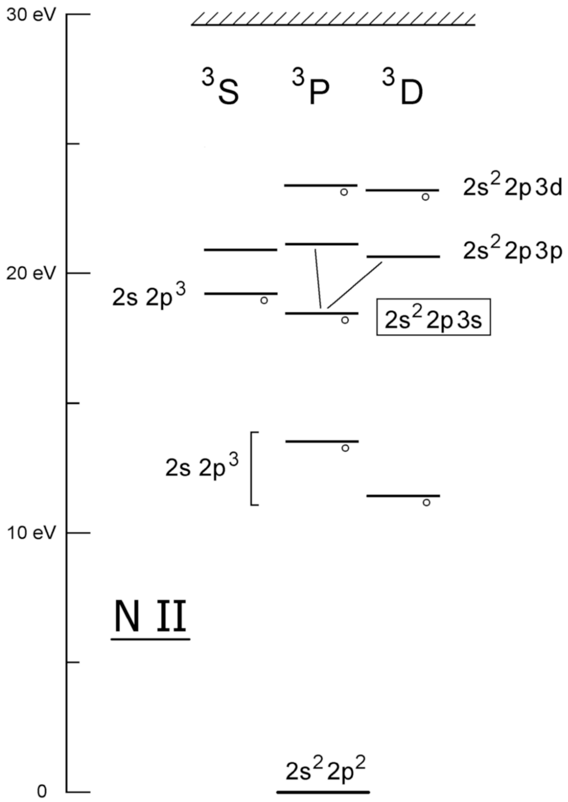

Figure 7.2: The lowest triplet levels of N II. Odd-parity levels such as $2s^2 2p3s$ ^{3}P^o are marked with small 'o's. I concentrate on the $2s^2 2p3s$ – $2s^2 2p3p$ transitions because they have observationally convenient wavelengths, see text.

HST STIS data obtained in 2009 June and December clearly show the N II $\lambda\lambda$5668–5712 lines, see Figure 7.3. In retrospect the faint N II spectral features can also be detected in *HST* STIS data from 1998–2004, but due to lower S/N they failed to attract notice before. Like the He I absorption, N II absorption was much weaker before 2003; less than 30% compared to 2009. The absorption strengths of both species increased gradually over the last 10 years (except during the 2003.5 and 2009.0 spectroscopic events). I determined the "stellar continuum" by a loess (locally weighted scatterplot smoothing) fit to the spectrum and find that the N II absorption is stronger than the emission. (The same is true for P Cygni; Beals 1935, Struve 1935). *Gemini* GMOS data appear to indicate the opposite, but their data quality is too low to determine a reliable continuum, and ground-based spectra are contaminated by narrow emission lines from

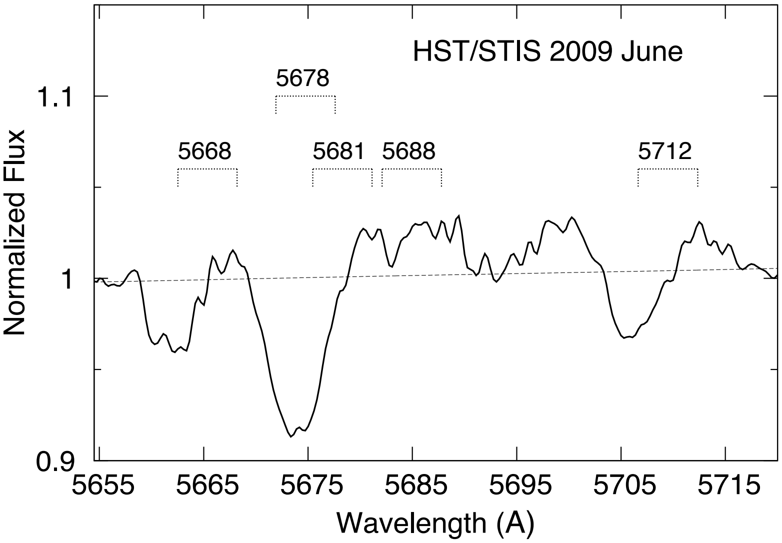

Figure 7.3: N II $\lambda\lambda$5668–5712 in *HST* STIS data from 2009 June. Zero velocity emission and absorption at -300 km s^{-1} are indicated with brackets. The dashed curve represents the stellar continuum. *HST's* high-spatial resolution shows the absorption much better than ground-based data. The strong N II $\lambda\lambda$5678,5681 absorption is blended with [Fe II] λ5675 in the *Gemini* spectra.

ejecta outside the wind, e.g., [Fe II] λ5675 blends with the N II $\lambda\lambda$5678,5681 absorption. Although these features were first noticed in the GMOS data, the high spatial resolution of *HST* data is essential for examining their character.

Most other permitted N II lines are too weak or blended with emission lines from the wind or nearby ejecta to be observed. However, similar behavior can be seen in the N II $2p3s$ ^{3}P^o – $2p3p$ ^{3}P series at $\lambda\lambda$4603,4608 Å (Figure 7.2). Transitions of the N II $2p3s$ ^{3}P^o – $2p3p$ ^{3}S series are too weak and blended with other lines.

Radiative excitation of level $2s^22p3s$ is very important as discussed later. The $2s2p^3$ levels are excited in the same way but lead to no observable results. Transitions from $2s2p^3$ ^{3}S^o to $2s^22p3p$ ($\lambda\lambda$6435–7265 Å) have small oscillator strengths and are therefore not observed. STIS data indicates the weak presence of the singlet N II λ3996 line but this line is blended with others in *Gemini* data and therefore the identification is not certain. Lines whose upper levels are above the $2p3p$ state like N II λ5007, even though they are strong in the laboratory, are not observed. The N II lines and their velocity shifts can also be seen in the reflected polar spectrum at location FOS4.

7.2 Line Formation and Significance

The same N II lines are seen in early type stars. In objects like P Cygni and shells of O-stars, $2p3s$ ^{1}P$^{\rm o}$ – $2p3p$ ^{1}S,^{1}P,^{1}D and $2p3s$ ^{3}P$^{\rm o}$ – $2p3p$ ^{3}S,^{3}P,^{3}D are very strong (Swings & Struve 1940). Large differences between WN stars indicate that these lines are sensitive to atmospheric conditions and/or the variability of the wind. They may also be very sensitive to the FUV flux since they are likely produced via continuum fluorescence (Herald et al. 2001).

In the case of η Car the N II absorption and emission almost certainly occur in the primary star's dense wind, for reasons noted later below. But three facts indicate that UV photons from the secondary star populate the critical $2p3s$ levels. (1) The velocity behavior strongly suggests some relation to the secondary, analogous to the He I features. (2) The $2p3s$ levels are about 18.5 eV above the ground state, a high value for the primary star's wind. According to (Hillier et al. 2001), the opaque-wind photospheric temperature is below $15,000$ K, and emission-line regions in the primary wind are mostly below $10,000$ K; much cooler than the O stars and WR objects mentioned above. The hot secondary star, on the other hand, produces a large flux of 18.5 eV photons (Fig. 10 in Mehner et al. 2010a). (3) This hypothesis appears quantitatively successful as outlined below. Any of these clues by itself might be debatable, but together they seem compelling.

Let us summarize an order-of-magnitude quantitative assessment of the absorption line strengths that one would expect in a simple model. For simplicity I include only the N^+ ground level '1' ($2p^2$ ^{3}P) and one excited level '2' ($2p3s$ ^{3}P$^{\rm o}$); the initial goal is to estimate the equilibrium population ratio n_2/n_1. A two-level system is justified because no permitted transitions connect level 2 to lower levels. Consider a uniformly-expanding local volume in the primary wind. Denote the incident continuum photon flux at $h\nu_{12} \approx 18.5$ eV by Φ_ν, not corrected for line absorption in the gas. As explained in section 8.5 in Lamers & Cassinelli (1999), and §8 in Martin et al. 2006a, the Sobolev approximation allows to write expressions for the radiative $1 \rightarrow 2$ excitation rate and the re-emission photon escape probability, as functions of the local expansion rate, a line profile function, and atomic parameters. The *effective* de-excitation rate is proportional to the escape probability, and the most complicated factors appear similarly in both the excitation rate and the escape probability. Consequently the equilibrium population ratio is simple:

$$\frac{n_2}{n_1} = \frac{g_2}{g_1} \cdot \frac{\lambda_{12}^2 \Phi_\nu}{8\pi} , \tag{7.1}$$

where g_1 and g_2 are the statistical weights. This expression remains valid when fine structure is taken into account. The same ratio would be found in an LTE case where Φ_ν / c is the Planckian photon density at $h\nu_{12} \approx 18.5$ eV. Above triplet levels of N II are mentioned, but singlet levels would also be excited in the same way from $2p^2\ ^1$D.

With conventional parameters for the two stars and their winds, Φ_ν at 18.5 eV is dominated by the hot secondary star. Reasonable values for it are $T_{\rm eff} \approx 40,000$ K, $R \approx 13\ R_\odot$, and $L \approx 4 \times 10^5\ L_\odot$ (Mehner et al. 2010a). According to a WM-basic atmosphere model (Pauldrach et al. 2001), such an object emits roughly 5×10^{33} photons Hz^{-1} s^{-1} at $h\nu = 18.5$ eV, about 30% less than a 40,000 K blackbody. With the type of orbit model that most authors currently favor (e.g., Okazaki et al. 2008), the separation between stars was about 13 AU when η Car was observed in 2009 June. The secondary star was then located roughly 1–5 AU closer to us than the primary, and roughly 10 AU from our line of sight to the primary – depending on the poorly known orbit orientation, of course (see Figure 7.4 for the geometrical arrangement). With these parameters, equation 7.1 gives $n_2/n_1 \approx 3 \times 10^{-8}$ at relevant locations between us and the primary star, i.e., in gas located about 10 AU from the secondary star. The equivalent excitation temperature is near 12,500 K.

The observed absorption lines have some geometrical complications. Since the opaque-wind photosphere is diffuse with a substantial size, a relevant "line of sight" can be any sample ray in a cylinder with diameter ~ 7 AU (Figure 7.4). Strong $2p3s$–$2p3p$ absorption occurs in regions that optimize a combination of attributes: (1) the inner wind is favored because of its high densities; (2) most of the nitrogen must be singly ionized; (3) the N$^+$ must be fairly close to the secondary star in order to maximize Φ_ν; and (4) the light path (possibly indirect, due to Thomson scattering) must pass close enough to the primary star to sample continuum radiation from its semi-opaque inner wind. Thus, in Figure 7.4, the strongest absorption is expected to occur near and above the symbol '1' that labels Region 1. The picture obviously changes as the secondary star moves along its orbit.

Most nitrogen in the primary wind is singly ionized, due to both the primary and the secondary radiation field (Hillier et al. 2001). Helium in zones 3 and 4 in Figure 7.4

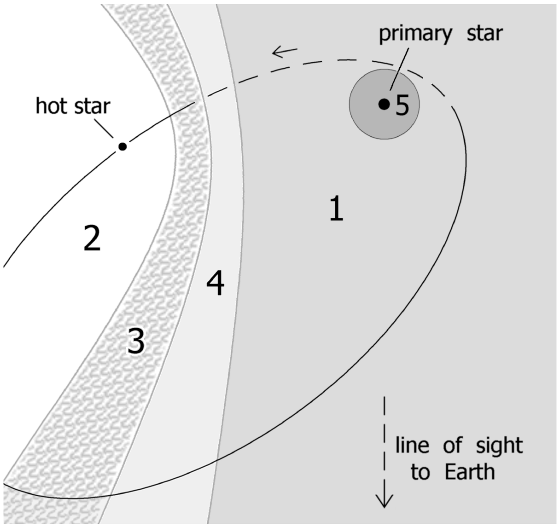

Figure 7.4: Schematic arrangement of a conventional model for the 2009 June observations. The line of sight to Earth lies in the plane of the Figure, and the secondary star's orbit is shown projected onto that plane. Regions 1 and 2 are undisturbed parts of the primary and secondary winds. The shocked wind-wind collision region is labeled 3, while region 4 is a He II zone in the primary wind, photoionized by the secondary star. N II is abundant in region 1 but zones 2–4 are more highly ionized. Region 5 is within the opaque-wind photosphere at visual wavelengths. The area shown is roughly 25 AU across, but all details are simplified and idealized.

provides the shielding which prevents the secondary radiation field from ionizing N^+ into N^{++}, but which allows the 18.5 eV radiation to penetrate. Suppose the primary mass-loss rate is $3 \times 10^{-4}\ M_\odot\ \mathrm{yr}^{-1}$ and nearly all the CNO is nitrogen (Davidson et al. 1986; Dufour et al. 1999).[17] Then the column densities outside $r = 4$ AU (for example) are

$$N(\mathrm{N}^+) \ \sim\ 2 \times 10^{20}\ \mathrm{cm}^{-2}\,,$$

$$N(\mathrm{N}^+\ 2p3s) \ \sim\ 6 \times 10^{12}\ \mathrm{cm}^{-2}\,.$$

This column density would produce a combined equivalent width of about 1 Å for the $\lambda 5681.14$ and $\lambda 5677.60$ Å absorption lines. Since this exceeds the observed value of 0.5 Å, *the proposed mechanism appears to be sufficient,* even if only a limited part of the

---

[17] The most often quoted mass loss rate for η Car is around $10^{-3}\ M_\odot\ \mathrm{yr}^{-1}$, but there are good reasons to believe that it has decreased substantially in the past decade (Mehner et al. 2010b; Corcoran et al. 2010; Kashi & Soker 2009a).

wind is involved. The parameter values in this sample calculation were chosen *ab initio* without knowing what result they would lead to; there was no readjustment to get a desired outcome. Note that the margin of error does not allow much smaller values of Φ_ν and gas densities.

The *emission* features have upper levels only moderately above $2p3s\ ^3\mathrm{P}^\mathrm{o}$, and they are no stronger than the P Cyg absorption; so they most likely resemble the pure scattering case of P Cyg lines. In other words, the observed $2p3s - 2p3p$ emission line strengths automatically follow from the absorption strengths. More detailed calculations will require elaborate geometrical models of the ionization and excitation zones.

As noted earlier, these N II features should arise chiefly in regions of the primary wind that are fairly close to the secondary star, and, therefore, close to the He^+ zones and wind-wind shocks. If shock instabilities do not distort it too much, the $\mathrm{He}^+/\mathrm{He}^0$ ionization front is expected to have a pseudo-hyperboloidal shape that is concave towards the secondary star (Figure 7.4). Adjoining primary-wind zones are spatially large enough to account for the N II lines. Generically, this type of model can explain the velocity variations, but authors disagree about details (e.g., Nielsen et al. 2007; Damineli et al. 2008a; Humphreys et al. 2008; Martin et al. 2006a).

Far more important than merely being consistent with some models of the η Car system, the N II features may disprove others. For example, it has been suggested that the helium lines originate in the acceleration zone of the secondary star's wind, or perhaps in an accretion disk around the secondary, rather than in the primary wind (Soker & Behar 2006; Kashi & Soker 2007; Steiner & Damineli 2004). But the N II features, with practically the same velocity behavior, almost certainly cannot represent such zones; so models of that type would be forced to explain the He I and N II velocities differently.

The arguments are simplest for absorption lines. First, note that with credible parameters for the two stars (e.g., Hillier et al. 2001; Mehner et al. 2010a), the primary wind accounts for at least 95% of the visual-wavelength continuum, most likely 98–99%. Therefore *the absorption features in Figure 7.3 definitely represent material located between us and the inner parts of the primary wind.* (In other words, blocking the entire secondary star would not produce absorption as deep as that shown in Figure 7.3, even if $\tau_{\mathrm{line}} \gg 1$.) Can that absorbing material be part of the secondary wind or an accretion disk? Presumably not; because in every proposed orbit model the relevant lines of sight either miss the secondary wind entirely at most times, or pass through only its outer regions. Those parts of the secondary wind have densities two orders of magnitude less than used in the calculations outlined above, the nitrogen there is mainly N III, and the velocity dispersion is too large for the observed absorption features. In other words, this type of model would fail the quantitative feasibility test that the "conventional" model passed. Regarding the N II emission features, they are fairly weak relative to the total observed continuum, but would be extraordinarily strong compared to the visual-wavelength continuum of just the secondary star.

The N II lines convey information that is not available in other spectral features. This is mainly because they arise in "normal" parts of the primary wind but they are sensitive to the current location of the secondary star. Helium lines also depend on UV from the secondary, but their emission zones are extremely difficult to model since they depend on the unstable primary shock, post-shock cooling, local "clumping," etc. In principle the N II zones are expected to be much steadier, and the excitation mechanism is relatively insensitive to inhomogeneities. For these reasons the N II features may be good indicators of average density in the wind combined with the secondary star's orbital motion. In particular one might expect their velocities to be easier to model than those of helium lines.

He I and N II absorption lines have grown in strength during the past 10 years. At first sight this appears counter-intuitive, since the wind density appears to have *decreased* (Mehner et al. 2010b). However, the situation has various dependences that tend to oppose each other so intuition may be a poor guide. Decreasing mass loss rate implies a smaller, denser opaque-wind photosphere; equation 7.1 becomes invalid if continuum absorption destroys the trapped 18.5 eV resonance photons before they escape; etc. This problem merits further attention. Whatever the solution,the N II lines are expected to provide different parameter contraints than the spectral features that are excited in more normal ways.

Chapter 8

Fe II, [Fe II], and [Fe III] Emission

The spectrum of η Car is rich in broad permitted Fe II and narrow forbidden [Fe II] emission lines. The Fe ionization structure, low electron temperature, the shape of blackbody radiation, and intense Lyα radiation provide conditions favorable for a rich Fe II spectrum. Iron ionizes to Fe^{+} by 7.9 eV radiation or collisions (and potentially charge exchange), and only 16.2 eV are required to reach Fe^{2+}.

Fe II lines are difficult to analyze because of complex radiative processes. Verner et al. (2002) presented numerical simulations that reproduce the features of [Fe II] and Fe II emission in spectra of the Weigelt knots BD obtained in 1998 with *HST* STIS. They concluded that Fe II and [Fe II] lines are due to; (1) pumping by the blackbody-like stellar radiation field from η Car in the range $\lambda\lambda$4000–6500 Å, (2) primary cascades after Lyα fluorescence for $\lambda\lambda$8000–10,000 Å and in particular Fe II $\lambda\lambda$2507,2509, and (3) collisional excitation dominates at wavelengths $\lambda\lambda$7000–9000 Å.

In this chapter, I discuss the spatial distribution of Fe II, [Fe II], and [Fe III] lines and their temporal variations throughout the spectroscopic cycle. I also comment on the peculiar Fe II $\lambda\lambda$2507,2509 lines.

8.1 Spatial Origin and Temporal Behavior

Narrow forbidden [Fe II] lines dominate the spectrum of the Weigelt knots BCD. Figure 8.1 shows a spatial map of the narrow [Fe II] λ7157 and the temporal flux variations of the narrow [Fe II] $\lambda\lambda$7157,5377,4729 lines. The spatial map resembles the ones for the

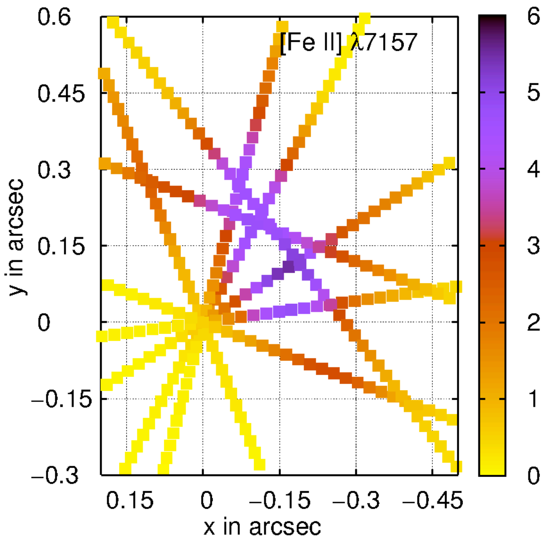

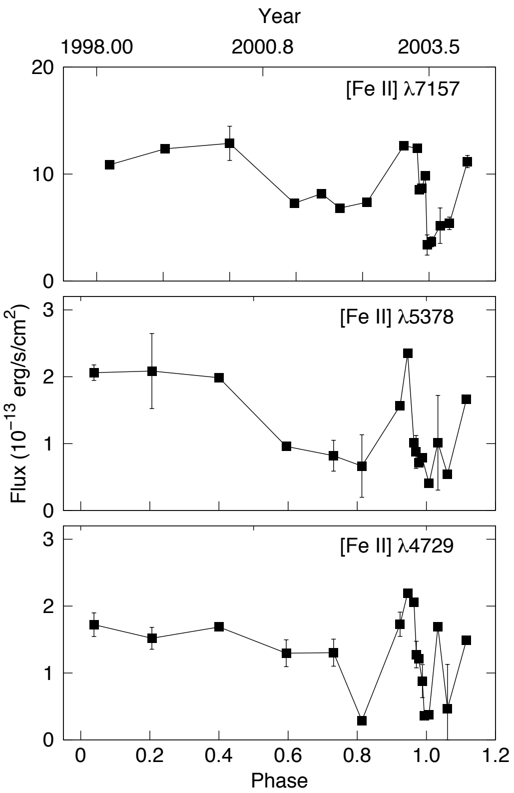

Figure 8.1: TOP: Spatial flux map of the narrow [Fe II] λ7157 emission. The emission is concentrated on the Weigelt knots. RIGHT: Temporal flux variations of the narrow [Fe II] λ7157, [Fe II] λ5377, and [Fe II] λ4729 lines on the star.

high-excitation emission in section 3.1 in that the flux is concentrated on the Weigelt knots. Variations in the line intensity mirror the high-excitation emission lines described in section 3.2; the flux peaks shortly before the "event" and then drops rapidly into a minimum.

Broad stellar H I, He I, and Fe II emission originates deep within the central core (Nielsen et al. 2007; Weigelt et al. 2007). Broad [Fe II] and [Fe III] emission, on the other hand, originates from extended regions around the star and trace the outer stellar wind and the wind-wind interaction region, photo-excited by mid-UV radiation (Hillier et al. 2001, 2006; Gull et al. 2009). Gull et al. (2009) showed that broad (±500 km s^{-1}) emission line structures extend $0.7''$ (≈ 1600 AU) from the stellar core. The emitting material most likely consists of compressed primary wind material on the primary side of the shock.

HST STIS 2009 June mapping data can be used to simulate spectra with different aperture sizes. Figure 8.2 shows a narrow $0.1''$ extraction on the star and a spectrum

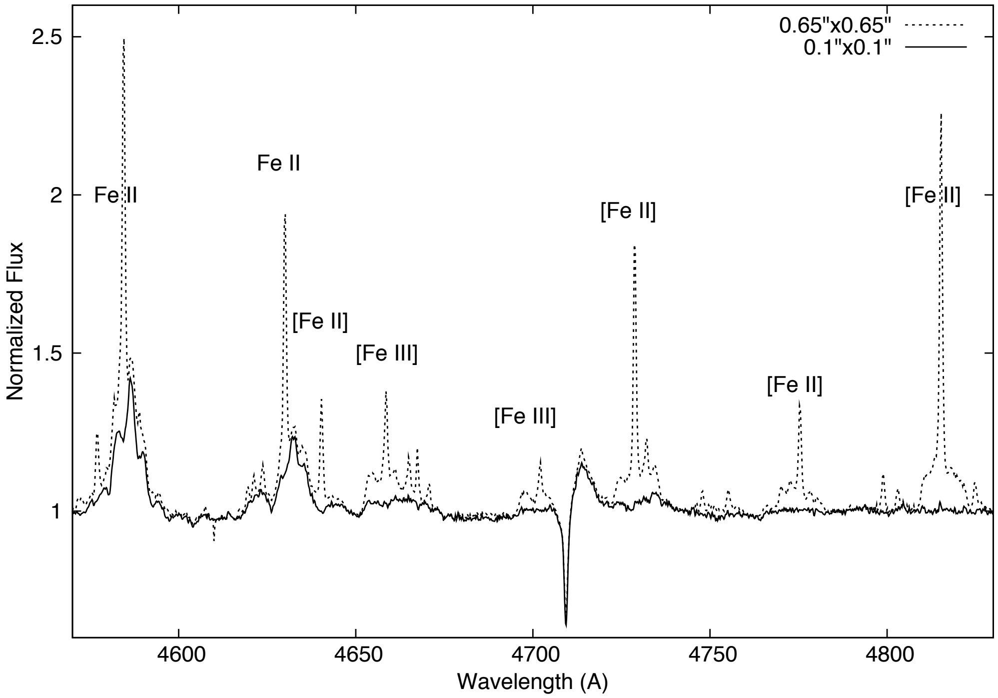

Figure 8.2: Narrow 0.1″ extraction on the star (solid line) and summed-up flux from a region 0.65″ around the star (dashed line) using *HST* STIS mapping data from 2009 June. Broad wind emission of forbidden [Fe II] and [Fe III] are only observed in the spectrum sampling an extended region around the star.

that samples a region of 0.65″ around the star. Broad permitted Fe II emission originates within 0.1″ from the star, see the two strong emission features around λ4600 Å. (The narrow lines originate from the nearby Weigelt knots and are not discussed here.) Broad forbidden [Fe II] and [Fe III] emission is only present in the spectrum that samples the 0.65″ region around the star, and therefore originates from lower density, outer regions of the extended wind.

The extended broad emission can be observed throughout the entire cycle with the exception of a few months during the "events," when it weakens considerably. It originates from an arc-like ring around η Car; emission can be observed in the NE, SE, and SW, more precisely at angles of 20–240° (N → E) around the central source. The emission is not present in the NW (region of the Weigelt knots). Figure 8.3 shows a spectral image of the forbidden [Fe III] λ4659 line observed on 2003 May 20 (phase=0.971). The position angle was $PA = 38°$. The extended arc-like emission is observed in velocity

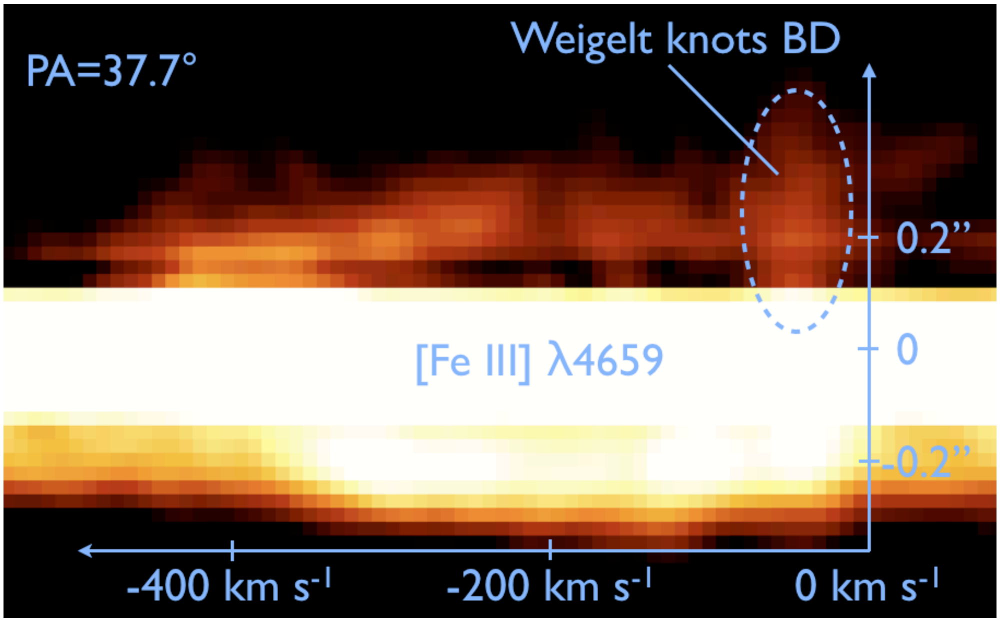

Figure 8.3: Spectral image of an observation with slit position angle $PA = 38°$ showing the arc-like extended broad emission of [Fe III] $\lambda4659$. The emission is bright in velocity space at -400 km s^{-1} and in spatial space at $0.2''$ from the star. The intensity is scaled as square root.

space at -400 km s^{-1} and in spatial space at $0.2''$ from the star. Figure 8.4 shows tracings along the slit showing the extended emission. The two panels on the left show tracings along slits with position angles of $PA = -28°$ at different phases; at mid-cycle and shortly before the 2003.5 “event.” The emission, especially the blue component indicated by the solid arrow, is not present NW of the star (red curves) but in the SE (blue curves). Note the very similar appearance of the emission at different phases. The panel on the right shows tracings along a slit with position angle of $PA = 38°$, showing that the emission features are present in the NE and SW. The bright blue component at -400 km s^{-1} which is part of this extended feature is described in section 3.3 and its spatial origin is shown in Figure 3.6.

Gull et al. (2009) showed that these broad emission features can be used to constrain the absolute orientation and direction of the binary orbit on the sky. (Models based on the observed X-ray light curve or other point-source data are ambiguous.) Madura et al. (2011) simulated the spatially resolved [Fe III] $\lambda4659$ emission line using 3-D Smoothed Particle Hydrodynamics (SPH) simulations of the binary wind-wind collision

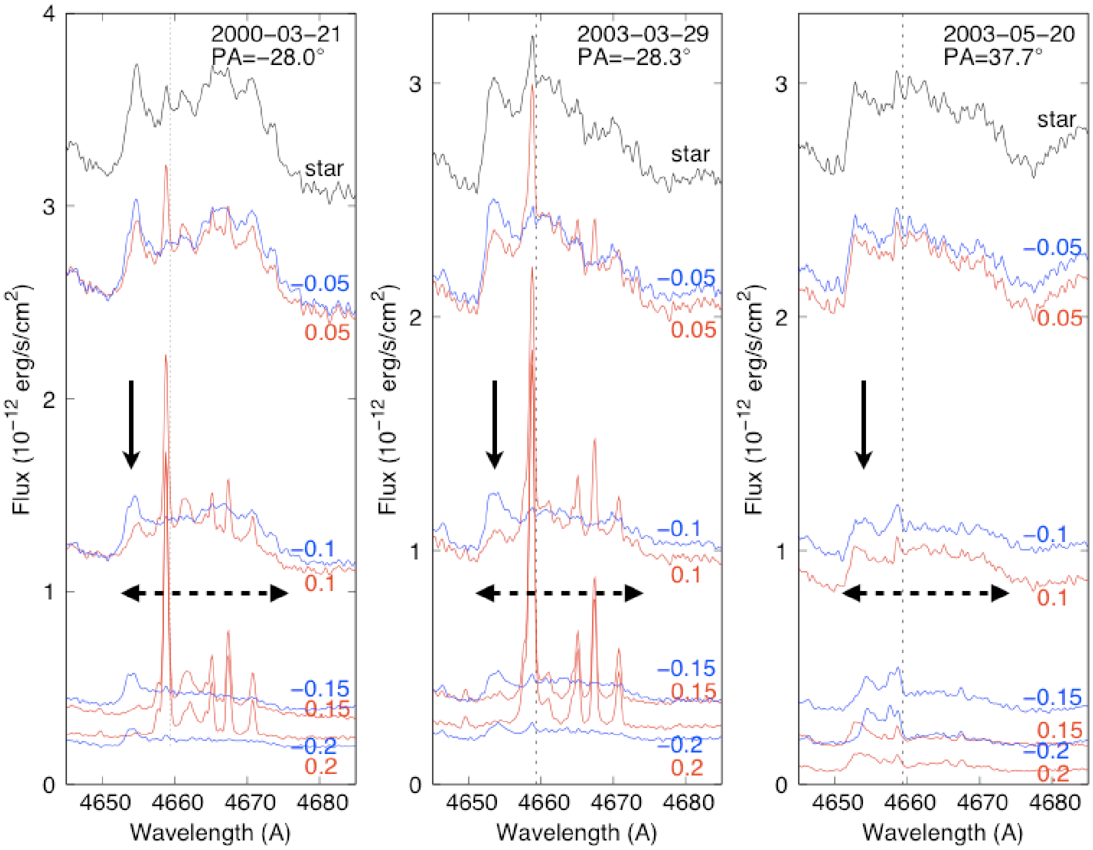

Figure 8.4: Tracings along the slit showing the locations of the broad [Fe III] λ4659 emission (dashed arrows) and its blue component (solid arrows). Extraction width are 0.1″, next to each tracing the offset from the star is given in arcsec. Positive numbers indicate that the extraction was offset towards where the slit points, negative numbers indicate the opposite.

together with radiative transfer codes. They found that the synthetic spectral images best matched the observed STIS observations if $i \approx 40 \pm 10°$ and $\omega \approx 255 \pm 15°$ with the orbital axis projected on the sky at position angle $\approx 312 \pm 15°$.

8.2 Fe II λλ2507,2509

Some of the most peculiar features in the spectrum of η Car are the unusually strong Fe II λλ2507,2509 lines identified by Johansson & Jordan (1984). These lines are among the strongest single features in the spectrum of η Car. They are transitions from two highly excited (11.1 eV) energy levels of Fe II. Johansson & Hamann (1993) suggested that a Bowen mechanism produces the unexpected large intensities of these UV lines. Johansson & Letokhov (2001) presented a physical model for the origin of these lines. They considered an excitation mechanism based on photoexcitation and photoionization of Fe II by intense Lyα radiation. In their model, Lyα is generated by the absorption of blackbody radiation from the central star ($>$ 13.6 eV) and then trapped within the optically thick environment of the Weigelt knots (high energy photons ionize hydrogen and the following recombination process provides intense Lyα radiation). However, these lines might also be pumped directly by Lyα radiation from the secondary star.

The left panel of Figure 8.5 shows a spatial map of the Fe II λ2507 emission. The flux was not normalized to illustrate that these lines do not vary much in strength throughout the cycle. In contrast to other iron lines, these lines are strongest at knot D and not knot C. The Fe II $\lambda\lambda$2507,2509 lines only weaken for a short time during the "events," see right panel of Figure 8.5 for line profiles during the 2003.5 "event" on Weigelt knot D. Line strengths recover within 100 days, in contrast to other high-excitation lines that need more than 200 days to recover (see Fig. 2 in Damineli et al. 2008a). The fast reappearance of the Fe II $\lambda\lambda$2507,2509 lines is consistent with the idea that they are Lyα pumped by radiation from the secondary star; they should react much faster to its "reappearance" than recombination lines.

In 1998–2004 several observations were conducted using a slit position angle of $PA = 152°$, which included Weigelt knots BD. In 2009 and 2010 observations covered mainly knot C with slit position angles of $PA = 122°$. Figure 8.6 shows the flux along the slits for these two slit position angles for different phases. The knots are very different in their spatial extension. Weigelt knots B and D are unresolved and Weigelt knot C has a "bump" at the far side from the star which might be part of knot C or an additional smaller knot. Also, the knots can be seen to move slowly away from the star over the last 10 years.

After the 2009 "event," the Fe II λ2507 line recovered fully to former maximum intensity but is decreasing since then, see Figure 8.7. The Figure shows the flux of Fe II λ2507 on Weigelt knots C and D since 1998. However, caution has to be exercised when drawing conclusions about possible longterm changes because, (1) there are no observations in 2004–2009, (2) observations before 2004 focused on knot D while observations

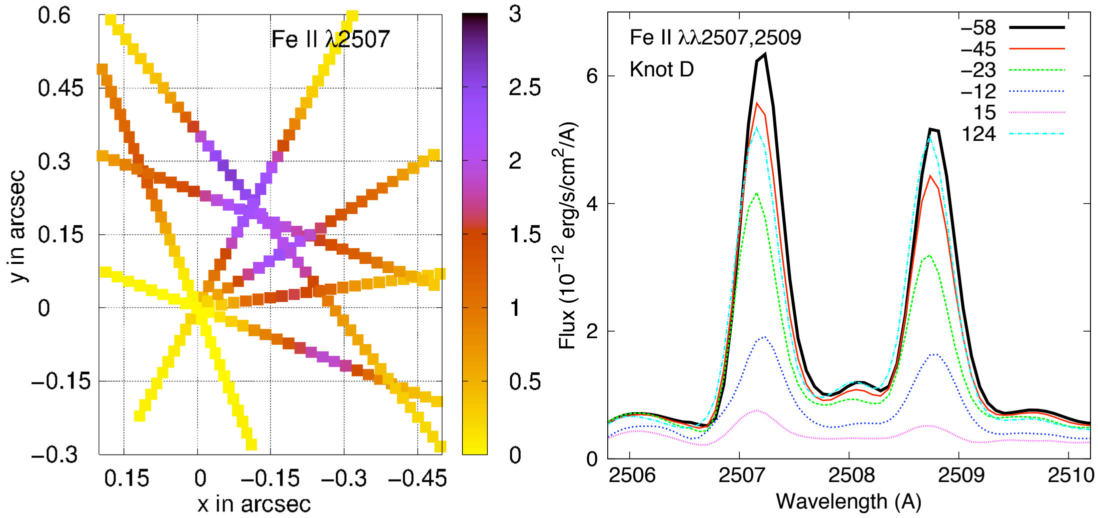

Figure 8.5: LEFT: Spatial map of Fe II λ2507 in *HST* STIS observations from 1998–2004 but outside the 2003.5 "event." The flux is concentrated at the Weigelt knots and dominates at knot D in contrast to other iron lines. RIGHT: Spectra of Fe II $\lambda\lambda$2507,2509 during the 2003.5 "event" at Weigelt knot D. Days before (−) and after (+) the "event" are indicated. The line strengths recover in about 100 days, much faster than other high-excitation emission lines.

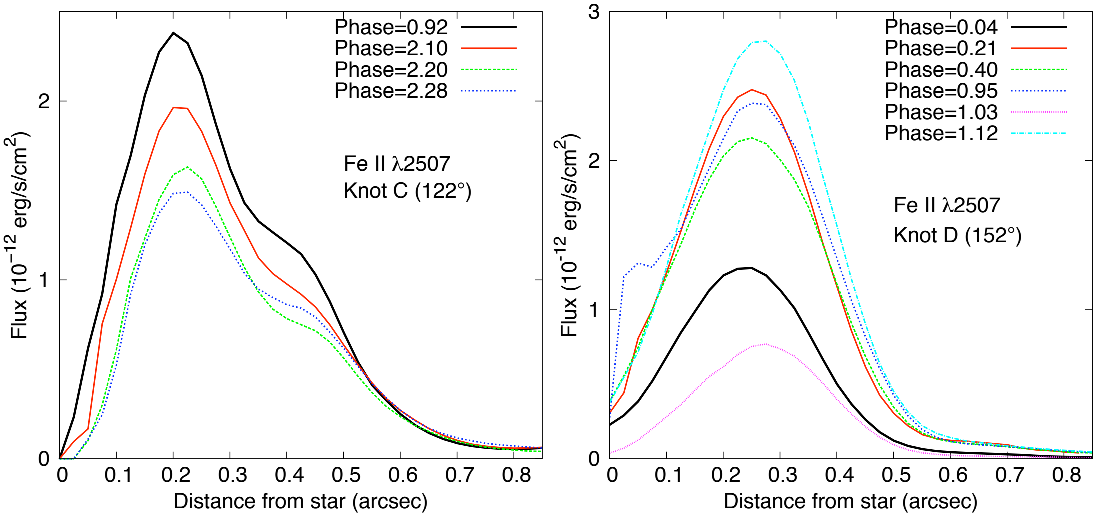

Figure 8.6: Fe II λ2507 at Weigelt knots C and D (slit position angles $PA = 122°$ and $PA = 153°$). Weigelt knot C is either elongated or has a close second knot. The knots can be seen to move slowly away from the central star (see also discussion in section 4.3).

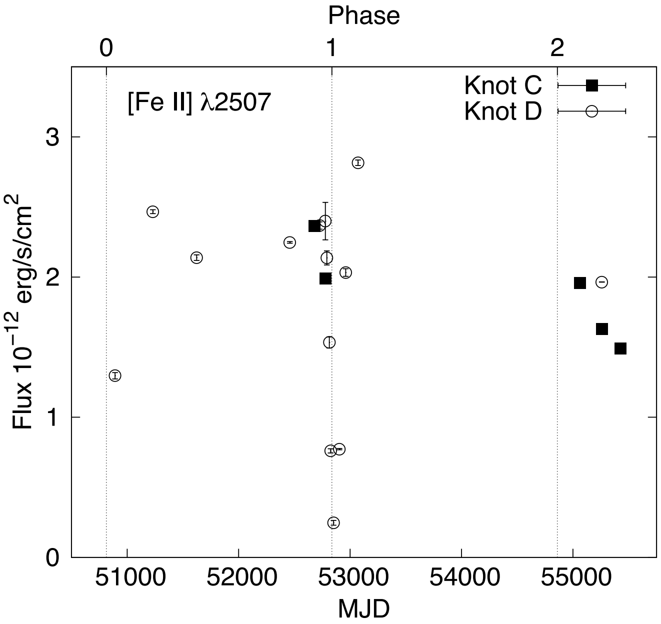

Figure 8.7: Flux of Fe II λ2507 at Weigelt knots C and D since 1998. Vertical dotted lines indicate the "events."

after 2009 focused on knot C, and (3) slit position angles vary by a few tenth of a degree and slight pointing errors occur. It is therefore difficult to assess if the observed decline in intensity after the 2009 "event" is significant. If so, it will be difficult to explain why those lines are decreasing. If the changes described in chapter 4 are due to a decreasing primary wind and Fe II $\lambda\lambda$2507,2509 were pumped directly by Lyα from the secondary star, the opposite would have been expected.

Chapter 9

Thoughts on the Secondary Star's Orbit

The identifications of periodic variations in the near-infrared by Whitelock et al. (1994) and Damineli (1996) gave strong support to the existence of a binary companion to η Car, moving in a highly eccentric orbit. The period of the η Car binary system is well determined; a 5.54-year periodicity can be observed in the X-ray, Radio, millimeter, IR and optical wavelength regions (e.g., Whitelock et al. 1994; Damineli 1996; Damineli et al. 2008b; Fernández-Lajús et al. 2010). Other orbital parameters are controversial because the stellar photospheres, from which orbital radial velocities are usually determined, are not visible.

The X-ray light curve of η Car gives the strongest argument for its binarity (Corcoran et al. 1995). The collision of massive stellar winds produces a substantial flux of soft X-rays from the shocked material in the wind-wind interaction region. Observed X-rays provide information about mass loss rate and wind velocity structure and can also be used to find orbital parameters. Most X-ray models of η Car find orbital parameters with inclinations close to $i = 45^\circ$ and an angle Φ with the semi-major axis of 0–30° on the side of apastron in prograde direction, i.e. an argument of periapsis $\omega = 243^\circ$ (Okazaki et al. 2008; Parkin et al. 2009). However, Ishibashi (2001) found that orbital parameters $i = 45^\circ$ and $\omega = 200^\circ$ fit the X-ray data well. All X-ray models strongly exclude a position of the secondary in front of η Car at periastron passage.

STIS and GMOS observations from 1998–2010 provide a long timeline to analyze

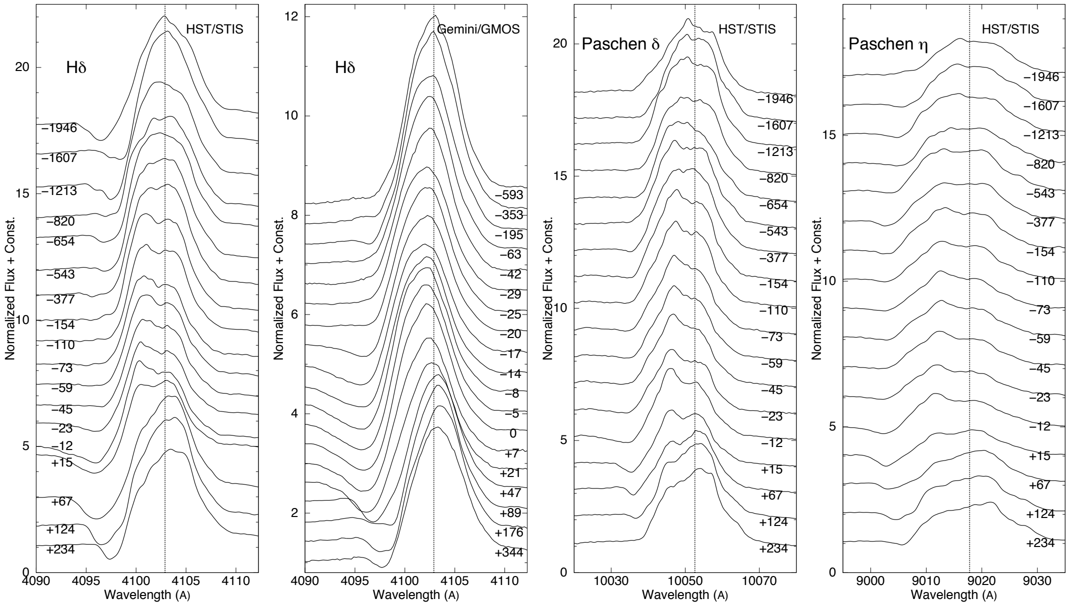

Figure 9.1: Hδ, Paschen δ, and Paschen η during "events" with *HST* STIS (2003.5) and *Gemini* GMOS (2009). Vertical lines correspond to the zero radial velocity. The broad emission profiles from the stellar wind did not show any shifts but developed a peak on the blue side during the 2003.5 "event."

the periodicity of emission and absorption lines such as of He II λ4687 and He I λ4714, see, e.g., Figures 5.5 and 5.4 for time sequences of several He I lines. Figures 9.1 and 9.2 show H I and Fe II in tracings of STIS observations during the 2003.5 "event" and GMOS observations during the 2009 "event." The broad wind profiles of hydrogen and Fe II emission features do not shift throughout the "events," though their emission profiles change considerable and a blue peak develops during the "events." Note the obvious similarities in the line profiles between Balmer and Paschen lines. Fe II line profiles are especially complex in the *HST* data, see Figure 9.2. The red side of the emission feature stayed basically unchanged over the cycle, but the blue side developed an additional bright emission component before the "events."

He I lines, however, behave similar to the He II λ4687 emission and shift towards bluer wavelengths during the "events," see section 5.1.1 and Figures 9.3 and 9.4. The Figures also show time sequences and measurements at FOS4 where a similar blueshift of the lines as in direct view can be observed. This has significant implications on any models concerning the origin of these lines and orbital models. In single stars, stellar

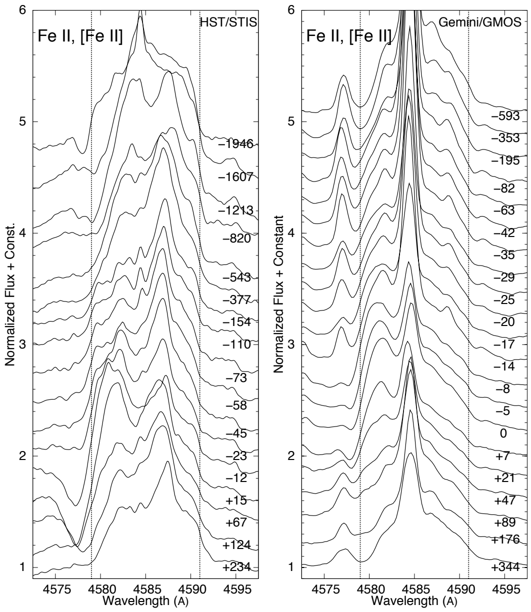

Figure 9.2: Broad stellar wind emission of Fe II, [Fe II] during "events" with *HST* STIS (2003.5) and *Gemini* GMOS (2009). The vertical lines indicate the extension of the broad emission profile in the blue and red.

wind He I emission is produced deep in the wind. However, if a hot secondary star exists, then some or even most of the emission could be attributed to ionization in the outer parts of the wind by the companion. Another possibility is that the He I lines originate in regions adjoining the wind-wind collision zone and Kashi & Soker 2008 assumed that the helium lines originate from the acceleration zone of the secondary wind.

It is thought that the He II emission observed in η Car during the "events" originates from shocked material in the wind-wind collision region (see, e.g., Martin et al. 2006a; Abraham & Falceta-Gonçalves 2007). Since the radial velocity and equivalent width of He I lines behave very similar to the He II emission, they probably form in adjoining regions.

Here, I assumed that the He II emission originates from the flow along the shock cone and I compared the observed radial velocities with velocities from a wind cone moving along different proposed orbits that are projected towards our line of sight or towards FOS4.

Abraham & Falceta-Gonçalves (2007), in similar work as described here, modeled the He II λ4687 line profiles observed close to the 2003.5 "event," assuming that the line

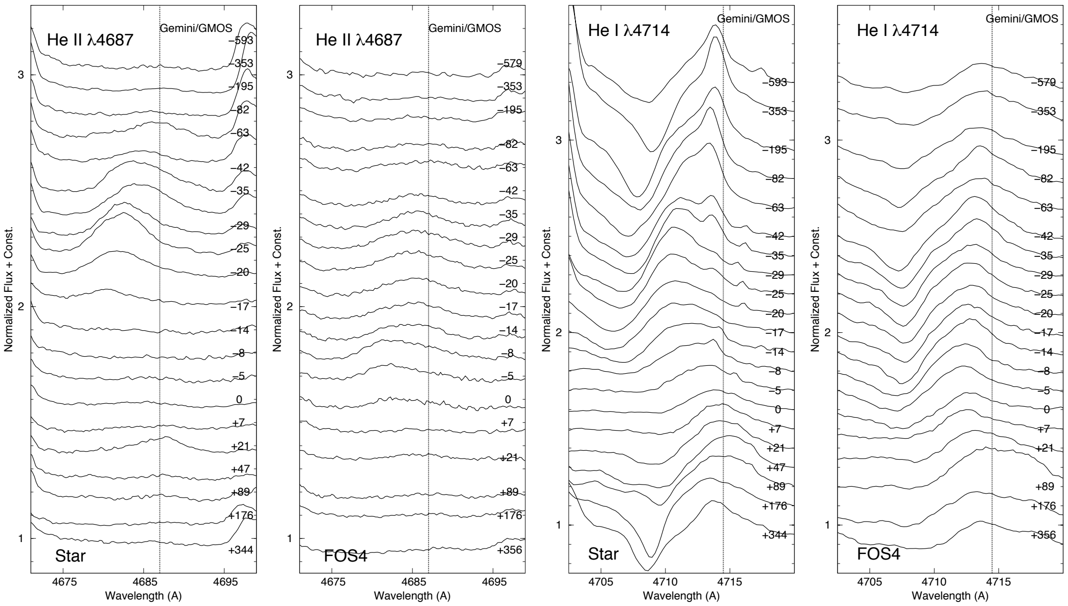

Figure 9.3: Time sequence of He II $\lambda4687$ and He I $\lambda4714$ during the 2009 "event" with *Gemini* GMOS. The vertical lines indicate zero radial velocity. Note that during most of the cycle He I is blueshifted. Outside the "events," a narrow emission line from the Weigelt knots can be observed.

was formed in the shocked gas that flows at both sides of the contact surface formed by the wind-wind collision. They introduced infinite opacity at the contact surface, so that only the side of the contact cone visible to the observer contributed to the line profile. They found that the line profiles fit best an orbit with $i = 90°$, $e = 0.95$, and an orientation of periastron at an angle $\Phi = 40°$ in prograde direction, i.e. an argument of periapsis $\omega = 130°$.

9.1 Lühr's Colliding Wind Model

The interaction of two colliding stellar winds gives rise to two oppositely faced shocks separated by a contact discontinuity. The location of the contact surface can be roughly determined by the condition that the wind momenta vectorially cancel. Since η Car's wind is much stronger, a cone-shaped bow shock region wraps around the secondary O star with the weaker wind. As material flows along the shock front, it cools and gives rise to line emission; (1) Near the vertex of the cone the temperature is above 10^7 K

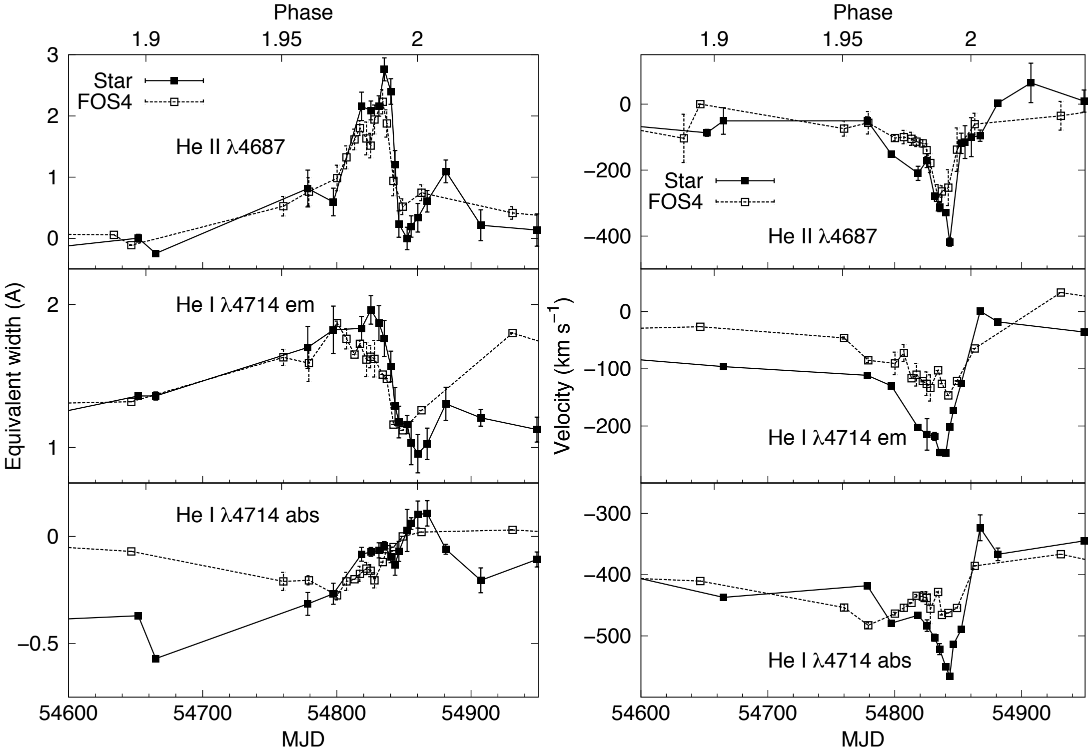

Figure 9.4: He II $\lambda4687$ and He I $\lambda4714$ emission and absorption on the star (filled squares) and at FOS4 (open squares) throughout the 2009 "event." The continuum for He I was set at $\lambda4605$ and $\lambda4744$ Å. The values at FOS4 are shifted by 18.2 days.

and the ionized gas is emitting mainly due to free-free transitions of electrons in the Coulomb fields of ions. (2) The adjacent region, where the gas is less heated, and the smaller impact angles of the winds reduce the collisional heating to $\sim 10^6$ K, the short cooling times support recombination. (3) In the outer regions of the wind cone where the temperatures are low and the impact angles are small, lower lines might be excited.

A full treatment here would be far too complex since complications such as radiation pressure from the two stars, whether or not the winds have reached terminal velocity, orbital motion, radiative cooling, etc. need to be considered. A limiting case, however, Lühr's simple geometrical model (Lührs 1997), already suffices to derive quantitative results which can be compared to the observations. Several assumptions were made to simplify the problem;

1. Neglect Shock Thickness

The approximation to neglect the thickness of the shock front compared with the separation D of the stars allows to neglect detailed consideration of the thermal and energetic conditions inside the shock. The mean free path l of particles in the interacting winds is normally very short. Consider the particle density $n = \dot{M}_{\eta \mathrm{Car}}(4\pi D^2 v_{\eta \mathrm{Car}}^2 m_{\mathrm{H}})^{-1}$ produced by η Car's wind at a typical distance D corresponding to the separation of the stars. With $l = (n\sigma)^{-1}$ and an averaged crossection σ for elastic collisions

$$\frac{l}{D} = \frac{5 \times 10^{-31}\ \mathrm{cm}^2}{\sigma} \frac{v_{\eta \mathrm{Car}}/1\ \mathrm{km\ s}^{-1}}{\dot{M}_{\eta \mathrm{Car}}/1\ M_{\odot}\ \mathrm{yr}^{-1}} (D/1\ \mathrm{AU})\ . \tag{9.1}$$

If the gas were neutral hydrogen, then $\sigma \approx 10^{-15}$ cm^2, and $l/D \approx 6 \times 10^{-10}...8 \times 10^{-9}$. The radiation of a companion star will, however, provide ionization, and then $\sigma \sim T^{-2} \sim 10^{-12}$ cm^2, reducing l/D to $\approx 6 \times 10^{-7}...8 \times 10^{-6}$. The interaction of the two winds will certainly produce a narrow shock front justifying the assumption.

2. Neglect Orbital Velocities

   Orbital rotation can only be neglected if v_{orb} is much smaller than the wind velocities. This can only be realized in very wide systems with small v_{orb}, or in systems, in which the components have winds of sufficiently large velocities. Maximum orbital velocity can be calculated using

$$v_{\mathrm{orb}} = \frac{2\pi a sini}{P(1-e^2)^{1/2}} [cos(\theta + \omega) + ecos\omega]\ . \tag{9.2}$$

   For $e = 0.85$ and $a = 16.6$ AU; $v_{\mathrm{orb,max}} \sim 314$ km s^{-1}. The approximation to neglect orbital motion is therefore not correct close to periastron passage (since $v_{\eta \mathrm{Car}} \approx 500$ km s^{-1}).

3. Neglect Coriolis Forces

   The axisymmetry of the cone model will be destroyed by the Coriolis force of the orbiting stellar system. Coriolis forces acting on the wind cone close to periastron passage cannot be neglected but can be approximately modeled by an angle θ_{C} between the axis through the centers of the two stars and the axis of the bow-shock region. This was not attempted here.

4. Terminal Velocities of Stellar Winds at the Shock Front

   For an O star the velocity of the matter outflow $v_{\mathrm{Ostar}}(r)$ at distance r from the center of the O star varies from almost zero on the O star surface, $r = R_{\mathrm{Ostar}}$, to $v^{\infty}_{\mathrm{Ostar}}$ for $r > r_{\mathrm{term}}$, where r_{term} is approximately equal to (3–5)$\times R_{\mathrm{Ostar}}$. Eta Car's companion star has $v^{\infty}_{\mathrm{Ostar}} \approx 3000$ km s^{-1}.

   - $r_{\mathrm{Ostar}} > r_{\mathrm{term}}$: Collision of winds with terminal velocities. This is a reasonable assumption during most of η Car's orbit (see next point).
   - $R_{\mathrm{Ostar}} < r_{\mathrm{Ostar}} < r_{\mathrm{term}}$: Gas does not reach the terminal velocity by the time it enters the shock. The radiation pressure of the O star is responsible for both the acceleration of the O star wind and the deceleration of η Car's wind. The variation of η Car's wind velocity along the line connecting the centers of η Car and its companion star can be written as

     $$v_{\eta\mathrm{Car}}(r) \approx [(v^{\infty}_{\eta\mathrm{Car}})^2 + (v_{\mathrm{Ostar}}(r))^2 - (v^{\infty}_{\mathrm{Ostar}})^2]^{1/2} \ , \tag{9.3}$$

     where r is the distance from the center of the O star. A realistic $v_{\mathrm{Ostar}}(r)$ distribution is

     $$v_{\mathrm{Ostar}}(r) \approx v^{\infty}_{\mathrm{Ostar}}(1 - \frac{R_{\mathrm{Ostar}}}{r})^{\mathrm{n}} \ , \tag{9.4}$$

     where $1/2 \leq n \leq 1$. The companion star has a stellar radius of $R_{\mathrm{Ostar}} \sim 13\ R_{\odot} = 0.06$ AU and r_{Ostar} at periastron passage is about 0.49 AU. It follows $v_{\mathrm{Ostar}}(0.49\ \mathrm{AU}) \approx v^{\infty}_{\mathrm{Ostar}}(0.88)^{\mathrm{n}}$. For $v^{\infty}_{\mathrm{Ostar}} = 3000$ km s^{-1} it follows that $v_{\mathrm{Ostar}}(0.49\ \mathrm{AU}) > 2630$ km s^{-1}. Most of the times the distance to the shock front is larger and one can therefore safely assume that the winds have reached their terminal velocities at the shock front. However, see section 5.1.2 and below; close to periastron passage the entire shock structure may collapse.
   - $r_{\mathrm{Ostar}} \leq R_{\mathrm{Ostar}}$: The wind of the O star is suppressed by the ram pressure of η Car's wind, on the side facing η Car. This scenario, i.e. collapse of the collision region onto the secondary star, was proposed by Soker (2005) during periastron passages.

Table 9.1: System parameters

Property	Value
$M_{\eta\mathrm{Car}}$	100 $M_\odot$
M_{Ostar}	50 $M_\odot$
$\dot{M}_{\eta\mathrm{Car}}$	10^{-3} $M_\odot$ yr^{-1}
$\dot{M}_{\mathrm{Ostar}}$	10^{-5} $M_\odot$ yr^{-1}
$\mathrm{v}^{\infty}_{\eta\mathrm{Car}}$	500 km s^{-1}
$\mathrm{v}^{\infty}_{\mathrm{Ostar}}$	3000 km s^{-1}
P	2023 days
e	0.85
a	16.6 AU

5. Neglect Instabilities

   Several instabilities are neglected. The contact discontinuity separating the shocked winds is subject to the *Kelvin-Helmholtz Instability* since there exists a velocity shear across the discontinuity because the two colliding winds have unequal wind velocity. In addition, one might expect *Thermal Instabilities* to be present when the cooling rate is rapid. When radiative cooling is rapid enough that a shell of cold, dense gas forms behind and parallel to the shock front, *Thin-Shell Instabilities* might occur.

6. Radially Symmetric Winds

   The model assumes that both stars have mass loss due to radially symmetric stellar winds. This is a crude simplification in η Car's case (Smith et al. 2003).

I used the system parameters listed in Table 9.1 in the calculations outlined below. Mass loss rate and velocity of the secondary star are estimates from X-ray and photoionization models (e.g. Pittard & Corcoran 2002; Mehner et al. 2010a). The period $P \approx 2023$ days of the companion's orbit in the η Car system is well observed (Whitelock et al. 1994; Damineli 1996; Damineli et al. 2008b; Fernández-Lajús et al. 2010). Commonly used values for the eccentricity range from $e = 0.8$–0.9. Here, I assume an eccentricity of $e = 0.85$. The period can be written as

$$P = \frac{2\pi a^{3/2}}{\sqrt{G(M_{\eta\mathrm{Car}} + M_{\mathrm{Ostar}})}} = 2023 \text{ d} . \tag{9.5}$$

Assuming $M_{\eta\mathrm{Car}} = 100\ M_\odot$ and $M_{\mathrm{Ostar}} = 50\ M_\odot$, the semimajor axis is $a = 16.6$ AU.

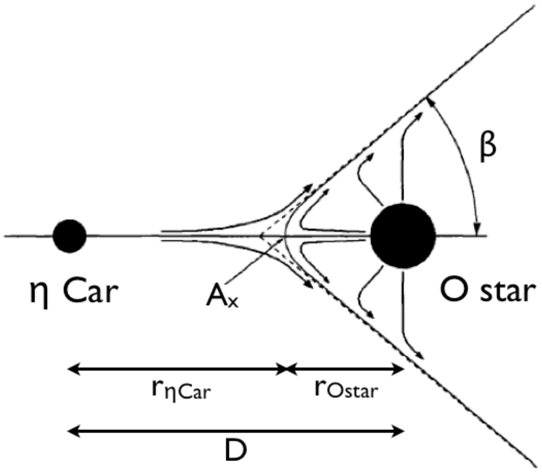

Figure 9.5: Schematic of colliding wind model, adapted from Lührs (1997).

The orbit equation for an elliptic orbit is

$$r = \frac{a(1-e^2)}{1+ecos\theta} \ , \tag{9.6}$$

with eccentricity e, semimajor axis a, and true anomaly θ, the angle between the direction of periastron passage and the current position of the body, as seen from the main focus of the ellipse. At periastron passage $r(\theta = 0) = a(1-e) = 2.5$ AU. At apastron passage $r(\theta = \pi) = a(1+e) = 30.7$ AU.

Figure 9.5 shows the simple geometric model adapted from Lührs (1997) used here; a fixed non-rotating coordinate system with the origin at the center of η Car, and the x-axis pointing towards the secondary star which is at a distance D. The approximation $v_{\rm orb} = 0$ km s^{-1} provides rotational symmetry about the x axis. Thus any arbitrary perpendicular direction for the y-axis can be chosen, and the geometry of the front needs to be described only in this x-y plane. The approximation to neglect the shock thickness means that all material is projected onto the surface.

When the stellar winds have unequal momentum flux, the contact discontinuity is a curved surface with the concave side facing the star with the weaker wind, here the companion star, labeled "O star." The wind cone with half-opening angle β is formed where the perpendicular components of the winds meet at equal dynamical pressures

$$\rho_{\eta\mathrm{Car}} v^2_{\eta\mathrm{Car}\perp} = \rho_{\mathrm{Ostar}} v^2_{\mathrm{Ostar}\perp} \ , \tag{9.7}$$

where $\rho_{\eta\mathrm{Car}}$ and ρ_{Ostar} are the densities of the gas near the shocks in the stellar winds of η Car and the secondary star. The geometrical structure of the shock front depends only on one parameter;

$$Q = \frac{\dot{M}_{\mathrm{Ostar}} v^{\infty}_{\mathrm{Ostar}}}{\dot{M}_{\eta\mathrm{Car}} v^{\infty}_{\eta\mathrm{Car}}} \ . \tag{9.8}$$

The apex, A_{x}, of the cone, i.e. the stagnation point of the winds, is located on the line which connects the centers of the two stars. The separation between the centers is D, and the distances from the centers to the apex A_{x} are $r_{\eta\mathrm{Car}}$ and r_{Ostar}, respectively;

$$D = r_{\eta\mathrm{Car}} + r_{\mathrm{Ostar}} \ , \tag{9.9}$$

$$r_{\eta\mathrm{Car}} = \frac{1}{1+Q^{1/2}} D \quad \text{and} \quad r_{\mathrm{Ostar}} = \frac{Q^{1/2}}{1+Q^{1/2}} D \ . \tag{9.10}$$

Figure 9.6 shows the orbit of the secondary star around η Car projected on the sky as favored by many authors (e.g. Okazaki et al. 2008; Parkin et al. 2009). The location of the apex of the shock front is shown and key observations of He II are indicated.

Usov (1995) derived a simple formula for estimating the half-opening angle β as a function of the momentum flux ratio Q. At intermediate distances from the O star the contact surface C approaches the conic surface with angle

$$\beta(^\circ) = 120(1 - \frac{Q^{2/5}}{4}) Q^{1/3} \quad \text{for} \quad 10^{-4} \le Q \le 1 \ . \tag{9.11}$$

Using parameters from Table 9.1, the momentum flux ratio $Q = 0.06$ and the half-opening angle $\beta = 43.17^\circ$.

Shocked material flows with constant velocity at both sides of the conic contact surface. When the wind density is high, radiative losses cool down the gas generating a range of temperatures and densities, favoring the production of turbulence. Lines can be formed and their profiles can be calculated from the projection of the flow velocity in the direction of the line of sight. Figure 9.7 illustrates the components of the wind

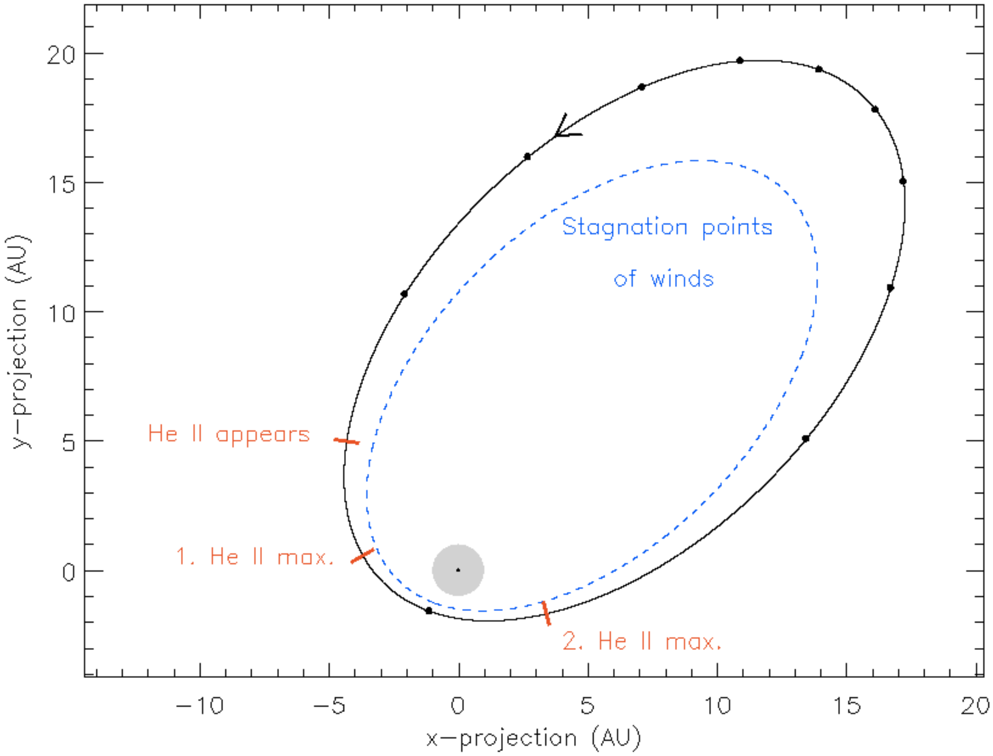

Figure 9.6: Orbit of secondary star projected on the sky. Parameters used are $a = 16.6$ AU, $e = 0.85$, $Q = 0.06$, $i = 45°$. Small filled circles along the orbit indicate phase steps of 0.1. The stagnation points of the winds are shown as a dashed blue curve. Key observations of the He II emission are indicated in red.

velocity $v_{\eta\mathrm{Car}}$ at point P and the projections onto the line of sight to the observer. The motion of η Car around the center of mass of the binary is described by the angle ϕ^* (obtained from the solution of Kepler's equation). When the opening of the wind cone points towards the observer, the emission peaks are at angle $\phi^* = 0°$ (uncorrected for Coriolis forces), ϕ^* increases when the secondary is moving away from us. The wind velocity in the line of sight to the observer can be calculated using

$$v_{\mathrm{obs}} = v_{\eta\mathrm{Car}}(-cos\beta cos\phi^* sini + sin\beta cos\alpha sin\phi^* sini - sin\beta sin\alpha cosi) \ . \tag{9.12}$$

With

$$\alpha^* = arctan(\frac{tan(90° - i)}{sin\phi^*}) \quad \text{and} \quad v^* = v_{\eta\mathrm{Car}} sin\beta\sqrt{1 - sin^2 icos^2\phi^*} \ , \tag{9.13}$$

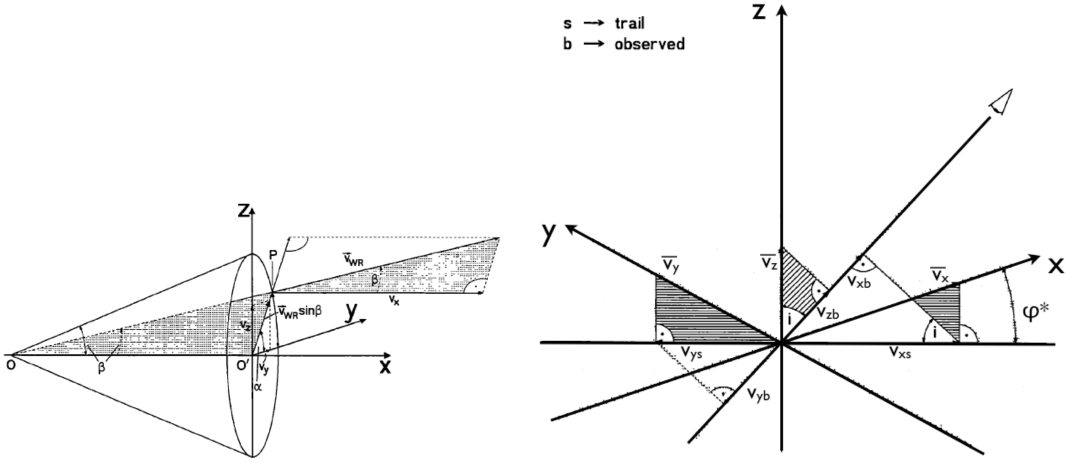

Figure 9.7: LEFT: Components of the wind velocity in the wind cone. RIGHT: Origin of the coordinate system which lies in the apex of the comoving cone. The x-axis corresponds to the axis of symmetry of the cone. The xyz components of the wind velocity in the bow-shock region are projected onto the line of sight of the observer, which is inclined to the z-axis by the angle i. Velocities $v_{\rm x}$ and $v_{\rm y}$ are first projected onto the traces of the components in the x-y plane and onto the line of sight. The z component is directly projected onto the line of sight. From Lührs (1997).

one obtaines

$$v_{\rm obs} = -v_{\eta {\rm Car}} cos\beta sin i cos\phi^* + v^* cos(\alpha + \alpha^*) \ . \tag{9.14}$$

Keeping $v_{\eta{\rm Car}}$, β, i, and ϕ^* constant, the first term represents a constant mean velocity $\bar{v}$,

$$\bar{v} = -v_{\eta {\rm Car}} cos\beta sin i cos\phi^* \ . \tag{9.15}$$

While α varies from 0° to 360°, $cos(\alpha + \alpha^*)$ varies between $+1$ and -1. Thus $v_{\rm obs}$ oscillates around $\bar{v}$, reaching two extreme radial velocities,

$$v_{\rm obs,red} = \bar{v} + v^* \quad \text{and} \quad v_{\rm obs,blue} = \bar{v} - v^* \ . \tag{9.16}$$

The difference $2v^* = v^{'}_{\rm red} - v^{'}_{\rm blue}$ is equal to the width of the peak profile.

Figures 9.8–9.9 show the projected velocities from a wind cone both in direct view and at FOS4 for half-opening angles $\beta = 45°$ and $\beta = 60°$ for orbit orientations favored by different authors (see Figure captions). Phases shown range from 0.8 to 1.2, close to the "event" at phase 1.0 when the largest velocity variations are observed. The

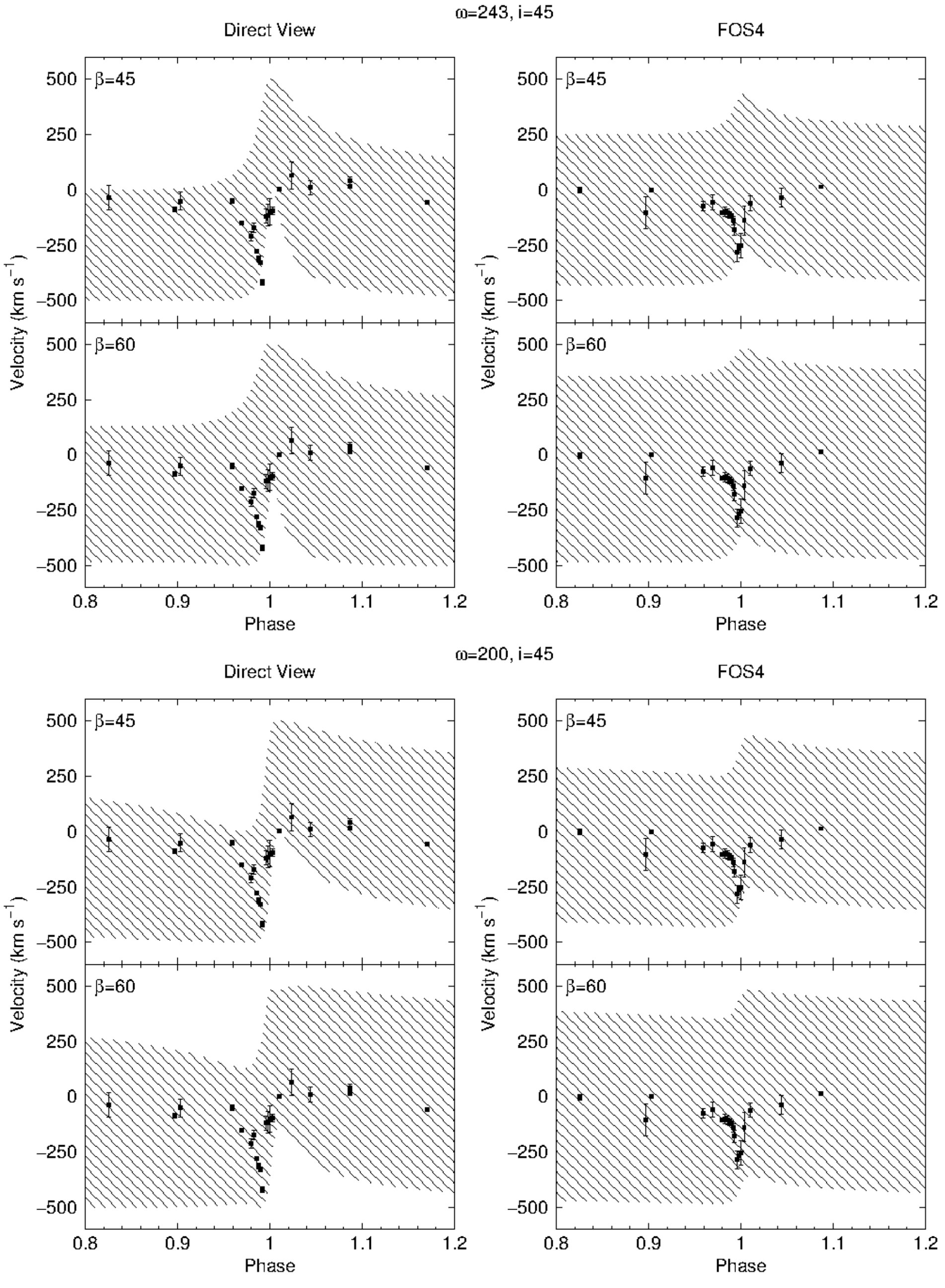

Figure 9.8: TOP: Projected velocities from a wind cone for an orbit orientation with i = 45°, ω = 243° and β = 45°, 60° favored by Okazaki et al. (2008). Overplotted are the radial velocity measurements of the He II emission line. Bottom: the same but for an orbit orientation favored by Ishibashi (2001) with $i = 45°$ and $\omega = 200°$.

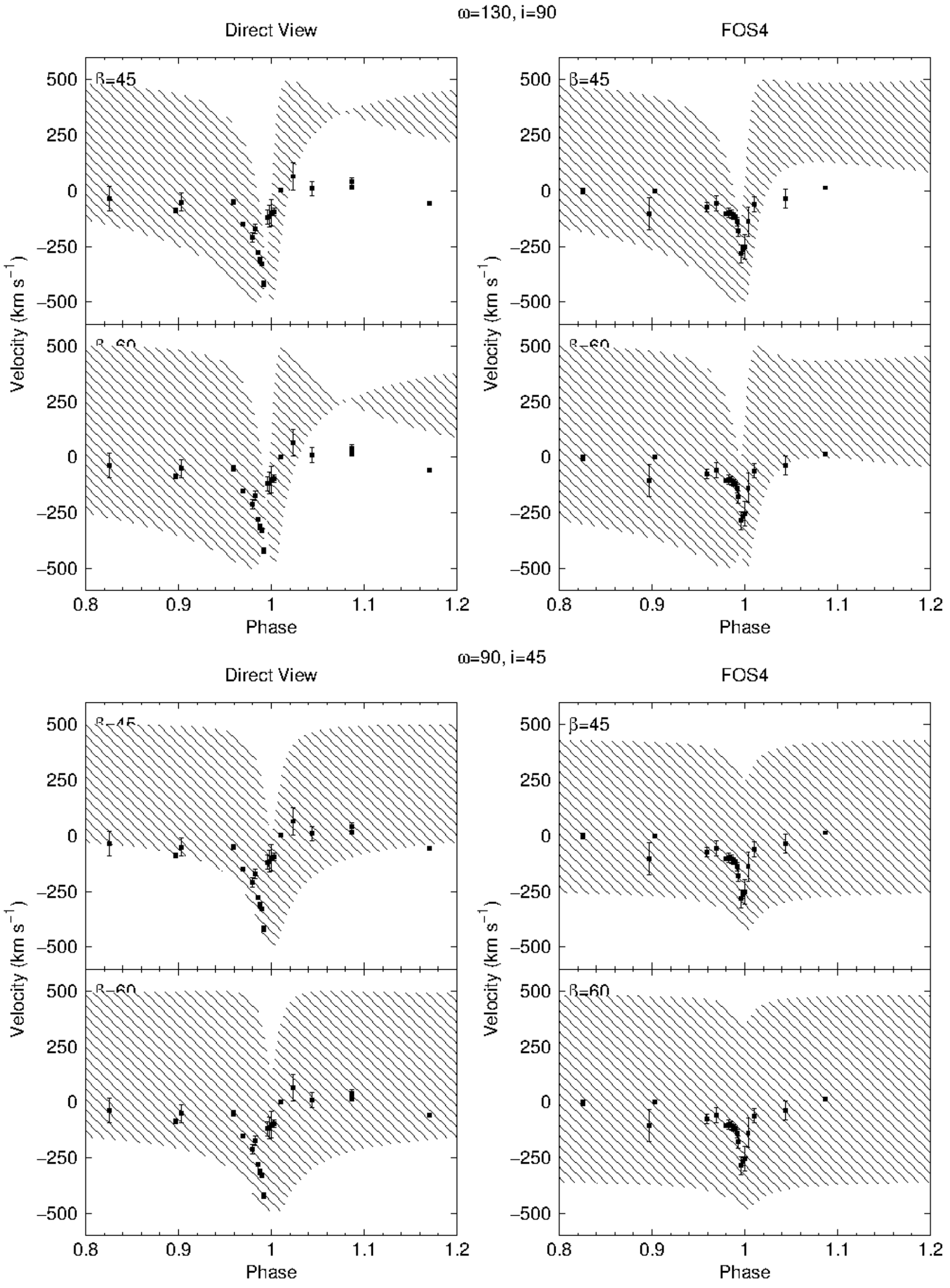

Figure 9.9: TOP: Projected velocities from a wind cone favored by Abraham & Falceta-Gonçalves (2007) with orbital parameters $i = 90°$ and $\omega = 130°$, see Figure 9.8. Bottom: Projected velocities from a wind cone in the model favored by Kashi & Soker (2008) with $i = 45°$ and $\omega = 90°$.

orientation of the orbital plane is described by the inclination i of the orbit plane and the argument of periapsis ω, the angle in the orbital plane from the ascending node to periastron. The gray areas indicate the parameter space of observable velocities from the moving wind cone (assuming no opacity) for both the direct view and FOS4. Overplotted are the radial velocities of the He II λ4687 emission line from those locations, described in detail in chapter 5.

In reality we would see mainly the side of the cone that is pointed towards us, i.e. its blue side. Orbit parameters favored by X-ray models fit the observed radial velocities the least. This might be evidence for a different He II emission region than adopted here or, for a different orbit orientation than favored by most X-ray models.

Chapter 10

Summary

I analyzed spectroscopic data of η Car to explore the variability and spatial distribution of the high-ionization lines and their implications on the nature of the secondary star. Observations, mostly with *HST* STIS, *Gemini* GMOS, and *VLT* UVES, covered more than ten years and therefore two spectroscopic cycles. Especially, close to the 2003.5 and the 2009 spectroscopic events many observations were obtained. This large data set made it possible to investigate cycle-to-cycle variations, differences in the last two "events," and long-term changes. Reflection spectra from the Homunculus were used to observe the star from different stellar latitudes.

Temporal and Spatial Behavior of High-excitation Emission. The behavior and the spatial origin of η Car's quasi-nebular high-excitation emission between spectroscopic events was not previously explored with adequate spatial and temporal sampling. Results presented here (and published in Mehner et al. 2010a) include maps of the emission, continuous evolution of the intensities through η Car's 5.54-year spectroscopic cycle, and a suggestive blueshifted component of each line. For instance, after the 1998 spectroscopic event the high-excitation features did not simply recover to constant "normal" intensities, but instead varied systematically throughout the 5.54-year cycle. Spatial maps of the [Ne III] and [Fe III] emission in the sub-arcsecond vicinity of η Car showed that high-excitation emission is strongly concentrated in the Weigelt knots BCD located at distances 0.15–0.35$''$ northwest of the star, rather than in a surrounding halo or in the region between the star and the knots as seemed possible before. Prior to this work most researchers would very likely have assumed that each knot produces high-excitation emission, but these maps are the first clear proof. Maps of the various ion species all show basically the same picture, except that those with higher ionization potentials seem a little more compact. The high-excitation lines all have broad extended emission features of which the blueshifted components in the velocity range -250 to -400 km s^{-1} are the most conspicuous. This fact was known before, but here it was shown that the blue component (1) originates mostly within $0.15''$ of the central star, and (2) the region is elongated along the equatorial (not polar) axis of the η Car system.

Parameters of the Secondary Star. Assuming that a hot companion star is responsible for the narrow high excitation emission lines from the Weigelt knots, constraints on its parameters were found based on photoionization calculations with Cloudy (Mehner et al. 2010a). The results are consistent with evolutionary considerations and, independently, with the colliding-wind X-ray temperature. The allowed region in parameter space (see Figure 3.13) is larger than some previous authors, e.g. Verner et al. (2005), suggested. For example, an O4–O6 giant with $L \sim 4 \times 10^5 \ L_\odot$, $T_{\rm eff} \approx 40,000$ K, and $M_{\rm ZAMS} \sim 40$–$50 \ M_\odot$ would fall near the center of the allowed range.

The 2009 Spectroscopic Event. The good time coverage of *Gemini* GMOS observations with identical slit position angle during the 2009 "event" made it possible to monitor spectroscopic changes from different directions. The peculiar He II λ4687 emission, which is only observed for a short time during the "events," was analyzed in spectra in the direct view and reflected at FOS4, which are representative of the more equatorial and more polar spectrum, respectively. The qualitative behavior of the He II equivalent width and radial velocity is very similar at both locations, however, with a time-delay of 18 days at FOS4. This time-delay is consistent with the expected additional time-travel time from geometrical considerations if the He II appearance were equal from both directions.[18] Any model explaining the He II has to account for this symmetry.

The energy budget for the He II emission is hard to account for because both stars emit few photons above 54 eV. It is therefore tempting to interpret the He II emission as originating from photoionization by associated soft X-ray or UV photons associated with

---

[18] Stahl et al. (2005) found a shorter time-delay, due to an inconsistent data set and poorer time coverage. This would have significant implications on any models explaining the He II emission because of the asymmetry.

the shock front of the colliding winds. It was noted before that the He II emission was anti-correlated with the X-rays and the fact that the He II emission peaked as the X-rays declined appeared to be consistent with a shock break up (Martin et al. 2006a). The 2009 "event" strengthened the case. The first strong peak in He II emission occurs when the X-rays drop into a minimum. The second smaller He II peak occurs shortly before the X-rays reappear. The correlation regarding the second peak in previous "events" is controversial since Teodoro et al. (2011) disagree with Steiner & Damineli (2004) on the timing. However, the anti-correlation between the He II emission and the X-rays is very evident during the 2009 "event" and supports a model where close to periastron the shock structure becomes unstable and disintegrates or collapses, briefly forming a complex ensemble of sub-shocks creating soft X-rays which lead to the observed He II emission. In this scenario the second He II peak can be explained with the formation of a large-scale shock structure. A collapse of the shock front not only explains the He II emission but also the length of the X-ray minimum which cannot be explained by a simple eclipse model.

The good time sampling of the GMOS data was also used to analyze the changing wind structure throughout the "event." Hydrogen lines behave as already discussed in Smith et al. (2003). Outside the 2009 "event" H I P Cygni absorption is observed at higher latitudes but not at lower, while during the "event" H I P Cygni absorption is also observed at lower latitudes. GMOS data show that the P Cygni absorption at lower latitudes appears within only a few days and is present for at least 70 days. He I P Cygni profiles show an additional episode not discussed in Smith et al. (2003), who found that outside the "events" He I P Cygni absorption is present at low latitudes but absent at higher latitudes, while during the "events" the absorption disappears at low latitudes, too. GMOS data show that shortly before the 2009 "event" He I absorption increases at higher latitudes to similar strength as at low latitudes. Then the absorption decreases slowly for about 2–3 months at all latitudes. Changes in the He I line profiles can be observed already 2 months before the H I lines show any changes and they return to their "normal" state up to 3 months later than the H I lines. Fe II absorption, only present at higher latitudes, becomes very strong during the 2009 "event" for several months.

N II λλ5668–5712. The source geometry of He I lines is complex and controversial.

Suggested regions are the primary wind, the shock zone, the acceleration zone of the secondary wind, or an accretion disk around the secondary star. However, most authors agree that the helium lines are strongly influenced by the hot secondary star. Since their radial velocity varies over the cycle they can potentially give us clues not only about their origin but also about the orbital parameters, which are still controversial. In the *Gemini* GMOS data I found broad emission and absorption lines of the N II series at $\lambda\lambda5668$–5712 Å, exhibiting radial velocity variations during the 2009 spectroscopic event similar to the helium lines (in press, Mehner et al. 2011). These lines are noteworthy because they depend on a form of excitation by the hot secondary star, but in different lower-ionization regions than the He I lines. The similar behavior of the N II and He I lines probably excludes some proposed models, such as those where He I lines originate in the secondary star's wind or in an accretion disk. The N II absorption features indicate material located between us and the inner parts of the primary wind. The absorbing material can probably not be part of the secondary wind since its wind densities are too low to account for the strong absorption and the nitrogen there is mainly N III. Most likely they arise in those parts of the primary wind that adjoin the He^+ zones, close to the wind-wind shocks. In summary, spectral features in η Car's wind can be assigned to these categories:

1. The "normal" lines of hydrogen, Fe II, etc. In principle these can be used to analyze the primary wind.

2. He I emission and absorption. Most authors agree that these are related in some way to the secondary star, but the details are controversial.

3. N II emission and absorption. These lines arise in normal-ionization parts of the primary wind, but they depend mainly on the proximity of the secondary star. In this sense they sample a new region of parameter space. It needs to be emphasized that the He I lines depend on photoionization, $h\nu > 24.6$ eV, whereas the N II lines depend on photoexcitation at $h\nu \sim 18.5$ eV. The ratio $f_\nu(> 25 \text{ eV})/f_\nu(18.5 \text{ eV})$ depends strongly on the secondary star's temperature.

4. He II $\lambda4687$. It depends on soft X-rays from the colliding-wind region, not UV from the secondary star.

Orbital Parameters. Orbital parameters are still very controversial. Several authors have attempted to model an orbit by fitting the observed radial velocities of He I and He II lines. Assuming that the observed He II λ4687 emission originates from the wind-wind collision zone, I calculated observable velocities from the wind cone when viewed in direct view and FOS4. In this scenario, the orbit favored by most X-ray models with $i = 45^\circ$ and $\omega = 243^\circ$ disagrees the most. The similarity of the He II emission in direct view and at FOS4 might suggest that the observed radial velocities are not orbital velocities. Most authors assume an orbit inclination of $i = 45^\circ$. In these models the view from FOS4 should be almost perpendicular to the plane of the orbit and no large velocity variations due to orbital motion should be observed there. Modeling of the He I lines which show similar velocity variations as the He II emission and most likely originate from the primary stellar wind (see chapter 7 and above) was not attempted here. Observed radial velocities are extremely difficult to understand in any orbit model, especially when additional information, e.g. implications from the X-ray light curve, is taken into account.

A Sea Change. About 15 years ago, η Car entered a phase of accelerated development with the central star showing a dramatic increase in brightness. The central star is now 3 times as bright as it was 10 years ago. The most obvious explanation is a decrease in the wind. But strangely no major changes in the broad stellar-wind emission lines were observed. However, recent observations starting in 2007–2010 with *Gemini* and *HST* in 2009 and 2010 reveal major spectral changes directly observed in the primary wind (Mehner et al. 2010b). The 2009–2010 data reveal the weakest broad-line wind spectrum ever seen in modern observations of this object, relative to the underlying continuum. The simplest explanation for these observed changes in the spectrum is a decrease in η Car's primary wind density. The mass loss rate may have gradually decreased by a factor of about 2–3 between 1999 and 2010. Spectra at the Weigelt knots and at FOS4 show smaller changes.

Future. Eta Car's behavior may provide spectroscopic opportunities not foreseen until recently. For instance, if the wind becomes semi-transparent, then the temperature and radius of the primary star may become observable for the first time. The luminous star will then photoionize the Homunculus nebula which will resemble a tremendously red super-planetary nebula. Moderate-sized instruments are valuable because *HST* and large telescopes will provide, at best, only sparse temporal sampling. Fortunately, ground-based observations now show the star itself more clearly than they did ten years ago, because the diffuse ejecta have not brightened as fast as the star. An obvious need is for instrumentally homogeneous series of spectra. Since the wind has characteristic size scales of several AU and velocities of several hundred km s^{-1}, changes may occur on timescales as short as a week.

Bibliography

Abraham, Z. & Falceta-Gonçalves, D. 2007, MNRAS, 378, 309

Aller, L. H. & Dunham, T. J. 1966, ApJ, 146, 126

Artigau, É., Martin, J. C., Humphreys, R. M., Davidson, K., Chesneau, O., & Smith, N. 2011, AJ, 141, 202

Beals, C. S. 1935, MNRAS, 95, 580

Castelli, F. & Kurucz, R. L. 2004, ArXiv Astrophysics e-prints

Corcoran, M. F. 2010, The RXTE X-ray Lightcurve of η Car (URL: http://asd.gsfc.nasa.gov/Michael.Corcoran/eta_rxte_lightcurve/index.html)

Corcoran, M. F., Hamaguchi, K., Pittard, J. M., Russell, C. M. P., Owocki, S. P., Parkin, E. R., & Okazaki, A. 2010, ApJ, 725, 1528

Corcoran, M. F., Ishibashi, K., Davidson, K., Swank, J. H., Petre, R., & Schmitt, J. H. M. M. 1997, Nature, 390, 587

Corcoran, M. F., Rawley, G. L., Swank, J. H., & Petre, R. 1995, ApJL, 445, L121

Damineli, A. 1996, ApJL, 460, L49

Damineli, A., Conti, P. S., & Lopes, D. F. 1997, New Astronomy, 2, 107

Damineli, A., Hillier, D. J., Corcoran, M. F., Stahl, O., Groh, J. H., Arias, J., Teodoro, M., Morrell, N., Gamen, R., Gonzalez, F., Leister, N. V., Levato, H., Levenhagen, R. S., Grosso, M., Colombo, J. F. A., & Wallerstein, G. 2008a, MNRAS, 386, 2330

Damineli, A., Hillier, D. J., Corcoran, M. F., Stahl, O., Levenhagen, R. S., Leister, N. V., Groh, J. H., Teodoro, M., Albacete Colombo, J. F., Gonzalez, F., Arias, J., Levato, H., Grosso, M., Morrell, N., Gamen, R., Wallerstein, G., & Niemela, V. 2008b, MNRAS, 384, 1649

Damineli, A., Kaufer, A., Wolf, B., Stahl, O., Lopes, D. F., & de Araújo, F. X. 2000, ApJL, 528, L101

Damineli, A., Stahl, O., Kaufer, A., Wolf, B., Quast, G., & Lopes, D. F. 1998, A&AS, 133, 299

Damineli, A., Stahl, O., Wolf, B., Kaufer, A., & Jablonski, F. J. 1999, in Astronomical Society of the Pacific Conference Series, Vol. 179, Eta Carinae at The Millennium, ed. J. A. Morse, R. M. Humphreys, & A. Damineli, 221

Davidson, K. 1987, in Astrophysics and Space Science Library, Vol. 136, Instabilities in Luminous Early Type Stars, ed. H. J. G. L. M. Lamers & C. W. H. de Loore, 127–135

Davidson, K. 1997, New Astronomy, 2, 387

Davidson, K. 1999, in ASP Conf. Ser., Vol. 179, Eta Carinae at The Millennium, ed. J. A. Morse, R. M. Humphreys, & A. Damineli, 304

Davidson, K. 2002, in ASP Conf. Ser., Vol. 262, The High Energy Universe at Sharp Focus: Chandra Science, ed. E. M. Schlegel & S. D. Vrtilek, 267

Davidson, K. 2005, in ASP Conf. Ser., Vol. 332, The Fate of the Most Massive Stars, ed. R. Humphreys & K. Stanek, 101

Davidson, K. 2006, in The 2005 HST Calibration Workshop: Hubble After the Transition to Two-Gyro Mode, ed. A. M. Koekemoer, P. Goudfrooij, & L. L. Dressel, 247

Davidson, K., Dufour, R. J., Walborn, N. R., & Gull, T. R. 1986, ApJ, 305, 867

Davidson, K., Ebbets, D., Johansson, S., Morse, J. A., & Hamann, F. W. 1997, AJ, 113, 335

Davidson, K., Ebbets, D., Weigelt, G., Humphreys, R. M., Hajian, A. R., Walborn, N. R., & Rosa, M. 1995, AJ, 109, 1784

Davidson, K., Gull, T. R., Humphreys, R. M., Ishibashi, K., Whitelock, P., Berdnikov, L., McGregor, P. J., Metcalfe, T. S., Polomski, E., & Hamuy, M. 1999a, AJ, 118, 1777

Davidson, K., Gull, T. R., & Ishibashi, K. 2001a, in ASP Conf. Ser., Vol. 233, P Cygni 2000: 400 Years of Progress, ed. M. de Groot & C. Sterken, 173

Davidson, K. & Humphreys, R. M. 1997, ARA&A, 35, 1

Davidson, K., Ishibashi, K., Gull, T. R., & Humphreys, R. M. 1999b, in Astronomical Society of the Pacific Conference Series, Vol. 179, Eta Carinae at The Millennium, ed. J. A. Morse, R. M. Humphreys, & A. Damineli, 227

Davidson, K., Ishibashi, K., Gull, T. R., Humphreys, R. M., & Smith, N. 2000, ApJL, 530, L107

Davidson, K., Martin, J., Humphreys, R. M., Ishibashi, K., Gull, T. R., Stahl, O., Weis, K., Hillier, D. J., Damineli, A., Corcoran, M., & Hamann, F. 2005, AJ, 129, 900

Davidson, K., Mehner, A., & Martin, J. C. 2009, IAU Circ., 9094, 1

Davidson, K. & Netzer, H. 1979, Reviews of Modern Physics, 51, 715

Davidson, K., Smith, N., Gull, T. R., Ishibashi, K., & Hillier, D. J. 2001b, AJ, 121, 1569

Dorland, B. N., Currie, D. G., & Hajian, A. R. 2004, AJ, 127, 1052

Dufour, R. J., Glover, T. W., Hester, J. J., Currie, D. G., van Orsow, D., & Walter, D. K. 1999, in ASP Conf. Ser., Vol. 179, Eta Carinae at The Millennium, ed. J. A. Morse, R. M. Humphreys, & A. Damineli, 134

Feast, M., Whitelock, P., & Marang, F. 2001, MNRAS, 322, 741

Ferland, G. J., Korista, K. T., Verner, D. A., Ferguson, J. W., Kingdon, J. B., & Verner, E. M. 1998, PASP, 110, 761

Fernández-Lajús, E., Fariña, C., Calderón, J. P., Salerno, N., Torres, A. F., Schwartz, M. A., von Essen, C., Giudici, F., & Bareilles, F. A. 2010, New Astronomy, 15, 108

Fernández-Lajús, E., Fariña, C., Torres, A. F., Schwartz, M. A., Salerno, N., Calderón, J. P., von Essen, C., Calcaferro, L. M., Giudici, F., Llinares, C., & Niemela, V. 2009, A&A, 493, 1093

Filippenko, A. V. 1982, PASP, 94, 715

Gaviola, E. 1953, ApJ, 118, 234

Goudfrooij, P., Wolfe, M. A., & Bohlin, R. C. 2009, Instrument Science Report STIS 2009-02

Gull, T. R. & Damineli, A. 2010, Highlights of Astronomy, 15, 373

Gull, T. R., Ishibashi, K., Davidson, K., & The Cycle 7 STIS Go Team. 1999, in

ASP Conf. Ser., Vol. 179, Eta Carinae at The Millennium, ed. J. A. Morse, R. M. Humphreys, & A. Damineli, 144

Gull, T. R., Johannson, S., & Davidson, K., eds. 2001, ASP Conf. Ser., Vol. 242, Eta Carinae and Other Mysterious Stars: The Hidden Opportunities of Emission Spectroscopy.

Gull, T. R., Nielsen, K. E., Corcoran, M. F., Madura, T. I., Owocki, S. P., Russell, C. M. P., Hillier, D. J., Hamaguchi, K., Kober, G. V., Weis, K., Stahl, O., & Okazaki, A. T. 2009, MNRAS, 396, 1308

Hamann, F., Davidson, K., Ishibashi, K., & Gull, T. R. 1999, in ASP Conf. Ser., Vol. 179, Eta Carinae at The Millennium, ed. J. A. Morse, R. M. Humphreys, & A. Damineli, 116

Hamann, F., Depoy, D. L., Johansson, S., & Elias, J. 1994, ApJ, 422, 626

Herald, J. E., Hillier, D. J., & Schulte-Ladbeck, R. E. 2001, ApJ, 548, 932

Hillier, D. J., Davidson, K., Ishibashi, K., & Gull, T. 2001, ApJ, 553, 837

Hillier, D. J., Gull, T., Nielsen, K., Sonneborn, G., Iping, R., Smith, N., Corcoran, M., Damineli, A., Hamann, F. W., Martin, J. C., & Weis, K. 2006, ApJ, 642, 1098

Hofmann, K.-H. & Weigelt, G. 1988, A&A, 203, L21

Humphreys, R. & Stanek, K., eds. 2005, ASP Conf. Ser., Vol. 332, The Fate of the Most Massive Stars

Humphreys, R. M., Davidson, K., & Koppelman, M. 2008, AJ, 135, 1249

Iben, Jr., I. 1999, in ASP Conf. Ser., Vol. 179, Eta Carinae at The Millennium, ed. J. A. Morse, R. M. Humphreys, & A. Damineli, 367

Ishibashi, K. 2001, in ASP Conf. Ser., Vol. 242, Eta Carinae and Other Mysterious Stars: The Hidden Opportunities of Emission Spectroscopy, ed. T. R. Gull, S. Johannson, & K. Davidson, 53

Ishibashi, K., Corcoran, M. F., Davidson, K., Swank, J. H., Petre, R., Drake, S. A., Damineli, A., & White, S. 1999a, ApJ, 524, 983

Ishibashi, K., Davidson, M. F., Corcoran, K., Drake, S. A., Swank, J. H., & Petre, R. 1999b, in ASP Conf. Ser., Vol. 179, Eta Carinae at The Millennium, ed. J. A. Morse, R. M. Humphreys, & A. Damineli, 266

Ishibashi, K., Gull, T. R., Davidson, K., Smith, N., Lanz, T., Lindler, D., Feggans, K., Verner, E., Woodgate, B. E., Kimble, R. A., Bowers, C. W., Kraemer, S., Heap, S. R., Danks, A. C., Maran, S. P., Joseph, C. L., Kaiser, M. E., Linsky, J. L., Roesler, F., & Weistrop, D. 2003, AJ, 125, 3222

Jenniskens, P. & Desert, F. 1994, A&AS, 106, 39

Johansson, S., Gull, T. R., Hartman, H., & Letokhov, V. S. 2005, A&A, 435, 183

Johansson, S. & Hamann, F. W. 1993, Physica Scripta Volume T, 47, 157

Johansson, S., Hartman, H., & Letokhov, V. S. 2006, A&A, 452, 253

Johansson, S. & Jordan, C. 1984, MNRAS, 210, 239

Johansson, S. & Letokhov, V. S. 2001, A&A, 378, 266

Johansson, S., Zethson, T., Hartman, H., Ekberg, J. O., Ishibashi, K., Davidson, K., & Gull, T. 2000, A&A, 361, 977

Kashi, A. & Soker, N. 2007, New Astronomy, 12, 590

—. 2008, MNRAS, 390, 1751

—. 2009a, ApJL, 701, L59

—. 2009b, NewA, 14, 11

—. 2009c, MNRAS, 394, 923

—. 2009d, MNRAS, 397, 1426

Kudritzki, R.-P. & Puls, J. 2000, ARA&A, 38, 613

Lamers, H. J. G. L. M. & Cassinelli, J. P. 1999, Introduction to Stellar Winds, ed. Lamers, H. J. G. L. M. & Cassinelli, J. P.

Lanz, T. & Hubeny, I. 2003, ApJS, 146, 417

Leitherer, C. 1988, ApJ, 326, 356

Lührs, S. 1997, PASP, 109, 504

Madura, T. I., Gull, T. R., Owocki, S. P., Okazaki, A. T., & Russell, C. M. P. 2011, Bulletin de la Societe Royale des Sciences de Liege, 80, 694

Maeder, A. & Desjacques, V. 2001, A&A, 372, L9

Maeder, A. & Meynet, G. 2000, A&A, 361, 159

Maeder, A., Meynet, G., & Hirschi, R. 2005, in Astronomical Society of the Pacific Conference Series, Vol. 332, The Fate of the Most Massive Stars, ed. R. Humphreys & K. Stanek, 3

Martin, J. C., Davidson, K., Humphreys, R. M., Hillier, D. J., & Ishibashi, K. 2006a, ApJ, 640, 474

Martin, J. C., Davidson, K., Humphreys, R. M., & Mehner, A. 2010, AJ, 139, 2056

Martin, J. C., Davidson, K., & Koppelman, M. D. 2006b, AJ, 132, 2717

Martin, J. C. & Koppelman, M. D. 2004, AJ, 127, 2352

Martins, F., Schaerer, D., & Hillier, D. J. 2005, A&A, 436, 1049

Meaburn, J., Wolstencroft, R. D., & Walsh, J. R. 1987, A&A, 181, 333

Mehner, A., Davidson, K., & Ferland, G. J. 2011, ArXiv e-prints

Mehner, A., Davidson, K., Ferland, G. J., & Humphreys, R. M. 2010a, ApJ, 710, 729

Mehner, A., Davidson, K., Humphreys, R. M., Martin, J. C., Ishibashi, K., Ferland, G. J., & Walborn, N. R. 2010b, ApJL, 717, L22

Morse, J. A., Humphreys, R. M., & Damineli, A., eds. 1999, ASP Conf. Ser., Vol. 179, Eta Carinae At The Millennium

Nahar, S. N. & Pradhan, A. K. 1996, A&AS, 119, 509

Najarro, F., Hillier, D. J., & Stahl, O. 1997, A&A, 326, 1117

Nielsen, K. E., Corcoran, M. F., Gull, T. R., Hillier, D. J., Hamaguchi, K., Ivarsson, S., & Lindler, D. J. 2007, ApJ, 660, 669

Nielsen, K. E., Kober, G. V., Weis, K., Gull, T. R., Stahl, O., & Bomans, D. J. 2009, VizieR Online Data Catalog, 218, 10473

Okazaki, A. T., Owocki, S. P., Russell, C. M. P., & Corcoran, M. F. 2008, MNRAS, 388, L39

Osterbrock, D. E. & Ferland, G. J. 2006, Astrophysics of gaseous nebulae and active galactic nuclei, ed. D. E. Osterbrock & G. J. Ferland (University Science Books)

Owocki, S. 2005, in Astronomical Society of the Pacific Conference Series, Vol. 332, The

Fate of the Most Massive Stars, ed. R. Humphreys & K. Stanek, 169

Parkin, E. R., Pittard, J. M., Corcoran, M. F., Hamaguchi, K., & Stevens, I. R. 2009, MNRAS, 394, 1758

Pauldrach, A. W. A., Hoffmann, T. L., & Lennon, M. 2001, A&A, 375, 161

Pittard, J. M. & Corcoran, M. F. 2002, A&A, 383, 636

Quinet, P. 1996, A&AS, 116, 573

Richardson, N. D., Gies, D. R., Henry, T. J., Fernández-Lajús, E., & Okazaki, A. T. 2010, AJ, 139, 1534

Ruiz, M. T., Melnick, J., & Ortiz, P. 1984, ApJL, 285, L19

Schaerer, D. & de Koter, A. 1997, A&A, 322, 598

Smith, L. J., Norris, R. P. F., & Crowther, P. A. 2002, MNRAS, 337, 1309

Smith, N. 2004, MNRAS, 351, L15

—. 2006, ApJ, 644, 1151

—. 2008, Nature, 455, 201

Smith, N., Davidson, K., Gull, T. R., Ishibashi, K., & Hillier, D. J. 2003, ApJ, 586, 432

Smith, N., Morse, J. A., Gull, T. R., Hillier, D. J., Gehrz, R. D., Walborn, N. R., Bautista, M., Collins, N. R., Corcoran, M. F., Damineli, A., Hamann, F., Hartman, H., Johansson, S., Stahl, O., & Weis, K. 2004, ApJ, 605, 405

Soker, N. 2003, ApJ, 597, 513

—. 2005, ApJ, 635, 540

—. 2007, ApJ, 661, 490

Soker, N. & Behar, E. 2006, ApJ, 652, 1563

Stahl, O., Weis, K., Bomans, D. J., Davidson, K., Gull, T. R., & Humphreys, R. M. 2005, A&A, 435, 303

Steiner, J. E. & Damineli, A. 2004, ApJL, 612, L133

Stevens, I. R., Blondin, J. M., & Pollock, A. M. T. 1992, ApJ, 386, 265

Stevens, I. R. & Kallman, T. R. 1990, ApJ, 365, 321

Stevens, I. R. & Pittard, J. M. 1999, in ASP Conf. Ser., Vol. 179, Eta Carinae at The Millennium, ed. J. A. Morse, R. M. Humphreys, & A. Damineli, 295

Struve, O. 1935, ApJ, 81, 66

Swings, P. & Struve, O. 1940, ApJ, 91, 546

Teodoro, M., Damineli, A., Arias, J. I., de Araújo, F. X., Barbá, R. H., Corcoran, M. F., Borges Fernandes, M., Fernández-Lajús, E., Fraga, L., Gamen, R. C., González, J. F., Groh, J. H., Marshall, J. L., McGregor, P. J., Morrell, N., Nicholls, D. C., Parkin, E. R., Pereira, C. B., Phillips, M. M., Solivella, G. R., Steiner, J. E., Stritzinger, M., Thompson, I., Torres, C. A. O., Torres, M. A. P., & Zevallos-Herencia, M. I. 2011, ArXiv e-prints

Thackeray, A. D. 1953, MNRAS, 113, 211

—. 1967, MNRAS, 135, 51

Usov, V. V. 1995, in IAU Symposium, Vol. 163, Wolf-Rayet Stars: Binaries; Colliding Winds; Evolution, ed. K. A. van der Hucht & P. M. Williams, 495

Verner, E., Bruhweiler, F., & Gull, T. 2005, ApJ, 624, 973

Verner, E. M., Gull, T. R., Bruhweiler, F., Johansson, S., Ishibashi, K., & Davidson, K. 2002, ApJ, 581, 1154

Viotti, R., Rossi, L., Cassatella, A., Altamore, A., & Baratta, G. B. 1989, ApJS, 71, 983

Walborn, N. R. 1995, in Rev. Mexicana Astron. Astrofis.Conference Series, Vol. 2, Rev. Mexicana Astron. Astrofis.Conference Series, ed. V. Niemela, N. Morrell, & A. Feinstein, 51

Weigelt, G., Albrecht, R., Barbieri, C., Blades, J. C., Boksenberg, A., Crane, P., Davidson, K., Deharveng, J. M., Disney, M. J., Jakobsen, P., Kamperman, T. M., King, I. R., Macchetto, F., Mackay, C. D., Paresce, F., Baxter, D., Greenfield, P., Jedrzejewski, R., Nota, A., & Sparks, W. B. 1995, in Rev. Mexicana Astron. Astrofis.Conference Series, Vol. 2, Rev. Mexicana Astron. Astrofis.Conference Series, ed. V. Niemela, N. Morrell, & A. Feinstein, 11

Weigelt, G. & Ebersberger, J. 1986, A&A, 163, L5

Weigelt, G., Kraus, S., Driebe, T., Petrov, R. G., Hofmann, K.-H., Millour, F., Chesneau, O., Schertl, D., Malbet, F., Hillier, J. D., Gull, T., Davidson, K., Domiciano de Souza, A., Antonelli, P., Beckmann, U., Bresson, Y., Chelli, A., Dugué, M., Duvert, G., Gennari, S., Glück, L., Kern, P., Lagarde, S., Le Coarer, E., Lisi, F., Perraut, K., Puget, P., Rantakyrö, F., Robbe-Dubois, S., Roussel, A., Tatulli, E., Zins, G., Accardo, M., Acke, B., Agabi, K., Altariba, E., Arezki, B., Aristidi, E., Baffa, C., Behrend, J., Blöcker, T., Bonhomme, S., Busoni, S., Cassaing, F., Clausse, J.-M., Colin, J., Connot, C., Delboulbé, A., Feautrier, P., Ferruzzi, D., Forveille, T., Fossat, E., Foy, R., Fraix-Burnet, D., Gallardo, A., Giani, E., Gil, C., Glentzlin, A., Heiden, M., Heininger, M., Hernandez Utrera, O., Kamm, D., Kiekebusch, M., Le Contel, D., Le Contel, J.-M., Lesourd, T., Lopez, B., Lopez, M., Magnard, Y., Marconi, A., Mars, G., Martinot-Lagarde, G., Mathias, P., Mège, P., Monin, J.-L., Mouillet, D., Mourard, D., Nussbaum, E., Ohnaka, K., Pacheco, J., Perrier, C., Rabbia, Y., Rebattu, S., Reynaud, F., Richichi, A., Robini, A., Sacchettini, M., Schöller, M., Solscheid, W., Spang, A., Stee, P., Stefanini, P., Tallon, M., Tallon-Bosc, I., Tasso, D., Testi, L., Vakili, F., von der Lühe, O., Valtier, J.-C., Vannier, M., Ventura, N., Weis, K., & Wittkowski, M. 2007, A&A, 464, 87

Weis, K., Stahl, O., Bomans, D. J., Davidson, K., Gull, T. R., & Humphreys, R. M. 2005, AJ, 129, 1694

Whitelock, P. A., Feast, M. W., Carter, B. S., Roberts, G., & Glass, I. S. 1983, MNRAS, 203, 385

Whitelock, P. A., Feast, M. W., Koen, C., Roberts, G., & Carter, B. S. 1994, MNRAS, 270, 364

Whitelock, P. A., Feast, M. W., Marang, F., & Breedt, E. 2004, MNRAS, 352, 447

Zanella, R., Wolf, B., & Stahl, O. 1984, A&A, 137, 79

Zethson, T. 2001, PhD thesis, AA(LUNDS UNIVERSITET (SWEDEN))

Zethson, T., Johansson, S., Davidson, K., Humphreys, R. M., Ishibashi, K., & Ebbets, D. 1999, A&A, 344, 211

Appendix A

Journal of *Gemini* GMOS observations

Table A.1: Journal of *Gemini* GMOS observations

Name[a]	Root [tgs...]	MJD	Phase	Cenwav (Å)	P$_{\rm Intend}$[b] (″)	PA[c] (	Airmass	P$_{\rm Actual}$[d] (″)
gH45_0010	S20070616S0045	54267.06	1.7069	4300	0.00	74.95	1.440	0.260
gH45_0020	S20070616S0046	54267.06	1.7069	4300	0.00	75.54	1.450	0.270
gH45_0030	S20070616S0047	54267.06	1.7069	4300	0.75	76.15	1.460	1.029
gH45_0040	S20070616S0048	54267.07	1.7069	4300	0.75	76.75	1.470	1.039
gH45_0050	S20070616S0049	54267.07	1.7069	4300	-0.75	77.62	1.480	-0.453
gH45_0060	S20070616S0050	54267.07	1.7069	4300	-0.75	78.21	1.490	-0.444
gH45_0070	S20070618S0011	54268.97	1.7078	4300	0.00	36.96	1.190	0.235
gH45_0080	S20070618S0012	54268.97	1.7078	4300	0.00	37.84	1.200	0.252
gH45_0090	S20070618S0013	54268.97	1.7078	4300	0.75	38.76	1.200	1.006
gH45_0100	S20070618S0014	54268.97	1.7078	4300	0.75	39.65	1.200	0.996
gH45_0110	S20070618S0015	54268.98	1.7078	4300	-0.75	40.95	1.210	-0.471
gH45_0120	S20070618S0016	54268.98	1.7078	4300	-0.75	41.81	1.210	-0.468
gH49_0010	S20070630S0026	54280.95	1.7138	6500	0.00	45.80	1.220	0.024
gH49_0020	S20070630S0027	54280.95	1.7138	6500	0.75	46.71	1.230	0.774
gH49_0030	S20070630S0028	54280.96	1.7138	6500	0.75	47.60	1.230	0.774
gH49_0040	S20070630S0029	54280.96	1.7138	6500	0.75	48.61	1.240	0.774
gH49_0050	S20070630S0030	54280.96	1.7138	6500	-0.75	51.11	1.250	-0.726
gH49_0060	S20070630S0031	54280.97	1.7138	6500	-0.75	51.98	1.250	-0.726
gH49_0070	S20070630S0032	54280.97	1.7138	6500	-0.75	52.94	1.260	-0.726
gH49_0080	S20070630S0033	54280.97	1.7138	6500	-2.00	55.32	1.270	-1.976
gH49_0090	S20070630S0034	54280.98	1.7138	6500	-2.00	56.14	1.280	-1.976
gH49_0100	S20070630S0035	54280.98	1.7138	6500	0.00	57.83	1.280	0.024

Continued on Next Page. . .

Table A.1 – Continued

Name^a	Root [tgs...]	MJD	Phase	Cenwav (Å)	P^b_{Intend} (″)	PA^c (	Airmass	P^d_{Actual} (″)
gH49_0110	S20070630S0040	54280.99	1.7138	5600	0.00	63.00	1.320	0.192
gH49_0120	S20070630S0041	54280.99	1.7138	5600	0.75	63.75	1.330	0.945
gH49_0130	S20070630S0042	54281.00	1.7138	5600	0.75	64.49	1.330	0.946
gH49_0140	S20070630S0043	54281.00	1.7138	5600	0.75	65.32	1.350	0.952
gH49_0150	S20070630S0044	54281.00	1.7138	5600	-0.75	67.39	1.360	-0.545
gH49_0160	S20070630S0045	54281.00	1.7138	5600	-0.75	68.10	1.370	-0.542
gH49_0170	S20070630S0046	54281.01	1.7138	5600	-0.75	68.89	1.380	-0.539
gH49_0180	S20070630S0047	54281.01	1.7138	5600	-2.00	70.88	1.400	-1.783
gH49_0190	S20070630S0048	54281.01	1.7138	5600	-2.00	71.61	1.410	-1.781
gH49_0200	S20070630S0049	54281.02	1.7138	7950	0.00	73.21	1.420	-0.174
gH52_0010	S20070711S0027	54291.96	1.7192	6500	0.00	63.75	1.330	0.018
gH52_0020	S20070711S0028	54291.97	1.7192	6500	0.40	65.41	1.340	0.418
gH52_0030	S20070711S0029	54291.97	1.7192	6500	0.70	67.09	1.360	0.718
gI11_0010	gS20080211S0087	54507.38	1.8257	4300	0.00	65.51	1.340	-0.518
gI11_0020	gS20080211S0088	54507.38	1.8257	4300	0.00	66.20	1.350	-0.484
gI11_0030	gS20080211S0091	54507.39	1.8257	4300	0.75	68.94	1.370	0.290
gI11_0040	gS20080211S0092	54507.39	1.8257	4300	0.75	69.63	1.380	0.278
gI11_0050	gS20080211S0093	54507.39	1.8257	4300	-0.75	70.61	1.390	-1.188
gI11_0060	gS20080211S0094	54507.39	1.8257	4300	-0.75	71.29	1.400	-1.177
gI11_0070	gS20080211S0095	54507.40	1.8257	4300	-2.00	72.27	1.420	-2.431
gI11_0080	gS20080213S0112	54509.13	1.8266	6500	0.00	-64.19	1.330	0.031
gI11_0090	gS20080213S0115	54509.13	1.8266	6500	0.75	-61.68	1.310	0.781
gI11_0100	gS20080213S0116	54509.14	1.8266	6500	0.75	-60.93	1.300	0.781
gI11_0110	gS20080213S0117	54509.14	1.8266	6500	0.75	-60.12	1.290	0.781
gI11_0120	gS20080213S0118	54509.14	1.8266	6500	-0.75	-59.22	1.290	-0.719
gI11_0130	gS20080213S0119	54509.14	1.8266	6500	-0.75	-58.46	1.280	-0.719
gI11_0140	gS20080213S0120	54509.14	1.8266	6500	-0.75	-57.65	1.280	-0.719
gI11_0150	gS20080213S0121	54509.15	1.8266	6500	-2.00	-56.73	1.270	-1.969
gI11_0160	gS20080213S0122	54509.15	1.8266	6500	-2.00	-55.91	1.270	-1.969
gI11_0170	gS20080213S0123	54509.15	1.8266	6500	-2.00	-54.83	1.260	-1.969
gI11_0180	gS20080213S0124	54509.15	1.8266	5600	0.00	-53.16	1.250	-0.050
gI11_0190	gS20080213S0127	54509.16	1.8266	5600	0.75	-49.44	1.240	0.710
gI11_0200	gS20080213S0128	54509.16	1.8266	5600	0.75	-48.57	1.230	0.705
gI11_0210	gS20080213S0129	54509.17	1.8266	5600	0.75	-47.58	1.230	0.708
gI11_0220	gS20080213S0130	54509.17	1.8266	5600	-0.75	-45.86	1.220	-0.779
gI11_0230	gS20080213S0131	54509.17	1.8266	5600	-0.75	-44.94	1.220	-0.777
gI11_0240	gS20080213S0132	54509.17	1.8266	5600	-0.75	-43.89	1.210	-0.773
gI11_0250	gS20080213S0133	54509.18	1.8266	5600	-2.00	-42.10	1.210	-2.019
gI11_0260	gS20080213S0134	54509.18	1.8266	5600	-2.00	-40.85	1.200	-2.015
gI11_0270	gS20080213S0135	54509.19	1.8266	6500	0.00	-37.94	1.190	0.031
gI11_0280	gS20080213S0136	54509.19	1.8266	6500	0.00	-37.01	1.190	0.031
gI11_0290	gS20080213S0137	54509.19	1.8266	6500	0.00	-36.07	1.190	0.031

Continued on Next Page...

Table A.1 – Continued

Name^a	Root [tgs...]	MJD	Phase	Cenwav (Å)	P$^b_{\text{Intend}}$ ($''$)	PA^c (	Airmass	P$^d_{\text{Actual}}$ ($''$)
gI41_0010	gS20080601S0007	54618.03	1.8804	6500	0.30	44.50	1.220	0.312
gI41_0020	gS20080601S0008	54618.03	1.8804	6500	0.70	45.40	1.220	0.712
gI41_0030	gS20080601S0009	54618.03	1.8804	6500	0.90	46.29	1.230	0.912
gI42_0010	gS20080603S0024	54619.96	1.8813	6500	0.30	10.69	1.150	0.304
gI42_0020	gS20080603S0025	54619.96	1.8813	6500	0.70	11.79	1.150	0.704
gI42_0030	gS20080603S0026	54619.97	1.8813	6500	0.90	12.89	1.150	0.904
gI50_0010	gS20080705S0033	54651.96	1.8972	6500	0.00	57.93	1.280	0.033
gI50_0020	gS20080705S0036	54651.97	1.8972	6500	0.75	61.31	1.310	0.783
gI50_0030	gS20080705S0037	54651.97	1.8972	6500	0.75	62.03	1.310	0.783
gI50_0040	gS20080705S0038	54651.98	1.8972	6500	0.75	62.82	1.320	0.783
gI50_0050	gS20080705S0039	54651.98	1.8972	6500	-0.75	63.70	1.330	-0.717
gI50_0060	gS20080705S0040	54651.98	1.8972	6500	-0.75	64.40	1.330	-0.717
gI50_0070	gS20080705S0041	54651.98	1.8972	6500	-0.75	65.16	1.340	-0.717
gI50_0080	gS20080705S0042	54651.98	1.8972	6500	-2.00	66.02	1.350	-1.967
gI50_0090	gS20080705S0043	54651.99	1.8972	6500	-2.00	66.72	1.350	-1.967
gI50_0100	gS20080705S0044	54651.99	1.8972	6500	-2.00	67.66	1.360	-1.967
gI50_0110	gS20080705S0045	54651.99	1.8972	5600	0.00	69.08	1.380	0.220
gI50_0120	gS20080705S0048	54652.00	1.8972	5600	0.75	72.08	1.410	0.978
gI50_0130	gS20080705S0049	54652.00	1.8972	5600	0.75	72.75	1.420	0.981
gI50_0140	gS20080705S0050	54652.00	1.8972	5600	0.75	73.51	1.430	0.984
gI50_0150	gS20080705S0051	54652.01	1.8972	5600	-0.75	74.78	1.440	-0.514
gI50_0160	gS20080705S0052	54652.01	1.8972	5600	-0.75	75.45	1.450	-0.511
gI50_0170	gS20080705S0053	54652.01	1.8972	5600	-0.75	76.19	1.460	-0.483
gI50_0180	gS20080705S0054	54652.01	1.8972	5600	-2.00	77.44	1.480	-1.728
gI50_0190	gS20080705S0055	54652.02	1.8972	5600	-2.00	78.28	1.490	-1.752
gI50_0200	gS20080705S0057	54652.03	1.8972	6500	2.02	81.81	1.540	2.052
gI50_0210	gS20080705S0058	54652.03	1.8972	6500	1.72	83.00	1.560	1.752
gI50_0220	gS20080705S0059	54652.03	1.8972	6500	1.42	84.13	1.590	1.452
gI50_0230	gS20080705S0064	54652.05	1.8972	6500	-0.91	87.99	1.670	-0.879
gI50_0240	gS20080705S0065	54652.05	1.8972	6500	-0.61	88.85	1.690	-0.579
gI50_0250	gS20080705S0066	54652.05	1.8972	6500	-0.31	89.42	1.700	-0.279
gI54_0010	gS20080718S0068	54664.99	1.9036	4300	0.00	80.24	1.520	0.314
gI54_0020	gS20080718S0069	54664.99	1.9036	4300	0.00	80.84	1.530	0.322
gI54_0030	gS20080718S0072	54665.00	1.9036	4300	0.75	83.21	1.570	1.103
gI54_0040	gS20080718S0073	54665.00	1.9036	4300	0.75	83.81	1.580	1.110
gI54_0050	gS20080718S0074	54664.00	1.9031	4300	-0.75	84.67	1.600	-0.374
gI54_0060	gS20080718S0075	54665.00	1.9036	4300	-0.75	85.25	1.610	-0.367
gI54_0070	gS20080718S0076	54665.00	1.9036	4300	-2.00	86.10	1.640	-1.593
gI85_0010	gS20081108S0070	54778.28	1.9596	6500	-0.42	-78.49	2.050	-0.343
gI85_0020	gS20081108S0073	54778.29	1.9596	6500	0.33	-80.20	1.990	0.407
gI85_0030	gS20081108S0074	54778.29	1.9596	6500	0.33	-80.67	1.970	0.407
gI85_0040	gS20081108S0075	54778.29	1.9596	6500	0.33	-81.19	1.950	0.407

Continued on Next Page. . .

Table A.1 – Continued

Name^a	Root	MJD	Phase	Cenwav	P$^b_{\text{Intend}}$	PA^c	Airmass	P$^d_{\text{Actual}}$
	[tgs...]			(Å)	(″)	(		(″)
gI85_0050	gS20081108S0076	54778.29	1.9596	6500	-1.17	-81.78	1.930	-1.093
gI85_0060	gS20081108S0077	54778.29	1.9596	6500	-1.17	-82.25	1.920	-1.093
gI85_0070	gS20081108S0078	54778.29	1.9596	6500	-1.17	-82.78	1.900	-1.093
gI85_0080	gS20081108S0079	54778.30	1.9596	6500	-2.42	-83.37	1.880	-2.343
gI85_0090	gS20081108S0080	54778.30	1.9596	6500	-2.42	-83.86	1.860	-2.343
gI85_0100	gS20081108S0081	54778.30	1.9596	6500	-2.42	-84.54	1.840	-2.343
gI85_0110	gS20081108S0082	54778.30	1.9596	5200	-0.42	-85.62	1.810	-0.816
gI85_0120	gS20081108S0085	54778.31	1.9596	5200	0.33	-87.69	1.760	-0.021
gI85_0130	gS20081108S0086	54778.31	1.9596	5200	0.33	-88.22	1.740	-0.016
gI85_0140	gS20081108S0087	54778.31	1.9596	5200	0.33	-88.81	1.720	-0.010
gI85_0150	gS20081108S0088	54778.32	1.9596	5200	-1.17	-89.86	1.700	-1.506
gI85_0160	gS20081108S0089	54778.32	1.9596	5200	-1.17	-89.60	1.690	-1.501
gI85_0170	gS20081108S0090	54778.32	1.9596	5200	-1.17	-89.00	1.670	-1.492
gI85_0180	gS20081108S0091	54778.32	1.9596	5200	-2.42	-87.93	1.650	-2.732
gI85_0190	gS20081108S0092	54778.33	1.9596	5200	-2.42	-87.21	1.630	-2.722
gI85_0200	gS20081108S0093	54778.33	1.9596	4300	-0.42	-85.88	1.610	-1.221
gI85_0210	gS20081108S0096	54778.34	1.9596	4300	0.33	-83.59	1.570	-0.419
gI85_0220	gS20081108S0097	54778.34	1.9596	4300	0.33	-83.04	1.550	-0.398
gI85_0230	gS20081108S0098	54778.34	1.9596	4300	-1.17	-82.22	1.540	-1.883
gI85_0240	gS20081108S0099	54778.34	1.9596	4300	-1.17	-81.67	1.530	-1.870
gI85_0250	gS20081108S0100	54778.35	1.9596	4300	-2.42	-80.84	1.510	-3.096
gI85_0260	gS20081108S0101	54778.35	1.9596	6500	-0.42	-78.49	1.480	-0.343
gI85_0270	gS20081108S0102	54778.35	1.9596	6500	-0.42	-77.92	1.480	-0.343
gI85_0280	gS20081108S0103	54778.36	1.9596	6500	-0.12	-77.34	1.470	-0.043
gI85_0290	gS20081109S0030	54779.30	1.9601	6500	-0.42	-85.27	1.820	-0.350
gI85_0300	gS20081109S0031	54779.30	1.9601	6500	0.78	-85.77	1.810	0.850
gI85_0310	gS20081109S0032	54779.30	1.9601	6500	1.38	-86.28	1.800	1.450
gI90_0010	gS20081127S0073	54797.28	1.9690	6500	-0.42	-86.96	1.630	-0.359
gI90_0020	gS20081127S0074	54797.28	1.9690	6500	-0.42	-86.45	1.620	-0.359
gI90_0030	gS20081127S0077	54797.28	1.9690	6500	0.33	-84.57	1.580	0.391
gI90_0040	gS20081127S0078	54797.28	1.9690	6500	0.33	-84.05	1.570	0.391
gI90_0050	gS20081127S0079	54797.29	1.9690	6500	0.33	-83.47	1.560	0.391
gI90_0060	gS20081127S0080	54797.29	1.9690	6500	-1.17	-82.82	1.550	-1.109
gI90_0070	gS20081127S0081	54797.29	1.9690	6500	-1.17	-82.29	1.540	-1.109
gI90_0080	gS20081127S0082	54797.29	1.9690	6500	-1.17	-81.70	1.530	-1.109
gI90_0090	gS20081127S0083	54797.29	1.9690	6500	-2.42	-81.03	1.520	-2.359
gI90_0100	gS20081127S0084	54797.30	1.9690	6500	-2.42	-80.48	1.510	-2.359
gI90_0110	gS20081127S0085	54797.30	1.9690	6500	-2.42	-79.71	1.500	-2.359
gI90_0120	gS20081127S0086	54797.30	1.9690	5200	-0.42	-78.49	1.480	-0.656
gI90_0130	gS20081127S0089	54797.31	1.9690	5200	0.33	-76.12	1.450	0.112
gI90_0140	gS20081127S0090	54797.31	1.9690	5200	0.33	-75.52	1.440	0.118
gI90_0150	gS20081127S0091	54797.31	1.9690	5200	0.33	-74.83	1.430	0.124

Continued on Next Page. . .

Table A.1 – Continued

Name^a	Root [tgs...]	MJD	Phase	Cenwav (Å)	$P^b_{\rm Intend}$ (″)	PA^c (	Airmass	$P^d_{\rm Actual}$ (″)
gI90_0160	gS20081127S0092	54797.31	1.9690	5200	-1.17	-73.61	1.420	-1.368
gI90_0170	gS20081127S0093	54797.32	1.9690	5200	-1.17	-72.99	1.410	-1.382
gI90_0180	gS20081127S0094	54797.32	1.9690	5200	-1.17	-72.29	1.400	-1.357
gI90_0190	gS20081127S0095	54797.32	1.9690	5200	-2.42	-71.03	1.390	-2.599
gI90_0200	gS20081127S0096	54797.32	1.9690	5200	-2.42	-70.18	1.380	-2.610
gI90_0210	gS20081127S0097	54797.33	1.9690	4300	-0.42	-68.61	1.360	-0.886
gI90_0220	gS20081127S0100	54797.34	1.9690	4300	0.33	-65.85	1.340	-0.097
gI90_0230	gS20081127S0101	54797.34	1.9690	4300	0.33	-65.19	1.330	-0.068
gI90_0240	gS20081127S0102	54797.34	1.9690	4300	-1.17	-64.20	1.330	-1.575
gI90_0250	gS20081127S0103	54797.34	1.9690	4300	-1.17	-63.53	1.320	-1.561
gI90_0260	gS20081127S0104	54797.34	1.9690	4300	-2.42	-62.53	1.310	-2.795
gI90_0270	gS20081127S0105	54797.35	1.9690	6500	-0.42	-59.37	1.290	-0.359
gI90_0280	gS20081127S0106	54797.35	1.9690	6500	-0.72	-58.66	1.280	-0.659
gI90_0290	gS20081127S0107	54797.35	1.9690	6500	-1.02	-57.95	1.280	-0.959
gI90_0300	gS20081127S0108	54797.36	1.9690	6500	-1.32	-57.22	1.280	-1.259
gI96_0010	gS20081218S0182	54818.29	1.9794	6500	-0.42	-62.96	1.310	-0.390
gI96_0020	gS20081218S0183	54818.29	1.9794	6500	-0.42	-61.50	1.300	-0.390
gI96_0030	gS20081218S0186	54818.29	1.9794	6500	0.33	-59.05	1.290	0.360
gI96_0040	gS20081218S0187	54818.30	1.9794	6500	0.33	-58.37	1.280	0.360
gI96_0050	gS20081218S0188	54818.30	1.9794	6500	0.33	-57.61	1.280	0.360
gI96_0060	gS20081218S0189	54818.30	1.9794	6500	-1.17	-56.73	1.270	-1.140
gI96_0070	gS20081218S0190	54818.30	1.9794	6500	-1.17	-56.03	1.270	-1.140
gI96_0080	gS20081218S0191	54818.30	1.9794	6500	-1.17	-55.25	1.260	-1.140
gI96_0090	gS20081218S0192	54818.31	1.9794	6500	-2.42	-54.36	1.260	-2.390
gI96_0100	gS20081218S0193	54818.31	1.9794	6500	-2.42	-53.63	1.250	-2.390
gI96_0110	gS20081218S0194	54818.31	1.9794	6500	-2.42	-52.60	1.250	-2.390
gI96_0120	gS20081218S0195	54818.31	1.9794	5200	-0.42	-50.95	1.240	-0.520
gI96_0130	gS20081218S0196	54818.31	1.9794	5200	-0.42	-50.20	1.240	-0.517
gI96_0140	gS20081218S0199	54818.32	1.9794	5200	0.33	-46.95	1.220	0.259
gI96_0150	gS20081218S0200	54818.32	1.9794	5200	0.33	-46.12	1.220	0.254
gI96_0160	gS20081218S0201	54818.32	1.9794	5200	0.33	-45.17	1.220	0.258
gI96_0170	gS20081218S0202	54818.33	1.9794	5200	-1.17	-43.47	1.210	-1.233
gI96_0180	gS20081218S0203	54818.33	1.9794	5200	-1.17	-42.61	1.210	-1.224
gI96_0190	gS20081218S0204	54818.33	1.9794	5200	-1.17	-41.62	1.200	-1.218
gI96_0200	gS20081218S0205	54818.34	1.9794	5200	-2.42	-39.87	1.200	-2.468
gI96_0210	gS20081218S0206	54818.34	1.9794	5200	-2.42	-38.67	1.190	-2.456
gI96_0220	gS20081218S0207	54818.34	1.9794	4300	-0.42	-36.47	1.190	-0.529
gI96_0230	gS20081218S0210	54818.35	1.9794	4300	0.33	-32.62	1.180	0.256
gI96_0240	gS20081218S0211	54818.35	1.9794	4300	0.33	-31.69	1.180	0.263
gI96_0250	gS20081218S0212	54818.35	1.9794	4300	-1.17	-30.30	1.180	-1.225
gI96_0260	gS20081218S0213	54818.35	1.9794	4300	-1.17	-29.36	1.170	-1.215
gI96_0270	gS20081218S0214	54818.36	1.9794	4300	-2.42	-27.95	1.170	-2.454

Continued on Next Page...

Table A.1 – Continued

Name[a]	Root [tgs...]	MJD	Phase	Cenwav (Å)	$\mathrm{P}^{b}_{\mathrm{Intend}}$ ($''$)	PA[c] (	Airmass	$\mathrm{P}^{d}_{\mathrm{Actual}}$ ($''$)
gI96_0280	gS20081218S0215	54818.36	1.9794	6500	-0.42	-24.06	1.160	-0.390
gI96_0290	gS20081218S0216	54818.37	1.9794	6500	-0.72	-23.08	1.160	-0.690
gI96_0300	gS20081218S0217	54818.37	1.9794	6500	-1.02	-22.09	1.160	-0.990
gI98_0010	gS20081225S0046	54825.29	1.9828	6500	-0.42	-52.46	1.250	-0.409
gI98_0020	gS20081225S0047	54825.29	1.9828	6500	-0.42	-51.74	1.250	-0.409
gI98_0030	gS20081225S0048	54825.29	1.9828	6500	-0.42	-50.99	1.240	-0.409
gI98_0040	gS20081225S0049	54825.30	1.9828	6500	-0.42	-50.25	1.240	-0.409
gI98_0050	gS20081225S0052	54825.30	1.9828	6500	0.33	-47.47	1.230	0.341
gI98_0060	gS20081225S0053	54825.30	1.9828	6500	0.33	-46.69	1.220	0.341
gI98_0070	gS20081225S0054	54825.30	1.9828	6500	0.33	-45.83	1.220	0.341
gI98_0080	gS20081225S0055	54825.31	1.9829	6500	-1.17	-44.83	1.220	-1.159
gI98_0090	gS20081225S0056	54825.31	1.9829	6500	-1.17	-44.03	1.210	-1.159
gI98_0100	gS20081225S0057	54825.31	1.9829	6500	-1.17	-43.16	1.210	-1.159
gI98_0110	gS20081225S0058	54825.31	1.9829	6500	-2.42	-42.14	1.210	-2.409
gI98_0120	gS20081225S0059	54825.31	1.9829	6500	-2.42	-41.31	1.200	-2.409
gI98_0130	gS20081225S0060	54825.32	1.9829	6500	-2.42	-40.13	1.200	-2.409
gI98_0140	gS20081225S0061	54825.32	1.9829	5200	-0.42	-38.26	1.190	-0.479
gI98_0150	gS20081225S0062	54825.32	1.9829	5200	-0.42	-37.41	1.190	-0.471
gI98_0160	gS20081225S0065	54825.33	1.9829	5200	0.33	-33.72	1.180	0.290
gI98_0170	gS20081225S0066	54825.33	1.9829	5200	0.33	-32.77	1.180	0.293
gI98_0180	gS20081225S0067	54825.33	1.9829	5200	0.33	-31.69	1.180	0.297
gI98_0190	gS20081225S0068	54825.34	1.9829	5200	-1.17	-28.55	1.170	-1.188
gI98_0200	gS20081225S0069	54825.34	1.9829	5200	-1.17	-27.58	1.170	-1.185
gI98_0210	gS20081225S0070	54825.34	1.9829	5200	-1.17	-26.45	1.170	-1.182
gI98_0220	gS20081225S0071	54825.34	1.9829	5200	-2.42	-24.47	1.160	-2.424
gI98_0230	gS20081225S0072	54825.35	1.9829	5200	-2.42	-23.13	1.160	-2.419
gI98_0240	gS20081225S0073	54825.35	1.9829	4300	-0.42	-20.65	1.160	-0.414
gI98_0250	gS20081225S0074	54825.35	1.9829	4300	-0.42	-19.68	1.160	-0.406
gI98_0260	gS20081225S0077	54825.36	1.9829	4300	0.33	-15.40	1.150	0.376
gI98_0270	gS20081225S0078	54825.36	1.9829	4300	0.33	-14.37	1.150	0.382
gI98_0280	gS20081225S0079	54825.36	1.9829	4300	-1.17	-12.84	1.150	-1.105
gI98_0290	gS20081225S0080	54825.36	1.9829	4300	-1.17	-11.80	1.150	-1.099
gI98_0300	gS20081225S0081	54825.37	1.9829	4300	-2.42	-10.26	1.150	-2.338
gI98_0310	gS20081225S0082	54825.37	1.9829	6930	-0.42	-6.85	1.150	-0.419
gI98_0320	gS20081225S0083	54825.37	1.9829	6930	-0.42	-5.41	1.150	-0.420
gI98_0330	gS20081225S0084	54825.38	1.9829	6930	-0.42	-3.05	1.150	-0.417
gI98_0340	gS20081225S0085	54825.38	1.9829	6930	-0.42	-1.60	1.150	-0.422
gI98_0350	gS20081225S0086	54825.38	1.9829	6930	-0.42	0.78	1.150	-0.424
gI98_0360	gS20081225S0087	54825.39	1.9829	6930	-0.42	2.25	1.150	-0.425
gI99_0010	gS20081231S0050	54831.28	1.9858	6500	-0.42	-47.76	1.230	-0.401
gI99_0020	gS20081231S0051	54831.29	1.9858	6500	-0.42	-46.48	1.220	-0.401
gI99_0030	gS20081231S0052	54831.29	1.9858	6500	-0.42	-45.70	1.220	-0.401

Continued on Next Page. . .

Table A.1 – Continued

Name^a	Root [tgs...]	MJD	Phase	Cenwav (Å)	P$^b_{\mathrm{Intend}}$ (″)	PA^c (	Airmass	P$^d_{\mathrm{Actual}}$ (″)
gI99_0040	gS20081231S0053	54831.29	1.9858	6500	-0.42	-44.90	1.220	-0.401
gI99_0050	gS20081231S0056	54831.30	1.9858	6500	0.33	-41.96	1.210	0.349
gI99_0060	gS20081231S0057	54831.30	1.9858	6500	0.33	-39.92	1.200	0.349
gI99_0070	gS20081231S0058	54831.30	1.9858	6500	0.33	-39.01	1.200	0.349
gI99_0080	gS20081231S0059	54831.30	1.9858	6500	-1.17	-37.95	1.190	-1.151
gI99_0090	gS20081231S0060	54831.30	1.9858	6500	-1.17	-37.10	1.190	-1.151
gI99_0100	gS20081231S0061	54831.31	1.9858	6500	-1.17	-36.16	1.190	-1.151
gI99_0110	gS20081231S0062	54831.31	1.9858	6500	-2.42	-35.08	1.190	-2.401
gI99_0120	gS20081231S0063	54831.31	1.9858	6500	-2.42	-34.19	1.180	-2.401
gI99_0130	gS20081231S0064	54831.31	1.9858	6500	-2.42	-32.94	1.180	-2.401
gI99_0140	gS20081231S0065	54831.32	1.9858	5200	-0.42	-30.94	1.180	-0.439
gI99_0150	gS20081231S0066	54831.32	1.9858	5200	-0.42	-30.04	1.170	-0.435
gI99_0160	gS20081231S0069	54831.32	1.9858	5200	0.33	-26.12	1.170	0.328
gI99_0170	gS20081231S0070	54831.33	1.9858	5200	0.33	-25.14	1.170	0.332
gI99_0180	gS20081231S0071	54831.33	1.9858	5200	0.33	-24.00	1.160	0.336
gI99_0190	gS20081231S0072	54831.33	1.9858	5200	-1.17	-21.99	1.160	-1.158
gI99_0200	gS20081231S0073	54831.33	1.9858	5200	-1.17	-20.97	1.160	-1.154
gI99_0210	gS20081231S0074	54831.34	1.9858	5200	-1.17	-19.81	1.160	-1.150
gI99_0220	gS20081231S0075	54831.34	1.9858	5200	-2.42	-17.75	1.160	-2.394
gI99_0230	gS20081231S0076	54831.34	1.9858	5200	-2.42	-14.70	1.150	-2.384
gI99_0240	gS20081231S0077	54831.35	1.9858	4300	-0.42	-12.13	1.150	-0.342
gI99_0250	gS20081231S0078	54831.35	1.9858	4300	-0.42	-11.11	1.150	-0.334
gI99_0260	gS20081231S0081	54831.36	1.9858	4300	0.33	-6.70	1.150	0.449
gI99_0270	gS20081231S0082	54831.36	1.9858	4300	0.33	-5.66	1.150	0.456
gI99_0280	gS20081231S0083	54831.36	1.9858	4300	-1.17	-4.10	1.150	-1.036
gI99_0290	gS20081231S0084	54831.36	1.9858	4300	-1.17	-2.12	1.150	-1.018
gI99_0300	gS20081231S0086	54831.37	1.9858	6920	-0.42	1.34	1.150	-0.416
gI99_0310	gS20081231S0087	54831.38	1.9859	6920	-0.42	5.91	1.150	-0.413
gI99_0320	gS20081231S0088	54831.38	1.9859	6920	-0.42	7.35	1.150	-0.420
gI99_0330	gS20081231S0089	54831.38	1.9859	6920	-0.42	9.70	1.150	-0.422
gI99_0340	gS20081231S0090	54831.38	1.9859	6920	-0.42	11.13	1.150	-0.423
gJ01_0010	gS20090104S0060	54835.26	1.9878	6500	-0.42	-53.43	1.250	-0.397
gJ01_0020	gS20090104S0061	54835.26	1.9878	6500	-0.42	-52.71	1.250	-0.397
gJ01_0030	gS20090104S0062	54835.26	1.9878	6500	-0.42	-51.98	1.250	-0.397
gJ01_0040	gS20090104S0063	54835.27	1.9878	6500	-0.42	-51.23	1.240	-0.397
gJ01_0050	gS20090104S0066	54835.27	1.9878	6500	0.33	-48.47	1.230	0.353
gJ01_0060	gS20090104S0067	54835.27	1.9878	6500	0.33	-47.71	1.230	0.353
gJ01_0070	gS20090104S0068	54835.27	1.9878	6500	-1.17	-46.81	1.220	-1.147
gJ01_0080	gS20090104S0069	54835.28	1.9878	6500	-1.17	-46.03	1.220	-1.147
gJ01_0090	gS20090104S0070	54835.28	1.9878	6500	-1.17	-45.17	1.220	-1.147
gJ01_0100	gS20090104S0071	54835.28	1.9878	6500	-2.42	-44.16	1.210	-2.397
gJ01_0110	gS20090104S0072	54835.28	1.9878	6500	-2.42	-43.35	1.210	-2.397

Continued on Next Page. . .

Table A.1 – Continued

Name^a	Root [tgs...]	MJD	Phase	Cenwav (Å)	P$^b_{\text{Intend}}$ (″)	PA^c (	Airmass	P$^d_{\text{Actual}}$ (″)
gJ01_0120	gS20090104S0073	54835.28	1.9878	6500	-2.42	-42.19	1.210	-2.397
gJ01_0130	gS20090104S0074	54835.29	1.9878	5200	-0.42	-40.26	1.200	-0.470
gJ01_0140	gS20090104S0075	54835.29	1.9878	5200	-0.42	-39.42	1.200	-0.467
gJ01_0150	gS20090104S0078	54835.30	1.9878	5200	0.33	-35.78	1.190	0.297
gJ01_0160	gS20090104S0079	54835.30	1.9878	5200	0.33	-34.89	1.190	0.300
gJ01_0170	gS20090104S0080	54835.30	1.9878	5200	0.33	-33.96	1.180	0.305
gJ01_0180	gS20090104S0081	54835.30	1.9878	5200	-1.17	-32.85	1.180	-1.192
gJ01_0190	gS20090104S0082	54835.30	1.9878	5200	-1.17	-31.90	1.180	-1.188
gJ01_0200	gS20090104S0083	54835.31	1.9878	5200	-1.17	-30.82	1.180	-1.187
gJ01_0210	gS20090104S0084	54835.31	1.9878	5200	-2.42	-28.89	1.170	-2.427
gJ01_0220	gS20090104S0085	54835.31	1.9878	5200	-2.42	-27.59	1.170	-2.423
gJ01_0230	gS20090104S0086	54835.32	1.9878	4300	-0.42	-25.18	1.170	-0.437
gJ01_0240	gS20090104S0087	54835.32	1.9878	4300	-0.42	-24.24	1.160	-0.430
gJ01_0250	gS20090104S0090	54835.32	1.9878	4300	0.33	-20.06	1.160	0.353
gJ01_0260	gS20090104S0091	54835.33	1.9878	4300	0.33	-19.06	1.160	0.360
gJ01_0270	gS20090104S0092	54835.33	1.9878	4300	-1.17	-17.72	1.160	-1.130
gJ01_0280	gS20090104S0093	54835.33	1.9878	4300	-1.17	-16.70	1.160	-1.121
gJ01_0290	gS20090104S0094	54835.33	1.9878	4300	0.33	-14.03	1.150	0.398
gJ01_0300	gS20090104S0095	54835.34	1.9878	4300	0.33	-13.04	1.150	0.405
gJ01_0310	gS20090104S0096	54835.34	1.9878	4300	-2.42	-11.77	1.150	-2.335
gJ01_0320	gS20090104S0097	54835.34	1.9878	6930	-0.42	-8.38	1.150	-0.403
gJ01_0330	gS20090104S0098	54835.35	1.9878	6930	-0.42	-6.50	1.150	-0.404
gJ01_0340	gS20090104S0099	54835.35	1.9878	6930	-0.42	-4.12	1.150	-0.408
gJ01_0350	gS20090104S0100	54835.35	1.9878	6930	-0.42	-2.24	1.150	-0.410
gJ01_0360	gS20090104S0101	54835.36	1.9878	6930	-0.42	0.14	1.150	-0.411
gJ01_0370	gS20090104S0102	54835.36	1.9878	6930	-0.42	2.03	1.150	-0.407
gJ02_0010	gS20090109S0056	54840.17	1.9902	6500	-0.42	-83.85	1.570	-0.392
gJ02_0020	gS20090109S0057	54840.17	1.9902	6500	-0.42	-83.34	1.560	-0.392
gJ02_0030	gS20090109S0058	54840.17	1.9902	6500	-0.42	-82.81	1.550	-0.392
gJ02_0040	gS20090109S0059	54840.17	1.9902	6500	-0.42	-82.28	1.540	-0.392
gJ02_0050	gS20090109S0062	54840.18	1.9902	6500	0.33	-80.16	1.510	0.358
gJ02_0060	gS20090109S0063	54840.18	1.9902	6500	0.33	-79.46	1.500	0.358
gJ02_0070	gS20090109S0064	54840.18	1.9902	6500	-1.17	-78.84	1.490	-1.142
gJ02_0080	gS20090109S0065	54840.18	1.9902	6500	-1.17	-78.29	1.480	-1.142
gJ02_0090	gS20090109S0066	54840.19	1.9902	6500	-1.17	-77.68	1.470	-1.142
gJ02_0100	gS20090109S0067	54840.19	1.9902	6500	-2.42	-76.98	1.460	-2.392
gJ02_0110	gS20090109S0068	54840.19	1.9902	6500	-2.42	-76.41	1.450	-2.392
gJ02_0120	gS20090109S0069	54840.19	1.9902	6500	-2.42	-75.61	1.440	-2.392
gJ02_0130	gS20090109S0070	54840.20	1.9902	5200	-0.42	-74.33	1.430	-0.657
gJ02_0140	gS20090109S0071	54840.20	1.9902	5200	-0.42	-73.76	1.420	-0.652
gJ02_0150	gS20090109S0074	54840.20	1.9902	5200	0.33	-71.27	1.390	0.117
gJ02_0160	gS20090109S0075	54840.21	1.9902	5200	0.33	-70.65	1.390	0.119

Continued on Next Page. . .

Table A.1 – Continued

Name[a]	Root [tgs...]	MJD	Phase	Cenwav (Å)	P^b_{Intend} ($''$)	PA[c] (	Airmass	P^d_{Actual} ($''$)
gJ02_0170	gS20090109S0076	54840.21	1.9902	5200	0.33	-70.01	1.380	0.125
gJ02_0180	gS20090109S0077	54840.21	1.9902	5200	-1.17	-69.25	1.370	-1.386
gJ02_0190	gS20090109S0078	54840.21	1.9902	5200	-1.17	-68.61	1.360	-1.380
gJ02_0200	gS20090109S0079	54840.21	1.9902	5200	-1.17	-67.87	1.350	-1.357
gJ02_0210	gS20090109S0080	54840.22	1.9902	5200	-2.42	-66.55	1.340	-2.599
gJ02_0220	gS20090109S0081	54840.22	1.9902	5200	-2.42	-65.66	1.330	-2.592
gJ02_0230	gS20090109S0082	54840.22	1.9902	4300	-0.42	-64.00	1.320	-0.848
gJ02_0240	gS20090109S0083	54840.22	1.9902	4300	-0.42	-63.35	1.320	-0.843
gJ02_0250	gS20090109S0086	54840.23	1.9902	4300	0.33	-60.47	1.300	-0.053
gJ02_0260	gS20090109S0087	54840.23	1.9902	4300	0.33	-59.79	1.290	-0.027
gJ02_0270	gS20090109S0088	54840.23	1.9902	4300	-1.17	-58.94	1.290	-1.532
gJ02_0280	gS20090109S0089	54840.24	1.9902	4300	-1.17	-58.23	1.280	-1.519
gJ02_0290	gS20090109S0090	54840.24	1.9902	4300	-2.42	-57.16	1.270	-2.752
gJ02_0300	gS20090109S0091	54840.24	1.9902	6930	-0.42	-54.76	1.260	-0.360
gJ02_0310	gS20090109S0092	54840.25	1.9902	6930	-0.42	-53.43	1.250	-0.362
gJ02_0320	gS20090109S0093	54840.25	1.9902	6930	-0.42	-51.71	1.240	-0.364
gJ02_0330	gS20090109S0094	54840.25	1.9902	6930	-0.42	-50.32	1.240	-0.365
gJ02_0340	gS20090109S0095	54840.26	1.9902	6930	-0.42	-48.55	1.230	-0.375
gJ02_0350	gS20090109S0096	54840.26	1.9902	6930	-0.42	-47.12	1.220	-0.368
gJ03_0010	gS20090112S0032	54843.27	1.9917	6500	-0.42	-39.56	1.200	-0.407
gJ03_0020	gS20090112S0033	54843.27	1.9917	6500	-0.42	-38.74	1.200	-0.407
gJ03_0030	gS20090112S0034	54843.27	1.9917	6500	-0.42	-37.89	1.190	-0.407
gJ03_0040	gS20090112S0035	54843.27	1.9917	6500	-0.42	-37.03	1.190	-0.407
gJ03_0050	gS20090112S0038	54843.28	1.9917	6500	0.33	-33.87	1.180	0.343
gJ03_0060	gS20090112S0039	54843.28	1.9917	6500	0.33	-32.99	1.180	0.343
gJ03_0070	gS20090112S0040	54843.28	1.9917	6500	-1.17	-31.98	1.180	-1.157
gJ03_0080	gS20090112S0041	54843.28	1.9917	6500	-1.17	-31.09	1.180	-1.157
gJ03_0090	gS20090112S0042	54843.28	1.9917	6500	-1.17	-30.09	1.170	-1.157
gJ03_0100	gS20090112S0043	54843.29	1.9917	6500	-2.42	-28.95	1.170	-2.407
gJ03_0110	gS20090112S0044	54843.29	1.9917	6500	-2.42	-28.02	1.170	-2.407
gJ03_0120	gS20090112S0045	54843.29	1.9917	6500	-2.42	-26.71	1.170	-2.407
gJ03_0130	gS20090112S0046	54843.29	1.9917	5200	-0.42	-24.62	1.170	-0.423
gJ03_0140	gS20090112S0047	54843.30	1.9917	5200	-0.42	-23.68	1.160	-0.419
gJ03_0150	gS20090112S0050	54843.30	1.9917	5200	0.33	-19.62	1.160	0.344
gJ03_0160	gS20090112S0051	54843.30	1.9917	5200	0.33	-18.62	1.160	0.348
gJ03_0170	gS20090112S0052	54843.31	1.9917	5200	0.33	-17.59	1.160	0.351
gJ03_0180	gS20090112S0053	54843.31	1.9917	5200	-1.17	-16.36	1.160	-1.145
gJ03_0190	gS20090112S0054	54843.31	1.9917	5200	-1.17	-15.31	1.150	-1.142
gJ03_0200	gS20090112S0055	54843.31	1.9918	5200	-1.17	-14.12	1.150	-1.137
gJ03_0210	gS20090112S0056	54843.32	1.9918	5200	-2.42	-12.01	1.150	-2.380
gJ03_0220	gS20090112S0057	54843.32	1.9918	5200	-2.42	-10.59	1.150	-2.377
gJ03_0230	gS20090112S0058	54843.32	1.9918	4300	-0.42	-7.99	1.150	-0.317

Continued on Next Page...

Table A.1 – Continued

Name^a	Root [tgs...]	MJD	Phase	Cenwav (Å)	P$^b_{\text{Intend}}$ (″)	PA^c (	Airmass	P$^d_{\text{Actual}}$ (″)
gJ03_0240	gS20090112S0059	54843.32	1.9918	4300	-0.42	-6.99	1.150	-0.310
gJ03_0250	gS20090112S0062	54843.33	1.9918	4300	0.33	-2.56	1.150	0.473
gJ03_0260	gS20090112S0063	54843.33	1.9918	4300	0.33	-1.53	1.150	0.476
gJ03_0270	gS20090112S0064	54843.33	1.9918	4300	-1.17	-0.25	1.150	-1.015
gJ03_0280	gS20090112S0065	54843.34	1.9918	4300	-1.17	0.80	1.150	-1.008
gJ03_0290	gS20090112S0066	54843.34	1.9918	4300	-2.42	2.36	1.150	-2.248
gJ03_0300	gS20090112S0067	54843.34	1.9918	6930	-0.42	5.80	1.150	-0.425
gJ03_0310	gS20090112S0068	54843.35	1.9918	6930	-0.42	7.68	1.150	-0.420
gJ03_0320	gS20090112S0069	54843.35	1.9918	6930	-0.42	10.04	1.150	-0.428
gJ03_0330	gS20090112S0070	54843.35	1.9918	6930	-0.42	11.89	1.150	-0.429
gJ03_0340	gS20090112S0071	54843.36	1.9918	6930	-0.42	14.23	1.150	-0.431
gJ03_0350	gS20090112S0072	54843.36	1.9918	6930	-0.42	16.07	1.160	-0.424
gJ04_0010	gS20090115S0173	54846.18	1.9932	6500	-0.42	-74.38	1.430	-0.398
gJ04_0020	gS20090115S0174	54846.18	1.9932	6500	-0.42	-73.81	1.420	-0.398
gJ04_0030	gS20090115S0175	54846.18	1.9932	6500	-0.42	-73.23	1.420	-0.398
gJ04_0040	gS20090115S0176	54846.18	1.9932	6500	-0.42	-72.64	1.410	-0.398
gJ04_0050	gS20090115S0179	54846.19	1.9932	6500	0.33	-70.48	1.380	0.352
gJ04_0060	gS20090115S0180	54846.19	1.9932	6500	0.33	-69.88	1.380	0.352
gJ04_0070	gS20090115S0181	54846.19	1.9932	6500	-1.17	-69.19	1.370	-1.148
gJ04_0080	gS20090115S0182	54846.19	1.9932	6500	-1.17	-68.58	1.360	-1.148
gJ04_0090	gS20090115S0183	54846.20	1.9932	6500	-1.17	-67.91	1.360	-1.148
gJ04_0100	gS20090115S0184	54846.20	1.9932	6500	-2.42	-67.13	1.350	-2.398
gJ04_0110	gS20090115S0185	54846.20	1.9932	6500	-2.42	-66.50	1.340	-2.398
gJ04_0120	gS20090115S0186	54846.20	1.9932	6500	-2.42	-65.60	1.330	-2.398
gJ04_0130	gS20090115S0187	54846.21	1.9932	5200	-0.42	-64.18	1.330	-0.593
gJ04_0140	gS20090115S0188	54846.21	1.9932	5200	-0.42	-63.53	1.320	-0.588
gJ04_0150	gS20090115S0191	54846.21	1.9932	5200	0.33	-60.72	1.300	0.179
gJ04_0160	gS20090115S0192	54846.22	1.9932	5200	0.33	-60.03	1.290	0.184
gJ04_0170	gS20090115S0193	54846.22	1.9932	5200	0.33	-59.31	1.290	0.187
gJ04_0180	gS20090115S0194	54846.22	1.9932	5200	-1.17	-58.46	1.280	-1.307
gJ04_0190	gS20090115S0195	54846.22	1.9932	5200	-1.17	-57.72	1.280	-1.304
gJ04_0200	gS20090115S0196	54846.22	1.9932	5200	-1.17	-56.88	1.270	-1.298
gJ04_0210	gS20090115S0197	54846.23	1.9932	5200	-2.42	-55.39	1.260	-2.540
gJ04_0220	gS20090115S0198	54846.23	1.9932	5200	-2.42	-54.38	1.260	-2.536
gJ04_0230	gS20090115S0199	54846.23	1.9932	4300	-0.42	-52.49	1.250	-0.695
gJ04_0240	gS20090115S0200	54846.23	1.9932	4300	-0.42	-51.76	1.250	-0.689
gJ04_0250	gS20090115S0203	54846.24	1.9932	4300	0.33	-48.46	1.230	0.100
gJ04_0260	gS20090115S0204	54846.24	1.9932	4300	0.33	-47.68	1.230	0.107
gJ04_0270	gS20090115S0205	54846.25	1.9932	4300	-1.17	-46.71	1.220	-1.380
gJ04_0280	gS20090115S0206	54846.25	1.9932	4300	-1.17	-45.90	1.220	-1.373
gJ04_0290	gS20090115S0207	54846.25	1.9932	4300	-2.42	-44.68	1.210	-2.608
gJ04_0300	gS20090115S0208	54846.25	1.9932	6930	-0.42	-41.93	1.210	-0.379

Continued on Next Page. . .

Table A.1 – Continued

Name^a	Root [tgs...]	MJD	Phase	Cenwav (Å)	P^b_{Intend} ($''$)	PA^c (	Airmass	P^d_{Actual} ($''$)
gJ04_0310	gS20090115S0209	54846.26	1.9932	6930	-0.42	-40.40	1.200	-0.387
gJ04_0320	gS20090115S0210	54846.26	1.9932	6930	-0.42	-38.43	1.190	-0.388
gJ04_0330	gS20090115S0211	54846.26	1.9932	6930	-0.42	-36.85	1.190	-0.384
gJ04_0340	gS20090115S0212	54846.27	1.9932	6930	-0.42	-34.83	1.180	-0.386
gJ04_0350	gS20090115S0213	54846.27	1.9932	6930	-0.42	-33.20	1.180	-0.387
gJ05_0010	gS20090121S0267	54852.27	1.9962	6500	-0.42	-21.66	1.160	-0.417
gJ05_0020	gS20090121S0268	54852.28	1.9962	6500	-0.42	-20.72	1.160	-0.417
gJ05_0030	gS20090121S0269	54852.28	1.9962	6500	-0.42	-19.76	1.160	-0.417
gJ05_0040	gS20090121S0270	54852.28	1.9962	6500	-0.42	-18.78	1.160	-0.417
gJ05_0050	gS20090121S0273	54852.29	1.9962	6500	0.33	-15.21	1.150	0.333
gJ05_0060	gS20090121S0274	54852.29	1.9962	6500	0.33	-14.23	1.150	0.333
gJ05_0070	gS20090121S0275	54852.29	1.9962	6500	-1.17	-13.09	1.150	-1.167
gJ05_0080	gS20090121S0276	54852.29	1.9962	6500	-1.17	-12.10	1.150	-1.167
gJ05_0090	gS20090121S0277	54852.29	1.9962	6500	-1.17	-11.00	1.150	-1.167
gJ05_0100	gS20090121S0278	54852.29	1.9962	6500	-2.42	-9.75	1.150	-2.417
gJ05_0110	gS20090121S0279	54852.30	1.9962	6500	-2.42	-8.74	1.150	-2.417
gJ05_0120	gS20090121S0280	54852.30	1.9962	6500	-2.42	-7.30	1.150	-2.417
gJ05_0130	gS20090121S0281	54852.30	1.9962	5200	-0.42	-5.04	1.150	-0.370
gJ05_0140	gS20090121S0282	54852.30	1.9962	5200	-0.42	-4.03	1.150	-0.363
gJ05_0150	gS20090121S0285	54852.31	1.9962	5200	0.33	0.29	1.150	0.396
gJ05_0160	gS20090121S0286	54852.31	1.9962	5200	0.33	1.33	1.150	0.399
gJ05_0170	gS20090121S0287	54852.31	1.9962	5200	0.33	2.41	1.150	0.402
gJ05_0180	gS20090121S0288	54852.32	1.9962	5200	-1.17	3.69	1.150	-1.088
gJ05_0190	gS20090121S0289	54852.32	1.9962	5200	-1.17	4.76	1.150	-1.085
gJ05_0200	gS20090121S0290	54852.32	1.9962	5200	-1.17	5.98	1.150	-1.087
gJ05_0210	gS20090121S0291	54852.32	1.9962	5200	-2.42	8.13	1.150	-2.331
gJ05_0220	gS20090121S0292	54852.32	1.9962	5200	-2.42	9.56	1.150	-2.327
gJ05_0230	gS20090121S0293	54852.33	1.9962	4300	-0.42	12.15	1.150	-0.187
gJ05_0240	gS20090121S0294	54852.33	1.9962	4300	-0.42	13.15	1.150	-0.180
gJ05_0250	gS20090121S0297	54852.34	1.9962	4300	0.33	17.46	1.160	0.606
gJ05_0260	gS20090121S0298	54852.34	1.9962	4300	0.33	18.45	1.160	0.612
gJ05_0270	gS20090121S0299	54852.34	1.9962	4300	-1.17	19.68	1.160	-0.881
gJ05_0280	gS20090121S0300	54852.34	1.9962	4300	-1.17	20.68	1.160	-0.875
gJ05_0290	gS20090121S0301	54852.35	1.9962	4300	-2.42	22.17	1.160	-2.116
gJ05_0300	gS20090121S0302	54852.35	1.9962	6930	-0.42	25.38	1.170	-0.449
gJ05_0310	gS20090121S0303	54852.35	1.9962	6930	-0.42	27.10	1.170	-0.450
gJ05_0320	gS20090121S0304	54852.36	1.9962	6930	-0.42	29.26	1.180	-0.452
gJ05_0330	gS20090121S0305	54852.36	1.9962	6930	-0.42	30.94	1.180	-0.453
gJ05_0340	gS20090121S0306	54852.36	1.9962	6930	-0.42	33.03	1.180	-0.454
gJ05_0350	gS20090121S0307	54852.37	1.9962	6930	-0.42	34.67	1.190	-0.443
gJ06_0010	gS20090124S0070	54855.32	1.9977	6500	-0.42	10.55	1.150	-0.421
gJ06_0020	gS20090124S0071	54855.32	1.9977	6500	-0.42	11.54	1.150	-0.421

Continued on Next Page. . .

Table A.1 – Continued

Name^a	Root [tgs...]	MJD	Phase	Cenwav (Å)	P^b_{Intend} (″)	PA^c (	Airmass	P^d_{Actual} (″)
gJ06_0030	gS20090124S0072	54855.32	1.9977	6500	-0.42	12.54	1.150	-0.421
gJ06_0040	gS20090124S0073	54855.32	1.9977	6500	-0.42	13.53	1.150	-0.421
gJ06_0050	gS20090124S0076	54855.33	1.9977	6500	-2.42	17.12	1.160	-2.421
gJ06_0060	gS20090124S0077	54855.33	1.9977	6500	-2.42	18.11	1.160	-2.421
gJ06_0070	gS20090124S0078	54855.33	1.9977	6500	-2.42	19.49	1.160	-2.421
gJ06_0080	gS20090124S0079	54855.34	1.9977	5200	-0.42	21.63	1.160	-0.296
gJ06_0090	gS20090124S0080	54855.34	1.9977	5200	-0.42	22.59	1.160	-0.294
gJ06_0100	gS20090124S0083	54855.34	1.9977	5200	-2.42	26.60	1.170	-2.280
gJ06_0110	gS20090124S0084	54855.35	1.9977	5200	-2.42	27.92	1.170	-2.277
gJ06_0120	gS20090124S0085	54855.35	1.9977	4300	-0.42	30.28	1.180	-0.066
gJ06_0130	gS20090124S0086	54855.35	1.9977	4300	-0.42	31.19	1.180	-0.049
gJ06_0140	gS20090124S0089	54855.36	1.9977	4300	-2.42	35.05	1.190	-2.031
gJ06_0150	gS20090124S0090	54855.37	1.9977	6930	-0.42	37.97	1.200	-0.462
gJ06_0160	gS20090124S0091	54855.37	1.9977	6930	-0.42	39.54	1.200	-0.463
gJ06_0170	gS20090124S0092	54855.37	1.9977	6930	-0.42	41.47	1.210	-0.465
gJ06_0180	gS20090124S0093	54855.37	1.9977	6930	-0.42	42.99	1.210	-0.466
gJ06_0190	gS20090124S0094	54855.38	1.9977	6930	-0.42	44.87	1.220	-0.468
gJ06_0200	gS20090124S0095	54855.38	1.9977	6930	-0.42	46.33	1.230	-0.469
gJ07_0010	gS20090129S0091	54860.30	2.0001	6500	-0.42	5.19	1.150	-0.420
gJ07_0020	gS20090129S0092	54860.30	2.0001	6500	-0.42	6.19	1.150	-0.420
gJ07_0030	gS20090129S0093	54860.30	2.0001	6500	-0.42	7.20	1.150	-0.420
gJ07_0040	gS20090129S0094	54860.30	2.0001	6500	-0.42	8.21	1.150	-0.420
gJ07_0050	gS20090129S0097	54860.31	2.0002	6500	0.33	11.88	1.150	0.330
gJ07_0060	gS20090129S0098	54860.31	2.0002	6500	0.33	12.87	1.150	0.330
gJ07_0070	gS20090129S0099	54860.31	2.0002	6500	0.33	13.89	1.150	0.330
gJ07_0080	gS20090129S0100	54860.31	2.0002	6500	-1.17	15.02	1.150	-1.170
gJ07_0090	gS20090129S0101	54860.31	2.0002	6500	-1.17	16.00	1.160	-1.170
gJ07_0100	gS20090129S0102	54860.32	2.0002	6500	-1.17	17.08	1.160	-1.170
gJ07_0110	gS20090129S0103	54860.32	2.0002	6500	-2.42	18.30	1.160	-2.420
gJ07_0120	gS20090129S0104	54860.32	2.0002	6500	-2.42	19.28	1.160	-2.420
gJ07_0130	gS20090129S0105	54860.32	2.0002	6500	-2.42	20.65	1.160	-2.420
gJ07_0140	gS20090129S0106	54860.32	2.0002	5200	-0.42	22.78	1.160	-0.292
gJ07_0150	gS20090129S0107	54860.33	2.0002	5200	-0.42	23.73	1.170	-0.286
gJ07_0160	gS20090129S0110	54860.33	2.0002	5200	0.33	27.70	1.170	0.474
gJ07_0170	gS20090129S0121	54860.36	2.0002	5200	-0.42	41.28	1.210	-0.239
gJ07_0180	gS20090129S0122	54860.36	2.0002	5200	-0.42	42.12	1.210	-0.238
gJ07_0190	gS20090129S0123	54860.36	2.0002	5200	-0.42	42.99	1.210	-0.236
gJ07_0200	gS20090129S0124	54860.36	2.0002	5200	-1.92	44.00	1.220	-1.729
gJ07_0210	gS20090129S0125	54860.36	2.0002	5200	-1.92	44.84	1.220	-1.728
gJ07_0220	gS20090129S0126	54860.37	2.0002	5200	-1.92	45.79	1.220	-1.726
gJ07_0230	gS20090129S0127	54860.37	2.0002	5200	-3.17	47.45	1.230	-2.985
gJ07_0240	gS20090129S0128	54860.37	2.0002	5200	-3.17	48.55	1.240	-2.962

Continued on Next Page. . .

Table A.1 – Continued

Name^a	Root [tgs...]	MJD	Phase	Cenwav (Å)	$\mathrm{P}^b_{\mathrm{Intend}}$ ($''$)	PA^c (	Airmass	$\mathrm{P}^d_{\mathrm{Actual}}$ ($''$)
gJ07_0250	gS20090129S0129	54860.38	2.0002	4300	-1.17	50.51	1.240	-0.670
gJ07_0260	gS20090129S0130	54860.38	2.0002	4300	-1.17	51.26	1.250	-0.656
gJ07_0270	gS20090129S0133	54860.39	2.0002	4300	-0.42	54.45	1.260	0.115
gJ07_0280	gS20090129S0134	54860.39	2.0002	4300	-0.42	55.18	1.270	0.128
gJ07_0290	gS20090129S0135	54860.39	2.0002	4300	-1.92	56.06	1.270	-1.370
gJ07_0300	gS20090129S0136	54860.39	2.0002	4300	-1.92	56.79	1.280	-1.356
gJ07_0310	gS20090129S0137	54860.39	2.0002	4300	-3.17	57.87	1.290	-2.592
gJ07_0320	gS20090130S0086	54861.33	2.0007	6930	-0.42	27.81	1.170	-0.454
gJ07_0330	gS20090130S0087	54861.33	2.0007	6930	-0.42	29.50	1.180	-0.455
gJ07_0340	gS20090130S0088	54861.34	2.0007	6930	-0.42	31.62	1.180	-0.468
gJ07_0350	gS20090130S0089	54861.34	2.0007	6930	-0.42	33.27	1.190	-0.470
gJ07_0360	gS20090130S0090	54861.34	2.0007	6930	-0.42	35.31	1.190	-0.471
gJ07_0370	gS20090130S0091	54861.35	2.0007	6930	-0.42	36.91	1.190	-0.459
gJ09_0010	gS20090205S0029	54867.20	2.0036	6500	-0.42	-42.70	1.210	-0.411
gJ09_0020	gS20090205S0030	54867.20	2.0036	6500	-0.42	-41.90	1.210	-0.411
gJ09_0030	gS20090205S0031	54867.20	2.0036	6500	0.33	-41.02	1.200	0.339
gJ09_0040	gS20090205S0032	54867.20	2.0036	6500	0.33	-40.19	1.200	0.339
gJ09_0050	gS20090205S0033	54867.20	2.0036	6500	-1.17	-39.24	1.200	-1.161
gJ09_0060	gS20090205S0034	54867.20	2.0036	6500	-1.17	-38.40	1.200	-1.161
gJ09_0070	gS20090205S0035	54867.21	2.0036	6500	-1.17	-37.47	1.190	-1.161
gJ09_0080	gS20090205S0036	54867.21	2.0036	6500	-2.42	-36.39	1.190	-2.411
gJ09_0090	gS20090205S0037	54867.21	2.0036	6500	-2.42	-35.52	1.190	-2.411
gJ09_0100	gS20090205S0038	54867.21	2.0036	6500	-2.42	-34.28	1.180	-2.411
gJ09_0110	gS20090205S0041	54867.22	2.0036	5200	-0.42	-29.49	1.170	-0.445
gJ09_0120	gS20090205S0042	54867.22	2.0036	5200	-0.42	-28.59	1.170	-0.440
gJ09_0130	gS20090205S0043	54867.22	2.0036	5200	0.33	-27.62	1.170	0.313
gJ09_0140	gS20090205S0044	54867.23	2.0036	5200	0.33	-26.67	1.170	0.316
gJ09_0150	gS20090205S0045	54867.23	2.0036	5200	0.33	-25.67	1.170	0.320
gJ09_0160	gS20090205S0046	54867.23	2.0036	5200	-1.17	-24.50	1.170	-1.176
gJ09_0170	gS20090205S0047	54867.23	2.0036	5200	-1.17	-23.50	1.160	-1.172
gJ09_0180	gS20090205S0048	54867.23	2.0036	5200	-1.17	-22.34	1.160	-1.169
gJ09_0190	gS20090205S0049	54867.24	2.0036	5200	-2.42	-20.32	1.160	-2.412
gJ09_0200	gS20090205S0050	54867.24	2.0036	5200	-2.42	-18.94	1.160	-2.408
gJ09_0210	gS20090205S0053	54867.25	2.0036	4300	-0.42	-13.22	1.150	-0.360
gJ09_0220	gS20090205S0054	54867.25	2.0036	4300	-0.42	-12.22	1.150	-0.352
gJ09_0230	gS20090205S0055	54867.25	2.0036	4300	0.33	-11.17	1.150	0.405
gJ09_0240	gS20090205S0056	54867.25	2.0036	4300	0.33	-10.16	1.150	0.411
gJ09_0250	gS20090205S0057	54867.25	2.0036	4300	-1.17	-8.89	1.150	-1.080
gJ09_0260	gS20090205S0058	54867.26	2.0036	4300	-1.17	-7.84	1.150	-1.070
gJ09_0270	gS20090205S0059	54867.26	2.0036	4300	-2.42	-6.29	1.150	-2.308
gJ09_0280	gS20090205S0060	54867.26	2.0036	6920	-0.42	-2.86	1.150	-0.419
gJ09_0290	gS20090205S0061	54867.27	2.0036	6920	-0.42	-0.97	1.150	-0.425

Continued on Next Page. . .

Table A.1 – Continued

Name^a	Root	MJD	Phase	Cenwav	$P^b_{\rm Intend}$	PA^c	Airmass	$P^d_{\rm Actual}$
	[tgs...]			(Å)	($''$)	(		($''$)
gJ09_0300	gS20090205S0062	54867.27	2.0036	6920	-0.42	1.40	1.150	-0.426
gJ09_0310	gS20090205S0063	54867.27	2.0036	6920	-0.42	3.29	1.150	-0.428
gJ09_0320	gS20090205S0064	54867.28	2.0036	6920	-0.42	5.66	1.150	-0.429
gJ09_0330	gS20090205S0065	54867.28	2.0036	6920	-0.42	7.53	1.150	-0.430
gJ13_0010	gS20090219S0063	54881.20	2.0105	6500	-0.42	-21.53	1.160	-0.416
gJ13_0020	gS20090219S0064	54881.20	2.0105	6500	-0.42	-20.57	1.160	-0.416
gJ13_0030	gS20090219S0065	54881.20	2.0105	6500	0.33	-19.55	1.160	0.334
gJ13_0040	gS20090219S0066	54881.20	2.0105	6500	0.33	-18.58	1.160	0.334
gJ13_0050	gS20090219S0067	54881.20	2.0105	6500	-1.17	-17.46	1.160	-1.166
gJ13_0060	gS20090219S0068	54881.20	2.0105	6500	-1.17	-16.49	1.160	-1.166
gJ13_0070	gS20090219S0069	54881.21	2.0105	6500	-1.17	-15.41	1.150	-1.166
gJ13_0080	gS20090219S0070	54881.21	2.0105	6500	-2.42	-14.19	1.150	-2.416
gJ13_0090	gS20090219S0071	54881.21	2.0105	6500	-2.42	-13.18	1.150	-2.416
gJ13_0100	gS20090219S0072	54881.21	2.0105	6500	-2.42	-11.76	1.150	-2.416
gJ13_0110	gS20090219S0075	54881.22	2.0105	5200	-0.42	-6.39	1.150	-0.373
gJ13_0120	gS20090219S0076	54881.22	2.0105	5200	-0.42	-5.37	1.150	-0.370
gJ13_0130	gS20090219S0077	54881.22	2.0105	5200	0.33	-4.30	1.150	0.387
gJ13_0140	gS20090219S0078	54881.23	2.0105	5200	0.33	-3.26	1.150	0.390
gJ13_0150	gS20090219S0079	54881.23	2.0105	5200	0.33	-2.18	1.150	0.390
gJ13_0160	gS20090219S0080	54881.23	2.0105	5200	-1.17	-0.91	1.150	-1.107
gJ13_0170	gS20090219S0081	54881.23	2.0105	5200	-1.17	0.17	1.150	-1.103
gJ13_0180	gS20090219S0082	54881.23	2.0105	5200	-1.17	1.40	1.150	-1.100
gJ13_0190	gS20090219S0083	54881.24	2.0105	5200	-2.42	3.55	1.150	-2.343
gJ13_0200	gS20090219S0084	54881.24	2.0105	5200	-2.42	4.99	1.150	-2.339
gJ13_0210	gS20090219S0087	54881.25	2.0105	4300	-0.42	10.86	1.150	-0.194
gJ13_0220	gS20090219S0088	54881.25	2.0105	4300	-0.42	11.86	1.150	-0.188
gJ13_0230	gS20090219S0089	54881.25	2.0105	4300	0.33	12.91	1.150	0.569
gJ13_0240	gS20090219S0090	54881.25	2.0105	4300	0.33	13.91	1.150	0.575
gJ13_0250	gS20090219S0091	54881.25	2.0105	4300	-1.17	15.14	1.150	-0.917
gJ13_0260	gS20090219S0092	54881.26	2.0105	4300	-1.17	16.16	1.160	-0.902
gJ13_0270	gS20090219S0093	54881.26	2.0105	4300	-2.42	17.69	1.160	-2.142
gJ13_0280	gS20090219S0094	54881.26	2.0105	6920	-0.42	20.96	1.160	-0.435
gJ13_0290	gS20090219S0095	54881.27	2.0105	6920	-0.42	22.74	1.160	-0.445
gJ13_0300	gS20090219S0096	54881.27	2.0105	6920	-0.42	24.96	1.170	-0.448
gJ13_0310	gS20090219S0097	54881.27	2.0105	6920	-0.42	26.69	1.170	-0.449
gJ13_0320	gS20090219S0098	54881.28	2.0105	6920	-0.42	28.85	1.180	-0.451
gJ13_0330	gS20090219S0099	54881.28	2.0105	6920	-0.42	30.54	1.180	-0.452
gJ20_0010	gS20090317S0067	54907.26	2.0234	6500	-0.42	56.79	1.280	-0.451
gJ20_0020	gS20090317S0068	54907.26	2.0234	6500	-0.42	57.49	1.280	-0.451
gJ20_0030	gS20090317S0073	54907.27	2.0234	5200	-0.42	62.09	1.310	-0.162
gJ20_0040	gS20090317S0074	54907.28	2.0234	5200	-0.42	62.75	1.320	-0.157
gJ20_0050	gS20090317S0075	54907.28	2.0234	4300	-0.42	63.50	1.320	0.181

Continued on Next Page. . .

Table A.1 – Continued

Name^a	Root [tgs...]	MJD	Phase	Cenwav (Å)	$\mathrm{P}^{b}_{\mathrm{Intend}}$ ($''$)	PA^c (	Airmass	$\mathrm{P}^{d}_{\mathrm{Actual}}$ ($''$)
gJ20_0060	gS20090317S0076	54907.28	2.0234	4300	-0.42	64.15	1.330	0.192
gJ32_0010	gS20090428S0044	54949.04	2.0440	6500	-0.42	-6.09	1.150	-0.421
gJ32_0020	gS20090428S0045	54949.04	2.0440	6500	-0.42	-5.08	1.150	-0.421
gJ32_0030	gS20090428S0046	54949.04	2.0440	6500	0.33	-4.01	1.150	0.329
gJ32_0040	gS20090428S0047	54949.04	2.0440	6500	0.33	-2.99	1.150	0.329
gJ32_0050	gS20090428S0048	54949.04	2.0440	6500	-1.17	-1.84	1.150	-1.171
gJ32_0060	gS20090428S0049	54949.04	2.0440	6500	-1.17	-0.83	1.150	-1.171
gJ32_0070	gS20090428S0050	54949.05	2.0440	6500	-1.17	0.29	1.150	-1.171
gJ32_0080	gS20090428S0051	54949.05	2.0440	6500	-2.42	1.57	1.150	-2.421
gJ32_0090	gS20090428S0052	54949.05	2.0440	6500	-2.42	2.60	1.150	-2.421
gJ32_0100	gS20090428S0053	54949.05	2.0440	6500	-2.42	4.04	1.150	-2.421
gJ32_0110	gS20090428S0056	54949.06	2.0440	5200	-0.42	9.46	1.150	-0.325
gJ32_0120	gS20090428S0057	54949.06	2.0440	5200	-0.42	10.46	1.150	-0.329
gJ32_0130	gS20090428S0058	54949.06	2.0440	5200	0.33	11.51	1.150	0.424
gJ32_0140	gS20090428S0059	54949.06	2.0440	5200	0.33	12.54	1.150	0.427
gJ32_0150	gS20090428S0060	54949.07	2.0440	5200	0.33	13.59	1.150	0.429
gJ32_0160	gS20090428S0061	54949.07	2.0440	5200	-1.17	14.83	1.150	-1.067
gJ32_0170	gS20090428S0062	54949.07	2.0440	5200	-1.17	15.88	1.160	-1.061
gJ32_0180	gS20090428S0063	54949.07	2.0440	5200	-1.17	17.07	1.160	-1.058
gJ32_0190	gS20090428S0064	54949.08	2.0440	5200	-2.42	19.12	1.160	-2.302
gJ32_0200	gS20090428S0065	54949.08	2.0440	5200	-2.42	20.51	1.160	-2.299
gJ32_0210	gS20090428S0068	54949.09	2.0440	4300	-0.42	26.05	1.170	-0.088
gJ32_0220	gS20090428S0069	54949.09	2.0440	4300	-0.42	26.98	1.170	-0.083
gJ32_0230	gS20090428S0070	54949.09	2.0440	4300	0.33	27.96	1.170	0.673
gJ32_0240	gS20090428S0071	54949.09	2.0440	4300	0.33	28.89	1.170	0.678
gJ32_0250	gS20090428S0072	54949.09	2.0440	4300	-1.17	30.02	1.180	-0.805
gJ32_0260	gS20090428S0073	54949.10	2.0440	4300	-1.17	30.97	1.180	-0.812
gJ32_0270	gS20090428S0074	54949.10	2.0440	4300	-2.42	32.35	1.180	-2.055
gJ32_0280	gS20090428S0075	54949.10	2.0440	6920	-0.42	35.33	1.190	-0.460
gJ32_0290	gS20090428S0076	54949.11	2.0440	6920	-0.42	36.93	1.190	-0.461
gJ32_0300	gS20090428S0077	54949.11	2.0440	6920	-0.42	38.92	1.200	-0.449
gJ32_0310	gS20090428S0078	54949.11	2.0441	6920	-0.42	40.48	1.210	-0.465
gJ32_0320	gS20090428S0079	54949.12	2.0441	6920	-0.42	42.40	1.210	-0.466
gJ32_0330	gS20090428S0080	54949.12	2.0441	6920	-0.42	43.90	1.220	-0.452
gJ56_0010	gS20090724S0023	55035.97	2.0870	6500	-0.42	78.67	1.490	-0.471
gJ56_0020	gS20090724S0024	55035.97	2.0870	6500	-0.42	79.21	1.500	-0.471
gJ56_0030	gS20090724S0025	55035.97	2.0870	6500	0.33	79.79	1.510	0.279
gJ56_0040	gS20090724S0026	55035.97	2.0870	6500	0.33	80.33	1.520	0.279
gJ56_0050	gS20090724S0027	55035.97	2.0870	6500	-1.17	80.92	1.530	-1.221
gJ56_0060	gS20090724S0028	55035.97	2.0870	6500	-1.17	81.45	1.540	-1.221
gJ56_0070	gS20090724S0029	55035.98	2.0870	6500	-1.17	82.04	1.550	-1.221
gJ56_0080	gS20090724S0030	55035.98	2.0870	6500	-2.42	82.69	1.560	-2.471

Continued on Next Page. . .

Table A.1 – Continued

Name^{a}	Root [tgs...]	MJD	Phase	Cenwav (Å)	P$^{b}_{\text{Intend}}$ ($''$)	PA^{c} (	Airmass	P$^{d}_{\text{Actual}}$ ($''$)
gJ56_0090	gS20090724S0031	55035.98	2.0870	6500	-2.42	83.23	1.570	-2.471
gJ56_0100	gS20090724S0032	55035.98	2.0870	6500	-2.42	83.97	1.590	-2.471
gJ56_0110	gS20090724S0035	55035.99	2.0870	5200	-0.42	86.73	1.640	-0.042
gJ56_0120	gS20090724S0036	55035.99	2.0870	5200	-0.42	87.23	1.650	-0.039
gJ56_0130	gS20090724S0037	55035.99	2.0870	5200	0.33	87.77	1.660	0.713
gJ56_0140	gS20090724S0038	55036.00	2.0870	5200	0.33	88.27	1.670	0.716
gJ56_0150	gS20090724S0039	55036.00	2.0870	5200	0.33	88.79	1.680	0.719
gJ56_0160	gS20090724S0040	55036.00	2.0870	5200	-1.17	89.36	1.700	-0.775
gJ56_0170	gS20090724S0041	55036.00	2.0870	5200	-1.17	89.88	1.710	-0.772
gJ56_0180	gS20090724S0042	55036.00	2.0870	5200	-1.17	89.51	1.730	-0.763
gJ56_0190	gS20090724S0043	55036.01	2.0870	5200	-2.42	88.46	1.750	-2.002
gJ56_0200	gS20090724S0044	55036.01	2.0870	5200	-2.42	87.77	1.780	-1.988
gJ56_0210	gS20090724S0047	55036.02	2.0870	4300	-0.42	84.94	1.850	0.712
gJ56_0220	gS20090724S0048	55036.02	2.0870	4300	-0.42	84.45	1.860	0.724
gJ56_0230	gS20090724S0049	55036.02	2.0870	4300	0.33	83.95	1.880	1.457
gJ56_0240	gS20090724S0050	55036.02	2.0870	4300	0.33	83.47	1.890	1.468
gJ56_0250	gS20090724S0051	55036.02	2.0870	4300	0.33	82.99	1.910	1.527
gJ56_0260	gS20090724S0052	55036.03	2.0870	4300	-1.17	82.45	1.930	0.047
gJ56_0270	gS20090724S0053	55036.03	2.0870	4300	-1.17	81.95	1.950	0.027
gJ56_0280	gS20090724S0054	55036.03	2.0870	4300	-2.42	81.23	1.990	-1.185
gJ56_0290	gS20090724S0055	55036.04	2.0870	6920	-0.42	79.63	2.030	-0.599
gJ56_0300	gS20090724S0056	55036.04	2.0870	6920	-0.42	78.77	2.070	-0.603
gJ56_0310	gS20090724S0057	55036.04	2.0870	6920	-0.42	77.68	2.110	-0.607
gJ56_0320	gS20090724S0058	55036.05	2.0870	6920	-0.42	76.82	2.150	-0.610
gJ56_0330	gS20090724S0059	55036.05	2.0870	6920	-0.42	75.73	2.200	-0.615
gJ56_0340	gS20090724S0060	55036.05	2.0870	6920	-0.42	74.87	2.240	-0.618
gK02_0010	gS20100108S0049	55204.30	2.1702	6500	0.00	-26.17	1.170	-0.005
gK02_0020	gS20100108S0050	55204.30	2.1702	6500	0.00	-25.25	1.170	-0.005
gK02_0030	gS20100108S0051	55204.31	2.1702	6500	0.75	-24.26	1.170	0.745
gK02_0040	gS20100108S0052	55204.31	2.1702	6500	0.75	-23.32	1.160	0.745
gK02_0050	gS20100108S0053	55204.31	2.1702	6500	0.75	-22.37	1.160	0.745
gK02_0060	gS20100108S0054	55204.31	2.1702	6500	-0.75	-21.18	1.160	-0.755
gK02_0070	gS20100108S0055	55204.31	2.1702	6500	-0.75	-20.22	1.160	-0.755
gK02_0080	gS20100108S0056	55204.31	2.1702	6500	-0.75	-19.25	1.160	-0.755
gK02_0090	gS20100108S0059	55204.32	2.1702	5200	0.00	-14.88	1.150	0.011
gK02_0100	gS20100108S0060	55204.32	2.1702	5200	0.00	-13.90	1.150	0.014
gK02_0110	gS20100108S0061	55204.33	2.1702	5200	0.75	-12.85	1.150	0.769
gK02_0120	gS20100108S0062	55204.33	2.1702	5200	0.75	-11.86	1.150	0.773
gK02_0130	gS20100108S0063	55204.33	2.1702	5200	0.75	-10.86	1.150	0.774
gK02_0140	gS20100108S0064	55204.33	2.1702	5200	-0.75	-9.60	1.150	-0.720
gK02_0150	gS20100108S0065	55204.33	2.1702	5200	-0.75	-8.60	1.150	-0.716
gK02_0160	gS20100108S0066	55204.33	2.1702	5200	-0.75	-7.59	1.150	-0.716

Continued on Next Page. . .

Table A.1 – Continued

Name[a]	Root [tgs...]	MJD	Phase	Cenwav (Å)	P^{b}_{Intend} ($''$)	PA[c] (	Airmass	P^{d}_{Actual} ($''$)
gK02_0170	gS20100108S0069	55204.34	2.1702	4300	0.00	-2.96	1.150	0.122
gK02_0180	gS20100108S0070	55204.35	2.1702	4300	0.00	0.02	1.150	0.143
gK02_0190	gS20100108S0071	55204.35	2.1702	4300	0.75	1.16	1.150	0.896
gK02_0200	gS20100108S0072	55204.35	2.1702	4300	0.75	2.17	1.150	0.903
gK02_0210	gS20100108S0073	55204.35	2.1702	4300	0.75	3.19	1.150	0.915
gK02_0220	gS20100108S0074	55204.35	2.1702	4300	-0.75	4.45	1.150	-0.582
gK02_0230	gS20100108S0075	55204.35	2.1702	4300	-0.75	5.46	1.150	-0.575
gK02_0240	gS20100108S0076	55204.36	2.1702	4300	-0.75	6.48	1.150	-0.568
gK02_0250	gS20100108S0077	55204.36	2.1702	6500	-2.00	7.85	1.150	-2.005
gK02_0260	gS20100108S0078	55204.36	2.1702	6500	-2.00	8.87	1.150	-2.005
gK02_0270	gS20100108S0079	55204.36	2.1702	6500	-2.00	10.29	1.150	-2.005
gK05_0010	gS20100120S0107	55216.26	2.1761	6500	-2.00	-31.18	1.180	-1.993
gK05_0020	gS20100120S0110	55216.27	2.1761	6500	-2.00	-27.31	1.170	-1.993
gK05_0030	gS20100120S0113	55216.28	2.1761	6500	-2.00	-22.96	1.160	-1.993
gK05_0040	gS20100120S0116	55216.28	2.1761	5200	-2.00	-17.83	1.160	-1.986
gK05_0050	gS20100120S0119	55216.29	2.1761	5200	-2.00	-13.27	1.150	-1.972

[a] Name given by Treasury Project.

[b] Offset along the P axis as intended in Phase II.

[c] Parallactic angle.

[d] Actual offset along the P axis taken into account atmospheric refraction and blind offset issues.

Appendix B

Definitions

Phase In this thesis, “phase” in the 5.54-year cycle is that used in the Eta Carinae Car HST Treasury Program archive: $P = 2023.0$ days, $t_0 =$ MJD 50814.0 = J1998.0 exactly. This zero point corresponds to phase ≈ 0.009 in a system proposed by Damineli et al. (2008b). Zero points based on specific phenomena in the spectroscopic events should be avoided for two reasons: The 1998.0, 2003.5, and 2009.0 “events” differed in major respects, and, also, successive revisions of t_0 have made comparisons among papers more difficult. All proposed orbit models are far too imprecise to be useful in this regard. The Treasury Program phase definition, on the other hand, has been extant *without alteration* for a number of years and its period is consistent with observations. Considering that the Treasury Program archive is the largest available set of data on η Car, it is the obvious reference standard. Phases 0.00, 1.00, and 2.00 mark the 1998.0, 2003.5, and 2009.0 spectroscopic events.

Wavelengths and Velocities Throughout this thesis I quote vacuum wavelengths and heliocentric Doppler velocities.